Title
Reliability Analysis of the Influence of Vegetation on Levee Performance

Author
Lanzafame, Robert C

Publication Date
2017

Peer reviewed|Thesis/dissertation

Reliability Analysis of the Influence of Vegetation on Levee Performance

By

Robert C Lanzafame

A dissertation submitted in partial satisfaction of the

requirements for the degree of

Doctor of Philosophy

in

Engineering – Civil and Environmental Engineering

in the

Graduate Division

of the

University of California, Berkeley

Committee in charge:

Professor Nicholas Sitar, Chair
Professor Raymond Seed
Professor William Dietrich

Fall 2017

Abstract

Reliability Analysis of the Influence of Vegetation on Levee Performance

by

Robert C Lanzafame

Doctor of Philosophy in Engineering – Civil and Environmental Engineering

University of California, Berkeley

Professor Nicholas Sitar, Chair

Much of the Central Valley of California is protected from flooding by levees, which can fail in numerous ways. Vegetation, including large trees, has been allowed to grow over many miles of levee, and although there is no case history of a tree leading directly to levee failure, vegetation is considered a low-level risk factor that could lead to failure. Due to the complexity and inherent variability of trees and their root systems, the influence of vegetation is generally not considered in engineering evaluations of levees. Thus, the objective of this research was to quantify the incremental effect on levee performance due to trees, through an assessment of root reinforcement, weight and wind loads in the context of seepage and stability analyses.

The model levee selected for analyses represents typical conditions found in the Pocket neighborhood of Sacramento. The levee is 5.2 m (17 ft) high with 2.5:1 H:V slopes and it is a sandy embankment underlain by a relatively low hydraulic conductivity cohesive blanket layer and sandy aquifer with an open hydraulic connection to the Sacramento River. Steady-state seepage analyses were used to evaluate pore pressures that concentrate in the blanket layer and reduce effective stress, controlling blanket layer strength. Stability of the levee slope was evaluated using Spencer's Method of slices to compute factor of safety (FS).

Previous work evaluating vegetation effects for slope stability analyses focuses on the root reinforcement of shallow sliding surfaces on steep slopes. If more complex slope failures are considered the spatial distribution of roots and their properties is often simplified. To properly assess the influence of vegetation the three-dimensional distribution of roots must be incorporated into a stability model. This is accomplished by the development of a biomass model that estimates key tree parameters from trunk diameter at breast height, including maximum lateral and vertical limits and the spatial distribution of root density and volume. The biomass model is supported by published allometric data for woody vegetation, with an emphasis placed on data from the Central Valley, and is incorporated into the stability model.

Reinforcement of roots in the slope is incorporated as an increase in soil cohesion and quantified proportionally to root area ratio, as estimated by the biomass model. Strength of individual roots is implicitly included by applying a probability distribution to root reinforcement representing the range of likely values; root diameter, orientation and tensile strength are not included explicitly in the biomass or slope stability models. When effective soil cohesion due to root reinforcement is unrealistically high, or prevents a solution for FS from being reached by the slope

stability model, limits on maximum values are defined which can be related to the expected reinforcement capacity of roots due to pullout and breakage (i.e., insufficient root-soil friction and root rupture, respectively). The root ball represents the highest density of a root system and is considered to be the area where weight and wind loads are transferred to the soil. Measurements of root pits from windthrow events are used to define the size of the root ball. Wind loads are implemented as horizontal and vertical forces that are equivalent to the ultimate moment that a tree can carry prior to uprooting. To address the three-dimensional interaction of slope failures and root distribution, two-dimensional analyses are used that incorporate tree spacing in the plane-strain direction to determine average values of vegetation effects.

Variability and complexity of seepage, strength and vegetation parameters considered herein are well-suited to evaluation with probabilistic analysis. Probability distributions are selected for fifteen parameters and the first-order reliability method (FORM) is used to evaluate probability that $FS \leq 1.0$ for seepage and stability. The FORM algorithm is specifically tailored to provide an invariant solution for the class of problems considered, at the cost of increasing computation time and complexity in numerical software. In addition to probability, FORM output includes an estimate of the most likely conditions at failure (the design point) and importance and sensitivity measures that rank the relative impact that each parameter input has on the solution. Fragility curves are developed by completing a FORM analysis at multiple levels of water level, illustrating the aleatory uncertainty in levee stability. Sensitivity measures are used to quantify the epistemic uncertainty in levee stability, represented by a one standard deviation confidence interval for fragility or FS.

Overall, vegetation effects are found to have a relatively small impact on levee stability with respect to seepage and strength parameters, producing ΔFS on the order of ± 0.1 for most cases. Incremental effects are generally positive, although tree location and position can be chosen to produce adverse conditions. Root reinforcement has the biggest effect on stability, with breakage and pullout limits for effective cohesion playing a significant role in the magnitude of ΔFS. When vegetation is applied to a potential sliding surface ΔFS is generally over estimated if a new minimum FS surface search is not performed. Non-circular surfaces are necessary to find a sliding surface geometry that is capable of avoiding the root reinforcement zone that can cause a misleadingly high estimate of FS. Tree weight increases linearly from $\Delta FS < 0$ with a tree at the levee crest to $\Delta FS > 0$ as the tree is moved downslope. Wind loads generally have small effect in comparison to the sliding mass of a slope failure and are found to produce $|\Delta FS| \lesssim \pm 0.1$ for the upslope and downslope direction.

Reliability results are consistent with deterministic analyses of levee stability. Importance measures indicate vegetation random variables have a small effect on stability in comparison to seepage and strength parameters. The most likely conditions expected for a slope failure occurrence (i.e., the design point) are essentially identical between reliability analyses with and without vegetation. An exception is the increased importance of root density and effective cohesion when a tree is located near the entry or exit point of a sliding surface; however, searches for alternative sliding surfaces that minimize factor of safety illustrate the ease with which slope failures can avoid high density root zones. Fragility curves decrease when vegetation effects are included but remain within the one standard deviation confidence bounds on fragility, illustrating the uncertainty in strength and seepage parameters has a bigger effect on levee performance than the effect of vegetation overall.

Contents

List of Figures

List of Tables

Acknowledgements

This research was funded by the California Levee Vegetation Research Program, lead by the Department of Water Resources. Much of the work in this dissertation is influenced by the thoughtful review of CLVRP advisors, particularly Ray Costa, Les Harder, Mick Klasson and George Qualley, as well as reviewers Alison Berry, Jon Bray, David Ford, Steve Mahnke, Arul Rajendram, Scott Shewbridge and Doug Shields. Special thanks goes to CLVRP Program Manager Cassandra Musto, without whom I can't imagine how this project would have been accomplished. Throughout this project I have benefited from many conversations with people of all backgrounds about vegetation on levees, and while they have helped shape my research, it would be impossible to thank them all.

I am deeply grateful for the guidance and opportunity provided by my supervisor, Professor Nicholas Sitar, ever since I walked into his office and asked to study levees and probability. Thank you for always being available when needed and for opening your home to my wife and I. Perhaps my only regret is that I wasn't around when you had a sailboat.

My graduate studies were greatly enhanced by Professors Dietrich, Kayen, Seed and Sitar, who not only inspired me with their passion for teaching, but also allowed me to contribute in their courses as a graduate student instructor. I hope I am able to pass on their lessons to others in the future. To all of my classmates in the geotechnical group: thank you for your companionship, advice and open ears over the years.

The support of all my family has imparted constant motivation to succeed, whether through encouragement and conversation at family gatherings, or by providing an exceptional "field office" in Alaska. To my parents: thank you for always supporting me, there is no way I could have accomplished this without you. I save the last, shortest, but most sincere expression of gratitude for my wife, Jessica. Thank you, especially, for tolerating me.

Chapter 1

Introduction

Levees are a critical component of the flood control system protecting the Central Valley of California. Historically, vegetation, including large trees, has been allowed to grow along many miles providing habitat for a variety of wildlife. In the past, engineering evaluation of levees has tended to neglect a quantitative assessment of vegetation, tree roots in particular, when evaluating overall levee performance due to the complexity of root-soil interaction and the highly variable subsurface conditions. While there is little evidence that vegetation directly causes or contributes to levee failures (Punyamurthula et al., 2011), scenarios can be hypothesized where vegetation *could* influence levee performance such that a failure resulting in flooding eventually occurs. The recognition of this potential issue has led to significant recent research efforts to obtain data on woody vegetation that can be used to better understand these conditions (Shields, 2014). Although vegetation influences many failure modes, in this study the focus is on seepage and stability. Specifically, the objective is to quantify the incremental effects of vegetation on levee performance due to the influence of tree size, location, weight and root density using seepage, stability and reliability analysis.

Levee Function and Performance

Levees or embankments, are earthen structures constructed to protect an area of land from flooding during a period of high water. In contrast to dams, typical levees are significantly longer than their width or height, retaining water only occasionally, during floods. Since first established in the mid-nineteenth century, most levees in California have been continually enlarged and lengthened responding to changing land use and changing regulatory environment (Kelley, 1998; Seed et al., 2012). Due to their location on a flood plain and in proximity to active stream channels, the foundation soils underlying a levee are unconsolidated floodplain deposits ranging in size from cobbles and gravel to clay, which can change character dramatically over a short distance (e.g., DWR, 2012a). The most common mechanism of failure is, of course, overtopping when the flood exceeds the height of the levee. Once overtopped, a levee rapidly erodes and a breach develops. Other common failure mechanism s are piping, i.e. internal erosion caused by seepage through or under the levee, and, less frequently, slope failures induced by seepage through the levee (e.g., ASCE, 2010). In addition to these common modes of failure many other conditions exist that can lead to failure, such as penetrations (e.g., pipes), mammal burrows, wave erosion and/or vegetation (DWR, 2012a). During periods of high water a hydraulic head difference exists between the wa-

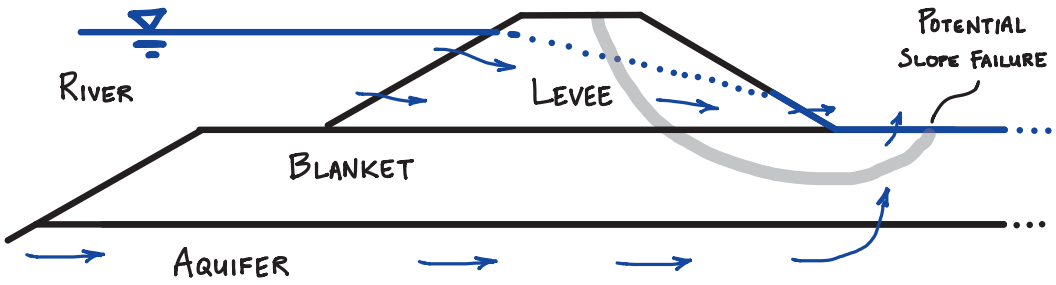

Figure 1.1: Conceptual representation of the model levee analyzed in this research. Hydraulic head from channel flows primarily to landside through levee and aquifer soil layers. Blanket layer condition is characterized by a relatively low hydraulic conductivity clay soil layer that concentrates pore pressures and reduces strength, increasing likelihood of slope instability. A potential sliding surface is illustrated by the gray line and dominant seepage paths through levee and aquifer illustrated by blue arrows. Phreatic surface is within earthen embankment and exits slope on landside face, as well as landside ground surface.

terside (i.e., river channel) and landside of a levee, inducing flow through the embankment and the foundation (e.g., Harr, 2012; Cedergren, 1997). The resulting seepage forces and pore pressures negatively influence stability of the slope by adding to the driving force and reducing soil strength, respectively (e.g., Duncan & Wright, 2005; Holtz & Kovacs, 1981).

Slope stability failures occur when the driving force on a slope (i.e., weight) exceeds the resisting force, provided primarily by shear strength of soil. A key component of a slope evaluation is to identify the "critical" potential sliding surface, which is geometrically defined by the specific potential failure plane that produces the lowest factor of safety against sliding (Duncan & Wright, 2005).

The levee model considered in this research includes a blanket layer of relatively low hydraulic conductivity clay soil that is typical of flood plain environment overbank deposits (aquifer; USACE, 1956), as illustrated in Figure 1.1. Due to the hydraulic conductivity, the blanket layer has the highest resistance to flow and as a result can induce high pore pressures, reducing soil strength that can lead to a slope stability failure (e.g., USACE, 1956, 2005). Depending on the seepage and strength characteristics of the embankment, the critical sliding surface can take on a variety of shapes and orientations (Duncan & Wright, 2005). Thus, slope stability is an important component of levee design and maintenance (DWR, 2012c), and it is prudent to consider the influence all potential risk factors on levee stability, including vegetation.

Levees and Vegetation

Although vegetation has been identified as a relatively low risk factor for levee failure (DWR, 2012a), there is still a need to understand its influence on levee failure mechanisms through updated geotechnical models that include root architecture and risk analysis methods (CLVRP, 2011). Past research related to the influence of vegetation on slope stability primarily focuses on the effect of root reinforcement, especially for steep slopes with shallow soil layers (Bellugi et al., 2015; Gray & Sotir, 1996; Montgomery et al., 2009; Schwarz et al., 2010) or of riverbank stability (Gray

& MacDonald, 1989; Pollen & Simon, 2005; Pollen-Bankhead et al., 2013; Thorne, 1990). This approach highlighted the importance of root reinforcement for shallow surfaces, but generally used simplified models of root density and effective cohesion for the entire slope. More sophisticated analysis methods have been used to evaluate the complexity of biomass in the subsurface for general slopes, but they either do not incorporate seepage forces or the various loads that are applied by a tree are greatly simplified (Greenwood, 2006; Kokutse et al., 2016; Roering et al., 2003), which are needed for proper evaluation of levee performance (e.g., Shields, 2014).

In contrast to the positive reinforcing effect of tree roots, the weight and wind loads from trees can have either a positive or a negative effect on slope stability depending on several factors (Gray & Sotir, 1996). In general, loads placed at the top of a slope tend to have a destabilizing effect whereas those placed at the bottom are reinforcing. The overall magnitude of load effects are dependent on the size of a potential sliding mass as well as pore pressures, which influence strength along the sliding surface. Wind loads further complicate the situation as they apply a moment to the slope. In order for tree effects on levee stability to be properly quantified, an assessment must be made of the three-dimensional distribution of roots. In this study an allometric biomass model is developed to estimate tree characteristics from trunk diameter at breast height (DBH), including: maximum root extent (MRE), maximum root depth (z_{max}), root ball diameter (L_{rb}), root area ratio (RAR) and root volume (RV) as a function of x,y and z. From these biomass properties the mechanical effects of root reinforcement, tree weight and wind loading are estimated and incorporated into stability analyses. Root area ratio is the cross-sectional area of roots per unit area of soil, which is proportional to the increase of soil strength by roots, decreasing from a maximum near the trunk to a negligible effect at the maximum lateral root extent and maximum root depth. The highest density of roots is located near the trunk and is often called the root ball, where a majority of tree weight and wind load is transferred to the soil. Wind exerts a load on the levee slope through the root system, which reaches a maximum just prior to failure of the tree by uprooting, or windthrow. The geometry of a root pit excavated by a fallen tree is controlled by a combination of root and soil strength, as well as the three-dimensional distribution of roots, and is assumed to be equivalent in lateral extent to the root ball.

Evaluation of seepage and stability underpin a majority of computations completed for analyses in this document, especially for limit-state function evaluations in reliability analyses. Furthermore, a significant portion of the influence of vegetation is quantified by comparing computed effects on seepage and stability to effects of other performance parameters. Non-stochastic analyses are often referred to as "deterministic" due to the single value nature of selected input parameters. An alternative designation is "mechanistic," referring to the mechanical nature of an algorithm. For example, slope stability is a mechanical model based on a system of equations balancing forces and moments. Existing software was modified and integrated to allow evaluation of seepage and stability models, in addition to the incorporation of vegetation effects for a model levee representative of the Pocket area near Sacramento, California. A saturated/unsaturated transient finite element seepage analysis allows pore pressures to be used with a generalized limit-equilibrium slope stability software to solve Spencer's method of slices for circular and non-circular surfaces. The potential sliding surface with a geometry having the lowest safety factor for a given set of conditions is then identified for a specific set of conditions with respect to stability.

Stochastic Approach

Incorporating the biomass model into the deterministic models of seepage and slope stability involves many additional parameters that are highly variable and uncertain due to the complex nature of root systems, as well as the natural variability in tree size and properties (Ang & Tang, 1975; Benjamin & Cornell, 1970). Furthermore, the soil properties needed for seepage and stability analyses are often subject to natural variability and uncertainty. As a result, the effects of vegetation on levee performance are well suited to probabilistic, or stochastic analyses. By characterizing the variability of input parameters by probability distributions (i.e., representing them as random variables) and performing seepage and stability analyses in combination with a stochastic method, an assessment can be made of the probability that a levee failure occurs. The term "failure" in this case refers to a specific event, which does not necessarily lead to failure of the entire levee. For this reason the term failure is avoided and "probability of exceedence" or simply "probability" is used to describe an unsafe condition instead, where driving forces are greater than resisting forces, or $FS < 1.0$. A fragility curve is a useful tool for evaluating levee performance and is found by computing probability of exceedence for a system under various load conditions (Casciati & Faravelli, 1985; Hall et al., 2003; Vorogushyn et al., 2009), schematically illustrated in Figure 1.2. Producing fragility curves for various conditions and comparing the results between cases with and without vegetation is the main method for evaluating vegetation effects in this research.

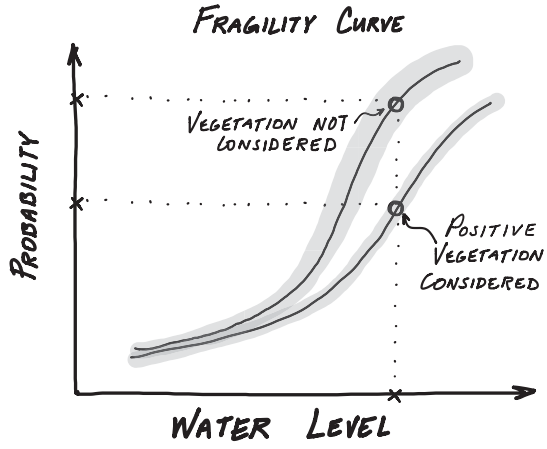

Figure 1.2: Conceptual representation of the incremental effect of vegetation on levee fragility. In this case vegetation has a positive effect overall, as probability decreases when vegetation is considered. Uncertainty in estimate is illustrated by gray zones, where the uncertainty due only to vegetation variables is smaller than the uncertainty for non-vegetation variables.

Uncertainty associated with input parameters and mechanistic models can be divided into two types, aleatory and epistemic, that control the overall probability of exceedence (Der Kiureghian & Ditlevsen, 2009; Vick, 2002). Aleatory uncertainty is associated with the natural variability of a phenomenon, for example, the equal probability that a value of one through six is rolled by a single die, or the maximum water level experienced on a levee in a given year. Epistemic uncertainty is associated with an incomplete state of knowledge, for example, insufficient data to describe a correlation, or the actual length of a tree root buried in the ground. In the context of this research, aleatory uncertainty represents the variation in random variables and controls the estimated probability that an unsafe seepage or slope stability event occurs. Epistemic uncertainty represents the effect of choosing probability distribution parameters and affects the estimate of fragility, as illustrated by the shaded bands in Figure 1.2. While vegetation effects can be quantified by their influence on deterministic models, greater insight is obtained by considering the effect on

fragility, and how underlying aleatory and epistemic uncertainty compare for analyses with and without vegetation included.

In this study the stochastic input parameters include soil properties, levee geometry, water level and vegetation parameters. In this context, the major incremental advance over previous studies is that we consider seepage forces and vegetation properties as random variables. Computation of probability of an event is accomplished by solving for the probability density of the Factor of Safety (FS) given probability distributions of the input parameters with the first-order reliability method (FORM). FORM is similar to a traditional sensitivity study, the main difference being consideration of probability distributions to understand how the likely values for specific variables influences expected performance of a system, such as a levee.

A major challenge in a stochastic analysis is obtaining an efficient, invariant solution that in addition to the computation of probability of failure also provides information on the sensitivity of the results to the individual input variables and their variance. This is especially important for variables with relatively small and/or localized impacts on computed probability, as occurs with vegetation. The FORM algorithm used in the analyses presented herein is specifically tailored to provide an invariant solution for the class of problems of interest in this study. The challenge in the FORM analysis is that the numerical codes used to obtain the requisite solutions of the physical problem, in this case seepage and slope stability, have to be very robust, stable, and accurate, since multiple realizations of the same problem have to be evaluated in the process of obtaining the solution.

In addition to probability, the FORM solution computes a value for each random variable that gives the highest probability of failure which are collectively referred to as the design point (i.e., one value for each input parameter with a probability distribution). The design point corresponds to the specific realization (values) of input parameters at which the model is most likely to reach an unsafe condition. In the case of slope stability it indicates the combination of parameter values that we would give the highest probability of $FS \leq 1.0$. The importance and sensitivity measures produced by the FORM analysis ranks the relative impact that each input parameter has on the solution and indicates whether a change in value causes a positive or negative influence on the computed FS in this case. This type of insight is not always apparent in a deterministic analysis. Sensitivity measures then provide magnitude of the change in probability (and reliability index) associated with each random variable and each probability distribution parameter, which gives a direct understanding of how uncertainty (e.g., standard deviation) in the solution is affected by the uncertainty in input parameters.

Computationally, in order to produce this extra information, a FORM analysis must repeatedly solve the physical problem, although this computation effort is significantly smaller than a Monte Carlo analysis. In order to obtain a computationally efficient solution, inputs and outputs of the mechanical model must be evaluated within the reliability software. To this end a saturated-unsaturated seepage code was combined with a generalized limit-equilibrium slope stability software. A biomass model was developed and added to allow the integration of trees and their root systems into the analyses. Since FORM requires the solution to be piece-wise continuous and differentiable it was necessary to create an allometric biomass model that could estimate key properties from DBH. Then, the stability code had to be modified to incorporate the biomass model and convert the resulting tree variables to loads that could be used in slope stability computations.

After describing the underlying theory for methods considered herein, seepage and stability conditions are evaluated with deterministic and stochastic analyses as a reference condition for a

levee in the urban Pocket area of Sacramento, California. To provide context for reliability analysis results a detailed description of the deterministic sensitivity is obtained for each random variable, in addition to the implications of selecting various probability distributions and parameters. The biomass model developed for evaluating vegetation effects is presented along with a description of key data used to develop the underlying allometric relationships. It is capable of modeling the physical response of a levee with significantly more detail than any previous analysis. While vegetation effects are generally small, root reinforcement in particular can have a large influence on stability computed from the model, and in general the position and tree size can be chosen to produce adverse conditions for a levee.

The fifteen total random variables are divided into seepage (3), strength (6) and vegetation (6) groups. Seepage variables include water surface elevation (WSE), blanket layer thickness (z_B) and hydraulic conductivity ratio (K_r) and strength parameters include unit weight (γ), cohesion (c) and friction angle (ϕ) of the embankment and blanket (foundation) soils. Three vegetation random variables describe the spread of root density in the biomass model and three describe the variability in mechanical loading due to root reinforcement, weight and wind. Reliability analyses confirm the results of deterministic sensitivity studies and show that given the wide range of possible values for vegetation parameters, their contribution to fragility and overall uncertainty is small relative to the influence of other factors influencing levee performance, such as soil strength and seepage properties. In fact, the incremental effect due to vegetation is generally found to be within the one standard deviation confidence interval range for fragility and safety factor.

Chapter 2

Analytical Tools and Methods

Seepage and stability analyses are the underlying mechanistic models used to evaluate levee performance. The FORM algorithm used in the analyses in this study is able to provide an invariant solution for the seepage and stability conditions of interest. However, the challenge of using the FORM analysis is that the numerical software used to obtain the requisite solutions of the physical problem have to be very robust, stable, and accurate, since multiple realizations of the same problem have to be evaluated in the process of obtaining the reliability solution.

2.1 Seepage Model

A saturated-unsaturated transient finite element code `UNSAT1` (Neuman, 1972) was used to compute the pore pressure distribution within the embankment. The advantage of using a saturated-unsaturated formulation is that is allows for a fixed mesh to solve for the position of the phreatic surface and pore pressure distribution. All analyses were extended until they reached steady state and only the steady state pressure distributions were used in the analyses. Figure 2.1 shows the nodes of the finite element mesh in and near the embankment, along with the phreatic surface for the 200-yr water surface (13 ft above toe). The mesh consisted of approximately 9,000 rectangular elements varying in size from 1.5 m at the bottom and side model boundaries to 0.2 m in and near the embankment, with a maximum aspect ratio of 3:1. Three types of boundary conditions were applied: constant head on the vertical sides and water-side surface; impermeable boundaries on the aquifer base and levee crest; and constant head seepage face conditions on the land-side slope and adjacent ground surface. The seepage model was extensively tested to make sure that the computed pore pressures and a phreatic surface position were consistent and efficient. Details of the implementation are given further in Appendix B.2.

In seepage problems containing a high contrast of hydraulic conductivity between soil layers, the ratio is more important than absolute values for controlling the distribtuion and magnitude of pore pressure (Batool et al., 2015; Chowdhury et al., 2012; USACE, 1999). Hydraulic conductivity ratio, $K_r = K_{a,h}/K_{b,v}$ relates horizontal aquifer conductivity, $K_{a,h}$, to vertical blanket conductivity, $K_{b,v}$. Thus, K_r is included as a single variable to simplify the levee model, a useful construct for reducing computation time in reliability analyses. Despite K_r being a single variable, specific values for $K_{a,h}$ and $K_{b,v}$ are still necessary to define within the seepage code `UNSAT`; however, infinite combinations of $K_{a,h}$ and $K_{b,v}$ can be chosen for a given K_r. Two cases were considered to

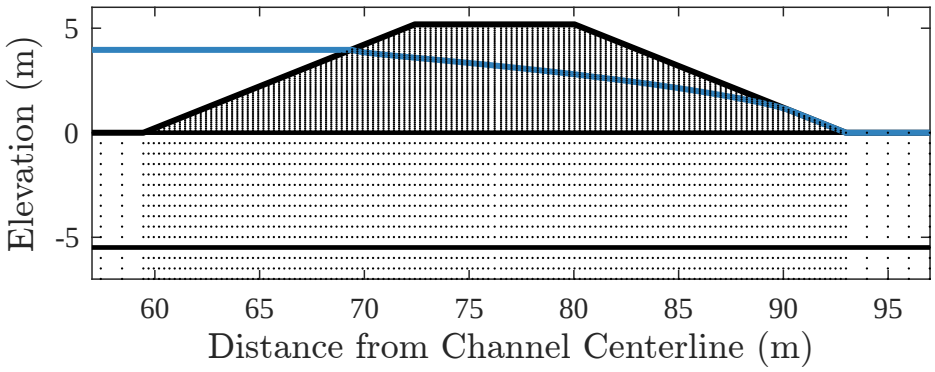

Figure 2.1: Nodes of finite element mesh for seepage analyses in UNSAT software. Phreatic surface is steady-state solution for 200-yr WSE (3.96 m or 13 ft)

evaluate the implications of choosing $K_{a,h}$ and $K_{b,v}$ from a given K_r: Case 1, hold $K_{a,h}$ constant and vary $K_{b,v}$; or Case 2, vary $K_{a,h}$ and hold $K_{b,v}$ constant, as discussed later in Chapter 3. For the range of interest the difference between Case 1 and 2 is negligible. The model was found to be insensitive to the presence of an aquitard below the aquifer, similar to findings of Benjasupattananan (2013); therefore, to improve computation time it is not included in the model.

The potential for levee erosion is evaluated using steady-state conditions for underseepage and throughseepage after Duncan et al. (2011). Safety factor for underseepage, FS_{us} is estimated using effective and total stress methods (i.e., $FS_{us,e}$ and $FS_{us,t}$). The effective stress approach finds the ratio of critical gradient, i_c, to computed vertical gradient across the blanket, i, whereas the total stress approach compares weight of soil to water pressure below the blanket:

$$FS_{us,e} = \frac{i_c}{i} \qquad \text{and} \qquad FS_{us,t} = \frac{FS_{us,e} i + 1}{i + 1} \tag{2.1}$$

where $i_c = (\gamma_t - \gamma_w)/\gamma_w$ is the critical gradient and γ_t is total unit weight (in this case γ_B). The main difference between these two approaches is that thickness of the blanket layer becomes part of the resisting force computation for the total stress method.

Throughseepage is evaluated with the solution for stability of an infinite slope, which is dependent upon γ, c' and ϕ' for the soil in addition to slope angle, θ, and potential sliding depth, z (for the $c' > 0$) case only:

$$FS = \frac{\tan\phi'}{\tan\theta}\left[1 - \frac{\gamma_w}{\gamma_t}(1 + \tan^2\theta)\right] + \frac{2}{\sin(2\theta)}\left[\frac{c'}{\gamma_t z_s}\right] \tag{2.2}$$

where θ is measured from horizontal and z_s is the depth of sliding.

2.2 Slope Stability Model

Slope stability is computed using Spencer's method of slices implemented in Matlab (MathWorks, 2015) by Tabarroki (2011). The software uses an efficient genetic algorithm (Wang et al., 2011) to

search for circular and non-circular surfaces that minimize safety factor, FS, but required a number of modifications to allow its integration with the seepage and reliability codes. The most significant being direct input of pore pressures from the finite element seepage software; incorporation of line loads and moments to facilitate evaluation of vegetation; and to search for the sliding surface with minimum reliability index, β (or maximum probability of occurrence). All analyses described in this document use drained strengths and steady-state seepage conditions, unless otherwise noted.

Position of the phreatic line within the embankment and seepage pressures at the base of a stability analysis slice were interpolated from the seepage solution using a Delaunay triangulation. Negative pore pressure found at the base of slices above the phreatic line and within the embankment were set to zero and unsaturated soil properties were not considered. Computed safety factors were generally found to be within at most ± 0.01 of FS computed with commercial slope stability software. Differences are due to geometry of the finite element mesh, numerical seepage parameters used to reach a steady-state condition, interpolated position of the phreatic line, and the interpolated pore pressures at the base of the slices.

2.3 Random Variables

Deterministic parameters become random variables when a probability distribution is assumed to define the uncertainty associated with their value. A distribution generally is defined by a probability density function (PDF), cumulative density function (CDF) and distribution parameters (typically two, but sometimes more). Distributions and associated parameters used in this research are listed in Table 2.1; detailed descriptions can be found in Appendix A. Notation $x \sim \text{LN}(\lambda, \zeta)$, for example, indicates a random variable x has the lognormal distribution with parameters λ and ζ. The PDF and CDF of x are represented $f_x(x)$ and $F_x(x)$, or if distribution parameters are included, as $f_x(x|\lambda, \zeta)$ and $F_x(x|\lambda, \zeta)$ (again for the lognormal case).

Distributions are ideally selected based on directly measured observations of empirical data, but in many cases this is not possible. For example, sufficient geotechnical testing may not be possible, or observation of a statistically significant number of floods is not practical. Therefore, additional information is often used to select a distribution, such as general statistical information from the literature (especially coefficient of variation) or physical characteristics of the variable of interest (i.e., non-negative values). If a statistical sample is available, the Kolmogorov-Smirnov test is used to test quality of fit for various distributions (Benjamin & Cornell, 1970). Symbols μ and σ are generally used to refer to the parameters of the normal distribution in addition to the mean and standard deviation of a population or sample interchangeably. When a distinction must be made between different μ or σ, $\bar{x}$ and $\bar{s}$ are used for the sample mean and standard deviation. For non-symmetric distributions or samples, the mean, median and mode are represented by subscripts x_a, x_{50} and x_{mo}, respectively. Coefficient of variation, δ, is the ratio of standard deviation to the mean ($\delta = \sigma/\mu$) and is a measure of dispersion for a sample or population. Small values of δ indicated most data will lie close the mean. Although it is useful for comparing the relative variability of different variables, δ is not as easily understood for populations with asymmetric distributions such as the lognormal. Published values of δ, summarized well by Baecher and Christian (2003) and Uzielli et al. (2006), guide the assumption of probability distributions for geotechnical parameters of interest; baseline ranges used in this document are summarized in Table 2.2.

Table 2.1: Summary of probability distributions, notation of parameters, justification and example applications as used in analyses for this document. See Appendix A for detailed description of distributions and additional background for certain random variables.

Normal	$\mathrm{N}(\mu, \sigma)$	symmetric, widely applied and understood; used for various soil properties, geometric and biomass variables
Truncated Normal	$\mathrm{N}_t(\mu, \sigma, x_l, x_u)$	limits distribution tails, useful for limiting non-physical values or preventing numerical issues; used for blanket thickness
Lognormal	$\mathrm{LN}(\lambda, \zeta)$	skewed positive, prevents negative values and useful for variables spanning orders of magnitude; used for various random variables and water surface elevation
Uniform	$\mathrm{U}(a, b)$	equal probability between limits, every value is equally likely; used for tree position
Gumbel	$\mathrm{Gmb}(u, \alpha)$	often used to describe rare events; used for water surface elevation
Gamma	$\mathrm{Gam}(\varepsilon, u, k)$	often used to describe rare events, includes Log-Pearson III and exponential as special case; used for water surface elevation
Exponential	$\mathrm{Exp}(\lambda)$	a strictly decreasing family of distributions; used for cohesion of "cohesionless" embankment soil

Table 2.2: Typical ranges of coefficient of variation, δ (also referred to as c.o.v.), for non-vegetation random variables.

Property	δ Range[a]	Notes
Unit Weight, γ	0.05 to 0.10	used $\delta = 0.10$ normal or lognormal
Cohesion, c	0.10 to 0.30	used $\delta = 0.30$ normal or lognormal
Friction Angle, ϕ	0.02 to 0.05	used $\delta = 0.05$ normal or lognormal
Friction Angle, $\tan\phi$	0.05 to 0.15	used $\delta = 0.10$ normal or lognormal
Hydraulic Conductivity, K	2.00 to 3.00 0.30, single layer[b]	$\delta = 2.00$ and $\delta = 0.30$ lognormal, Section 3.2
Blanket Thickness, z_B	N/A site dependent	$\delta = 0.25$ and $\delta = 0.35$ trunc. normal, Section 3.3
Water Surface El., WSE	N/A site dependent	lognormal or Gumbel Section 3.1

[a] Baecher and Christian (2003) and Uzielli et al. (2006)
[b] USACE (1999)

2.4 First-Order Reliability Method (FORM)

Reliability of some event or condition, R, is inversely related to the probability of occurrence such that $R = 1 - p$, and is the eponym for reliability analyses. Probability and reliability can be used interchangeably in engineering practice depending on the magnitude of each or the perspective of the discussion. Regardless, these concepts are the output of stochastic analyses seeking to understand how uncertain conditions relate to a particular uncertain outcome. Mathematically, reliability methods integrate a probability density function, $f(\mathbf{x})$, over the unsafe domain represented here as Ω:

$$R = 1 - p = 1 - \int_{\Omega} f(\mathbf{x})\,\mathrm{d}\mathbf{x} \tag{2.3}$$

Where $\mathbf{x}$ is a vector containing values for n random variables considered; the value for a single random variable i is represented x_i. In this research unsafe domain includes all possible combinations of $\mathbf{x}$ leading to a condition where $FS(\mathbf{x}) \leq 1.0$ for levee seepage and stability. Unfortunately, the PDF of $FS(\mathbf{x})$ is not known, but can be estimated using various reliability methods. Numerous methods for evaluating reliability have been used in geotechnical applications (see e.g., Baecher & Christian, 2003; USACE, 1999, 2010).

First-order reliability methods use the first-order Taylor's series approximation to evaluate reliability, with significant variations in how computations are performed and the solution obtained. The First-order second moment (FOSM) algorithm (Ang & Cornell, 1974) estimates the mean and variance assuming a normal or lognormal distribution to compute reliability. Due to its simplicity it is the most common method used in geotechnical engineering. A significant problem with FOSM is lack of invariance, a condition that produces a different solution when the problem is formulated differently (see e.g., Phoon et al., 2003). USACE (1999) incorporates FOSM while acknowledging the "unknown error" associated with invariance of second moment methods. In general, FOSM functions well as a simplified method of evaluating relative differences between various reliability analyses. The problem of invariance was solved by Hasofer and Lind (1974) and extended by Rackwitz and Flessler (1978) using an algorithm now referred to as HL-RF (Liu & Der Kiureghian, 1991). Although the solution is more robust, HL-RF incorporates an iterative algorithm that generally requires more computations and a more sophisticated software than FOSM. Convergence of the solution using HL-RF was improved by (Zhang & Der Kiureghian, 1995). Their formulation is referred to as iHL-RF and is used in this study. Further details of the theoretical foundations of this approach used are given in Der Kiureghian (2005), Ditlevsen and Madsen (2005) and Zhang and Der Kiureghian (1995).

FORM Overview

The FORM algorithm computes probability by propagating the uncertainty of input parameters through a "physics based" model to quantify uncertainty of the numerical output. The term physics-based model (i.e., non-stochastic or mechanistic) refers to an actual process model such as the slope stability analysis and seepage analysis in the cases under consideration. FORM input variables consist of parameters describing the geometry and properties of the modeled domain and include their mean, variance, and associated probability distribution. Given the output is uncertain, its PDF, $f(\mathbf{x})$, is used to estimate probability, as illustrated in Figure 2.2 for the simple case of one and two variables (x_1 and x_2). For each case the probability density of $FS(\mathbf{x})$ is represented by a

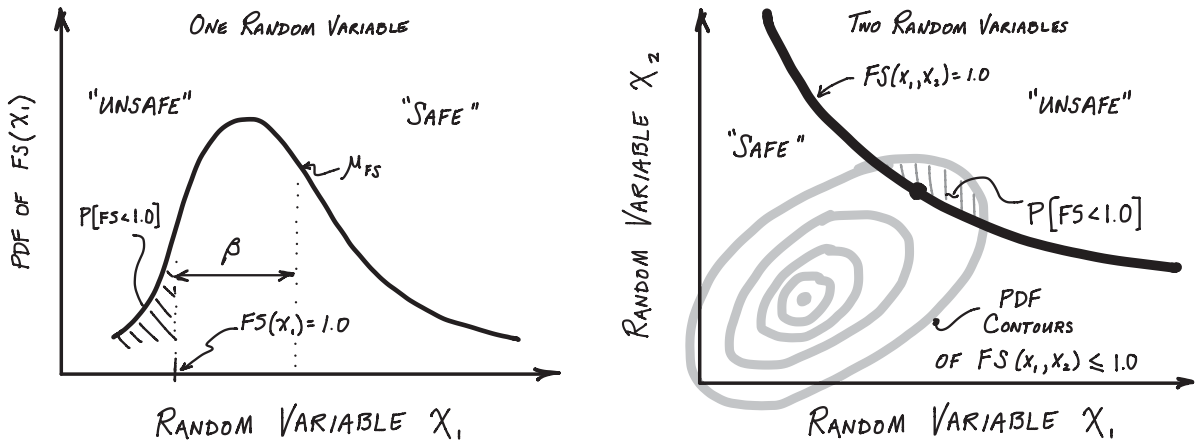

Figure 2.2: Conceptual illustration of reliability, $R = 1 - p$, for one random variable, x_1 **(a)**, and two random variables, x_1 and x_2 **(b)**. A probability distribution is assumed (not shown) for x_i and used by the reliability algorithm to estimate probability of "failure." In this case failure refers to an unstable condition, $FS \leq 1.0$, not necessarily failure of the levee in general. Thus reliability methods estimate $P[FS \leq 1.0]$.

hatched region of the curve or surface, where "unsafe" is defined as the condition $FS(\mathbf{x}) \leq 1.0$, thus FORM computes the probability $\mathrm{P}[FS(\mathbf{x}) \leq 1.0]$.

For each reliability analysis the numerical condition of "safe" or "unsafe" is defined by the limit-state function, $g(\mathbf{x})$, which is dependent on random variables, $\mathbf{x}$, each of which has a probability distribution. For analyses in this document, the limit-state function is defined in terms of safety factor:

$$g(\mathbf{x}) = FS(\mathbf{x}) - 1.0 \tag{2.4}$$

Thus the system is stable when $FS(\mathbf{x}) > 1.0$ or $g(\mathbf{x}) > 0$ and reliability is computed as:

$$R = 1 - P[FS(\mathbf{x}) \leq 1.0] = 1 - P[g(\mathbf{x}) \leq 0] \tag{2.5}$$

Obtaining a solution to Equation 2.5 is the core task of FORM and other reliability methods, all of which require repeated evaluations of $g(\mathbf{x})$ while incorporating probability information from each random variable, x_i.

For most problems, the actual probability distribution of $g(\mathbf{x})$ is unknown. Furthermore, there is no guarantee the PDF of $g(\mathbf{x})$ may even match that of a known distribution (e.g., normal, Gumbel, etc). FORM deals with this issue by transforming all input random variables to standard normal distributions and completing all probability computations in the standard normal space, as illustrated in Figure 2.3. The transformation incorporates complete probability distribution information from each random variable into the reliability analysis, unlike simplified second-moment approaches; see Der Kiureghian (2005), Ditlevsen and Madsen (2005), Hohenbichler and Rackwitz (1981) for more detail. Probability, $\mathrm{P}[G(\mathbf{u}) \leq 0]$, is estimated by integrating the PDF, $\phi(\mathbf{u})$, beyond a linear approximation (i.e., first-order) to the limit-state function at the design point (described below). Note that random variables in Figure 2.3 are transformed to the standard normal variables, $\mathbf{u}$, implying a mean of $\mu_{\mathbf{u}} = 0$ and standard deviation of $\sigma_{\mathbf{u}} = 1$. The limit-state function is represented by $G(\mathbf{u})$ when evaluated in the transformed "standard normal" space $\mathbf{u}$ instead of in

the "original" space, $\mathbf{x}$. Because $G(\mathbf{u})$ is a function of standard normal variables, it has the multivariate standard normal distribtuion (also with $\mu = 0$ and $\sigma = 1$), which is why, in contrast to $g(\mathbf{x})$ in Figure 2.2, probability contours of the PDF for $G(\mathbf{u})$ are concentric circles with a maximum probability density at the origin.

Design Point, $\mathbf{x}^*$ and $\mathbf{u}^*$

A critical aspect of the FORM solution is finding the combination of random variables, $\mathbf{x}$, where the limit-state is reached while maximizing probability density of in the standard normal space, $\phi(\mathbf{u})$. In other words, FORM finds the point in Figures 2.2 and 2.3 lying on the limit-state surface ($G(\mathbf{u}) = 0$) and simultaneously reaching the highest PDF contour. This point is known as the design point, $\mathbf{u}^*$, and represents *the combination of parameters most likely to result in an unsafe condition*; it is a vector containing a single value for each random variable. When $\mathbf{u}^*$ is transformed back to the original space it becomes $\mathbf{x}^*$ and the values for each random variables can be used for further deterministic analysis. In the standard normal space $\mathbf{u}^*$ describes distance of the design point to its median, scaled by standard deviation (the standard normal variate is described in Appendix A). Thus, magnitude gives a sense for how likely the value may be while sign (i.e., $\pm$) indicates whether the value is above or below the median. Solving for the design point in the standard normal space is the main reason FORM is able to produce an invariant solution for reliability.

Reliability Index, β

The reliability index, β, represents a widely used concept measuring the likelihood of some event or condition (Cornell, 1969), and is interpreted as the distance of some value of interest, i.e. the design point, from the mean, $\beta = \mu/\sigma$ (Figure 2.2a). If a variable u has the normal distribution, probability can be computed using the standard normal PDF:

$$p = \Phi(-\beta) \tag{2.6}$$

Thus, p and β are inversely related and non-linear (as are p and R), making references to probability, reliability or reliability index analogous. In FORM the solution is obtained in the standard normal space. Reliability index is still related to probability by $p = \Phi(-\beta)$, and represents the distance from the mean of $G(\mathbf{u})$ to the design point in the standard normal space (Figure 2.3), given mathematically as:

$$\beta = \alpha \mathbf{u}^* \tag{2.7}$$

where α is a vector output of FORM relating location of $\mathbf{u}^*$ to distance from the origin, β. Using the lognormal distribution to relate β to p is common when second moment methods are applied (e.g., Duncan & Wright, 2005; USACE, 1999); however, the probability transformation and computation of FORM in the standard normal space makes this unnecessary.

Importance Vector, α

An important component of the FORM algorithm is α, an n-length vector consisting of the negative normalized limit-state function gradient evaluated at the design point

$$\alpha = -\frac{\nabla G(\mathbf{u}^*)}{\|\nabla G(\mathbf{u}^*)\|}\ , \tag{2.8}$$

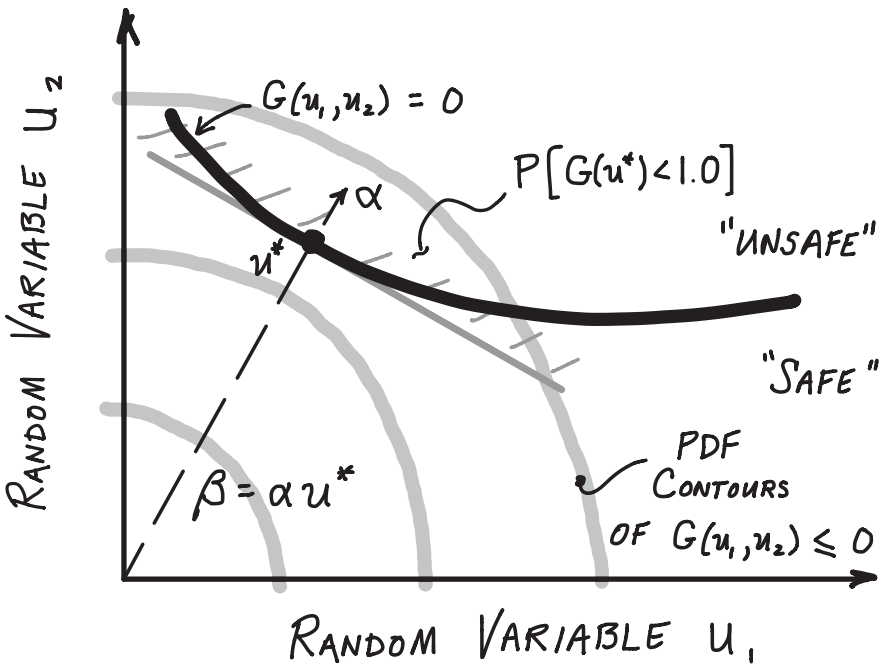

Figure 2.3: Conceptual representation of FORM solution for two random variables, x_1 and x_2, transformed to the standard normal space, u_1 and u_2. Also illustrated are the limit-state function and limit-state, $G(\mathbf{u}) = 0$, design point, u^*, reliability index, β, and importance vector, α. Note the linear approximation to the limit-state used for computing probability density in the unsafe region, and location of the design point as the combination of parameters u_1 and u_2 such that the limit-state is reached, $G(u_1, u_2) = 0$, *and* probability density is maximized, $\max[\phi(u_1, u_2)]$. Probability is estimated in FORM by integrating probability density beyond the linear approximation of $G(\mathbf{u})$ at $\mathbf{u}^*$. The origin represents the mean of both random variables and the maximum probability density, a consequence of all u_i having the normal distribution and $G(\mathbf{u})$ the multivariate normal distribution.

where each element of $\nabla G(\mathbf{u}^*)$ is a partial derivative of the limit-state function with respect to random variable, x_i, evaluated at $\mathbf{u}^*$:

$$\nabla G(\mathbf{u}^*) = \left[\frac{\partial G(\mathbf{u}^*)}{\partial x_1} \quad \frac{\partial G(\mathbf{u}^*)}{\partial x_2} \quad \dots \quad \frac{\partial G(\mathbf{u}^*)}{\partial x_n} \right] \tag{2.9}$$

This can also be interpreted as the contribution of each random variable to the total variance of the limit-state function. Linear algebra indicates α is the unit normal to the planar approximation of the limit-state function at the design point, pointing into the unsafe domain (Figure 2.3). A unit vector has the property

$$\alpha_1^2 + \alpha_2^2 + \dots + \alpha_n^2 = 1, \tag{2.10}$$

allowing for a relative comparison between each random variable. A value of α_i greater than zero indicates random variable i contributes to variance of the limit-state function and is therefore a *demand* variable. Variance is decrease for $\alpha_i < 0$, implying variable i is a *capacity* variable. Furthermore, magnitude of α_i determines the relative importance of variable i, which is why α is known as the importance vector. For a three variable case importance can be represented as follows:

$$|\alpha_i| > |\alpha_j| > |\alpha_k| \quad \rightarrow \quad \text{Imp}(\alpha_i) > \text{Imp}(\alpha_j) > \text{Imp}(\alpha_k) \tag{2.11}$$

Finally, it should be noted α corresponds to the design point in the standard normal space, $\mathbf{u}^*$, which is equivalent to the original space only when all random variables are statistically independent. For statistically dependent cases an alternative importance vector γ is used, which provides the same insight to reliability results as α for $\mathbf{u}^*$.

Importance Vectors, δ and η

Sensitivity vectors can be constructed using gradient vectors similar to Equation 2.9 for alternative parameters. For example, sensitivity of reliability index to the mean and standard deviations of a random variable distribution: $\nabla_\mu \beta$ and $\nabla_\sigma \beta$. Taking these sensitivity vectors and scaling by standard deviation produces the dimensionless importance vectors δ and η:

$$\delta = \nabla_\mu \beta \, \sigma_{\mathbf{x}} = \left[\frac{\partial \beta}{\partial \mu_1}\sigma_1 \quad \frac{\partial \beta}{\partial \mu_2}\sigma_2 \quad \dots \quad \frac{\partial \beta}{\partial \mu_n}\sigma_n \right] \tag{2.12}$$

$$\eta = \nabla_\sigma \beta \, \sigma_{\mathbf{x}} = \left[\frac{\partial \beta}{\partial \sigma_1}\sigma_1 \quad \frac{\partial \beta}{\partial \sigma_2}\sigma_2 \quad \dots \quad \frac{\partial \beta}{\partial \sigma_n}\sigma_n \right], \tag{2.13}$$

where $\sigma_{\mathbf{x}}$ is the matrix representation for the standard deviations of $\mathbf{x}$. These importance measures quantify the relationship between absolute value and variance for each random variable on reliability. The vector η is particularly useful as it can directly illustrate the change in probability caused by a change in standard deviation. For example, using the importance measure to find $\Delta\beta$ after a site investigation reduces σ of a sample for random variable i:

$$\Delta\beta = \frac{\eta_i}{\sigma_i}\Delta\sigma_i \tag{2.14}$$

Change in probability can be computed using:

$$\Delta p = \Phi\big[-(\beta + \Delta\beta)\big] - \Phi\big[-\beta\big] \tag{2.15}$$

Numerous alternative sensitivity vectors can be constructed from a FORM analysis using the appropriate partial derivatives, for example limit-state function parameters, θ_g, or probability distribution parameters, θ_f.

2.5 Fragility

Fragility curves are plots of probability of occurrence conditioned on a specific random variable of interest, illustrated conceptually for random variable x in Figure 2.4 (e.g., Casciati & Faravelli, 1991; Shinozuka et al., 2000; Veneziano et al., 1983). They are a critical component for risk analysis methods utilizing event trees, and although the most widespread application is in earthquake engineering (Casciati & Faravelli, 1985; Der Kiureghian & Fujimura, 2009), they have been increasingly used for flood control evaluations (Buijs et al., 2005; Hall et al., 2003; HRW/UB, 2004; Vorogushyn et al., 2009). As a single curve, fragility eliminates the *aleatory* variability of one variable (i.e., the x-axis), but additional random variables are still included in the stochastic analysis. For example, probability increases with rising water surface elevation (WSE) because the PDF of $FS(\mathbf{x})$ (Equation 2.3) is a function of the aleatory variability of random variables $\mathbf{x}$ (e.g., soil properties and blanket geometry). Levee evaluations often incorporate fragility curves, whether as a local system evaluation (Hui et al., 2016; Ketchum et al., 2011) or region-wide risk analysis (DWR, 2012b; URS/JBA, 2008a). A variety of stochastic methods are available (USACE, 2010) and this research uses FORM to compute β at various water levels.

To estimate the PDF $f(\mathbf{x})$, distribution parameters must be selected for a stochastic analysis and are one source of *epistemic* uncertainty, which is illustrated by the dashed bands in Figure 2.4. Epistemic parameters are represented with the vector θ, and are implicitly present in reliability computations:

$$R = 1 - p = 1 - \int_{\Omega} f(\mathbf{x}, \theta)\, \mathrm{d}\mathbf{x} \tag{2.16}$$

As such, results from FORM are essentially "best estimates" of β and p, and confidence bounds can be found using the sensitivity vectors discussed in previous sections. Following Der Kiureghian (1989), Gardoni et al. (2002a, 2002b), variance of β is estimated as:

$$\sigma_\beta^2 \approx \nabla_\theta \beta \, \Sigma_{\theta\theta} \, \nabla_\theta \beta \,, \tag{2.17}$$

where $\Sigma_{\theta\theta}$ is the covariance matrix, consisting of correlation coefficient and standard deviation information for each parameter θ. Parameters representing aleatory variability are contained in the vector θ, which can generally be taken to represent model error. In this research θ includes the mean and standard deviation associated with all distribution parameters of $\mathbf{x}$; for example, μ_{μ_i} and σ_{μ_i} for variable x_i. Typically an initial assumption is $\sigma_{\mu_i} = \sigma_i$, with the adjustments to the former being made as more data is collected. Although this "distribution of a distribution" concept may seem convoluted, it provides a powerful method of comparing the relative impact of different

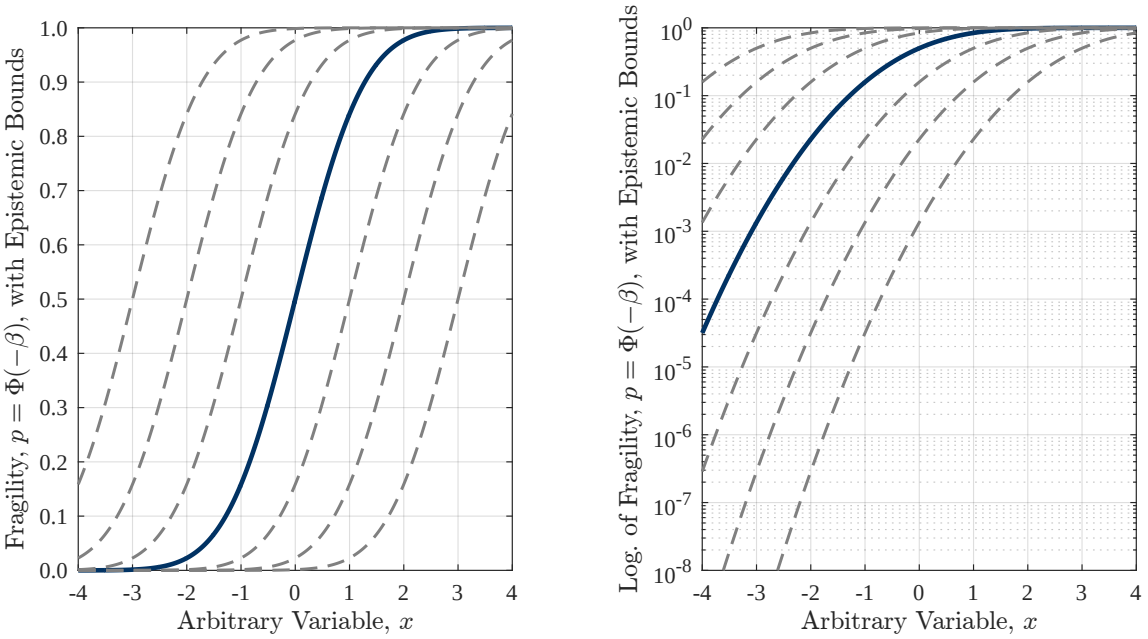

Figure 2.4: Conceptual representation of fragility as a function of x. Fragility is computed using FORM as $p = \Phi(-\beta)$, representing the aleatory variability due to random variables $\mathbf{u}$. Epistemic uncertainty is included in FORM as θ, the set of parameters for each random variable distribution, and implies a probability distribution on β, defined by $\mu_\beta = \beta$ and σ_β. The dashed lines illustrate epistemic uncertainty as $\mu_\beta \pm k\,\sigma_\beta$, for $k = 1, 2, 3$. Because fragility in this conceptual example used the standard normal distribution, x is equivalent to $-\beta$ and therefore illustrates the non-linear Δp for a given $\Delta\beta$, which depends on the initial value β_0; for example $\Delta\beta = +1$ decreases p from 1.35% to 0.003% when $\beta_0 = 3.0$, but from 50% to 34% when $\beta_0 = 0.0$.

random variables. In the statistically independent case $\Sigma_{\theta\theta}$ simplifies to a diagonal matrix of σ_j^2, and Equation 2.17 simplifies to the following:

$$\sigma_\beta \approx \sqrt{\sum_j (\nabla_{\theta_j} \beta \, \sigma_j)^2}, \tag{2.18}$$

where j is an index corresponding to each of the parameters considered. For example, σ_β due to model uncertainty from the mean value of each $\mathbf{x}$ would be found as follows for n random variables:

$$\sigma_\beta \approx \sqrt{\left(\frac{\partial \beta}{\partial \mu_1}\sigma_{\mu_1}\right)^2 \quad \left(\frac{\partial \beta}{\partial \mu_2}\sigma_{\mu_2}\right)^2 \quad \dots \quad \left(\frac{\partial \beta}{\partial \mu_n}\sigma_{\mu_n}\right)^2} \tag{2.19}$$

Note that σ_β can easily be computed from importance vectors δ and η (Equations 2.12–2.13). For example, if $\sigma_{\mu_i} = \sigma_i$ then $\sigma_\beta \approx \|\delta\|$. Furthermore, if σ_β were to include uncertainty from the mean *and* standard deviation of each $\mathbf{x}$ there would be $2n$ terms in Equation 2.19. Fragility bounds for the estimate of β from FORM (i.e., μ_β) are computed for specific confidence intervals, for example the one standard deviation, or 15% and 85% probability levels $\mu_\beta \pm \sigma_\beta$:

$$P\big[\mu_\beta + \sigma_\beta,\ \mu_\beta - \sigma_\beta\big] = \big\{\Phi(-\mu_\beta - \sigma_\beta),\ \Phi(-\mu_\beta + \sigma_\beta)\big\} \tag{2.20}$$

Figure 2.4 illustrates bounds for one, two and three standard deviations of β, since the conceptual example has a standard normal distribution $\sigma_\beta = 1$. Given the non-linear relationship between β and p, it clear that Δp is dependent on the mean estimate of β. As shown on the log-plot of fragility, epistemic uncertainty causes probability to vary over multiple orders of magnitude for negative values of the arbitrary variable x, but much less so for x near zero. As p approches 1, the differences lose engineering significance. The potentially large variation in p due to σ_β is especially important when the difference in two fragility curves is small.

For non-normal distributions sensitivity of β to the mean and standard deviation produce unrealistically high values of σ_β due to the non-linear dependence of μ and σ on distribution parameter(s), p. A distribution has n parameters, collected in the vector $\mathbf{p} = [p_1\ p_2\ \dots\ p_n]$, and sensitivity is denoted $\nabla_{\mathbf{p}}\beta$. To prevent computation of unrealistic uncertainty bounds for fragility, σ_β can be computed with Equation 2.17 using sensitivity to the distribution parameters directly. For example, $\nabla_{\mathbf{p}}\beta$ uses μ_t and σ_t instead of μ and σ for the truncated normal distribution. For the truncated normal case the mean and standard deviation of the truncated normal distribution are similar to the distribution parameters, as long as truncation limits are not to restrictive, and $\sigma_{\mu_t} \approx \sigma_\mu$. This may not be the case for other distributions, and an appropriate estimate for σ_j in Equation 2.18 should be chosen.

Results from FORM also provide information on the probability distribution for the limit-state function, which can be an alternative method of presenting fragility. By definition, $\beta = \mu_g/\sigma_g$, the ratio of mean to standard deviation of the limit-state function, $g(\mathbf{x})$, and α is the first-order approximation of the variance of $g(\mathbf{x})$. It follows that $\sigma_g = \|\nabla g(\mathbf{x}^*)\|$ and $\mu_g = \beta\sigma_g$. The level of conservatism incorporated into a deterministic analysis can be assessed by comparing the confidence interval for $g(\mathbf{x})$ to deterministic analysis. For example, how $FS(\mathbf{x})$ for best-estimate parameters $\mathbf{x}$ compares to μ_g. Note that when $g(\mathbf{x}) = FS(\mathbf{x}) - 1.0$ the mean of $FS(\mathbf{x})$ is $\mu_{FS} = \mu_g + 1.0$.

Fragility curves represent aleatory variability for random variables included in the stochastic analysis, and model uncertainty can be incorporated by producing bounds on fragility curves. Although the inclusion of epistemic uncertainty adds an extra level of complexity to the stochastic model, it provides an invaluable method of comparison between the individual effects due to each random variable, especially vegetation effects.

2.6 Analysis Software

All analyses were completed using Matlab (MathWorks, 2015), which incorporated the following existing software: `UNSAT` for seepage analysis (Sitar & Cawlfield, 1984; Neuman, 1972), written in Fortran; `USlopeM` for stability analysis (Tabarroki, 2011), written in Matlab; and `FERUM` for reliability analysis (Bourinet, 2010; Der Kiureghian et al., 2006). In general, numerous Matlab scripts and functions were written to facilitate communication of software input/output between `UNSAT`, `USlopeM` and `FERUM`, process results of analyses and troubleshoot source code "bugs" that arose during implementation. Deterministic results are accurate and follow methods well-defined by standard practice for levee design (URS, 2014; USACE, 2000); however, reliability analyses require a more stringent precision since convergence to a solution is dependent on computation of gradients and a relatively smooth function is critical. Unfortunately standard geotechnical practice for seepage and stability evaluations do not typically use algorithms that produce sufficiently smooth and precise levee response for FORM to function readily. As such, the software used for analyses in this document had to be modified to address several numerical issues to be used with FORM and are discussed in Appendix B.

Chapter 3

Model Levee Configuration and Site Conditions

All analyses in this document used a levee model that is representative of the Pocket area of Sacramento, California, located on the East bank of the Sacramento River, approximately 5 miles South of downtown. In this area sandy levees are typically located on top of a low hydraulic conductivity and cohesive blanket layer. A relatively thick aquifer provides a hydraulic connection to the river, causing pore pressures to concentrate in the blanket layer. Layer geometry and soil properties produce a condition such that the levee is marginally stable (i.e., $FS \sim 1.0$) when the water surface is at the crest, assuming a steady-state seepage condition.

The embankment is 5.2 m (17 ft) tall with a 6.6 m wide crown (25 ft) and 2.5:1 H:V slopes; a 6.1 m wide berm (20 ft) is located along the waterside toe at the top of the blanket layer, with the river bed 10.7 m (35 ft) below the landside toe. The cross-section is shown in Figure 3.1. Design water levels were determined from previous hydraulic studies in the area (GEI/HDR, 2015) and recommended design practice (URS, 2014): the 200–yr WSE is 4.0 m (13 ft) above the landside toe; hydraulic top of levee (HTOL) is 4.9 m (16 ft) above the landside toe (Table 4.1).

Soil properties are summarized in Table 3.1, in addition to seepage and strength parameters used for drained and undrained conditions. These values are also the arithmetic means used in reliability analyses, and along with the cross section dimensions were selected to be representative

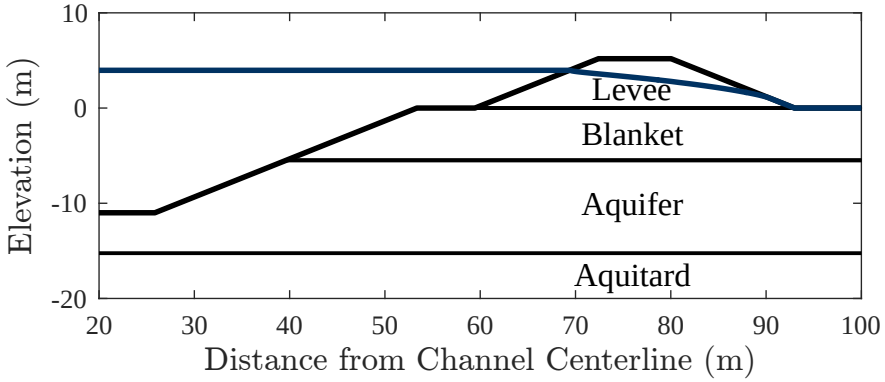

Figure 3.1: Levee cross-section with phreatic surface for 200-yr *WSE*

of the Pocket site in general, where the levee is marginally stable (i.e., $FS \sim 1.0$) when WSE is near the crest. Deterministic values in Table 3.1 are often referred to as "design" values elsewhere in this document.

Table 3.1: Summary of design values for parameters used in deterministic stability analyses, which are also mean values for random variables distributions in stochastic analyses (drained strength parameters only).

Soil Layer USCS	Thickness	K_h	K_v/K_h	γ	Strength			
					c'	ϕ'	c	ϕ
	m (ft)	m/s	-	kN/m^3 (pcf)	kPa (psf)	◦	kPa (psf)	◦
Embankment SP-SM	5.18 (17)	8e-5	1.0	18.8 (120)	0	38	–	–
Blanket ML	5.49 (18)	2e-7	0.25	18.1 (115)	1.20 (25)	36	19.1 (400)	10
Aquifer SP–SM	9.76 (32)	8e-5	1.0	18.8 (120)	0	35	–	–
Aquitard ML	-	2e-7	0.25	18.1 (115)	4.79 (100)	33	64.6 (1350)	10
Seepage Wall SCB	3.10 (20)	1e-8	1.0	18.8 (120)	17.2 (360)	4	23.9 (500)	0

3.1 Water Surface Elevation, WSE

Return periods and associated exceedance probabilities for specific water surface elevations were obtained from a levee project on the West Bank of the Sacramento River (index point 6, river mile 52.75), located directly across from the Pocket area, which represents the model levee considered in this document (USACE, 2014b). These levels are consistent with those reported by GEI/HDR (2015) for I Street Bridge and Freeport gauges, located several miles up and downstream, respectively. Site-specific WSE for each return period was found by correlating the 200-yr WSE from USACE (2014b) to the elevation used to define the representative Pocket cross section in Section 3 and Table 4.1 (data from GEI/HDR (2015)). Return period and equivalent exceedance probability are summarized in Table 3.2. A PDF is approximated using the increment of cumulative probability

Table 3.2: Return period and probability of exceedence for WSE (also WSE normalized by levee height, H). Return periods are from hydrologic analysis in USACE (2014b) for western levee of Sacramento River, directly across from the Pocket site. Elevations converted to eastern levee by equating 200-yr WSE from GEI/HDR (2015). PDF estimated by dividing exceedence probability by increment of WSE (Figure 3.2).

WSE (m)	WSE/H (–)	Return Period (yr)	Exceedance Probability (–)	Approx. PDF (–)
0.82	0.16	1	0.999	0.0012
1.83	0.35	2	0.500	0.4960
2.23	0.43	10	0.100	1.0076
3.05	0.59	25	0.040	0.0729
3.23	0.62	50	0.020	0.1093
3.42	0.66	100	0.010	0.0546
3.96	0.76	200	0.005	0.0091
4.39	0.85	500	0.002	0.0070

density between each entry divided by the difference in WSE. The PDF and CDF are plotted with lognormal, Gumbel and gamma distributions in Figure 3.2 using best fit distribution parameters from an algorithm in Matlab (MathWorks, 2015). Probability density fits nicely over all WSE, but Table 3.2 shows the 200- and 500-year levels match poorly; this is problematic because these water levels are important for common practice in deterministic levee design (URS, 2014). Alternative parameters are selected for each distribution such that CDF for 200- and 500-yr WSE matches the return period (i.e., $1-F(WSE_{200})=0.005$ and $1-F(WSE_{500})=0.002$), also presented in Figure Figure 3.2 and Table 3.2. The PDF appears to fit high return period levels well, but the mode matches poorly. Alternatively, in Figure 3.3 the upper tails of the distribution, show a good match with the 200/500-yr fit, however, the best fit parameters are still within a percent. Interestingly, despite being selected for high WSE, the 200/500-yr fit for mid-level WSE seems to match best. No method or distribution seems to match the more common events better than the others. Thus, depending on results of reliability analyses there may not be an appreciable distinction between distributions.

Table 3.3: Numerical comparison of WSE distribution and parameters against design levels from USACE (2014b) for the same curves in Figure 3.2 and 3.3. All combinations match low and moderate water levels well, but best-fit distribution parameters result in large over-estimates of return period for high WSE. Average WSE is 0.5 m lower for 200/500-yr fit compared to best fit distributions.

Distribution			LN(λ, ζ) best fit		Gmb(u, α) best fit		Gam(k, λ) best fit		LN(λ, ζ) 200/500-yr fit		Gmb(u, α) 200/500-yr fit	
Parameter 1			0.7997		2.0746		27.8792		0.5052		1.4991	
Parameter 2			0.1838		3.1029		12.3069		0.3385		2.1494	
Distribution μ			2.2627		2.2606		2.2653		1.7550		1.7677	
Distribution σ			1.5042		1.5035		1.5051		1.3248		1.3295	
Design Level			$P_e = 1 - F(WSE)$ (-) and R (yr) computed from distribution									
$\frac{WSE}{H}$	P_e	R	P_e	R	P_e	R	P_e	R	P_e	R	P_e	R
0.16	0.999	1	1.000	1	1.000	1.00	1.000	1.00	0.981	1.02	0.986	1.01
0.35	0.500	2	0.857	1.17	0.883	1.13	0.848	1.18	0.385	2.59	0.389	2.57
0.43	0.100	10	0.499	2.00	0.465	2.15	0.512	1.95	0.192	5.22	0.189	5.29
0.59	0.040	25	0.043	23.1	0.048	21.1	0.044	23.0	0.036	27.9	0.035	28.5
0.64	0.020	50	0.021	47.4	0.027	36.8	0.020	50.2	0.024	41.3	0.024	42.0
0.66	0.010	100	0.010	101	0.016	64.5	0.009	118	0.016	61.2	0.016	61.9
0.76	0.005	200	0.001	1190	0.003	350	0.001	2190	0.005	200	0.005	200
0.85	0.002	500	1e-4	9180	8e-4	1320	3e-5	3.0e4	0.002	500	0.002	500

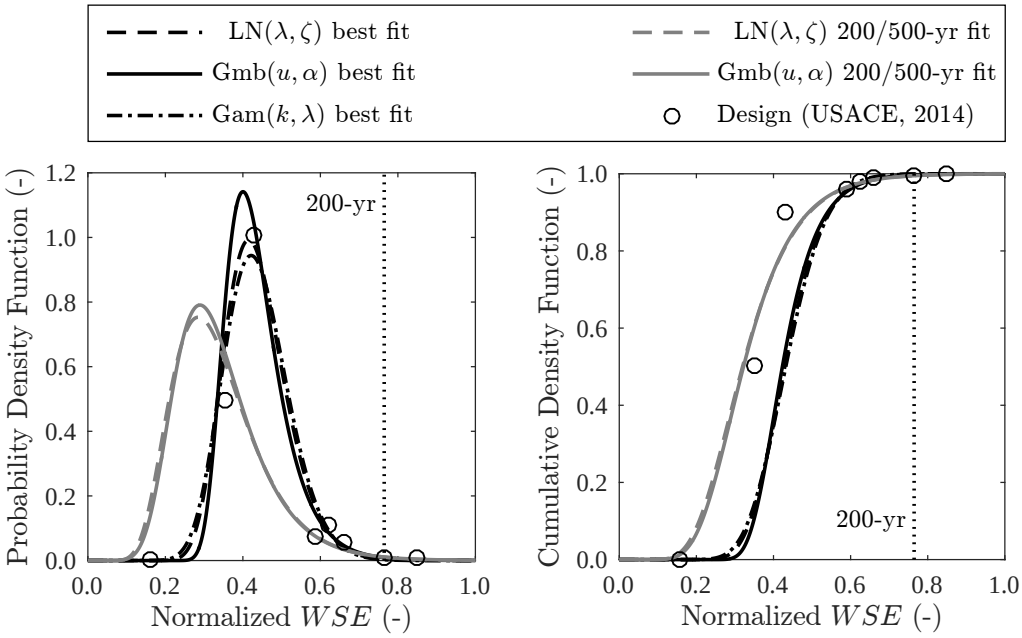

Figure 3.2: PDF and CDF of *WSE* for lognormal, Gumbel and gamma distributions and comparison to hydrologic design levels from USACE (2014b), Table 3.2. Black curves use distribution parameters for best-fit of all design levels, gray curves match only 200-yr and 500-yr *WSE* (for lognormal and Gumbel only). Figure 3.3 illustrates the same curves for high return period events (high values of the CDF). Table 3.3 provides distribution parameters and numeric comparison.

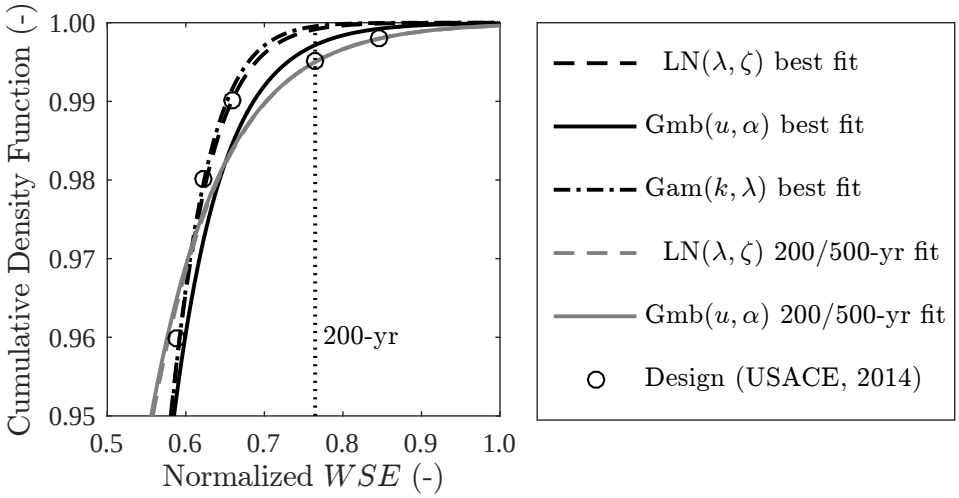

Figure 3.3: CDF of *WSE* for high return periods, using same parameters as Figure 3.2. Lognormal and Gumbel parameters for 200/500-yr match produce identical results in this range, and best-fit parameters are similar. The Gumbel distribution with best-fit parameters is closer to the 200/500-yr probability. Table 3.3 provides distribution parameters and a numeric comparison.

3.2 Hydraulic Conductivity

Hydraulic conductivity and permeability are often used interchangeably in the literature; in this document hydraulic conductivity refers to the flow of water through pore spaces of a soil in units of [L/T], typically m/s. Hydraulic conductivity is most often considered a lognormal random variable for two reasons: values for a given soil can span multiple orders of magnitude and a there is a physical limit precluding negative values (Benson, 1993; Freeze, 1975; Law, 1944; Lee et al., 1983). Law (1944) is commonly cited as the first to apply the lognormal distribution, and the history of doing so is concisely described by Freeze (1975), who also acknowledges that other distributions are acceptable. For example, Ricciardi et al. (2005) reevaluated the Law (1944) dataset and found the beta distribution matches well.

Because it is expensive to compile a site-specific dataset of hydraulic conductivity for statistical evaluation, over the last several decades it has been common for stochastic analyses to assume a lognormal distribution and report coefficient of variation, δ, without consideration of new data (Fenton & Griffiths, 2008; Uzielli et al., 2006). While this is an acceptable approach, it has led analysts evaluating shallow, unconsolidated and generally Quaternary-age soils to depend on a small number of data sets for stochastic hydraulic conductivity characterization, the most prominent of which are listed below:

- Law (1944): 59 measurements of the Dominguez formation, a regional oil producing sedimentary deposit in Los Angelos County, CA; widely cited as justification for lognormal distribution applicability
- Lumb (1971): 42 measurements on 4 samples of silty sand from Hong Kong, finding $\delta = 22\%$ for test accuracy and $\delta = 240\%$ at a site (this is the only source with repeated tests on the same soil); Lumb (1966): 53 measurements on alluvial sandy clay from Hong Kong; cited by Baecher and Christian (2003) and Lee et al. (1983)
- Nielsen et al. (1973): 120 measurements of near-surface soils an approximately half mile square field; cited by Harr (1996)
- Benson (1993): 2497 measurements of compacted clay landfill liners and covers from 57 sites in North America; cited by Baecher and Christian (2003)

The sources listed above are the predominant data sources for hydraulic conductivity δ summarized by Baecher and Christian (2003), Fenton and Griffiths (2008), Harr (1996), Jones et al. (2002), Uzielli et al. (2006) and their preceding publications, which generally recommend using δ up to 200%. Phoon and F. H. Kulhawy (1999) refers to a dataset for hydraulic conductivity in F. Kulhawy and Mayne (1990), but there is no way to obtain δ. Willardson and Hurst (1965) describe an excellent dataset for 12 sites with nearly 1500 test data for seven shallow soils, indicating a range of δ from 40% to 310%, with an average of 110%. Indirect measurements of hydraulic conductivity can be found from consolidation coefficient data reported by Lumb (1971), reporting 32% for test accuracy and 47% at a site, and Harr (1996) reporting 30% to 90% for laboratory test results. For similar stress states the coefficient of variation for coefficient of consolidation should apply to hydraulic conductivity, since they are proportional and are scaled by stiffness and unit weight (Holtz & Kovacs, 1981). URS (2014) provides data on 302 tests at 17 sites for alluvial near-surface soils in California. Analysis of this data gave a δ of 60% to 210% for several soils. When separated by soil type, direction and location (i.e., horizontal and vertical), groups with over

5 samples had a δ of 50% to 190%, which is not a significant reduction, perhaps due to the fact that these subgroups still represented samples from nearly 40 different boreholes. The USACE (1999) uses δ of around 30% to represent the variability of hydraulic conductivity within a single layer for seepage reliability analyses and explicitly assumes the large range of data found in the literature is due to aleatory variability between sites. Note that, as a result, for the same coefficient of variation a soil with lower hydraulic conductivity will vary over a larger range of magnitudes than a soil with higher hydraulic conductivity.

Hydraulic Conductivity Ratio

The first and second moments of a function of random variables such as K_r can be found in terms of the dependent variables; Table 3.4 presents distribution parameters of K_r as a function of $K_{a,h}$ and $K_{b,v}$ for various values of δ, all with a constant median for K_r of $x_{50} = 1600$, which is the deterministic value used in reference analyses. Thus if $\delta = 0.30$ for the blanket and aquifer, K_r has $\delta = 0.42$, with a median value of 1600, mean of 1740 and a range of 1060 to 2420 containing 68% of the data (i.e., the normal distribution $\mu \pm \sigma$ equivalent; Table 3.4, Case A). Similarly, when $\delta = 2.00$ for blanket and aquifer, the high end reported in the literature, $\delta = 4.90$ for K_r. Although mathematically correct, $\delta = 4.90$ implies 78% of the probability density is located between the distribution median and mode, which is highly dispersed (Table 3.4, Case C). In other words, likely values of K_r could be almost anything. Clearly the distribution parameters should be selected such that a smaller range of reasonable values for K_r are used in reliability analyses. USACE (1999) uses a δ of 20% to 30% for an individual layer, which targets 20% to 30% for the blanket ratio, K_r. Several published works following the general USACE guidelines for risk analysis seem to incorporate the K_r recommendation when evaluating seepage stochastically (Benjasupattananan, 2013; Ketchum et al., 2011; Perlea & Ketchum, 2011; Sibley et al., 2017), although other researchers have used higher values (Rice & Polanco, 2012).

Of the distributions considered in Table 3.4 only cases B and C have a significant portion of the PDF below the sensitive threshold for $K_{a,h}$ and $K_{b,v}$ selection, specifically $x_{50}e^{-\zeta^2} < 1000$. For case A, only about a 15% of the PDF is below $K_r = 1000$. Thus, while Cases A–C in Table 3.4 illustrate the effect of changing variance for K_r, the wide range of possible values warrants consideration of different central tendency measures, especially for values of K_r that are more sensitive to pore pressure. An additional set of distribution parameters is defined such that the median, x_{50}, is 10, 100 and 1000, keeping $K_{a,h}$ constant and setting $K_{b,v} = K_{a,h}/K_r$ for $\delta = 0.3$ and 2.0 (Table 3.5). In each case, spread of the distribution increases dramatically from $\delta = 0.3$ to 2.0; however, the ratios between values remain constant between cases A and B or 10, 100 and 1000. For example, $x_{50}e^{\pm\zeta^2}$ increases from about 1.66 to 60.1 for Case B–10 versus 166 to 6010 for Case B–1000, but the ratio is 36 for each case. Case A is identical in behavior, although the ratio is only 2.3. Thus, for a given range across the PDF increasingly larger ranges of K_r will be encountered as x_{50} increases. Because the sensitivity of pore pressure to K_r is essentially negligible for $K_r \gtrsim 1000$, the large range of possible values for high x_{50} becomes unimportant.

Table 3.4: Comparison of lognormal distribution metrics of K_r for various coefficient of variation values of the dependent variables $K_{a,h}$ and $K_{b,v}$[a]. The terms $x_{50}e^{\pm\zeta^2}$ for the lognormal distribution are equivalent to $\mu \pm \sigma$ for the normal, containing 68.3% of the PDF. As δ increases, the likely range of K_r increases dramatically. Appendix A plots the lognormal distribution for various combinations of parameters λ and ζ.

Distribution Parameter	Case A		Case B		Case C	
δ for $K_{a,v}$ & $K_{b,h}$	0.30		1.00		2.00	
δ for K_r[b]	0.43		1.73		4.90	
	K_r	$F(K_r)$	K_r	$F(K_r)$	K_r	$F(K_r)$
x_a	1740	0.582	3200	0.722	8000	0.815
x_{50}	1600	0.500	1600	0.500	1600	0.500
x_{mo}	1350	0.339	400	0.120	64	0.036
$x_{50}e^{+\zeta^2}$	2420	0.841	5190	0.841	9620	0.841
$x_{50}e^{-\zeta^2}$	1060	0.159	493	0.159	266	0.159

[a] $\mu = 8e-5$ m/s for $K_{a,v}$ and $5e-8$ m/s for $K_{b,h}$ in Cases A–C
[b] ζ for K_r in Cases A–C is 0.415, 1.18 and 1.79 ($\lambda = 7.38$ for all)

Table 3.5: Comparison of lognormal distribution metrics of K_r for $x_{50} = 10$, 100 and 1000, along with coefficient of variation values of 0.3 and 2.0 for dependent variables $K_{a,h}$ and $K_{b,v}$, equivalent to Cases A and C in Table 3.4. The terms $x_{50}e^{\pm\zeta^2}$ for the lognormal distribution are equivalent to $\mu \pm \sigma$ for the normal, containing 68.3% of the PDF. Appendix A plots the lognormal distribution for various combinations of parameters λ and ζ.

Distribution Parameter	Case A–10	Case B–10	Case A–100	Case B–100	Case A–1000	Case B–1000
δ for $K_{a,v}$ & $K_{b,h}$	0.30	2.00	0.30	2.00	0.30	2.00
δ for K_r	0.43	4.90	0.43	4.90	0.43	4.90
λ	2.30	2.30	4.61	4.61	6.91	6.91
ζ	0.415	1.79	0.415	1.79	0.415	1.79
x_a	10.9	50.0	109	500	1090	5000
x_{50}	10.0	10.0	100	100	1000	1000
x_{mo}	8.42	0.400	84.2	4.00	842	40.0
$x_{50}e^{+\zeta^2}$	15.1	60.1	151	601	1510	6010
$x_{50}e^{-\zeta^2}$	6.60	1.66	66.0	16.6	660	166

[a] Cases letter refers to δ for $K_{a,h}$ and $K_{b,v}$; number refers to median of K_r

3.3 Blanket Layer Thickness

Thickness of the blanket layer influences stability through the concentration of pore pressures within the blanket layer. Therefore, blanket thickness is a key component of USACE reliability analysis for underseepage (Sibley et al., 2017; USACE, 1999), and while in some cases probability distributions have been applied in analyses directly (Benjasupattananan, 2013; Polanco & Rice, 2014; Rice & Polanco, 2012), several studies have used expert elicitation (URS/JBA, 2008a) or at least considered sensitivity using non-stochastic models (Batool et al., 2015; Chowdhury et al., 2012). Site-specific data is obviously critical for this parameter, as the blanket depends largely on gelogic and geomorphic conditions, as well as historic human activities. Field data collected by GEI/HDR (2015) was used to evaluate blanket layer thickness variability. For the entire project area (approximately from the American River to South of the Pocket) blanket thickness had an average of 5.94 m (19.5 ft) and coefficient of variation of 0.39 ($N = 120$). For Reach 15 to 27, which includes only the Pocket area (Station 1341+00 1640+00) blanket thickness had an average of 5.78 m (19.0 ft) and coefficient of variation of 0.34 ($N = 61$), a slight decrease in average and variability. Minimum and maximum thicknesses for the Pocket were 1.80 and 10.3 m (5.89 and 33.9 ft), a range of 8.5 m (27.9 ft).

Figure 3.4 shows how normal, truncated normal and lognormal distributions fit the data. We want the mean and dispersion of the distribution to reflect the mean and dispersion of the data, which means selecting parameters such that qualities of the distribution match the data. As can be seen in the figure, preventing negative values has a visible effect on the shapes of the PDF, pushing the mode higher and compressing the upper tail, which can also be seen at the upper end of the CDF. Visually the lognormal distribution does not fit the data as well as the normal, especially in the lower end of the distribution, but it seems to do better overall than the truncated normal. Comparing each CDF shows that probability of the blanket being less than 5 m, $\mathrm{P}(z_B < 5.0\ \mathrm{m})$, is 0.398, 0.360 and 0.395 for each distribution; clearly the truncated normal diverges from the others. To understand the characteristics of the truncated normal distribution consider three cases where distribution parameters μ_t and σ_t have been matched to the data (Cases A, B and C, assuming $\mu = 5.488$ m and δ is 0.25, 0.35 and 0.05). Figure 3.5 shows each distribution still compresses laterally with increasing δ. Also shown is the effect of two different truncation limits: $(x_l, x_u) = (3, 10)$ and $(x_l, x_u) = (0, \infty)$. Each distribution still has very similar shapes for $\delta = 0.25$ and 0.35, but the increase in x_{mo} is larger for higher δ because a more significant portion of the PDF is normalized from the tails beyond x_l and x_u. Furthermore, we see a shift of the mode to the left for higher δ, since the left limit, x_l is closer to the center of the distribution than the right limit, x_u. As the PDF and CDF show, more stringent limits cause the data fit to become worse. For example, $\mathrm{P}(z_B < 5.0\ \mathrm{m})$ goes from 0.355 to 0.361 for Case A and 0.397 to 0.399 for Case B, which could be a significant change if a reliability solution is sensitive to blanket layer thickness.

Quantitative effects are further explored in Table 3.6, which compares central tendency measures of the normal and truncated normal distributions. Distributions presented in Figure 3.5 and Table 3.6 have the following parameters:

- Case A: $z_B \sim \mathrm{N}(5.488, 1.372)$ and $z_B \sim \mathrm{tN}(5.406, 1.172, 3, 10)$
- Case B: $z_B \sim \mathrm{N}(5.488, 1.921)$ and $z_B \sim \mathrm{tN}(5.207, 1.386, 3, 10)$
- Case C: $z_B \sim \mathrm{N}(5.488, 0.274)$ and $z_B \sim \mathrm{tN}(5.488, 0.524, 3, 10)$

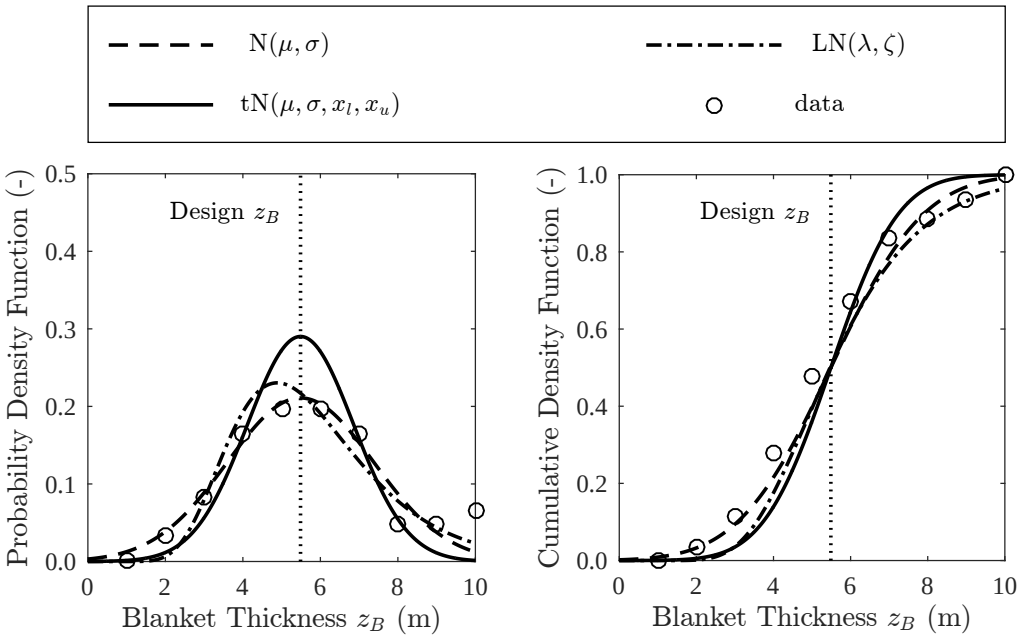

Figure 3.4: Distribution comparison for blanket layer thickness, z_B, (PDF and CDF). Normal, truncated normal and lognormal distributions evaluated with distribution parameters selected from GEI/HDR (2015) data in the Pocket area: $\mu = 5.78$ m (19.0 ft), $\delta = 0.34$, $N = 61$. Truncated normal distribution is only limited on the lower tail: $x_l = 0$ m and $x_u = \infty$. Normal distribution has the best match; the truncated normal overestimates the PDF at the mean due to weighting from the truncated tail, whereas the lognormal has a positive skew.

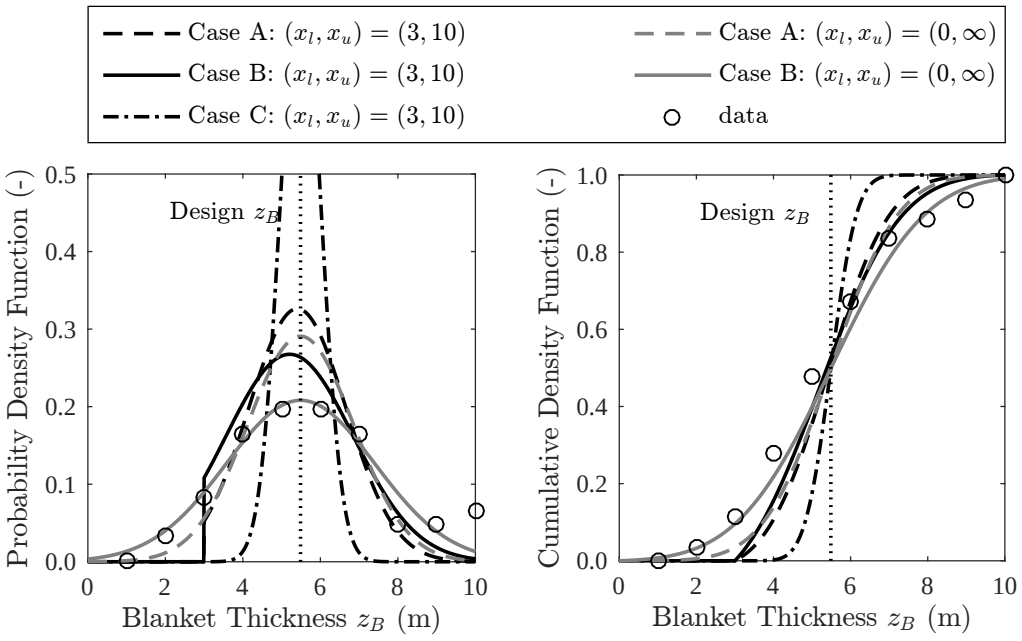

Figure 3.5: Comparison of truncated normal distribution parameters for blanket layer thickness, z_B, (PDF and CDF). Parameters μ_t and δ_t are selected such that the truncated distribution has one of three δ values (0.25, 0.35 and 0.05 for Case A, B and C) and an arithmetic mean matching GEI/HDR (2015) data in the Pocket area ($\mu = 5.78$ m (19.0 ft), $N = 61$). Truncation limits are $x_l = 3$ m and $x_u = 10$ m for Cases A-C, and $x_l = 0$ m and $x_u = \infty$ for Cases A and B.

Distribution parameters are selected such that μ and δ of the data are matched by the distribution (δ_t is used to represent the ratio of truncated normal distribution parameters σ_t/μ_t). Mean and median each decrease, confirming the shift in skewness observed in Figure 3.5. For Cases A and B dispersion decreases, evidenced by changes in δ, σ of the distribution and $x_a \pm \sigma$, but the opposite occurs for Case C, which is an effect of the relatively narrow distribution shape with respect to the limits. Areas of low probability density are present for much of the region between x_l and x_u and are much more affected by scaling of the PDF and CDF with probability density outside the limits, causing an overall increase in dispersion of the distribution when compared to the normal equivalent.

The examples presented here illustrate that the truncated normal distribution is capable of modeling blanket thickness, although the normal and lognormal distributions are also sufficient, if not better, when it is more desirable to match the PDF and CDF to data. Although distribution limits can cause significant changes in probability density for site-specific data, they are acceptable where physical justification exists. Once the design point of a reliability analysis is known and the critical region of a random variable PDF is known, modifications to distribution parameters can be made for subsequent analyses.

3.4 Strength and Unit Weight Properties

Considerable data is available to statistically define strength (cohesion, c, and friction angle, ϕ) and unit weight (γ). Correlations and recommended values for coefficient of variation can be found in most of the references cited in previous sections of this document. Fortunately, site-specific data from the Pocket (GEI/HDR, 2015) is available for γ and ϕ, which is summarized in Table 3.7, along with the typical values summarized in Table 2.2 for comparison. Although the number of tests is limited, it appears that the site-specific data generally conforms to expected δ for γ, but given the relatively small data set for ϕ, it is more appropriate to use a typical value of 0.05.

Table 3.6: Comparison of normal and truncated normal distribution statistics for blanket layer thickness, z_B[a]. Parameters μ_t and δ_t are selected such that the truncated distribution has one of three δ values (0.25, 0.35 and 0.05 for Case A, B and C) and an arithmetic mean matching GEI/HDR (2015) data in the Pocket area ($\mu = 5.78$ m (19.0 ft), $N = 61$).

Matched Data[b]	Case A		Case B		Case C	
μ	5.488		5.488		5.488	
δ	0.25		0.35		0.05	
Distribution Parameter	N	tN	N	tN	N	tN
μ or μ_t	5.488	5.406	5.488	5.207	5.488	5.488
δ or δ_t	0.250	0.233	0.350	0.315	0.050	0.095
x_{50}	5.488	5.450	5.488	5.387	5.488	5.488
x_{mo}	5.488	5.406	5.488	5.207	5.488	5.488
σ or σ_t	1.372	1.172	1.921	1.386	0.274	0.524
$x_a + \sigma$ or σ_t	6.860	6.578	7.409	6.593	5.762	6.012
$x_a - \sigma$ or σ_t	4.116	4.235	3.567	3.821	5.213	4.964

[a] $x_l = 3.0$ m and $x_l = 10.0$ m for all cases
[b] μ and δ refer to the data; $\mu = 5.488$ for all cases

Table 3.7: Coefficient of variation, δ, for strength and unit weight, computed from Pocket data reported by GEI/HDR (2015). All data fit a normal or lognormal distribution per Kolmogorov-Smirnov tests. Expected δ are values from literature (Table 2.2).

Property	Expected δ	N	δ from Data
Unit Weight, γ silty sands	0.10	75	0.077
Unit Weight, γ silts	0.10	234	0.056
Unit Weight, γ clays	0.10	49	0.069
Friction, ϕ Blanket	0.05	24	0.072
Friction, ϕ Embankment	0.05	5	0.012
z_B, Blanket Thickness	N/A	61	0.340

Chapter 4

Analysis Results: Levee Without Vegetation

4.1 Seepage Analysis

Steady-state seepage analyses determine pore pressure at finite element nodes and interpolate the location of the phreatic surface. Breakout height is the landside slope location below which seepage exits the soil (i.e., nodes with a saturated condition), and gradient is measured vertically across the blanket layer. Figure 4.1 shows the elements of a seepage analysis solution across all WSE, and the phreatic surface solution is illustrated in several figures throughout this document. For effective and total stress methods $FS_{us,t}$ and $FS_{us,e}$ approach 1 as water level approaches the levee crest, with $FS_{us,t} < FS_{us,e}$. Gradient has a linear relationship with WSE, and breakout height can nearly reach the slope midpoint.

Throughseepage can occur in the embankment material when breakout height rises up the landslide slope. For a completely cohesionless embankment FS_{ts} becomes the worst-case scenario at 0.57. For a given slope angle, θ, and soil properties ϕ'_E and γ_E, factor of safety (FS_{ts}) is dependent primarily on cohesion, c'_E, and an assumed sliding depth, z_s, as computed in Figure 4.2 for the Pocket levee (slope is 2.5:1 H:V). In the cohesionless case FS_{ts} is constant, but when c'_E is increased slightly FS_{ts} can increase significantly, especially for small z_s. As z_s increases FS_{ts} approaches the cohesionless case.

Pore pressures from the seepage analysis are used directly in stability analyses and at a given WSE are governed primarily by hydraulic conductivity ratio, K_r, and blanket layer thickness, z_B. Because pore pressures have such a large influence on the stability assessment, sensitivity of the seepage solution to seepage parameters is described in the sections on stability.

4.2 Stability Analysis

With no vegetation considered, the landside slope is marginally stable when water is at the crest, where the least stable sliding surface has FS of 1.0 for circular and 0.9 for non-circular surfaces. Both begin at the edge of the crest and extend a couple meters into the blanket, returning to the surface about 5 meters beyond the toe (Figure 4.3), the primary difference in geometry being the planar segment of the non-circular surface within the embankment soil, which is the expected failure mode in a cohesionless soil. A summary of FS (circular and non-circular) for the sliding surface shown in Figure 4.3 at various water levels is presented in Table 4.1. Although sliding sur-

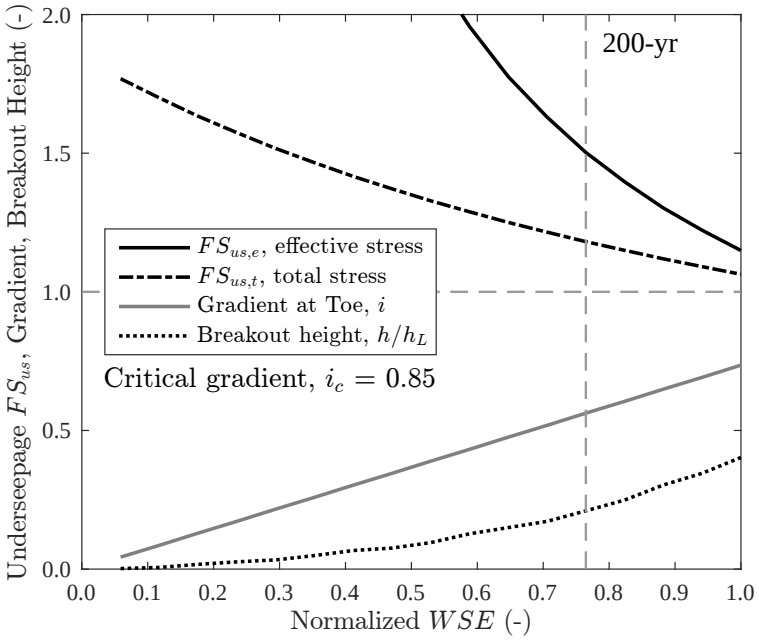

Figure 4.1: FS, breakout height and gradient versus WSE for underseepage (FS_{us}). Gradient is computed vertically across the entire blanket at the toe ($z_B = 2.87$ m, or 18 ft), critical gradient is based on $\gamma_B = 18.1$ kN/m^3 (115 pcf).

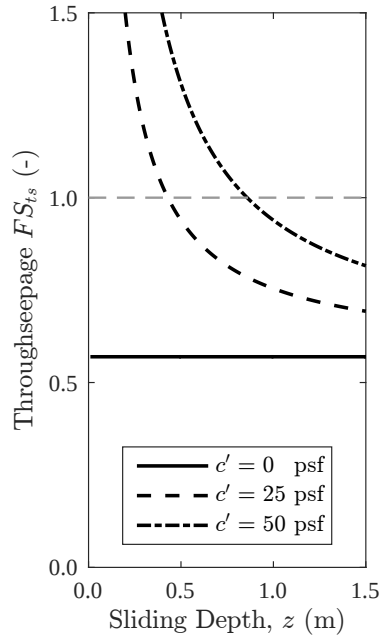

Figure 4.2: FS for throughseepage in embankment (FS_{ts}) with varied sliding depth and soil cohesion of 0, 25 and 50 psf (1.20 and 2.39 kPa). Slope is 2.5:1 (H:V), $\gamma_E = 18.8$ kN/m^3 (120 pcf). Assumes infinite slope failure surface, per Duncan et al. (2011), with $c' > 0$ case approaching $c' = 0$ case for large z (when $z \gg c'/\gamma_t$).

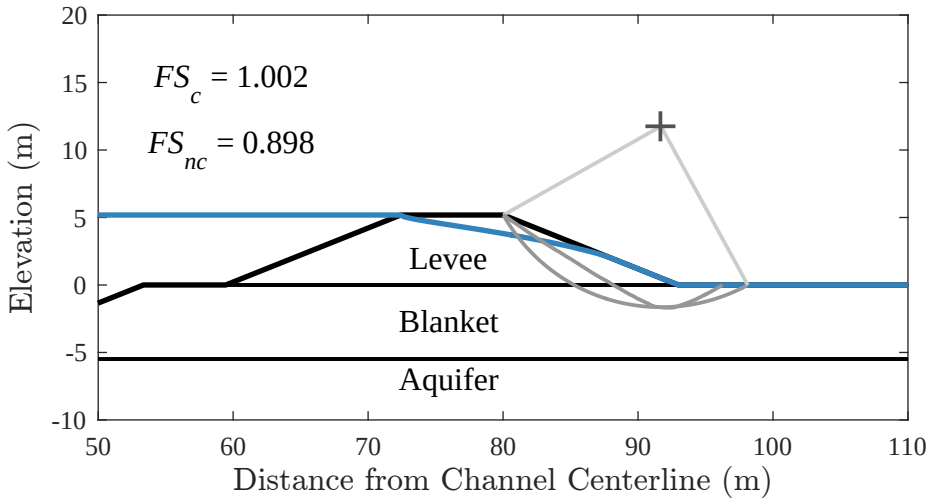

Figure 4.3: Landside hinge potential sliding surfaces (circular and non-circular), which are also minimum FS (i.e., critical) surfaces for all WSE, summarized in Table 4.1. The term "critical surface" refers to stability only, not general levee performance for all failure modes.

face changes somewhat with changes in WSE, the results presented in Table 4.1 are representative of the overall response, as the geometry of all surfaces was similar.

Non-circular surfaces often produce lower values of FS when compared to circular surfaces with identical properties. This is in part due to critical surfaces being linear in cohesionless material and circular in cohesive material. For the Pocket levee the critical non-circular surface is planar in the cohesionless embankment and curves in the cohesive blanket. In addition, the ability to compute non-circular critical surfaces is a key factor to understanding the effects of vegetation, as seen in Chapter 6.

To illustrate how FS changes for different slope stability failure modes, several additional potential sliding surfaces are presented here, including:

- Complete crest (circular and non-circular): begins at waterside hinge and extends over two-thirds of the way through the blanket layer before reaching the ground surface just over ten meters beyond the landside toe; illustrated in (Figure 4.4)
- Shallow hinge/toe circle: just over one meter deep in the middle, this shallow "cosmetic" sliding surface begins at the landside hinge and ends at the landside toe (Figure 4.4)
- Wedge surfaces: four completely planar surfaces that exit the slope at the landside toe and enter at equal intervals along the crest (Figure 4.5)

Each of these surfaces has a FS about 0.3–0.5 greater than the minimum FS geometry, depending on water level. Surfaces that encompass the complete crest were determined by searching for the minimum FS geometry while fixing the left endpoint at the waterside edge of the crest. As with the landside hinge surfaces, the non-circular case ($FS = 1.213$) is linear within the embankment soil and FS is about 0.1 less than the circular geometry ($FS = 1.320$). The shallow hinge/toe circle is primarily a cosmetic failure in the landside slope, and along with the steeper wedge failures can be

WSE/H	WSE	WSE	FS_c	FS_{nc}	Notes
–	ft	m	–	–	–
0.177	3.0	0.9	2.041	2.108	
0.353	6.0	1.8	1.851	1.896	
0.500	8.5	2.6	1.672	1.692	Midpoint
0.647	11.0	3.4	1.482	1.474	
0.765	13.0	4.0	1.322	1.285	200–yr
0.912	15.5	4.7	1.118	1.038	
0.941	16.0	4.9	1.081	0.993	HTOL
1.000	17.0	5.2	1.002	0.898	Crest

Table 4.1: Summary of FS versus WSE for critical (i.e., minimum FS) circular and non-circular potential slip surfaces for Pocket levee, illustrated in Figure 4.3. H is levee height, used for normalization of WSE. HTOL is hydraulic top of levee; the 200-yr and HTOL design levels are from GEI/HDR (2015).

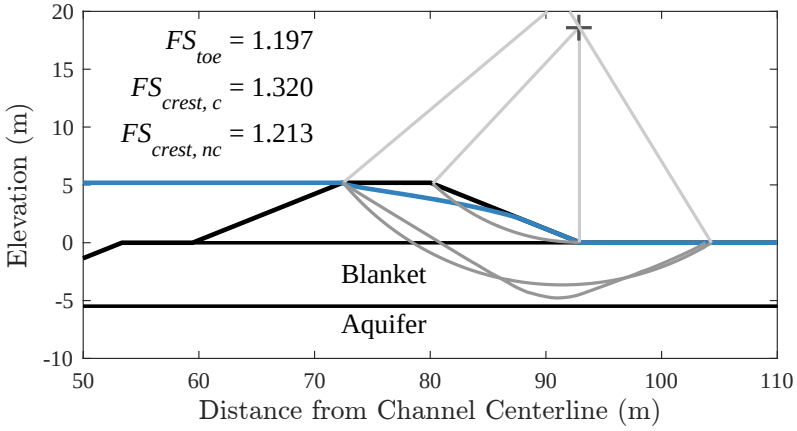

Figure 4.4: Potential sliding surfaces for complete crest (circular and non-circular) and shallow hinge/toe circle for $WSE/H = 1$.

used to compare vegetation effects described in this document to other published work, of which a large portion relies on infinite slope analyses.

Relative stability across all WSE for the potential sliding surfaces described above are compared on Figures 4.6 and 4.7. Hydraulic conditions have a similar influence on FS for the non-wedge surfaces, with $\Delta FS \sim 1$ as WSE rises from toe to crest ($\Delta FS \sim 0.25$ per meter), which is a result of rising pore pressure in the blanket layer (except for the shallow hinge/toe case). Phreatic surface location within the embankment also influences the decrease of FS with increasing WSE, as illustrated by the shallow hinge/toe and wedge surfaces, which are only affected as water level rises above the half height of the embankment. This is due to the phreatic surface intersecting each surface as it moves towards the landside slope. In general, FS has a monotonic response to changing WSE; however, this is not the case at small scales, as described in the sections below.

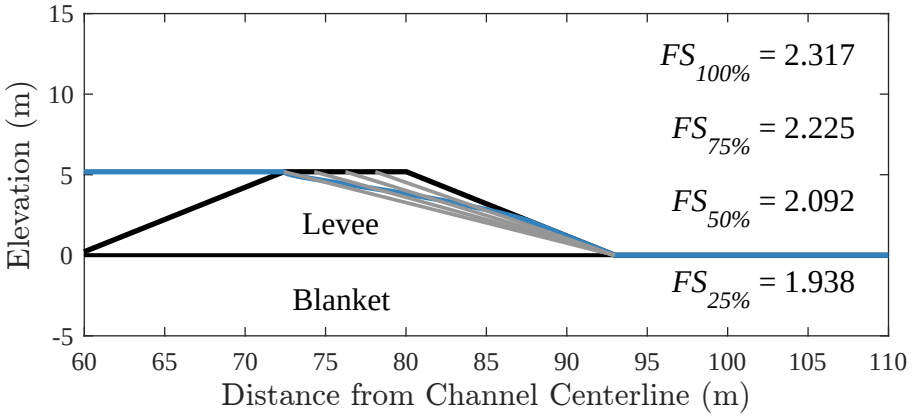

Figure 4.5: Potential sliding surfaces for wedges exiting embankment at landside toe.

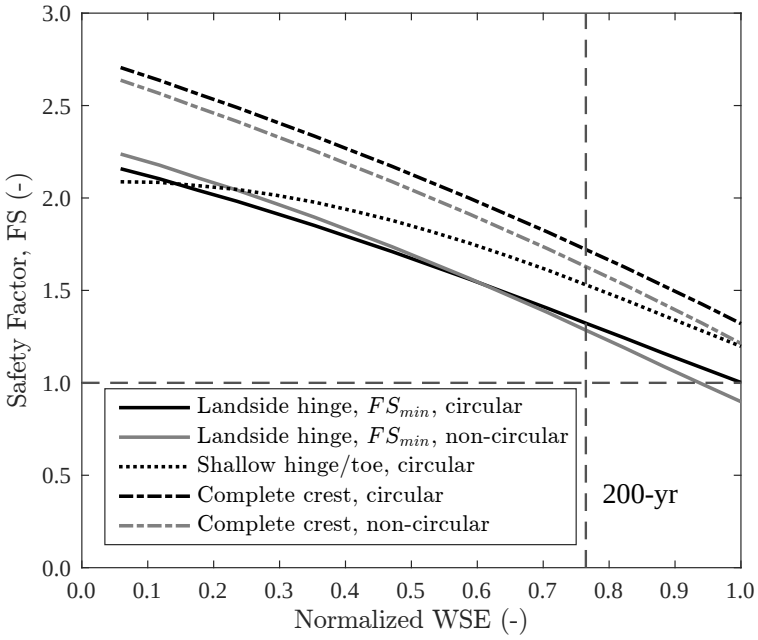

Figure 4.6: FS versus WSE for landside hinge (minimum FS), complete crest and shallow hinge/toe surfaces

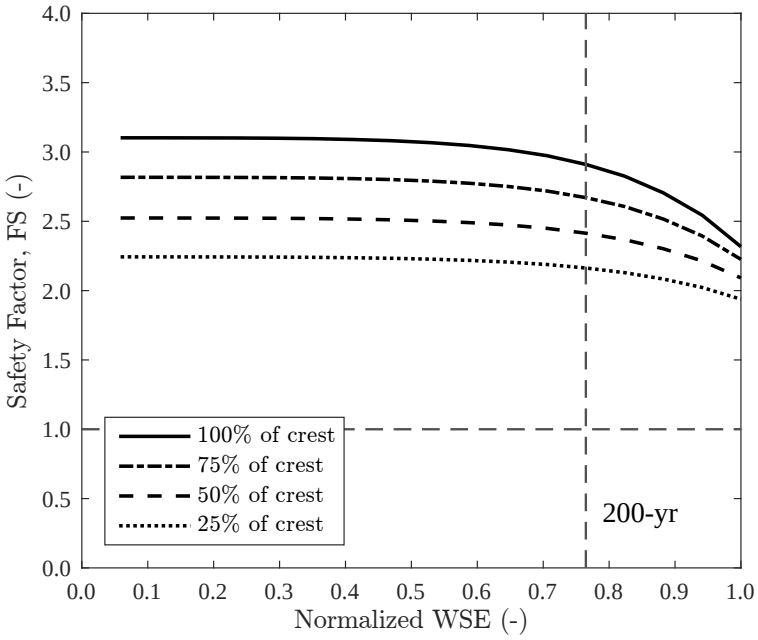

Figure 4.7: FS versus WSE for potential wedge surfaces

4.3 Sensitivity to Selected Variables

The influence of key properties in seepage and stability analyses can be understood by evaluating the change in $FS(\mathbf{x})$ due to each variable in $\mathbf{x}$ for different potential slip surfaces. In this document sensitivity is evaluated as ΔFS due to Δx_i for a single WSE, the 200-yr level, or 3.96 m (13 ft), since the effects are generally consistent across the entire range. For very low WSE sensitivity may change but is considered irrelevant due to extremely high values of $FS(\mathbf{x})$. For very high WSE sensitivity may be undefined if Spencer's method is not capable of finding a solution for FS (i.e., FS is too low or numerically sensitive to extreme values of certain properties). The relationship between $FS(\mathbf{x})$ and each x_i serves several functions: it captures the computation limits of seepage and stability software; it is used in evaluating the partial derivative of levee response, which is the gradient computation necessary for FORM; and it provides one of the measures of the relative importance of each parameter.

Figure 4.8 compares sensitivity of FS to strength, unit weight and thickness of the blanket; Figure 4.9 to strength and unit weight of the embankment; and Figure 4.10 to hydraulic conductivity ratio, including the method for implementing $K_{a,h}$ and $K_{b,v}$, as described above. Although the ranges of parameter values extend beyond what is appropriate to use in a deterministic analyses, the plots show the computation limits for seepage and stability, which is important for certain cases where FORM converges on relatively low probability events. The design value for each parameter corresponds to the value used in deterministic analyses, which is why the sensitivity, ΔFS, is zero at that plot location. Up to six potential sliding surfaces are shown for each sensitivity plot: circular and non-circular pairs of landside hinge (Figure 4.3) and complete crest surfaces (Figure 4.4), the shallow hinge/toe circle (Figure 4.4) and complete crest wedge (4.5). As the shallow hinge/toe and wedge surfaces do not intersect the blanket layer, they have no sensitivity to blanket strength, unit weight and thickness. However, hydraulic ratio influences pore pressure and the phreatic surface within the embankment, so despite corresponding to a layer not physically intersected by these

surfaces, FS is still influenced by K_r.

All parameters are positively correlated with FS except hydraulic conductivity ratio (for all surfaces) and blanket unit weight for the complete crest surfaces. Positive correlation with unit weight is due to drained strength generally increasing more than driving load on the sliding surface, which is not the case for the large mass of embankment material for the complete crest case, which are negatively correlated. Furthermore, most sensitivity plots generally illustrate linear relationships, the exceptions being hydraulic conductivity and blanket layer thickness.

Hydraulic conductivity ratio has a non-linear relationship with FS (Figure 4.10a): i.e. all potential sliding surfaces are affected only after K_r decreases below 1000, reaching maximum increases in FS of about 0.2–0.8 when K_r is below unity. For $K_r < 1.0$ the blanket layer no longer is controlling water flow below the embankment as the underlying aquifer has a lower hydraulic conductivity. Thus, decreasing pore pressures cause an increase in FS until no further change occurs, resulting in the constant values in FS for $K_r < 0.1$. The effects of K_r on FS are largest for the surfaces with the longest portion of its overall length in the blanket layer. Figure 4.10b shows the difference in FS when $K_{b,v}$ or $K_{a,h}$ are held constant in seepage analyses for a given value of K_r (Case I or II, respectively). While the difference reaches a maximum of 0.2–0.4 for various surfaces, they occur for K_r less than one, which is not the blanket layer seepage condition characteristic of the Pocket area. Although there is a difference when $K_r > 1.0$, the effect is generally small ($\Delta FS < 0.15$).

Figure 4.10b compares the effect of defining K_r as a function of $K_{a,h}$ and $K_{b,v}$ in seepage analyses for Cases I and II, as described previously. Constant values are set to the design value and compared using the difference in FS of stability for each case and for various sliding surfaces. The effect is computed as $FS(\text{Case I}) - FS(\text{Case II})$, indicating FS is insensitive to the absolute value of hydraulic conductivity when K_r is greater than about 100. Reliability computations generally converge to K_r well above 100; therefore Case 1 is used in all analyses for this document since the seepage results do not depend on the absolute values of hydraulic conductivity in this range. Although FS is more conservative for Case II, it is more appropriate to vary $K_{b,v}$, as it is the more difficult property to determine in practice due to increased variation for soils with low hydraulic conductivity (Section 3.2) in addition to less certain condition and performance of blanket layers in general (URS, 2014). Close inspection of Figure 4.10b reveals slightly negative values of ΔFS between K_r of about 100 to the design value of 1600. The maximum difference is $\Delta FS =$1e–3 for all surfaces and most are much less. Therefore, this is not expected to significantly affect results.

4.4 Reliability Analysis of Levee Stability

Reliability analyses for the levee model were performed using the FORM algorithm. Random variables in the analysis are blanket thickness (z_B) hydraulic conductivity ratio (K_r) unit weight (γ_B), cohesion (c_B), friction angle (ϕ_B) of the blanket layer; unit weight (γ_E), friction angle (ϕ_E) of the embankment and water surface elevation (WSE). Subsets of these eight non-vegetation properties are variously referred to as seepage, stability, blanket and/or hydraulic random variables for convenience, although for many cases their influence is not mutually exclusive (e.g., z_B could be considered a seepage or blanket variable; γ_E is a stability or embankment variable). Table 4.2 summarizes the stochastic parameters used for most reliability analyses discussed in this document, and deviations will be noted as needed. Distribution mean and standard deviation are presented

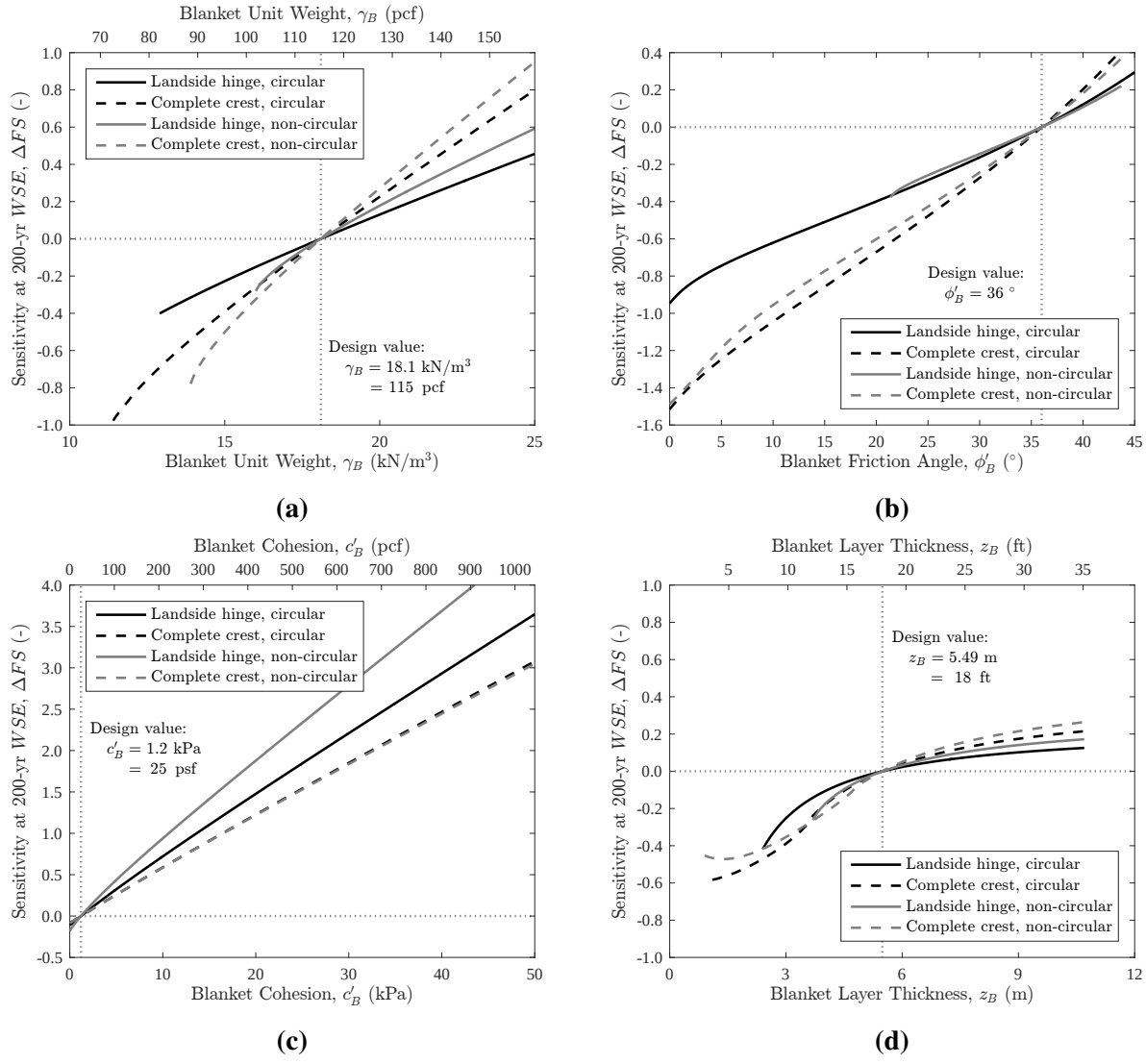

Figure 4.8: Sensitivity of FS for stability at 200-yr WSE to blanket properties, γ_E, ϕ_E, c_B and z_B

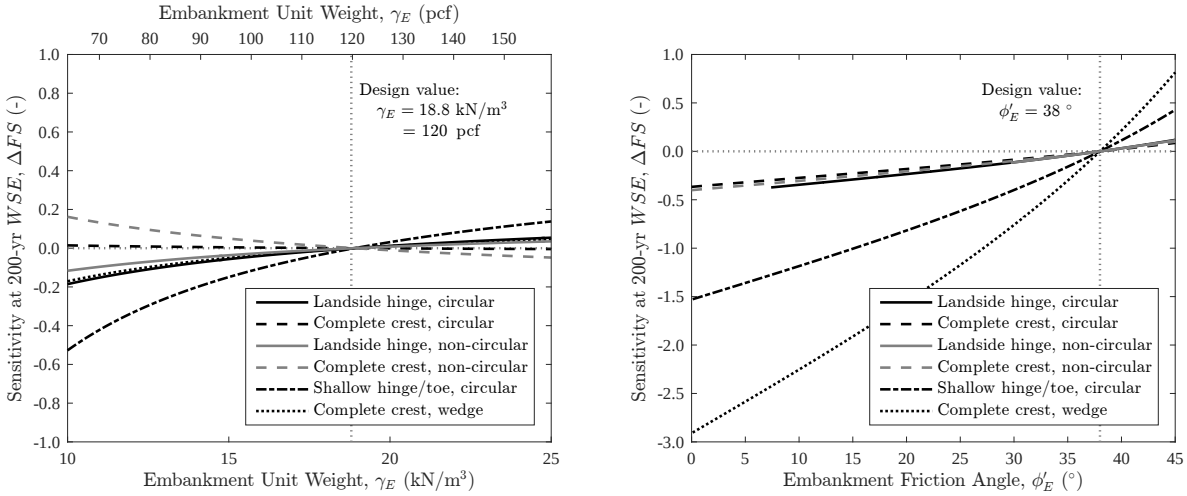

Figure 4.9: Sensitivity of FS at 200-yr WSE to embankment properties, γ_E and ϕ_E

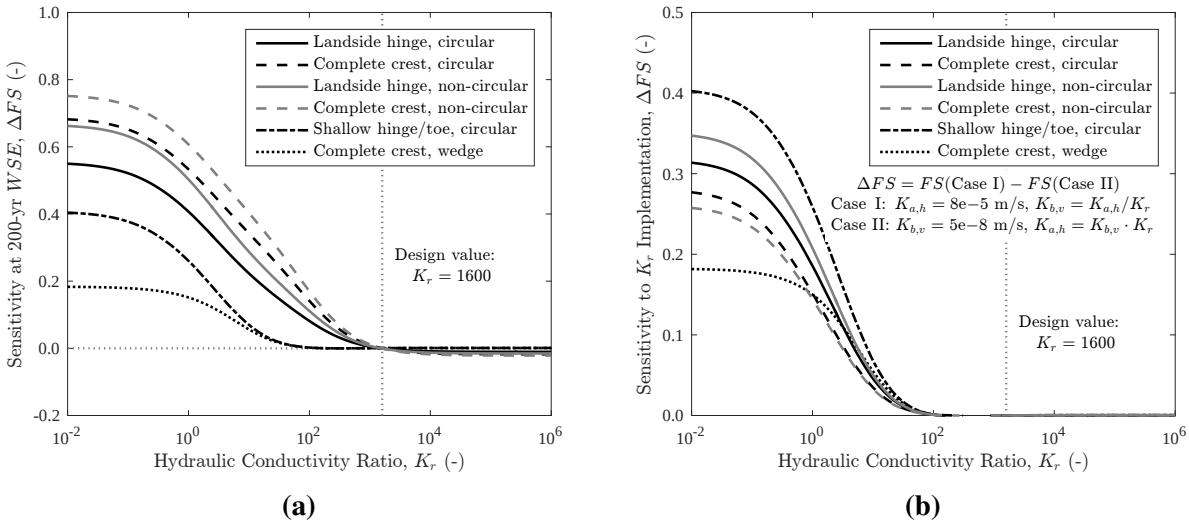

Figure 4.10: Sensitivity of FS at 200-yr WSE to (a) hydraulic conductivity and (b) implementation of $K_{b,v}$ and $K_{a,h}$ given K_r, Case I and II. Sensitivity for (b) is computed as the difference in FS when $K_{b,v}$ or $K_{a,h}$ is held constant given K_r (Case I and II, respectively).

Table 4.2: Random variable distributions for reference FORM analysis of landside hinge circle without vegetation. These parameters and distributions are used in all reliability analyses unless noted otherwise. Statistics μ and σ are for distributions, not data, which are equivalent for the normal distribution only.

RV	Type	Distribution	Unit	μ	σ	δ[a]
γ_B	Stability	$\mathrm{N}(\mu,\sigma)$	pcf (kN/m^3)	115 (18.1)	8.05 (1.81)	0.07
c_B	Stability	$\mathrm{N}(\mu,\sigma)$	psf (kPa)	25.0 (1.20)	7.50 (0.359)	0.30
ϕ_B	Stability	$\mathrm{N}(\mu,\sigma)$	$^\circ$	36.0	1.80	0.05
z_B[b]	Seepage	$\mathrm{tN}(\mu,\sigma,x_l,x_u)$	ft (m)	18.2 (5.54)	5.61 (1.71)	0.31
γ_E	Stability	$\mathrm{N}(\mu,\sigma)$	pcf (kN/m^3)	120 (18.9)	8.40 (1.32)	0.07
ϕ_E	Stability	$\mathrm{N}(\mu,\sigma)$	$^\circ$	38.0	1.90	0.05
K_r[c]	Seepage	$\mathrm{LN}(\lambda,\zeta)$	–	8000	39200	4.90
WSE[d]	Hydraulic	$\mathrm{Gmb}(u,\alpha)$	ft (m)	5.80 (1.77)	1.96 (0.597)	0.34

[a] μ (arithmetic mean), σ and δ are distribution, not data; $\delta = \sigma/\mu$ is coefficient of variation
[b] $\mathrm{tN}(5.49, 1.87, 1.70, 10)$ for landside hinge circle, $\delta = 0.34$ for data
[c] median, $x_{50} = 1600$; $\mathrm{LN}(7.38, 1.79)$ from Case C, Table 3.4
[d] WSE not included as RV for fragility curves; $\mathrm{Gmb}(1.50, 2.15)$ from 200/500-yr fit, Table 3.3

for each random variable distribution, along with non-normal distribution parameters, which were discussed previously. Note that μ and σ are equivalent for the data and distribution only for the normal case. In general, the distribution parameters were selected to match site-specific δ, where available.

FORM results for the circular landside hinge failure surface (minimum FS) are summarized in Table 4.3, and are generally used as a reference case throughout this document. Reliability index $\beta = 2.99$ implies a probability of $P[FS(\mathbf{x}) \leq 1] = 0.14\%$. Since the probability distribution of WSE is chosen as an annual extreme value distribution, p represents annual probability of the landside hinge surface failing under steady-state seepage conditions. Note that this does not necessarily imply levee failure (i.e., flooding will occur). Because the landside hinge has the lowest $FS(\mathbf{x})$, it will likely have a relatively high p compared to other sliding geometry, but it is not guaranteed to be the most likely surface to slide. In other words, other potential sliding surfaces (circular or non-circular) may have a higher p or lower β. Further insight to the reference reliability case is gained from the design point and importance vectors.

Importance Vector, α

Each element of the importance vector, α, ranks the relative impact each random variable has on the variance of $FS(\mathbf{x})$, and the sign notes the effect as either a capacity ($\alpha_i < 0$) or demand ($\alpha_i > 0$). For both analyses WSE is the most important variable, followed by blanket thickness and blanket unit weight. It is interesting that despite the large variability of hydraulic conductivity ratio, blanket properties still control the analysis (except for the obvious dominance of WSE). This information can be used to guide further investigation of levee performance. For example, if a limited budget is available for further field investigation, it would be most effective to spend the money evaluating blanket unit weight or thickness rather than performing hydraulic conductivity tests. The only two demand variables are hydraulic conductivity ratio and water surface elevation, a logical result considering that they are inversely proportional to $FS(\mathbf{x})$. Note that $\alpha_i > 0$ defines a demand variable because $\alpha_i \propto \beta^{-1}$ and $\beta \propto FS(\mathbf{x})$ or p. All strength and unit weight variables are capacities, although their importance is relatively small, given that they do not produce a large change in $FS(\mathbf{x})$ within the context of each probability distribution. Thus, importance is a reflection of the sensitivity of the limit-state function with respect to $\mathbf{x}$ *in combination* with the associated probability density of each random variable.

Design Point, $\mathbf{x}^*$

The design point represents parameter values most likely to exist for condition $FS(\mathbf{x}) = 1.0$, a condition that is often misleadingly be labeled "failure." For the reference analysis, values of the design point indicate the levee is most likely to fail when WSE covers nearly three-quarters of the embankment ($WSE/H = 0.71$), which is coincidentally very close to the 200-yr level. Blanket thickness is 2.66 m (8.74 ft), just under half the mean value found from field explorations at the Pocket site, and identical to expected results from a deterministic evaluation where the critical geographic location of a levee system would be where a thin blanket is encountered. In the standard normal space, $\mathbf{u}^*$ indicates distance of the design point from the median (and mean for normal distributions), of which WSE has the largest magnitude at $+2.5$, illustrating its dominance as a demand variable. All other values of $\mathbf{u}^*$ are within one standard deviation, except z_B, with $u_i^* = -1.7$. Large values of u_i^* indicate extreme values of specific parameters will exist when unstable conditions occur.

Sensitivity Vector, δ and η

Vectors δ and η consist of the sensitivity of β to the distribution mean and standard deviation, respectively, for each random variable. Sensitivity is scaled by standard deviation to make each element unit-less and possible to be compared equally. In general, elements of both sensitivity vectors are proportional to β and inversely proportional to p. For sensitivity to distribution mean, capacity variables will typically have positive values and demand variables will be negative. For sensitivity to distribution standard deviation the opposite is generally true, since increasing uncertainty will lead to lower β.

Examination of the values in Table 4.3 reveals that sensitivity measures generally follow the relationships found for α in that WSE and z_B have a bigger influence (i.e., δ_i and η_i have greater magnitude). However, we are also able to see that relative magnitudes have become more disparate: δ and η range from 1 to 10^{-3}, whereas α is 10^{-1} to 10^{-2}. Because the distributions for c, ϕ and

γ have relatively low coefficients of variation, the FORM solution is not very sensitive to the distribution μ and σ. The relative magnitude of each value illustrates the contribution of aleatory uncertainty for each random variable to reliability, since δ and η are directly proportional to σ_β.

Standard deviation of the blanket layer seems to have an extremely large effect, as it is several orders of magnitude greater than most of the other random variables. Although not tabulated here, the values of δ and η for z_B vary significantly in relative magnitude and sign for various water surface elevations (when WSE is not a random variable); in all cases α remains the most important variable. This behavior is caused by the non-linear relationship between the distribution statistics (μ and σ) and the distribution parameters (μ_t, σ_t, x_l and x_u). In this situation it is more appropriate to use distribution parameter sensitivity for evaluating reliability results, which can be found in Table 4.4, along with sensitivity to distribution mean and standard deviation (i.e., δ and *eta* without being scaled by σ). Distribution parameter sensitivity is equivalent to sensitivity to μ and σ for random variables with the normal distribution, and generally similar for non-normal cases (z_B, K_r and WSE), with $\partial\beta/\partial\sigma$ for z_B being the exception. Parameter sensitivity is much more consistent with other reliability results such as α and $\mathbf{u}^*$. Furthermore, β is sensitive to the lower truncation limit, x_l, but not to x_u. In fact, x_l has a larger impact on the result than nearly every other random distribution parameter, except for WSE and γ_B.

4.5 Effect of Probability Distribution

Selection of distribution type and specific distribution parameters will have varying effects on the results of a FORM analysis. Sensitivity and importance vectors such as δ and η can provide useful insight but not the entire picture. When changing distribution type or specific parmaeters, relative changes in β, p, α and $\mathbf{x}^*$ can be evaluated to understand the overall influence for each random variable. Distribution effects are described below for WSE, K_r and z_B with respect to the reference FORM results presented above. Due to the relatively small influence and well-known distributions of γ, c and ϕ it is assumed that distribution effects are of a lower magnitude and they are not addressed in this document.

Water Surface Elevation, WSE

FORM results for WSE are compared for the lognormal and Gumbel distributions with two combinations of fitting flood frequency data from USACE (2014b), as defined previously (Table 4.5). These analyses did not include K_r and z_B as random variables to preclude associated numerical effects, thus the absolute values are different than the reference analysis. Clearly there is a quantifiable but small effect due to distribution parameters causing a larger change than the distribution choice. The design point ranges between 72–85% of the levee height, which is very close to the 200–500-yr WSE range (76–85% of H). Overall, the choice of WSE distribution and parameters does not significantly change FORM results.

Hydraulic Conductivity Ratio, K_r

As illustrated in Figure 4.10, K_r has a very non-linear relationship to $FS(\mathbf{x})$ over a large range of magnitudes. Lognormal distributions are compared for three median values of K_r: 10, 100 and

Table 4.3: Reliability results for reference FORM analysis of landside hinge circle without vegetation. Importance vector, α indicates WSE is the most important variable, followed by the blanket properties z_B and γ_B; WSE and K_r are the only demand variables. The design point indicates the critical WSE is very close to the 200-yr level, with a blanket thickness nearly half of the average value. Distribution statistics for z_B have the biggest influence on reliability index, per importance measures δ and η.

RV	Unit	$\mathbf{x}^*$	$\mathbf{u}^*$	α	δ	η
γ_B	kN/m^3	1.74e+1	–5.24e–1	–1.75e–1	1.75e–1	–9.19e–2
c_B	kPa	1.13e+0	–1.94e–1	–6.51e–2	6.51e–2	–1.26e–2
ϕ_B	°	3.57e+1	–1.45e–1	–4.87e–2	4.87e–2	–7.08e–3
γ_E	kN/m^3	1.86e+1	–1.95e–1	–6.53e–2	6.53e–2	–1.27e–2
ϕ_E	°	3.77e+1	–1.40e–1	–4.70e–2	4.70e–2	–6.59e–3
z_B	m	2.66e+0	–1.69e+0	–5.67e–1	–1.26e+0	7.57e+0
K_r	m/s	2.31e+3	2.05e–1	6.85e–2	–3.46e–1	3.25e–2
WSE	m	3.69e+0	2.37e+0	7.94e–1	–3.75e–1	–1.21e+0

[a] $\beta = 2.985$ and $p = 1.419e-03$

[b] Order of Importance, α: WSE, z_B, γ_B, K_r, γ_E, c_B, ϕ_B, ϕ_E

[c] All vectors are unitless except design point, $\mathbf{x}^*$; alternate units: γ_B =111 pcf, c_B =23.5 psf, γ_E =118 pcf, z_B =8.74 ft, WSE =12.11 ft ($WSE/H = 0.71$)

Table 4.4: Parameter sensitivity for reference FORM analysis of landside hinge circle without vegetation.

RV	$\frac{\partial\beta}{\partial\mu}$	$\frac{\partial\beta}{\partial\sigma}$	$\frac{\partial\beta}{\partial p_1}$	$\frac{\partial\beta}{\partial p_2}$
γ_B	1.39e–1	–7.26e–2	1.39e–1	–7.26e–2
c_B	1.81e–1	–3.52e–2	1.81e–1	–3.52e–2
ϕ_B	2.71e–2	–3.93e–3	2.71e–2	–3.93e–3
γ_E	4.95e–2	–9.64e–3	4.95e–2	–9.64e–3
ϕ_E	2.47e–2	–3.47e–3	2.47e–2	–3.47e–3
z_B	–7.40e–1	4.43e+0	2.55e–1	–3.15e–1
K_r	–8.84e–6	8.29e–7	–3.82e–2	–7.82e–3
WSE	–6.28e–1	–2.03e+0	–6.28e–1	6.41e–1

[a] Order of Importance, α: WSE, z_B, γ_B, K_r, γ_E, c_B, ϕ_B, ϕ_E
[b] for z_B ~tN: $\partial\beta/\partial x_l = 0.159$ and $\partial\beta/\partial x_u = 0.003$

Table 4.5: Effect of distribution for WSE using lognormal and Gumbel with parameters, keeping all other distributions set to reference analysis values. Random variables K_r and z_B left out of analysis to avoid numeric effects. Parameters chosen as best fit match of return period data from USACE (2014b) or match of 200 and 500-yr water levels, and are identical to values in Table 3.3 and Figures 3.2–3.3. Only term for WSE in α is presented; all other values are comparable, but not identical, to the reference analysis.

Distribution	Fit	β	p	α	$\mathbf{x}^*$ (m)	$\mathbf{x}^*$ (ft)
Lognormal	best fit	3.741	9.16e–5	+0.745	3.71	12.2
Gumbel	best fit	3.370	3.76e–4	+0.855	4.08	13.4
Lognormal	200/500-yr	3.160	7.88e–4	+0.921	4.44	14.6
Gumbel	200/500-yr	3.161	7.86e–4	+0.917	4.42	14.5

Table 4.6: Effect of distribution for K_r using lognormal with various median, x_{50} and δ, keeping all other distributions set to reference analysis values. Parameters match values in Table 3.5. Only term for K_r in α is presented; all other values are comparable, but not identical, to the reference analysis. $\text{Imp}(K_r) > \text{Imp}(z_B) > \text{Imp}(\gamma_B)$ for Case B–10 and $\text{Imp}(K_r) > \text{Imp}(\gamma_B)$ for Case B–100, otherwise relative importance is the same as reference analysis.

Case	Median of K_r	δ for $K_{a,v}$ & $K_{b,h}$	β	p	α	$\mathbf{x}^*$ (–)
A–10	10	0.3	3.988	3.34e–5	+0.117	12.1
B–10	10	2.0	3.626	1.44e–4	+0.391	128
A–100	100	0.3	3.377	3.66e–4	+0.099	114
B–100	100	2.0	3.216	6.49e–4	+0.252	424
A–1000	1000	0.3	3.023	1.25e–3	+0.031	1040
B–1000	1000	2.0	3.007	1.32e–3	+0.093	1640

1000, corresponding to high, moderate and low sensitivity of $FS(\mathbf{x})$ to K_r, respectively. For Cases A and B a low and high variance condition is assumed for $K_{a,h}$ and $K_{b,v}$ with $\delta = 0.3$ (A) and $\delta = 2.0$ (B); results are summarized in Table 4.6. As variance increases, the design point, probability and importance all increase, as expected. Interestingly, distribution parameters seems to have the greatest effect on the importance measure, especially for lower values of the median. This effect is understandable given $FS(\mathbf{x})$ is most sensitive to K_r for relatively low values. When compared to other random variables $\text{Imp}(K_r) > \text{Imp}(z_B) > \text{Imp}(\gamma_B)$ for Case B–10 and $\text{Imp}(K_r) > \text{Imp}(\gamma_B)$ for Case B–100, otherwise relative importance is the same as reference analysis. Although K_r has more importance for lower values, it contributes to lower overall reliability of the embankment when the median value is higher. Thus, the overall effect of K_r is controlled by the non-linear interaction of distribution parameters and mechanical limit-state sensitivity.

Blanket Layer Thickness, z_B

Of all random variables considered, distribution effects for z_B have the most dramatic effect on FORM results, but only when truncation parameters are too restrictive. Table 4.7 compares the reference analysis to seven combinations of truncated normal distribution parameters: three different variance levels with $\delta = 0.25$, 0.35 and 0.05 (case A, B or C) and three sets of truncation limits, 3.0–10 m, 1.7–∞ m and 1.7–10 m (case 1, 2 or 3). Note that parameters μ and σ are slightly different in Cases 2 and 3, due to δ differences in how data were matched; however, the effect is negligible.

Although there are larger differences between FORM results for z_B than WSE or K_r, β and p are consistent. In contrast, α and $\mathbf{x}^*$ vary widely, with importance dropping an order of magnitude for the same distribution cases where the design point becomes very large. Specifically, this occurs

Table 4.7: Effect of distribution for z_B using truncated normal with parameters $\text{tN}(\mu_t, \sigma_t, x_l, x_u)$, keeping all other distributions set to reference analysis values. Case 0 is the reference reliability analysis; letters refer to coefficient of variation for the data, 0.25, 0.35 and 0.05 for A, B and C, respectively; and the number indicates varying truncation limits. Parameters for A–1, B–1 and C–1 match values in Table 3.6 and Figure 3.5. Only term for z_B in α is presented; all other values are comparable, but not identical, to the reference analysis.

No.	$\text{tN}(\mu, \sigma, x_l, x_u)$	β	p	α	$\mathbf{x}^*$ (m)	$\mathbf{x}^*$ (ft)
0	(5.486,1.865,1.700,10.00)	2.985	1.42e–3	–0.567	2.66	8.74
A–1	$(5.406, 1.172, 3.000, 10.00)$	3.173	7.46e–4	–0.229	4.61	15.1
B–1	$(5.207, 1.386, 3.000, 10.00)$	3.125	8.88e–4	–0.279	4.21	13.8
C–1	$(5.488, 0.524, 3.000, 10.00)$	3.236	6.06e–4	–0.089	5.38	17.5
A–2	$(5.486, 1.372, 1.700, \infty)$	3.144	8.33e–4	–0.311	4.16	13.6
B–2	$(5.486, 1.920, 1.700, \infty)$	2.971	1.49e–3	–0.559	2.68	8.79
A–3	$(5.486, 1.372, 1.700, 10.00)$	3.143	8.37e–4	–0.313	4.16	13.6
B–3	$(5.486, 1.920, 1.700, 10.00)$	2.968	1.50e–3	–0.558	2.67	8.76

for Cases A–1, B–1 and C–1, where $x_l = 3.0$ m; less than $\mathbf{x}^*$ for the reference analysis. A similar, but less dramatic effect occurs for Cases A–2 and A–3, when $\delta = 0.25$, but not for Cases B–2 and B–3, when $\delta = 0.35$. These observations imply that restriction of the lower tail of the distribution, whether by a truncation parameter or limiting variance, prevents the limit-state from being reached. In other words, z_B cannot become low enough to cause $FS(\mathbf{x}) \leq 1.0$. This behavior is evidenced by the change in relative importance for each distribution combination: for Cases A–1, B–1 and C–1, $\text{Imp}(z_B)$ becomes less than all other random variables (except ϕ_E and K_r for B–1). Furthermore, while $\text{Imp}(z_B)$ is still second-highest (behind WSE) for Cases A–2 and A–3, the design point remains high due to the way a probability density is redistributed when a truncation limit is applied. By forcing the entire CDF between 1.7 and 10 m, values of z_B close to 1.7 m have a lower probability of occurrence, and the most likely condition at the limit-state (i.e., the design point) has a higher value.

Comparison of Cases A and B for infinite upper limit, x_u, indicates a negligible effect on importance and design point. Thus, while the truncated normal distribution can have significant impact on FORM results, careful selection of x_l with respect to the anticipated design point can produce realistic results; a FORM solution should be checked to ensure x_l or x_u are not too close to $\mathbf{x}^*$. Unfortunately for evaluation of slope stability with a sliding surface that extends relatively deep into the blanket layer selecting x_l without significantly affecting $\mathbf{x}^*$ may not be possible.

4.6 Fragility

Reliability is computed using FORM at various WSE to generate fragility curves. For WSE less than approximately half the levee height the deterministic $FS(\mathbf{x})$ is relatively high and extreme values of $\mathbf{x}$ are required by FORM to reach the design point. Due to the underlying mechanics of the limit-equilibrium formulation for slope stability it is generally not possible to compute $FS(\mathbf{x})$, and thus reliability, for such extreme parameter values to reach $FS(\mathbf{x}) = 1.0$.

Figure 4.11 illustrates fragility of the landside hinge sliding surface for the reference reliability analysis discussed above; values are also presented in Table 4.8. At the levee crest, $p \approx 50\%$, but decreases below 0.1% as WSE reaches half of the embankment height. Aleatory uncertainty in levee stability is represented by the value of p (or β) and is due to inherent randomness of the seven random variables included in the analysis. Epistemic uncertainty is caused by imperfect knowledge; in this case the exact probability distribution parameters for each random variable, which could theoretically be obtained given sufficient data. Uncertainty in the reliability estimate is represented by σ_β, and computed using sensitivity of β to distribution parameters $\mathbf{p}$ and an estimate of the variability for each parameter, $\sigma_\mathbf{p}$: $\sigma_\beta = f(\nabla_\mathbf{p}\beta, \sigma_\mathbf{p})$. For normal distributions $\sigma_\mu = \sigma$, for truncated normal $\sigma_{\mu_t} = \sigma_t$ and for lognormal $\sigma_\lambda = \zeta$, since these parameters are generally equivalent to the mean and standard deviation of the distribution. Alternate estimates of parameter uncertainty would be used for other distributions. In most cases $\sigma_\sigma \ll \sigma_\mu$ and can be ignored, since $\sigma_\beta \propto \sigma_\mathbf{p}^2$. For this example σ_β due to epistemic uncertainty in distribution variance is only 4%, on average, of epistemic uncertainty due to distribution mean. As fragility results show, σ_β is approximately 0.9 for all WSE, resulting in an increasingly wide range of p as WSE increases. For low WSE p varies across 3 orders of magnitude, which could have significant impact for risk analyses that are controlled by these higher frequency events.

Figure 4.12 presents the aleatory uncertainty of $FS(\mathbf{x})$, which is a result of inherent randomness of the seven random variables included in the analysis, estimated using μ_{FS} and σ_{FS}. Standard deviation is not constant for all WSE due to the changing importance of the random variables, α. Although not illustrated here, α_i generally varies in a concave-up or concave-down relationship with WSE; however, the variation is within an order of magnitude and relative magnitudes between random variables remains constant. The deterministic case is consistently below the mean of $FS(\mathbf{x})$, indicating an inherent level of conservatism when using "best-estimates" of parameters $\mathbf{x}$. However, the mean values for random variables for this research were purposely selected to represent the marginally stable case for $WSE/H = 1.0$, which is why the deterministic and stochastic curves intersect on the figure.

Figures 4.11 and 4.12 rank each random variable by aleatory and epistemic uncertainty, and as expected, z_B is still the most important variable for both cases. For the epistemic case c_B becomes the second ranked variable, indicating uncertainty in its mean value has a more significant impact on the estimate of reliability. In general, μ_β and σ_β are dominated by the uncertainty of z_B because it is the only variable which has a large enough mechanical sensitivity to cause $FS(\mathbf{x}) \leq 1$. When variance of z_B is higher the likelihood of an extreme values of z_B (relative to the PDF) and thus p increases, along with sensitivity measures α, δ and η.

Table 4.8: Fragility of landside hinge sliding surface, $p = \mathrm{P}[FS(\mathbf{x}) \leq 1.0]$, computed using FORM as μ_β for reference reliability analysis. Changing probability with WSE is aleatory uncertainty and epistemic uncertainty is represented by confidence interval, $\mu_\beta \pm \sigma_\beta$, where σ_β uncertainty in random variable distribution parameters. FORM also provides an estimate of the mean and standard deviation of safety factor, $FS(\mathbf{x})$.

Water Surface Elevation, WSE/H	0.53	0.76	1.00
Reliability, μ_β	3.112	1.537	–0.04
Fragility, $p = \Phi(-\mu_\beta)$	9.297e–4	6.211e–2	5.016e–1
Standard deviation, σ_β	0.817	0.890	0.967
Confidence interval, $\mu_\beta + \sigma_\beta$	3.929	2.427	0.963
Confidence interval, $\Phi(-\mu_\beta - \sigma_\beta)$	4.26e–5	7.60e–3	1.68e–1
Confidence interval, $\mu_\beta - \sigma_\beta$	2.294	0.647	–0.971
Confidence interval, $\Phi(-\mu_\beta + \sigma_\beta)$	1.09e–2	2.59e–1	8.34e–1
Mean safety factor, $\mu_{FS} = \beta\sigma_{FS}$	0.763	0.518	–0.01
Standard deviation, $\sigma_{FS} = \|\alpha\|$	0.245	0.337	0.172

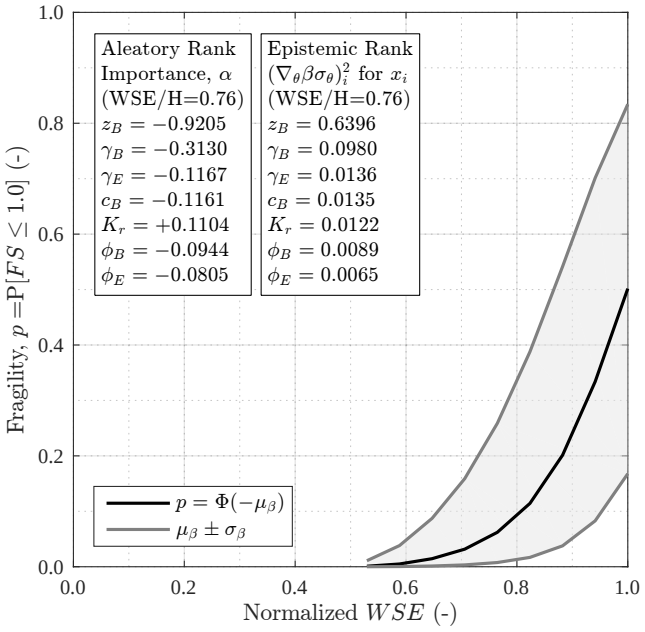

Figure 4.11: Fragility of landside hinge sliding surface, $p = \mathrm{P}[FS(\mathbf{x}) \leq 1.0]$, computed using FORM as μ_β for reference reliability analysis. Aleatory uncertainty is illustrated by changing probability with WSE, with relative contribution to variance by each random variable estimated by α. Epistemic uncertainty is estimated from distribution parameters and illustrated by the shaded region, $\mu_\beta \pm \sigma_\beta$, where relative contribution to variance by each random variable is $(\nabla_\theta \beta \sigma_\theta)_i^2$.

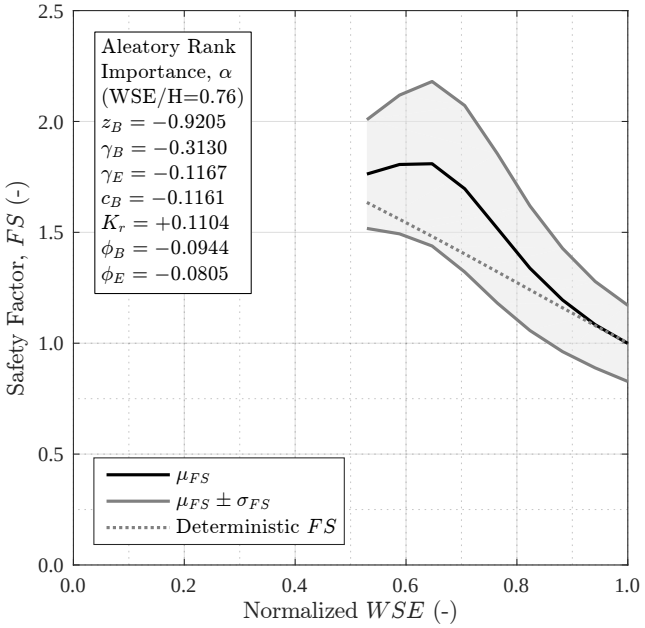

Figure 4.12: Mean and standard deviation of $FS(\mathbf{x})$ for landside hinge sliding surface, computed using FORM as $\sigma_{FS} = \|\nabla g(\mathbf{x}^*)\|$ and $\mu_{FS} = \beta\sigma_{FS} + 1$. Aleatory uncertainty is illustrated by the shaded region, $\mu_{FS} \pm \sigma_{FS}$, with relative contribution to variance by each random variable estimated by α. Results of the deterministic analysis are within one standard deviation below the mean.

4.7 Reliability Analysis of Levee Seepage

FORM analyses were performed the limit-state functions $g(\mathbf{x}) = FS_{us}(\mathbf{x}) - 1.0$ for underseepage and $g(\mathbf{x}) = FS_{ts}(\mathbf{x}) - 1.0$ for throughseepage. Many of the results for reliability of stability described above apply to seepage, for example probability distribution effects and interpretation of FORM results.

Underseepage

Up to four random variables influence the underseepage analysis used in this document: blanket layer unit weight (γ_B) and thickness (z_B), hydraulic conductivity ratio (K_r), and water surface elevation (WSE). Results from FORM show that z_B is the most important variable, followed by WSE and $\gamma(B)$ (Table 4.9). The estimated probability of the limit-state is 1.3%, and the design point indicates a most-likely water level of 2.5 m (8.1 ft), which are both below results from the stability case (i.e., $p = 0.01\%$ and $x_i^* = 3.7$ m for WSE). Epistemic uncertainty for underseepage has a larger contribution from the variance of each random variable, in contrast to stability, as illustrated by the wide uncertainty band in Figure 4.13, as well as larger values of $\partial\beta/\partial p_2$ in Table 4.10.

When WSE is included as a random variable, using effective and total stress methods produces different estimates of FS_{us} for the deterministic case. For stochastic analyses nearly identical results are obtained from FORM regardless of the method used. When WSE is removed from the analysis to produce fragility curves, however, a different behavior is observed. Figure 4.14 shows lower fragility than the effective stress method, much lower variance on $\mu_F S$ and $\text{Imp}(\gamma_B) > \text{Imp}(z_B)$. The total stress method reduces the importance of blanket thickness because it is incorporated as a contributor to driving and resisting forces (i.e., weight of the blanket and vertical drainage length). Thus, when WSE is constant z_B no longer has the same effect on uplift because it is inversely proportional to i, but proportional to the total blanket weight. Thus, for fragility of the total stress method blanket unit weight is the most important property.

Throughseepage

Throuseepage is evaluated using an infinite slope solution coupled with three random variables: embankment unit weight (γ_E), cohesion (c'_E) and friction angle (ϕ'_E). Slope angle (θ), sliding depth (z_s) and unit weight of water (γ_w) are constant. For erosion to occur it is implicitly assumed the phreatic surface exits the slope above the location of interest for a throughseepage analysis, making the solution independent of water level and pore pressures. Since $FS_{ts(\mathbf{x})}$ is evaluated with a closed-form solution (i.e., not dependent on a finite element mesh), computations are relatively fast and unencumbered by the numerical issues associated with underseepage. Fragility curves are not presented for throughseepage since the value of FS_{ts} is independent of WSE when the phreatic surface exits the slope.

In deterministic analyses the embankment is considered cohesionless ($c'_E = 0$), but it is well-known that small values of cohesion can have a large impact on stability. An exponential distribution is used to include c'_E as a random variable while also ensuring only an extremely low amount of cohesion is evaluated in the embankment. This single-parameter distribution, $c'_E \sim \text{Exp}(\lambda)$, concentrates probability density near $c'_E = 0$. For $\lambda = 1$, 5 or 10, there is an approximately 60, 8 or 1% chance that $c'_E > 0.5$ kPa (10 psf), illustrating the compact distribution shape. Results of a FORM

Table 4.9: Reliability results for reference FORM analysis of underseepage without vegetation. Importance vector, α indicates z_B is the most important variable, followed by WSE and γ_B. Computed using effective stress method for FS_{us}, which are nearly identical to total stress method when WSE is a random variable.

RV	Unit	$\mathbf{x}^*$	$\mathbf{u}^*$	α	δ	η
γ_B	kN/m^3	1.73e+1	–5.96e–1	–2.68e–1	2.68e–1	–1.60e–1
z_B	m	2.55e+0	–1.78e+0	–7.99e–1	–1.33e+0	9.74e+0
K_r	m/s	2.23e+3	1.85e–1	8.29e–2	–4.21e–1	3.98e–2
WSE	m	2.47e+0	1.19e+0	5.33e–1	–3.83e–1	–4.48e–1

[a] $\beta = 2.227$ and $p = 1.297e-02$
[b] Order of Importance, α: z_B, WSE, γ_B, K_r
[c] All vectors are unitless except design point, $\mathbf{x}^*$; alternate units: γ_B =110 pcf, z_B =8.37 ft, WSE =8.09 ft ($WSE/H = 0.48$)

Table 4.10: Parameter sensitivity for reference FORM analysis of underseepage without vegetation. Computed using effective stress method for FS_{us}, which are nearly identical to total stress method when WSE is a random variable.

RV	$\frac{\partial\beta}{\partial\mu}$	$\frac{\partial\beta}{\partial\sigma}$	$\frac{\partial\beta}{\partial p_1}$	$\frac{\partial\beta}{\partial p_2}$
γ_B	2.12e–1	–1.26e–1	2.12e–1	–1.26e–1
z_B	–7.80e–1	5.70e+0	3.54e–1	–4.55e–1
K_r	–1.07e–5	1.01e–6	–4.62e–2	–8.55e–3
WSE	–6.41e–1	–7.50e–1	–6.41e–1	2.88e–1

[a] Order of Importance, α: z_B, WSE, γ_B, K_r
[b] for z_B ~tN: $\partial\beta/\partial x_l = 0.263$ and $\partial\beta/\partial x_u = 0.004$

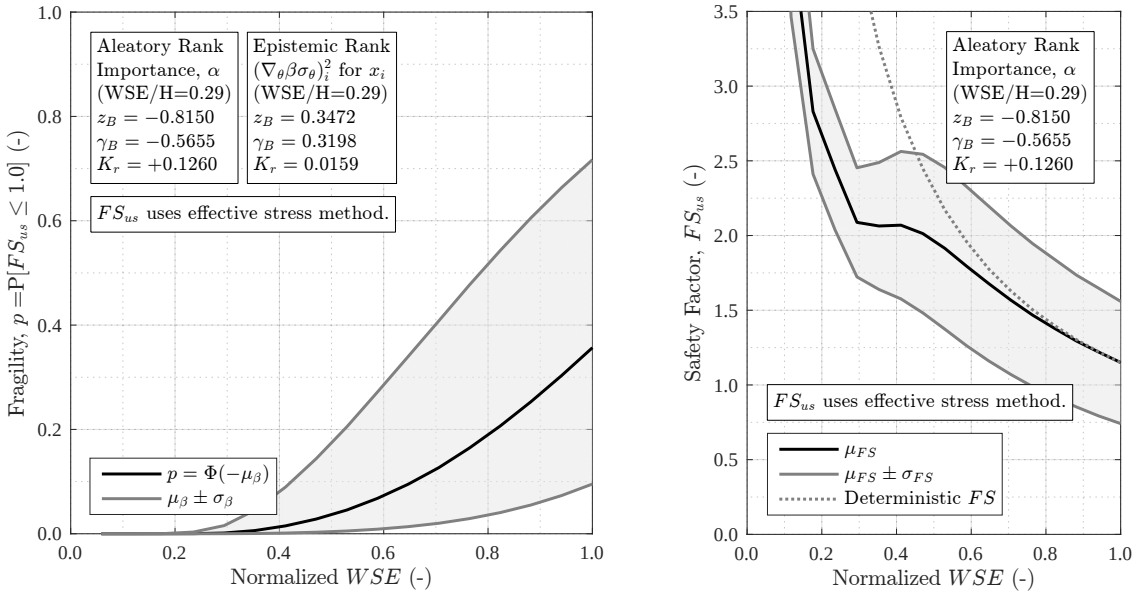

(a) **(b)**

Figure 4.13: Fragility and μ_{FS} for underseepage using effective stress method.

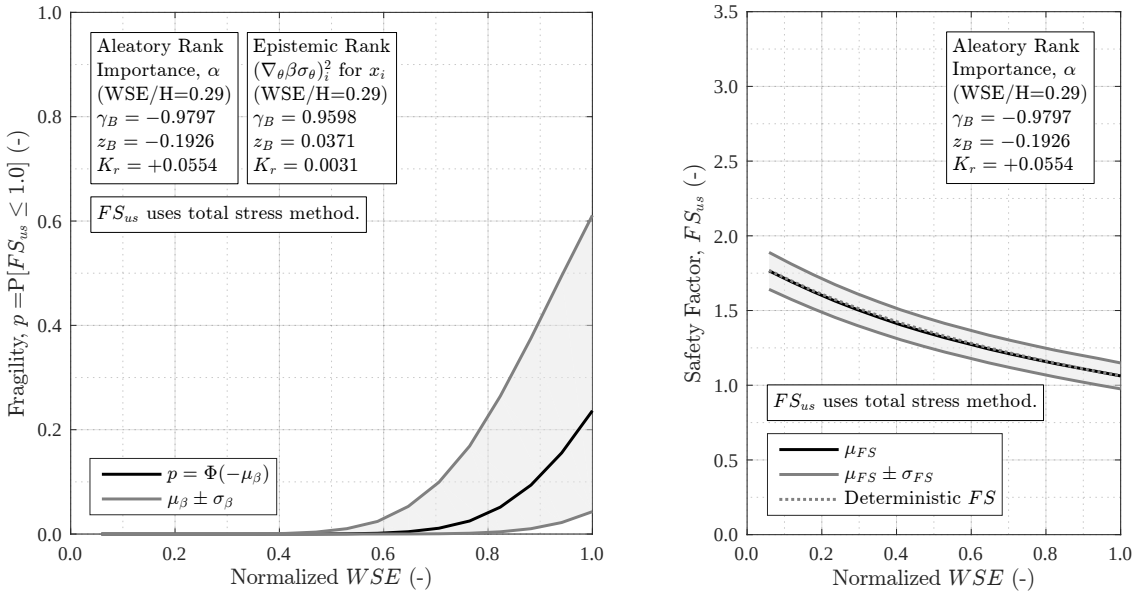

(a) **(b)**

Figure 4.14: Fragility and μ_{FS} for underseepage using total stress method.

Table 4.11: Reliability results for reference FORM analysis of throughseepage without vegetation. The exponential distribution with $\lambda = 10$ is applied to c'_E to account for non-zero, yet very small values. Importance vector, α indicates c'_E is the most important variable, followed by γ_E and ϕ'_E. Sliding depth is assumed to be $z_s = 0.3$ m (1.0 ft).

RV	Unit	$\mathbf{x}^*$	$\mathbf{u}^*$	α	δ	η
γ_E	kN/m^3	1.87e+1	–1.17e–1	–1.85e–1	1.85e–1	–2.18e–2
ϕ_E	°	3.78e+1	–9.69e–2	–1.53e–1	1.53e+0	–3.10e+1
c_E	kPa	3.15e–2	–6.13e–1	–9.71e–1	2.14e+0	–1.47e+0

[a] $\beta = 0.632$ and $p = 2.638e-01$
[b] Order of Importance, α: c_E, γ_E, ϕ_E
[c] All vectors are unitless except design point, $\mathbf{x}^*$; alternate units: γ_E =119 pcf, c_E =0.7 psf

analysis are presented in Table 4.11, with c'_E having greatest importance despite an extremely low design point value of 0.03 kPa (0.70 psf). Selection of alternate values for parameters λ and z_s change the computed β but not relationships between random variables for the design point and sensitivity vectors. For example, $P[FS_{ts} \leq 1.0]$ is 0.14, 3.1 and 26% for $\lambda = 1$, 5 or 10.

Epistemic uncertainty results in $\sigma_\beta = 0.24$, with the contribution from parameter μ for γ_E and ϕ_E (3e-2 and 2e-2) being much more significant than λ for c_E (5e-5). The mean value of FS_{ts} is $\mu_{FS} = 1.23$, with a standard deviation $\sigma_{FS} = 0.36$.

4.8 Summary

The analyses presented in this chapter provide deterministic and stochastic reference cases for levee seepage and stability that will be used to compare the effects of vegetation. Sensitivity of each parameter was evaluated to understand important characteristics of the mechanistic models and their role in reliability analyses. Key results regarding the model levee include:

- marginal performance in terms of FS approaching 1 for seepage and stability as WSE reaches the levee crest
- the minimum FS slope stability surface enters the slope at the landside hinge, travels through the blanket and exits beyone the toe with $FS = 1.322$ for the circular case and 1.285 for the non-circular case for the 200-yr WSE
- reliabiltiy analyses show that blanket layer properties control stability, particularly blanket layer thickness (z_B) and unit weight (γ_B)
- based on deterministic sensitivity analyses, cohesion of the blanket (c_B) and friction angle of the embankment (ϕ_E) produce the largest magnitude change in FS across the entire range of

possible values; however, results of reliability analyses show these parameters are the least important in terms of their contribution to the uncertainty in FS

- although hydraulic conductivity is commonly considered to be a critical variable due to its variability over orders of magnitude, reliability analyses show it is only moderately important to overall stability
- most random variables are insensitive to selection of distribution type with the exception of z_B, which must be revisited after FORM analyses are completed to ensure that convergence to the design point is not limited by truncation of the normal distribution
- fragility curves illustrate the relatively high probability of an unsafe condition for seepage and stability, with distribution parameters for blanket layer properties controlling epistemic uncertainty

Chapter 5

Tree Root Biomass Model

To properly quantify the effects of vegetation a robust model of root distribution in the subsurface was developed principally using data from studies in the Central Valley of California. A rich data set was developed from detailed terrestrial LiDAR scans of Central Valley trees and their root systems within levee slopes completed by Berry and Chung (2013) and Chung (2013). A total of 20 trees was measured at 3 different locations in the Central Valley: five cottonwood (*DBH* 0.22 to 0.36 m) and fifteen valley oak (*DBH* 0.08 to 0.32 m), where *DBH* is diameter at breast height, a common allometric parameter. This data set is enhanced with data from other studies, as appropriate, concentrating on data from the Central Valley of California. The specific focus was on *Populus fremontii* (Fremont cottonwood) and *Quercus lobata* (valley oak) due to the extensive data set collected by Berry and Chung (2013). These trees are hereafter referred to as simply cottonwood and oak.

The term "biomass" is used to describe root cross-sectional area (*RCSA*), root area ratio (*RAR*) or root volume (*RV*) as a function of x, y and z (dimensions illustrated in Figure 5.1 and 5.15), where:

- the $\hat{x}$ direction is perpendicular to the levee alignment in the horizontal plane; the local origin for a specific tree is $x = 0$ and represents the trunk center
- the $\hat{y}$ direction is parallel to the levee alignment in the horizontal plane; $y = 0$ is the origin and trunk center
- the $\hat{z}$ direction measures vertical depth; local origin, $z = 0$, is the ground surface, with positive values representing increasing depth
- subscripts u and d upslope and downslope directions ($+\hat{x}$ and $-\hat{x}$, respectively)
- subscript y is applied to lateral direction ($\hat{y}$ is symmetric); lateral root zone parameters are generally an average of the up and downslope directions
- the $\hat{l}$ direction is radial distance in the horizontal plane; $l = 0$ is the origin and trunk center
- θ is angle in the horizontal plane; $\theta = 0$ is aligned with the $+\hat{x}$, thus polar coordinates can be found per $x = l\cos\theta$ and $y = l\sin\theta$

When results are presented for a single tree the local coordinate system is defined with the trunk center and ground surface as the origin. For biomass on sloped ground all coordinates are computed in horizontal and vertical planes and mapped vertically to the sloped surface.

5.1 Root Area Ratio

The most commmon measure used to represent the root system is root area ratio, *RAR*, the cross-sectional area of roots per unit area of soil. In general, 10^{-4}, or 0.01%, is considered to be the measurable limit for *RAR*, especially with respect to studies of root systems for trees. This value corresponds to a single 1.1 cm diameter root per 1 m^2 area of soil, or a 0.14 in diameter root per 1 ft^2 area of soil. Single equivalent root diameters for $RAR = 10^{-5}$ and 10^{-6} are 0.36 and 0.11 cm (or 0.04 and 0.01 in). In this study $RAR = 10^{-4}$ is generally used by the biomass model to define lateral root limits, unless otherwise stated, as it matches observed data well.

Berry and Chung (2013) quantify biomass with an exponential regression model that relates root cross-sectional area, *RCSA* to radial distance from the tree trunk, l:

$$\ln(RCSA) = \alpha_0 - \nu l \tag{5.1}$$

RCSA is measured on a vertically oriented cylinder with radius l, called virtual trench profiles (VTP), illustrated schematically in Figure 5.1. By evaluating data in the appropriate quadrant, parameters were also developed in the upslope and downslope directions. Estimates of α_0 and ν were found using a mixed linear regression model in Berry and Chung (2013) and Chung (2013) for the processed 3D LiDAR data; reported regression parameters produced $RCSA \sim [\mathrm{cm}^2]$. *RAR* can be determined from *RCSA* as determined from the VTP concept.

Beginning with the regression model described above, α_0 can be represented by $A_0 = \exp \alpha_0$, which leads to a direct equation for root cross sectional area for a virtual trench profile:

$$RCSA = A_0 \exp(-\nu l) \tag{5.2}$$

where $A_0 = \exp(\alpha_0)$ is the interpolated intercept of *RCSA* in $[\mathrm{L}^2]$ at the trunk center. Note there is little physical meaning of this parameter at the exact trunk center point; it primarily contributes the biomass distribution shape away from the trunk, along with ν. *RCSA* will decrease rapidly with distance due to the exponential dependence on ν: 39 %/m for $\nu = 0.5$, 63 %/m for $\nu = 1.0$ and 98 %/m for $\nu = 4.0$.

The virtual trench concept of Equation 5.1 provides cross-sectional root area, $RCSA(l)$, that would be evaluated on the wall of a circular trench excavated distance l from the trunk center, where $l = \sqrt{x^2 + y^2}$, with infinitesimal area $A = \mathrm{d}y$. Each VTP cylinder has surface area $A_{cyl} = 2\pi l z_{max}$, where z_{max} is maximum root depth considered, as illustrated in Figure 5.1. Dividing $RCSA(l)$ by the cylindrical surface area represents root area ratio averaged vertically over the entire root zone at distance l from the trunk, denoted $\overline{RAR}_l(l)$:

$$\overline{RAR}_l(l) = \frac{RCSA(l)}{A_{cyl}} = \frac{A_0 \exp(-\nu l)}{2\pi l z_{max}} \tag{5.3}$$

This equation describes *RAR* in the horizontal plane, but must be expressed in terms of x and y for incorporation into levee analyses.

Biomass decreases more rapidly in the upslope than downslope direction, thus the parameter ν is spatially dependent. Berry and Chung (2013) provide parameters in the upslope and downslope directions, ν_u and ν_d (Table 5.2), and it may be assumed that the transverse direction ($+\hat{y}$) is an

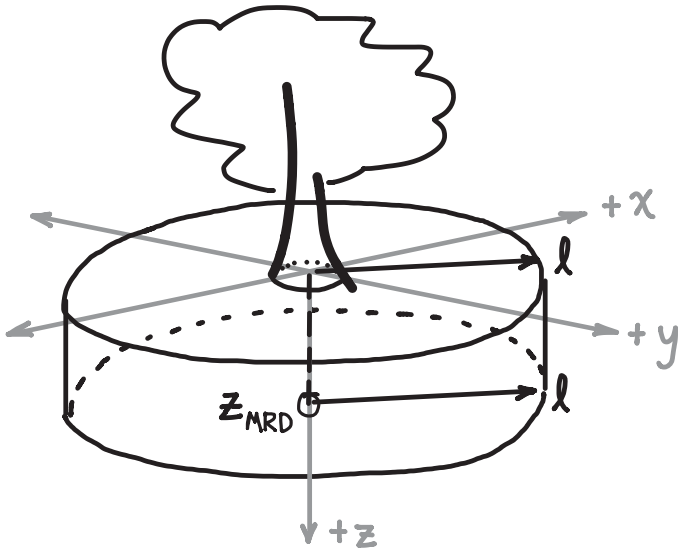

Figure 5.1: Virtual trench profile and biomass coordinate system. $\hat{y}$ is parallel to the levee alignment and $\hat{x}$ is perpendicular, with downslope positive with respect to the landside. Radial distance from the trunk center is l.

average of the two: $\nu_t = (\nu_u + \nu_d)/2$. An interpolating function can be defined to describe radial biomass decrease away from the primary axes using a smoothly varying function:

$$\nu(\theta) = \frac{\nu_d - \nu_u}{2}\cos\theta + \frac{\nu_d + \nu_u}{2} \tag{5.4}$$

where $\theta = 0$ is aligned with the down-slope direction (i.e., ν_d and $+\hat{x}$) and ν_t is average of ν_u and ν_d when $\theta = \pi/2$ and $3\pi/2$ ($+\hat{y}$ and $-\hat{y}$, respectively). In (x,y) coordinates, $\theta = \cos^{-1}(x/l)$ and $l = \sqrt{x^2+y^2}$, as measured from the tree center. Combining with Equations 5.3 and 5.4 gives

$$\overline{RAR}_{xy}(x,y) = A_0 \frac{\exp\left\{ -\left[\frac{\nu_d-\nu_u}{2}\cos\left(\cos^{-1}\left(\frac{x}{\sqrt{x^2+y^2}}\right)\right) + \frac{\nu_d+\nu_u}{2}\right]\sqrt{x^2+y^2}\right\}}{2\pi z_{max}\sqrt{x^2+y^2}} \tag{5.5}$$

which can be rearranged as the complete equation for $\overline{RAR}_{xy}(x,y)$:

$$\overline{RAR}_{xy}(x,y) = A_0 \frac{\exp\left\{ \sqrt{x^2+y^2}\frac{\nu_d+\nu_u}{2} - x\frac{\nu_d-\nu_u}{2}\right\}}{2\pi z_{max}\sqrt{x^2+y^2}} \tag{5.6}$$

Equation 5.6 defines the depth-averaged root area ratio at any position (x,y) as measured from the tree center. Figure 5.2 shows $\overline{RAR}_l$ for two values of A_0 and three values of ν, averaged over a maximum root depth of 1 m. Because ν_d and ν_d are equal in this example and $y = 0$, RAR computed in Figure 5.2 represents a tree on level ground, and l is radial distance from the tree trunk center. The $\nu_u = \nu_d$ case is also equivalent to $\overline{RAR}_{xy}(x = l, y = 0)$ and $\overline{RAR}_{xy}(x = 0, y = l)$. Values for ν of 0.5, 1.0 and 5.0 approximately correspond to trees of diameter 1.0, 0.5 and 0.1 m (respectively; any

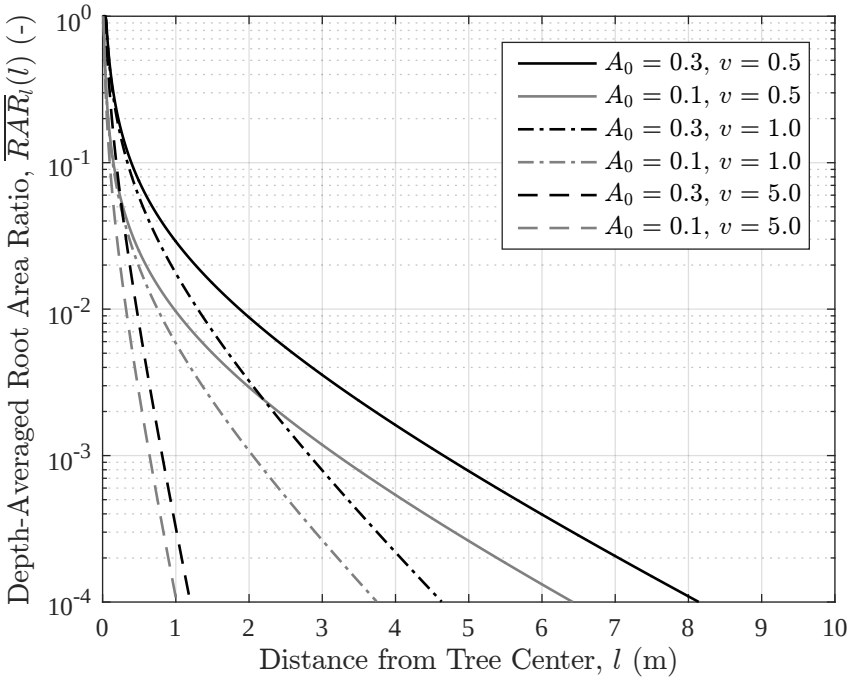

Figure 5.2: Depth-averaged root area ratio, $\overline{RAR}_l(l)$, from biomass model with varying A_0 and v. Distance l is the virtual trench cylinder radius, measured from trunk center. Computed for level ground case $v_u = v_d$, which is equivalent to $\overline{RAR}_{xy}(x = l, y = 0)$ and $\overline{RAR}_{xy}(x = 0, y = l)$. Scaling by $f_{RAR}(z)$ provides 3D point-estimate of *RAR* (along the x and y axis only for this plot).

species), whereas A_0 of 0.1 and 0.3 are equivalent to the regression results for oak and cottonwood. Biomass decreases exponentially and it is clear that v has a much larger impact on the magnitude of *RAR* than A_0.

Due to the VTP model applied by Berry and Chung (2013), $RAR(x,y)$ exponentially decreases with distance and reaches an infinite value directly beneath the tree center. This is potentially problematic, as the maximum physical value of *RAR* is 1, where a given cross-sectional area in the subsurface is entirely root material. Setting $RAR_l(l) = 1$ in Equation 5.3 and solving for the radial distance l_1 requires use of the Lambert W function:

$$2\pi l_1 z_{max} = A_0 \exp(-v l_1)$$

$$v l_1 \exp(v l_1) = \frac{v A_0}{2\pi z}$$

$$z_{max} = \mathscr{W}(z_{max} \exp z_{max}) \quad \rightarrow \quad v l_1 = \mathscr{W}(v l_1 \exp(v l_1)) = \mathscr{W}\left(\frac{v A_0}{2\pi z_{max}}\right)$$

$$l_1 = \frac{1}{v}\mathscr{W}\left(\frac{v A_0}{2\pi z_{max}}\right) \tag{5.7}$$

For the possible range of values for A_0, v and z, l_1 is always less than 0.1 m, which generally

lies within the trunk diameter of the tree. This result intimates the interesting physical meaning of *RAR* at the trunk, which is entirely woody material. However, incorporating the physical transition from above to below ground biomass at the trunk origin would add unreasonable complexity to the biomass model given the relatively small area it represents. Therefore, *RAR* is incorporated as presented in Equation 5.6 such that $\overline{RAR}_{xy} \leq 1.0$. In addition, Equation 5.7 can be generalized to identify the distance at which *RAR* takes on any value:

$$l(RAR) = \frac{1}{\nu} \mathscr{W}\left(\frac{\nu A_0}{2\pi z_{max} RAR}\right) \tag{5.8}$$

which is useful for definition and evaluation of several components of the biomass model.

Biomass Regression Intercept, A_0

Parameter α_0 represents the horizontal intercept of *RCSA* (tree trunk center) and was reported by Chung (2013) to be 0.29 for cottonwood and 7.93 for oak trees with standard errors of 0.50 and 0.34, respectively (Table 5.1); values of α_0 computed by Berry and Chung (2013) were not reported. Note that α_0 are converted to A_0 for the biomass model herein. Given the relatively small influence on $\overline{RAR}$ with respect to ν (Figure 5.2) and lack of reported values, A_0 is assumed to be constant and generally set to 0.30 for cottonwood and 0.10 for oak.

Rate of Biomass Decrease, ν

Parameter ν represents the exponential biomass reduction with distance and was reported by Chung (2013) as 0.47 and 2.12 for cottonwood and oak, corresponding to an exponential reduction of 38% and 88% per meter, respectively, summarized in Table 5.1 and illustrated as dashed lines in Figure 5.3). Upslope and downslope values of reduction rate (ν_u and ν_d) are also presented in Berry and Chung (2013), summarized in Table 5.2 and illustrated as points in Figure 5.3. Biomass consistently has a smaller spread in the upslope direction when looking at values averaged by species: 4.64 and 3.30 for cottonwood, 5.65 and 1.40 for oak. However, there are two problems with the reported results. First, it is unclear why the computed regression parameters for ν (by species) by Chung (2013) are outside the upslope and downslope values as presented in Berry and Chung (2013) (Figure 5.3). For each species ν_u and ν_d range from 0.78 to 8.08 for cottonwood and 1.24 to 10.28 for oak, well above the values of 0.47 and 2.12 from Chung (2013) (Table 5.1). In other words, the lines should be average values of the points, but they clearly represent minimum values. Standard deviations from Berry and Chung (2013, Table 5.1) are also much higher than standard error from Chung (2013, ; 5.2). Furthermore, there seems to be a decrease in ν_u and ν_d with increasing *DBH* (Figure 5.3). The trend becomes much more obvious when the lower-left and upper-right data points in Figure 5.3 are excluded. The second issue with Berry and Chung (2013) concerns the implication that rate of biomass decrease is greater for oak than for cottonwood. While comparing ν_u and ν_d for each species supports this conclusion, it may overlook correlation of ν with *DBH*. Figure 5.3 shows that the sample of trees includes larger *DBH* oaks than cottonwoods. If there is indeed a correlation between ν and *DBH*, the conclusion that ν is greater for oak than cottonwood is may be incorrect. Unfortunately there is not enough data available to resolve this issue. As such, we choose to assume an exponentially decreasing correlation between ν and

Table 5.1: Regression parameter summary from log-linear regression of root cross-sectional area (*RCSA*) with radial distance from trunk (l) after Chung (2013). Standard error, σ, is from mixed model linear regression and $\delta = \mu/\sigma$.

	A_0 (m^2)[b]	α_0	σ_{α_0}	δ_α	ν	σ_ν	δ_ν
Cottonwood	0.2890	7.969	0.5006	0.0628	0.4705	0.1421	0.3020
Oak	0.0793	6.676	0.3416	0.0512	2.121	0.2102	0.0991

[b] $A_0 = 10^{-4} \exp \alpha_0 = [m^2]$ computed here from α_0 of Berry and Chung (2013) and Chung (2013)

Table 5.2: Regression parameter ν from log-linear regression of root area, after Berry and Chung (2013). Standard deviation, σ, computed independently from values from Berry and Chung (2013).

Species	n	DBH (m)		ν		ν_u		ν_d	
		μ	σ	μ	σ	μ	σ	μ	σ
Cottonwood	3	0.16	0.06	3.97	1.85	4.64	2.24	3.30	1.05
Oak	13	0.27	0.08	3.53	3.47	5.65	4.06	1.40	0.24

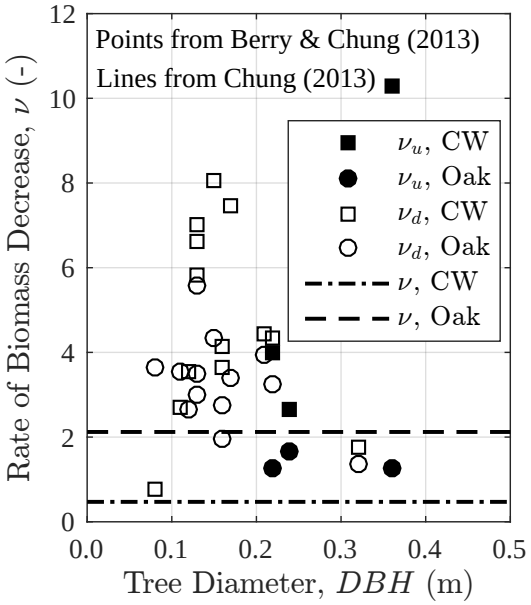

Figure 5.3: Comparison of parameter ν from log-linear regression of root area. Data from Berry and Chung (2013) are reported for each tree and generally decrease with increasing *DBH*; data from Chung (2013) is reported as a constant value for all trees (dashed lines).

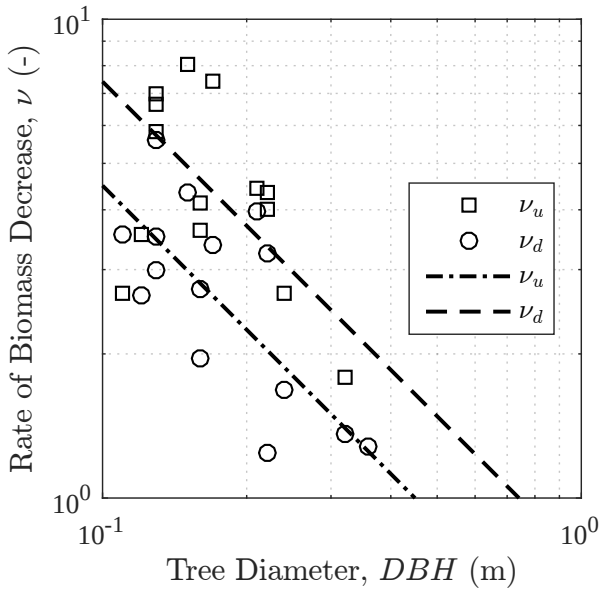

Figure 5.4: Comparison of ν for the biomass model to values reported by Berry and Chung (2013).

DBH that is independent of species to control the rate of biomass decrease, allowing for different values of A_0 to control the absolute value of *RAR* for each species.

The species-independent log-linear relation of ν and *DBH* is defined:

$$\ln \nu = \beta_{\nu,0} + \beta_{\nu,1} \ln (DBH) \tag{5.9}$$

Parameters $\beta_{\nu,0}$ and $\beta_{\nu,1}$ are selected using the slope of a log-linear regression analysis for ν_d, which had the higher R^2. To simplify the biomass model, the downslope parameter, ν_d is computed directly using Equation 5.9, and the upslope parameter, ν_u, is determined as a function of ν_d, offset by a constant value $\Delta\nu_{ud}$:

$$\nu_u = \nu_d + \Delta\nu_{ud} \tag{5.10}$$

where $\Delta\nu_{ud}$ is set to 0.5, which is approximately the average distance between the two data sets, $\nu_u - \nu_d$. This simplification incorporates the observation by Berry and Chung (2013) that biomass decreases faster in the upslope than downslope direction when a tree is located on a slope. If a level-ground condition is desired then the average value of ν_u and ν_d is used for both directions. The regression lines and data from Berry and Chung (2013) are shown in Figure 5.4 along with fit lines using parameters $\beta_{\nu,0} = -0.8$, $\beta_{\nu,1} = -1.0$ and $\Delta\nu_{ud} = 0.5$.

5.2 Vertical Root Distribution

Root density variation in the vertical direction is non-uniform and can be described by average depth, z_a, depth containing 90% of biomass (z_{90}) and maximum depth, z_{max}. Due to apparent inconsistencies between Berry and Chung (2013) and Chung (2013) only 15 of the 20 scanned trees were used herein. As illustrated in Figure 5.5 there is a moderate correlation between the depth descriptors and *DBH*: R^2 is 0.39 for z_a, 0.60 for z_{90}, and 0.59 for z_{max}. Table 5.3 summarizes the vertical root data, and compares the ratio between each parameter: while there is some variation, in general there is a doubling in value from z_a to z_{90} and from z_{90} to z_{max}. Average rooting depth

Table 5.3: Summary of vertical root distribution data from trees excavated by Berry and Chung (2013), computed herein from 15 of the 20 trees reported. Ratios are computed using the data from each tree, not the ratio of computed averages. All R^2 values are recomputed using the subset of 15 trees.

	DBH (m)	z_a (m)	z_{90} (m)	z_{max} (m)	z_a/z_{max}	z_{90}/z_{max}	z_a/z_{90}
Average	0.17	0.54	0.96	1.57	0.36	0.62	0.58
Minimum	0.08	0.36	0.38	0.62	0.27	0.43	0.42
Maximum	0.36	0.80	1.55	2.61	0.58	0.70	0.95
R^2 with *DBH*	–	0.39	0.59	0.60	0.27	0.01	0.16

was around 0.5 m and although z_{max} reaches a peak value of 2.61 m, the peak value for z_{90} of 1.55 m shows that most of the root mass is generally below 2 m. These data are consistent with: observation by Berry (personal communication) that nearly all roots are located in the upper 1.0 to 1.5 m; maximum root pit depth of 2 m for larger trees reported by Coder (2010) and USACE (2014a); and with maximum root pit data of around 1.7 m for larger trees reported by Peterson and Claassen (2012) for larger trees. With taproot excluded, z_a was essentially uncorrelated with *DBH* ($R^2 = 0.1$), having an average value of around 0.5–0.6 m. Figure 5.5 shows that if the correlations is extended beyond the dataset limit of $DBH = 0.4$ the values of z_a, z_{90} to z_{max} will become unrealistically large. For example, at $DBH = 1.0m$, z_{90} would be on the order of 4.0 m, which is more than twice the maximum pit depth reported by Peterson and Claassen (2012) at that tree size. Thus, for large trees z_{max} should be considered independent of *DBH*.

As a part of the work by Berry and Chung (2013) and Chung (2013) virtual horizontal planes were used to evaluate biomass in a similar manner to the VTP discussed above. While these results would provide extremely useful details on the shape of root distribution with depth, they were not included in either document. Unfortunately, all attempts to obtain the information were unsuccessful.

The low R^2 of 0.27, 0.01 and 0.016 for z_a/z_{max}, z_{90}/z_{max} and z_a/z_{90} with respect to *DBH* (Table 5.3) indicate the proportional relationship between depth parameters is consistent across all tree sizes. To explore further z_a and z_{90} were regressed to z_{max} and z_a to z_{90}, producing much higher R^2 than with *DBH*:

$$z_{avg} = 0.18 + 0.23 \cdot z_{max}, \qquad R^2 = 0.75 \tag{5.11}$$

$$z_{90} = 0.13 + 0.52 \cdot z_{max}, \qquad R^2 = 0.82 \tag{5.12}$$

$$z_a = 0.20 + 0.35 \cdot z_{90}, \qquad R^2 = 0.61 \tag{5.13}$$

Figure 5.6 illustrates the regressions (solid lines) and visually confirms higher R^2 when compared to Figure 5.5. Due to the small data set, and to simplify the biomass model, a set of ratios is used to

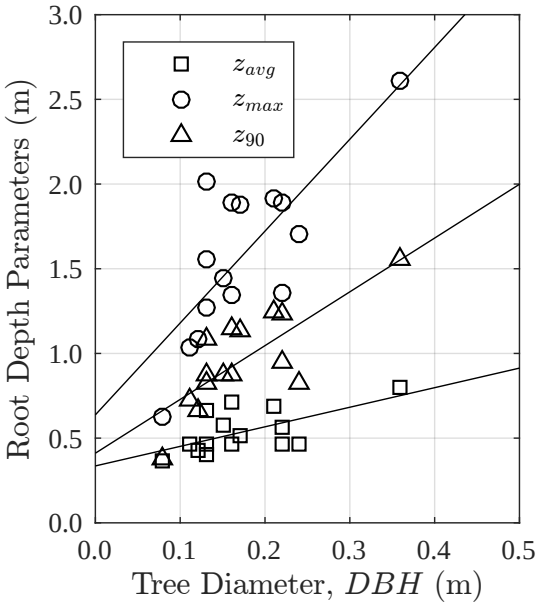

Figure 5.5: Average, maximum and 90% root depth versus *DBH* (Berry & Chung, 2013)

relate z_a, z_{90} and z_{max}, rather than using the linear regression equations. As can be seen in 5.6 and Equations 5.11–5.13, za is about $1/4$–$1/3$ of z_{max} and z_{90} is about $1/2$–$2/3$ of z_{max}. These ratios are also illustrated on Figure 5.6 as dotted lines.

A point-estimate of root-area ratio can be described as a function of depth, $RAR(x,y,z)$, which is equivalent to the measurement in a trench wall survey over an infinitesimal area $A = \mathrm{d}y\,\mathrm{d}z$. A density function is defined, $f_{RAR}(z)$, to describe the relative change in *RAR* with depth. When integrated over z this function produces an average of root area ratio, $\overline{RAR}_z$:

$$\overline{RAR}_z = \frac{1}{z_2 - z_1} \int_{z_1}^{z_2} f_{RAR}(z)\,\mathrm{d}z \tag{5.14}$$

The lateral component of the biomass model $\overline{RAR}_{xy}$ is computed for a given tree at location (x,y). Vertical distribution of *RAR* with depth is needed to compute the point-estimate in three dimensions, $RAR(x,y,z)$ (or $RAR_{PS}(x,y_{PS},z)$, described below) and is accomplished by scaling $f_{RAR}(z)$ such that the integral in Equation 5.14 equals 1:

$$\frac{1}{z_{max}} \int_0^{z_{max}} f_{RAR}(z)\,\mathrm{d}z = 1 \tag{5.15}$$

This allows the scaling function to provide the point-estimate in three dimensions as:

$$RAR(x,y,z) = f_{RAR}(z) \cdot \overline{RAR}_{xy}(x,y) \tag{5.16}$$

Note that Equation 5.15 may imply the scaling function to be greater than 1 for certain z. This is generally acceptable due to the exponential decay of $\overline{RAR}_{xy}$ which will prevent $RAR(x,y,z)$ from exceeding 1. For simplification in this section $RAR(x,y,z)$ is referred to as $RAR(z)$

This work uses the lognormal distribution for the shape of $f_{RAR}(z)$ and is defined by parameters λ and ζ. Note that in this application it is not used as a probability density function for

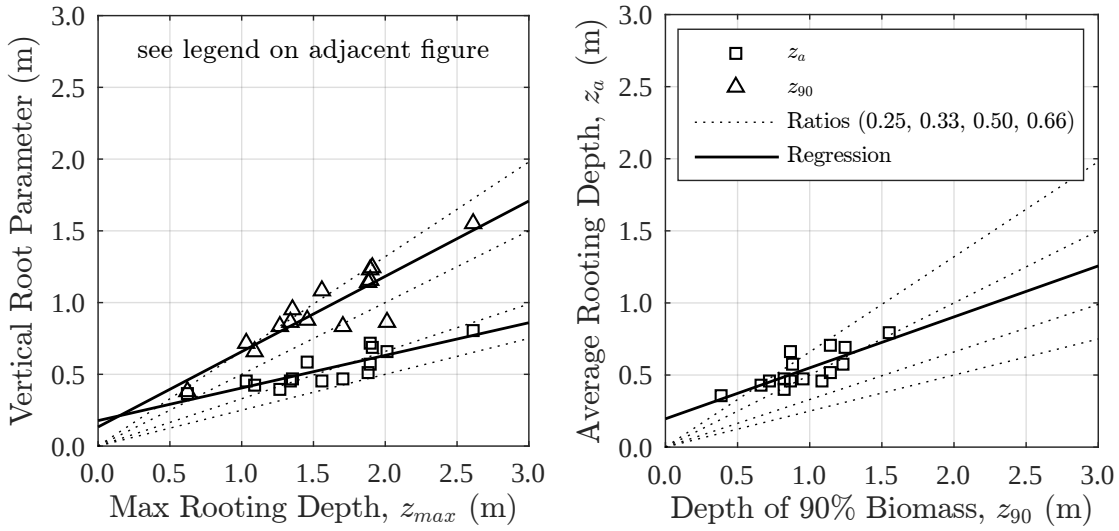

Figure 5.6: Comparison of vertical root distribution parameters to data reported by Berry and Chung (2013). Dotted lines illustrate ratios of 1/4, 1/3, 1/2 and 2/3 for z_a/z_{max}(a), z_{90}/z_{max}(a) and z_a/z_{90}(b).

$RAR(z)$, but rather as a geometric description of changing root density with depth, scaled such that depth-averaged root area is matched when integrated and averaged across the entire root zone. Furthermore, the statistics of this shape function are known, making computations straightforward. The mean and standard deviation of z (μ_z and σ_z) are used to find the mean and standard deviation of $\ln(z)$ (i.e., λ and ζ) with Equations 5.17 and 5.18:

$$\zeta = \sqrt{\ln(1 + \frac{{\sigma_z}^2}{\mu_z})} \tag{5.17}$$

$$\lambda = \ln z_a - \frac{1}{2}\zeta^2 \tag{5.18}$$

Although σ_z is not provided by Berry and Chung (2013) or Chung (2013), it is possible to use $\mu_z = z_a$ and z_{90} to define the spread of $f_{RAR}(z)(z)$. Parameter z_{90a} is defined as the ratio of 90$^{\text{th}}$ biomass percentile to average rooting depth ($z_{90a} = z_{90}/z_a$). The standard lognormal variate, $Z_{\%}$, for any cumulative percentile (in this case 90%; $Z_{90} = 1.282$) relates z_a, z_{90a}, λ and ζ:

$$P(Z_{90}) = \Phi(Z_{90}) = \Phi\left(\frac{\ln z_{90} - \lambda}{\zeta}\right) \quad \rightarrow \quad Z_{90} = \frac{\ln z_{90} - \lambda}{\zeta} \tag{5.19}$$

Combining Equations 5.17, 5.18 and 5.19 and solving for ζ and λ in terms of z_a, z_{90a}, and Z_{90}:

$$\zeta = Z_{90} \pm \sqrt{Z_{90}^2 - 2\ln z_{90a}} \tag{5.20}$$

$$\lambda = \ln(2z_a) - \zeta Z_{90} \tag{5.21}$$

The two quadratic roots of Equation 5.20 produce different shapes of the lognormal distribution; the larger value (i.e., the + in Eq. 5.20) produces an exponential shape, whereas the smaller root produces a lognormal shape and is used for all computations herein. All that remains is to set the values of z_a and z_{90a}.

Consider the case where $z_a = 0.33$ m, $z_{90} = 0.66$ m and $z_{max} = 1.00$ m. Using the $Z_{90} = 1.282$ to set distribution spread (i.e., Equation 5.19) results in $\lambda = -1.41$ and $\zeta = 0.77$. This combination of parameters keeps 97% of the biomass distribution within the upper 1 m; thus 3% of biomass is below z_{max}, which is supposed to be the max value for the model. Solving for the depth at which $f_{RAR}(z) = 1 \times 10^{-4}$, the typical value for max root extent in the lateral direction gives $z = 4.36$ m; this is much deeper than the values obtained by either Berry and Chung (2013) or Peterson and Claassen (2012). Thus, while z_a and z_{90} are appropriate fractions of z_{max}, the spread of biomass at z_{max} and beyond is not as well represented. Fortunately the problem can be addressed by using $z_a = 0.25$ m and $z_{90} = 0.50$ m (see Figure 5.6). Following the same math as above places only 1% of biomass below z_{max}, and a depth for $RAR(z) = 1 \times 10^{-4}$ at $z = 3.3$ m. The distribution is illustrated in Figure 5.7 and the key central tendencies are compared in Figure 5.8. This combination of parameters is deemed to be the best balance between matching the existing data (i.e., the lines for z_a and z_{90}; Figure 5.8 are near the bottom of the data) and limiting excessive vertical spread for the biomass model (i.e., z_{max} contains 99% of cumulative biomass; Figure 5.7).

Numerous studies have observed and applied the exponential decrease of root density with depth and fit parameters to site-specific data (e.g., Bellugi et al., 2015; Jackson et al., 1996; Roering, 2008; Shields & Gray, 1992). These efforts are usually focused on capturing root distribution over a vegetated region to capture the reinforcing effects on shallow landsliding, whereas this research is focused on evaluating reinforcing effects of a single tree at a specific location within the root zone. An exponential shape for root density places the maximum reinforcement at the ground surface, which can cause problems in slope stability analyses, as discussed in the next chapter. Bellugi et al. (2015) acknowledge problems fitting an exponential distribution within 10–20 cm and Coder (2010) recommends a gamma distribution, which gives the mode of root density the option of being zero or non-zero (i.e., similar to the exponential or lognormal, respectively); data reported by Bischetti et al. (2005) is fit to a lognormal or gamma shape. The gamma distribution was not used in this research because it requires three parameters and would be difficult to fit to the available data.

Site-specific data of vertical root distribution is generally needed to fit a function for $f_{RAR}(z)$, consisting of measured root diameter or *RAR* with depth. These data were interpreted by Berry and Chung (2013) but unfortunately not made available for this study. Instead, statistical measures of vertical root distribution from their report were be used (i.e., z_a, z_{90} and z_{max}), as described above. To provide a comparison to published research, an exponential distribution was evaluated of the form $\alpha \exp -\beta z$ for $f_{RAR}(z)$, where $\alpha \sim [-]$ is a scaling parameter and $\beta \sim [1/L]$ is a shape parameter. Selecting $\alpha = 5$ and $\beta = 5$ m^{-1} satisfies Equation 5.15 and is comparable to the relationship used by Montgomery et al. (2009) and Bellugi et al. (2015) for conifer forests. As illustrated in Figure 5.7, the exponential and lognormal models produce similar relationships, but differ in statistical characteristics. Average, median and 90$^{\text{th}}$ percentile rooting depths are 0.20, 0.14 and 0.46 for the exponential model and 0.25, 0.19 and 0.50 for the lognormal. Although similar statistically, the lognormal distribution is better able to match the parameters reported by Berry and Chung (2013) while also preventing numerical issues with stability computations.

There is no depth at which computed $RAR(z)$ becomes zero because the lognormal distribution

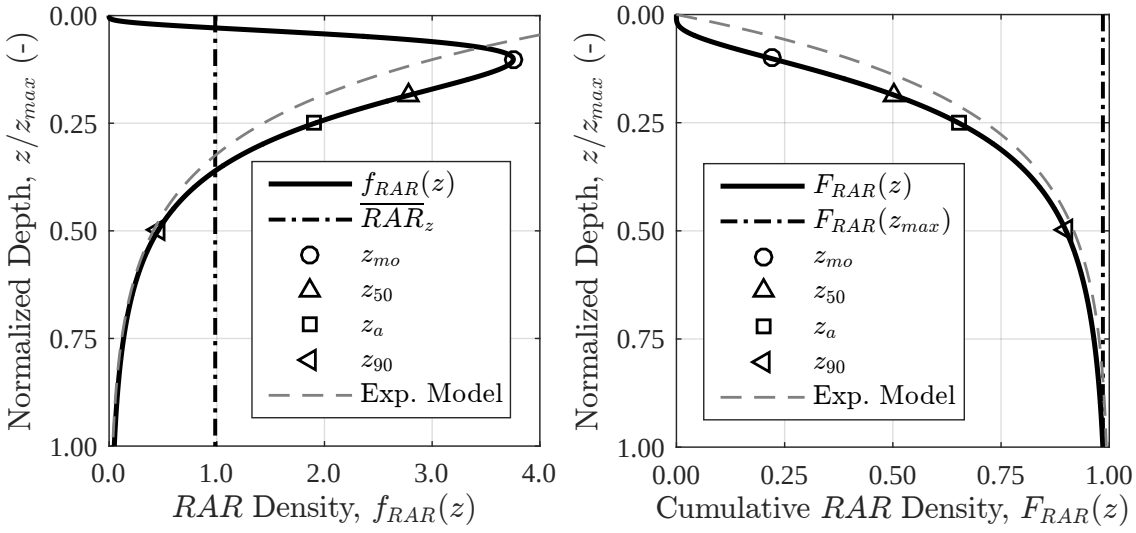

Figure 5.7: Lognormal *RAR* density function, $f_{RAR}(z)$, and cumulative density, $F(z)$. Function is scaled to z_{max} by statistical parameters $z_a/z_{max} = 0.25$ and $z_{90}/z_{max} = 0.50$ to match data reported by Berry and Chung (2013) and $\overline{RAR}_z = 1.0$ such that $RAR(x,y,z) = f_{RAR}(z)\overline{RAR}_{xy}(x,y)$. Due to asymptotic form $\overline{RAR}_z = F(z_{max}) = 0.99$ and z =3.3 m when f_{RAR} =1e–4. An exponential model is shown for comparison with rate parameter of 5 m^{-1} and $z_a = 0.20$, $z_{50} = 0.14$, $\overline{RAR}_z(z_{max}) = 0.99$ and z =2.2 m when f_{RAR} =1e–4.

is asymptotic with increasing z. Despite what the name may indicate, $RAR(z)$ is not set to zero when $z > z_{max}$ for analyses herein to prevent numerical discontinuities causing computation problems. Alternatively, z_{max} is used as an analytic index to: scale z_a and z_{90}; calibrate the biomass model output with empirical data; and to serve as a random variable in reliability analyses. Except for sensitivity studies, z_{max} is not varied with *DBH*. While this is consistent with the data described above it ignores the possible correlation between vertical root distribution and *DBH* for small trees (i.e., *DBH* < 1 m). However, there is sufficient variation in the rate of biomass decrease (v) with *DBH* to represent the full range of possible values because $RAR(z)$ simply scales the depth-averaged value $\overline{RAR}_{xy}$. Thus, in the analyses herein z_{max} is essentially considered to be a constant from 1.0 to 2.0 m, where $z_a/z_{max} = 0.25$ and $z_a/z_{90} = 0.50$ are selected to balance a match of empirical data and to limit the biomass predicted for $z > z_{max}$.

5.3 Maximum Root Extent

Maximum root extent, *MRE*, defines the maximum distance of roots in the horizontal $\hat{x}$–$\hat{y}$ plane; L_u, L_d and L_y are used to define this dimension in the upslope, downslope and lateral direction. Berry and Chung (2013) correlated *MRE* to *DBH* in the up and downslope direction (shown in Figure 5.9), finding upslope root extent is around half of downslope extent. Results are generally below the correlation of *MRE* from Schwarz et al. (2010), compiled from 6 data sets on flat and sloping ground for roots with diameters greater than 1–2 mm. All roots less than 8 mm were

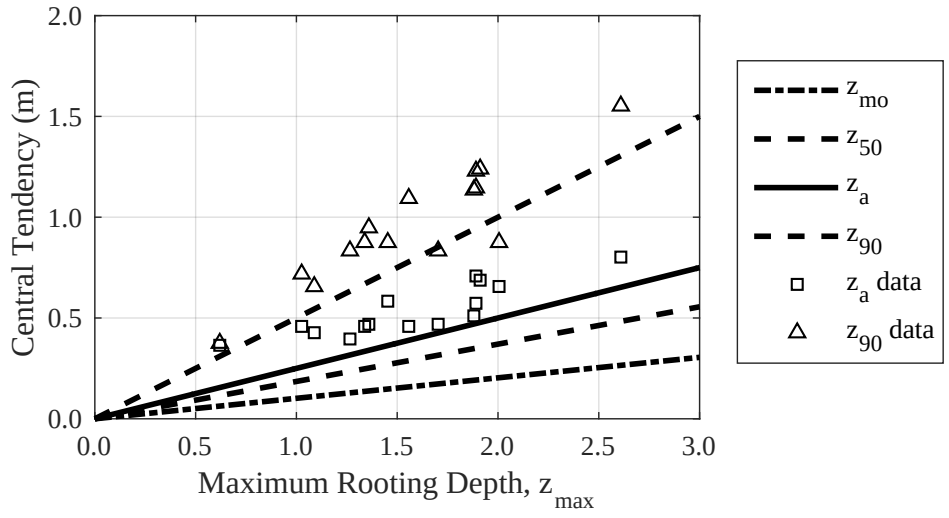

Figure 5.8: Central tendency parameters for lognormal distribution of roots with depth.

trimmed during field excavation of the root system (Chung, 2013) and it is assumed this is the smallest size of an individual root at *MRE*. Ranges of *MRE* reported Coder (2010) and Coder (2014) were compared to those of Berry and Chung (2013) as an additional source for the biomass model and were found to match well with the line for upslope direction in Figure 5.9.

Data for *MRE* data has an acceptable correlation with *DBH*, but given the exponential decrease of *RAR* from trunk center would produce insignificantly small values of *RAR* when used in levee seepage and stability analyses. For example, *RAR* is 10^{-6} to 10^{-5} at *MRE* for $DBH > 0.2$ m in the downslope direction (Figure 5.10). Specifying a minimum *RAR* beyond which no roots are assumed to exist, RAR_{min}, can minimize computation time, especially when numerical integration is concerned (i.e., for plane-strain averaged values). Using Equation 5.8, the upslope and downslope limits for *MRE*, L_u and L_d, can be computed for a given RAR_{min} (as done in Figure 5.10). L_u and L_d are radial distances measured in the horizontal plane, with respect to the tree trunk center. *MRE* in the lateral direction is set to $y_{MRE} = (L_u + L_d)/2$, and Equation 5.4 is applied to define *MRE* as a function of θ. Due to the presence of A_{cyl} in Equation 5.3, the *RCSA* implied by RAR_{min} is dependent on distance from the trunk (i.e., L_u or L_d) and depth of the root zone (i.e., z_{max}). Combining the cross-sectional area of a single circular root ($d = \pi d^2/4$) with Equation 5.3 produces the equivalent diameter of a single root, d_1, at distance l given *RAR* and z_{max}:

$$d_1 = \sqrt{8 \cdot l(RAR) \cdot RAR \cdot z_{max}} \tag{5.22}$$

where l is a function of *RAR*. The single-root equivalent diameter scaled by the square root of unit length $\sqrt{l}$ can be used as a reference value for visualizing the amount of biomass at a constant *RAR*. Scaled single-root equivalent diameter, $d_1/\sqrt{l}$, is presented in Table 5.4 in cm for various values of RAR_{min} and z_{max}. An estimate of d_1 at the maximum root extent is found by multiplying $d_1/\sqrt{l}$ by *MRE*. Considering most trees measured by Berry and Chung (2013) had *MRE* of 1 to 5 m, the values of d_1 are generally consistent with the 0.8 cm limit that defines *MRE* for that study. In other words, most of the values in Table 5.4 are on the order of 1 cm when multiplied by 1–2.2.

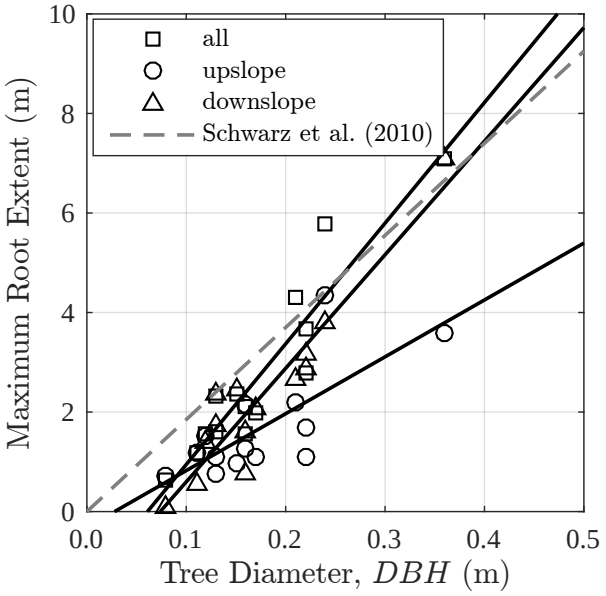

Figure 5.9: Maximum horizontal extent of excavated roots reported by Berry and Chung (2013). $R^2 = 0.88$, 0.58 and 0.89 for all, upslope and downslope directions. "All" includes lateral directions in addition to upslope and downslope. Schwarz et al. (2010) is a correlation of 6 literature sources for roots down to 1–2 mm diameter: $MRE = 18.5 \cdot DBH$ ($R^2 = 0.76$).

$d_1/\sqrt{l}$		z_{max}		
d_1 in cm, l in m		1.0 m	1.5 m	2.0 m
RAR_{min}	1×10^{-3}	8.9	11	12
	1×10^{-4}	2.8	3.5	4.0
	1×10^{-5}	0.9	1.1	1.3

Table 5.4: Scaled single-root equivalent diameter, $d_1/\sqrt{l}$, of a single root for specified combination of RAR_{min} and z_{max}. Computed for a unit distance from trunk (1 m) per Equation 5.22; actual equivalent root diameter at *MRE* for a specific tree is found by multiplying by $\sqrt{l}$. Units are cm for d_1 and m for l.

Figure 5.10 illustrates the predicted *MRE* for RAR_{min} =1e–4, 1e–5 and 1e–6. All predictions match the data well for low *DBH*; however RAR_{min} =1e–4 is very low for *DBH* beyond 0.2 m. Relatively small roots would be expected at large *MRE*, consistent with the 1–2 mm diameter limit for data from Schwarz et al. (2010), and even the 8 mm diameter limit of Berry and Chung (2013). Although larger diameter roots can travel long distances, the reinforcing capacity of a small number of outliers is small relative to the potential slide mass in slope stability analyses. Thus, despite the under prediction of *MRE* for RAR_{min}, using a lower value can be acceptable for the engineering applications considered herein. Based on remarks above, the general match between Berry and Chung (2013), Coder (2010) and Schwarz et al. (2010) data, and the small amount of root volume in the vicinity of *MRE* (see Section 5.6), it seems appropriate to limit biomass computations to $RAR > 10^{-4}$. If an analyses are found to be sensitive to *RAR* below 1e–4, RAR_{min} can be adjusted accordingly, at the cost of more time-consuming computations.

5.4 Root Ball Radius and Pit Depth

Root ball radius, L_{rb} defines the portion of the root zone where weight and wind loading are transferred to the soil and acts with more rigidity than the roots further from the trunk. This zone is

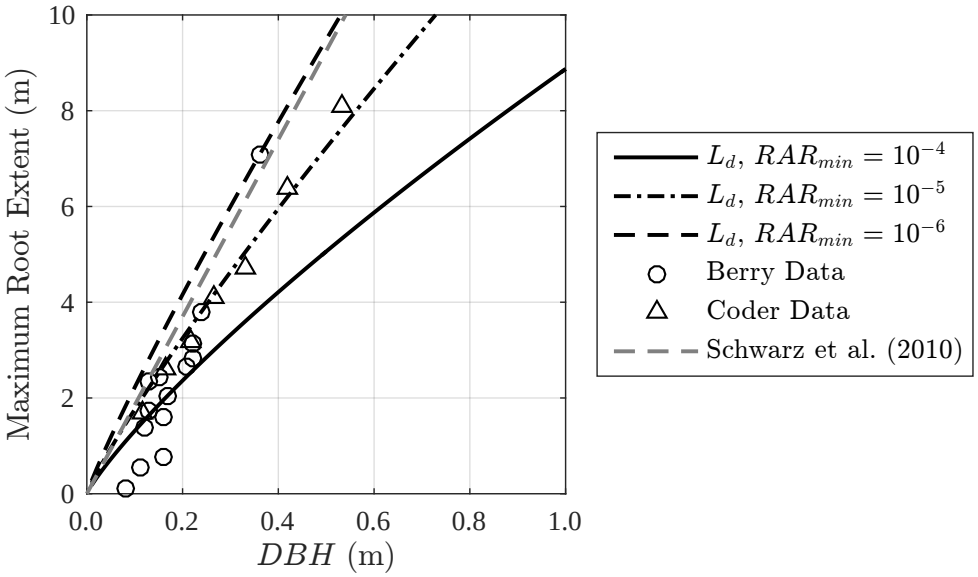

Figure 5.10: Comparison of maximum root extent, L_d, computed by the biomass model and data reported by Berry and Chung (2013) and Coder (2010) for various values of parameter RAR_{min}. Curves also can be interpreted as distance from the trunk to a contour of $\overline{RAR}_{xy} = RAR_{min}$. Schwarz et al. (2010) is a correlation of 6 literature sources for roots down to 1–2 mm diameter: $MRE = 18.5 \cdot DBH$ ($R^2 = 0.76$). MRE is under predicted for RAR_{min} =1e-4, which does not have significance to engineering applications herein.

also considered to be the portion of the root zone that pulls out of the ground when a tree fails due to wind loading. After windthrow occurs the resulting divot is described by root pit depth, z_B, and L_{rb}. Berry and Chung (2013) and Chung (2013) studies made no assessment of root ball radius, but fortunately there is a wide body of literature reporting root pit dimensions and DBH.

Numerous windthrow studies have been analyzed by the USACE (2014a) to make recommendations for root ball radius and pit depth. A consistent relationship was found between 676 observations across many species and locations for root ball, $L_{rb} = 19.5 \cdot DBH + 43.9$ with $R^2 = 0.64$. While a useful correlation was not found for root pit depth, over 100 observations from four sources were used to confirm the field recommendation by Coder (2010) that $z_{pit} = 3.6 \cdot DBH$ forms an upper bound for the majority of windthrow pits, up to a maximum of $z_{pit} = 2.0$ m. Furthermore, 46.5% of the almost 3,500 observations considered had z_{pit} less than 1 m, 50% were between 1 and 2 m and 3.5% were greater than 2 m. Interpretations of data from a California study on cottonwood and oak trees by Peterson and Claassen (2012) matched well the recommendations by USACE (2014a) and is used herein for site-specific correlations of root ball, root depth and wind load components of the biomass model.

Peterson and Claassen (2012) studied root pits formed after cottonwood and oak trees with DBH of 0.13 to 1.28 m were winched to failure. A total of 70 trees were loaded with a winch until failure occurred, 40 of which resulted in uprooting and 30 in broken trunks; the latter tended to be smaller diameter trees. Critical overturning moment was computed from winch load and tree mass (i.e., moment due to tree bending from vertical); Figure 5.11 illustrates the relationship of critical moment with DBH for uprooted trees only.

Area and depth were measured for each pit excavated by uprooted trees, but pit volume was too variable in shape to measure consistently. Pit radii ranged from 0.5 to 2.3 m with an average of 1.3 m, whereas depth ranged from 0.4 to 1.7 m with an average of 1.0 m (most pits were less than 1.0 m). As illustrated in Figure 5.12, a consistent trend exists for smaller pits in oak when compared to a similar diameter cottonwood; however, root pit is very scattered, appearing to increase with diameter until a maximum value between 0.5 to 2.0 m is reached for diameters greater than 0.5 m. Furthermore, the largest cottonwood trees did not produce the largest pit radii and Peterson and Claassen (2012) hypothesize this behavior has to do with either: large cottonwood roots cover a smaller area than for oak; or, a larger percentage of biomass is left in the ground due to the failure location of cottonwood roots. The lower biomass reduction rate, ν, found by Berry and Chung (2013) for cottonwood compared to oak indicates the second hypothesis is more viable; perhaps the strength of woody material controls. It is anticipated that the root pit depths from Peterson and Claassen (2012) are upper limits of what most trees would excavate when failing under natural circumstances. Since trees are more likely fall when their root systems have been compromised with rot or soil erosion it would also be expected that the root pit dimensions would decrease, seeking out the weaker root zone. Furthermore soil excavation would decrease under wet conditions that exist for flood events; increased saturation of the soil results in a tendency for roots to fail by pulling out of soil rather than breaking (Section 6.1). Finally, field observations of the root systems of trees that have fallen in storms over the last two winter seasons were made as a part of this project. Based on observations from dozens of trees, primarily large eucalyptus, oak and cottonwood, the vast majority produce an extremely shallow root plate when failed by root pullout. Coder (2014) summarizes L_{rb} that are nearly double the radius from Peterson and Claassen (2012). Since the data from Coder (2014) has no description of methods and Peterson and Claassen (2012) is specific to the Central Valley trees considered in this document Coder (2014) data for L_{rb} is ignored.

Unfortunately there is not sufficient data to directly incorporate an allometric relationship for z_{pit} that captures the complex 3D structure of windthrow pits observed in the literature in addition to matching other root distribution dimensions described herein. Figure 5.13 combines z_a, z_{90} and z_{max} from Berry and Chung (2013) with z_{pit} of Peterson and Claassen (2012); immediately it is apparent only a few tens of centimeters overlap the coverage of *DBH* in the two data sets. Despite this, z_{pit} appears to be consistently less than z_{90} for $DBH < 0.5$ m; beyond this z_{pit} seems to reach a maximum of 1.5 to 1.7 m, and is well below the trend line for z_{90}. This behavior is part of the reason for not relating vertical root distribution to *DBH* in the biomass model (Section 5.2). If z_{max} increases and z_{pit} remains constant, a smaller portion of total biomass is predicted within the root ball as *DBH* increases (i.e., growing distance from z_{max} and z_{90} in Figure 5.13). Furthermore, there is significant evidence in data sources described herein supporting upper limits on vertical root dimensions, especially as *DBH* increases. For a larger root ball enough soil mass is incorporated that roots begin to break at a certain depth regardless of the tree size. This is analogous to the fiber break phenomena observed and modeled by Pollen and Simon (2006), where roots break rather than pull out of the soil (Section 6.1). Although root pit does not match up with a consistent value of $RAR(z)$, applying a maximum value for z_{pit} provides a conservative means of evaluating the effect that an excavated root pit might have on the subsurface seepage conditions and load transfer to the levee.

Implementation of root ball radius, L_{rb}, in the biomass model uses the linear regression from

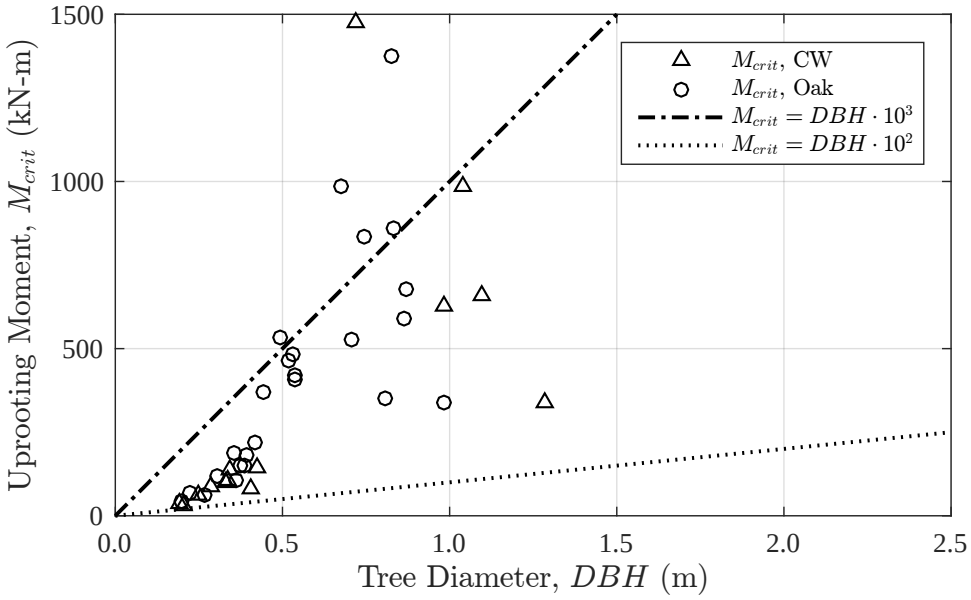

Figure 5.11: Critical moment, M_{crit}, for trees failed by uprooting and computed using winch load and tree mass measurements (Peterson & Claassen, 2012). Dashed and dotted lines of 1000*DBH* and 100*DBH* enclose most of the data.

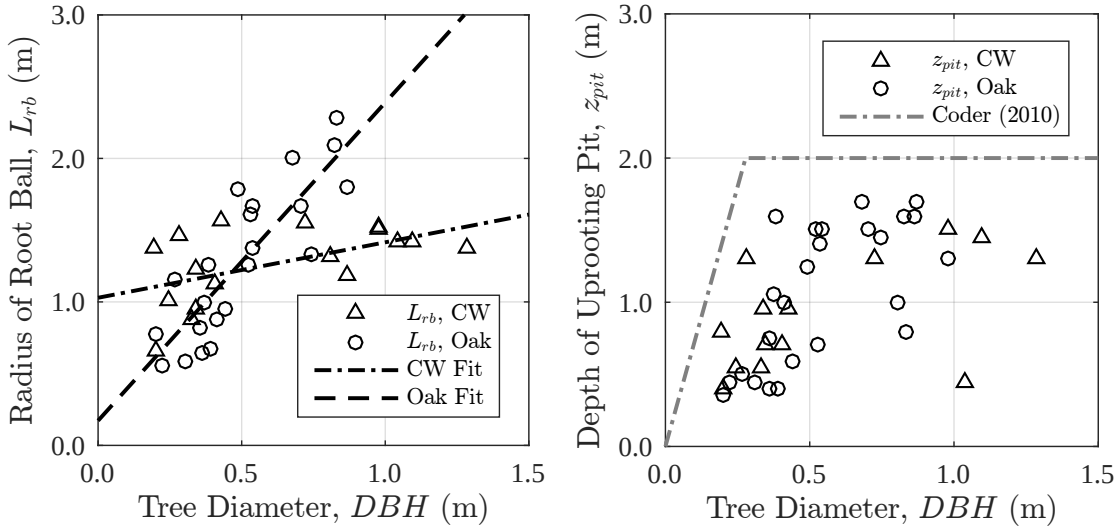

Figure 5.12: Root ball radius, L_{rb}, and pit depth, z_{pit}, from winching tests by Peterson and Claassen (2012), separated by tree species. L_{rb} is computed from reported diameter assuming a circular pit. Bounding line is from Coder (2010) for $z_{pit} < 3.6 \cdot DBH$ to a maximum of $z_{pit} = 2.0$ m.

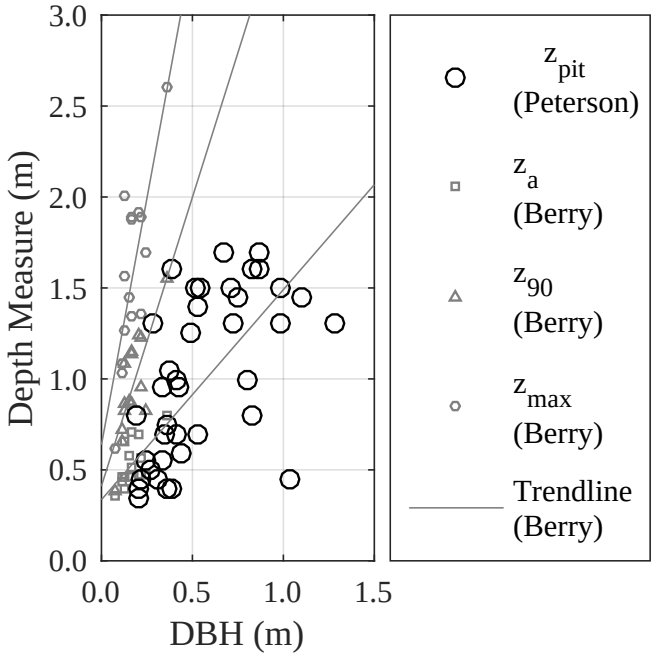

Figure 5.13: Comparison of data reported by Peterson and Claassen (2012) and Berry and Chung (2013) for root pit depth, including linear best-fit regressions.

	$\beta_{RB,0}$	$\beta_{RB,1}$
Cottonwood	1.0289	0.3865
Oak	0.1723	2.2169
Average	0.8014	0.8573

Table 5.5: Linear regression parameters for root ball radius, L_{rb}, and DBH after data reported by Peterson and Claassen (2012). Average parameters are used for analyses with unspecified tree species.

Peterson and Claassen (2012):

$$L_{rb} = \beta_{rb,0} + \beta_{rb,1} \cdot DBH \tag{5.23}$$

which has been modified from its original presentation in terms of area to use radius by assuming a circular root ball. Parameters $\beta_{rb,0}$ and $\beta_{rb,1}$ are summarized in Table 5.5 and plotted in Figure 5.12

5.5 Plane-Strain Interpretation

A plane-strain equivalent of $\overline{RAR}_{xy}$ is necessary for incorporating the biomass model into stability analyses. This value can be found at any location x along the levee transect through trunk center by integrating Equation 5.6 over the root zone parallel to the levee axis ($\hat{y}$) and dividing by the integration interval, y_{PS}:

$$\overline{RAR}_{PS}(x) = \frac{\int \overline{RAR}_{xy}(x,y)\,\mathrm{d}y}{y_{PS}} \tag{5.24}$$

Equation 5.24 computes $\overline{RAR}_{PS}(x)$, the depth- and plane-strain averaged value of $RAR(x,y,z)$ at some horizontal distance x from the tree trunk center, illustrated in Figure 5.14, which uses

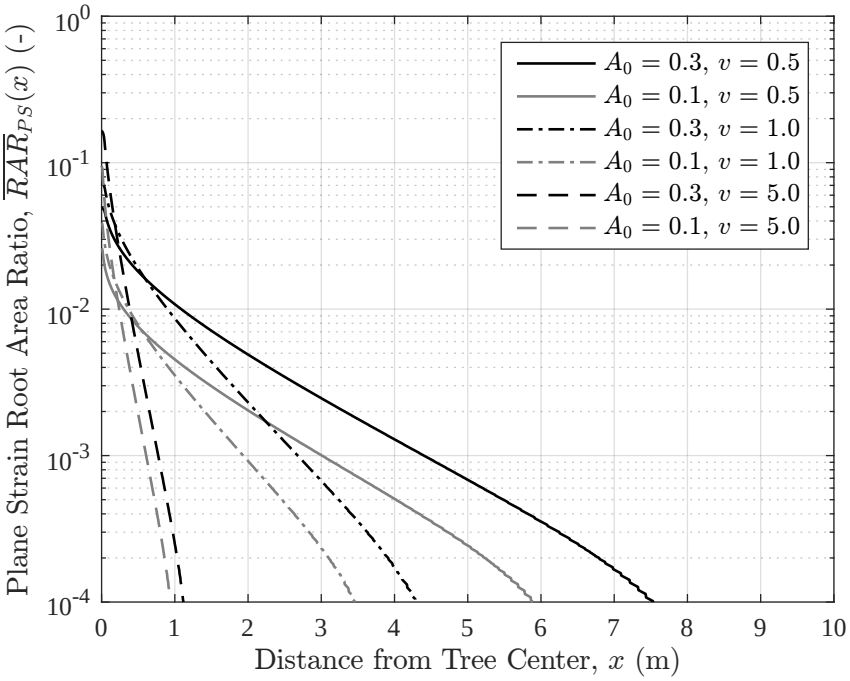

Figure 5.14: Plane-strain depth-averaged root area ratio, $\overline{RAR}_{PS}(x)$, from biomass model with varying A_0 and ν and $y_{PS} = 15$ m, averaged in levee parallel direction. Computed for level ground case $\nu_u = \nu_d$. Scaling by $f_{RAR}(z)$ provides 2D point-estimate of $RAR_{PS}(x,z)$.

the same values of A_0 and ν as Figure 5.2 in Section 5.1. Integration limits in $\hat{y}$ are set to the maximum root extent for each combination of A_0 and ν. As with root cross-sectional area, the depth and plane-strain averaged $\overline{RAR}_{PS}(x)$ decreases exponentially with distance from tree center as shown in; however, due to the relatively small values of *RAR* at large y, the function decreases more rapidly than a simple exponential reduction as x increases.

Note that applying Equation 5.24 with integration limits across the root zone (y_{MRE}) is equivalent to a plane-strain slope stability analysis $RAR(x)$ representing trees spaced such that the maximum extent of one root system exactly matches with the root zone edge of the next tree. A more sparse tree spacing can be incorporated by using a length such that $y_{TS} > y_{MRE}$, as shown in Figure 5.15. Numerical implementation of the root function forces *RAR* to zero when beyond *MRE*, so setting $y_{PS} = y_{TS} > y_{MRE}$ limits the stability analysis to one tree and root system. A condition where $y_{PS} = y_{TS} < y_{MRE}$ represents a tree spacing results with overlapping root systems. In this case the *RAR* due to root ends of adjacent trees is not counted, as the numerical value is far less than that of the root zone near the trunk, and implementation would unnecessarily complicate the algorithm.

Unfortunately, Equation 5.24 does not have an analytic solution and must be evaluated numerically; to minimize the number of computations, integration limits are set to the maximum root extent, as $\overline{RAR} = 0$ is assumed outside these bounds. Even with this truncation the small values of *RAR* make numerical integration a time consuming component analyses. To maximize efficiency an approximating function is matched to $\overline{RAR}_PS(x)$ for $L_u \leq x \leq L_d$ whenever a new tree config-

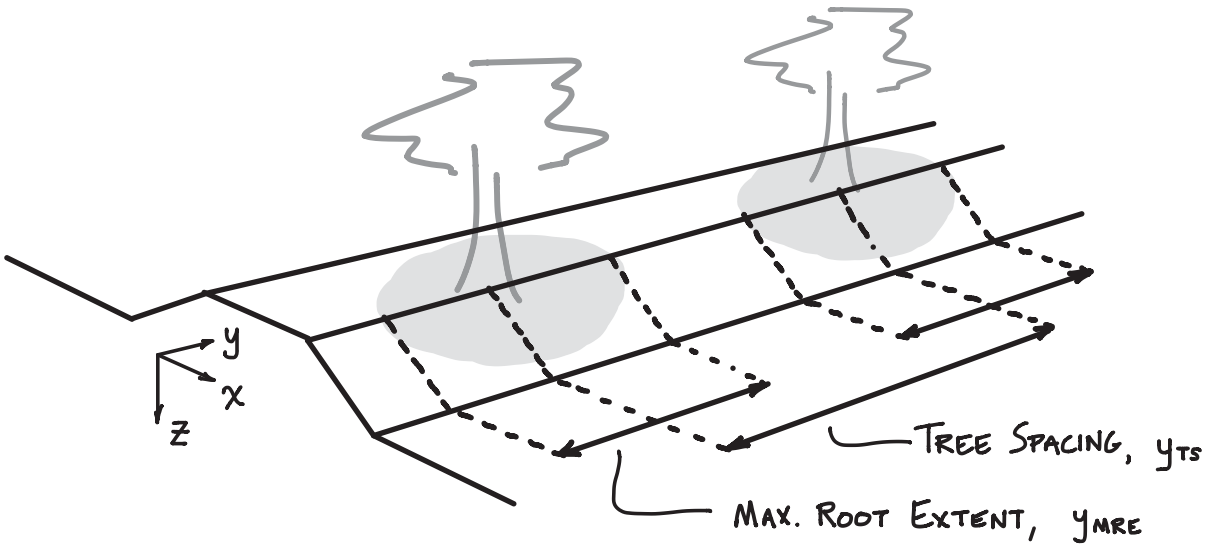

Figure 5.15: Plane-strain tree spacing schematic.

uration is called for. Parameters for the approximating function are subsequently passed through functions in the analysis as long as that configuration is needed. For example, a suite of minimum FS surface search in a stability evaluation, or one iteration of a FORM analysis with DBH as a random variable. This approach only requires the numerical integration be completed once per configuration.

5.6 Root Volume

Root volume, $RV(x,y,z)$, is computed by integrating root area ratio over a volume of interest. The integral can be thought of as an extrusion of $RCSA$ with length and is integrated numerically:

$$RV = \iiint_{\mathrm{V}} RAR(x,y,z)\,\mathrm{dV} \tag{5.25}$$

where the integration volume can take several forms, for example: $\mathrm{dV} = \mathrm{d}x\,\mathrm{d}y\,\mathrm{d}z$ or $\mathrm{dV} = \mathrm{d}l\mathrm{d}\theta\,\mathrm{d}z$. The most common form used in this research is:

$$RV(x_1,x_2) = \int_{x_1}^{x_2} \overline{RAR}_{PS}(x)dx \tag{5.26}$$

where integrals over $\hat{y}$ and $\hat{z}$ are incorporated into $\overline{RAR}_{PS}(x)$. Root volume is used to determine the distribution of weight and wind loading that is applied to soil in the root ball. It is assumed that load transfer is proportional to root density, represented by the fraction of root volume within region (x_1,x_2), normalized by the total root volume in the root ball: $RV(x_1,x_2)/RV(-L_{rb},+L_{rb})$.

Root volume can also be computed across the MRE of the tree to understand how biomass is distributed. As shown in Figure 5.16, 60% of biomass is located within the root ball when

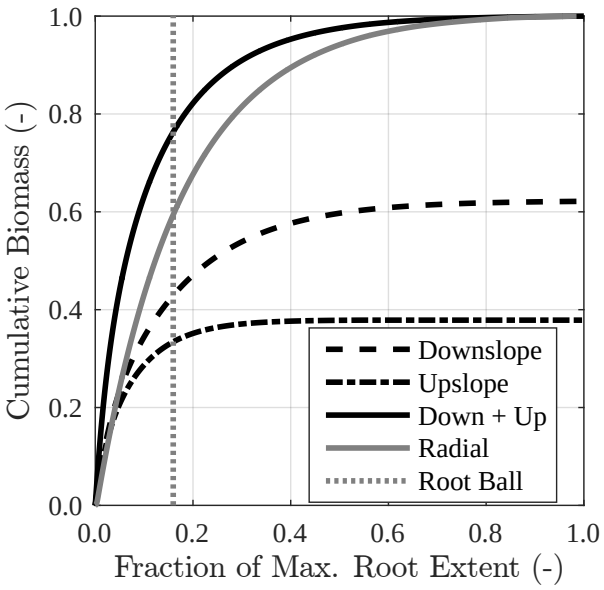

Figure 5.16: Cumulative root volume, *RV*, integrated from 0 to L_{MRE} and normalized by the total root volume. Downslope and upslope curves integrate along $+(\hat{x})$ and $-\hat{x}$, respectively. Radial curve (and total root volume) integrated along l using polar coordinates. Distance normalized by L_{MRE} and relative position of the root ball is shown.

integrated radially (i.e., 3D). For the plane-strain case on a slope, about 38% and 62% of biomass is located up and downslope, respectively. Within the root ball the upslope and downslope biomass is more similar, with both close to 40%. Furthermore, it is interesting to note that nearly the entire upslope biomass is located within the root ball (about 35% inside, 3% outside). Finally, when upslope and downslope are considered together, the plane-strain case has just over 75% of biomass inside the root ball.

Log-linear correlations of biomass (as mass) and *DBH* are available for numerous tree species (e.g., Bolte et al., 2004; Drexhage & Colin, 2001; Goff & Ottorini, 2001; Pellinen, 1986), and can be used with wood density to estimate root volume (e.g., Namm & Berrill, 2012). Attempts to verify the biomass model with published correlations produced estimates of root volume that were generally within an order of magnitude for smaller diameter trees, but incapable of matching across the entire range of interest. Estimates of mass were lower than empirical correlations for larger diameter trees, which may be due to a bias in the databases used for small trees. Another more likely reason is that roots smaller than 8 mm were removed from the roots collected by Berry and Chung (2013), which may dramatically underestimate the amount of biomass in the subsurface. Therefore, root volume is only used as a general scaling parameter for comparing other biomass properties, for example, cumulative biomass within a subset of the root zone as in Figure 5.16.

5.7 Tree Weight

Regressions for mass as a function of *DBH* are presented by Jenkins et al. (2004), which are also used by the USACE in their vegetation analyses. However, regressions in Jenkins et al. (2004) should be increased by 20% as they apply only to above-ground biomass and do not include mass of the root system (Jenkins et al., 2003). Due to scatter in the empirical correlations and the disregard of roots smaller than 8 mm by Berry and Chung (2013) and it is difficult to estimate the true subsurface biomass for Central Valley tree. The log-linear regression for mass in kg and *DBH*

Hardwood	$\beta_{mt,0}$	$\beta_{mt,1}$
Aspen, alder, cottonwood, willow	-2.2094	2.3867
Hard maple, oak, hickory, beech	-2.0127	2.4342
Composite	-2.1	2.4

Table 5.6: Tree mass parameters for log-linear regression of mass (kg) and diameter (cm) as reported by Jenkins et al. (2004) for hardwood species. Composite values can be used to represent a generic tree species.

in cm for $DBH > 2.5$ cm is presented below, with parameters in Table 5.6):

$$\ln m_t = \beta_{mt,0} + \beta_{mt,1} \ln(DBH) + \varepsilon_W \tag{5.27}$$

The term ε_W is root mean squared error estimate of standard deviation in natural log units, reported as 0.507 for hardwood species including cottonwood and 0.236 for hardwood species including oak. For a 1 m *DBH* tree predicted mass is approximately 7800 kg (17 kips) and 1200 kg (2.6 kips) for cottonwood and oak, or 9300 kg (21 kips) using composite parameters. When ε_{RMSE} is applied to the composite parameters predicted mass ranges from 7200–12000 kg (16–26 kips) $\varepsilon_{RMSE} = 0.25$ and 5600–15000 kg (12–33 kips) $\varepsilon_{RMSE} = 0.50$. The range of one standard deviation encompasses the difference in predicted mass between each species. Using $3\varepsilon_{RMSE} = 1.50$ predicts a range of 2100–42000 kg (5–93 kips).

5.8 Model Results

Biomass model results are presented in Tables 5.7 and 5.8 for oak and cottonwood trees with 0.5, 1.0 and 1.5 m *DBH*. Maximum root extent (L_u and L_d) is larger for cottonwood but the root ball(L_{rb}) is larger for oak, all of which increase with *DBH*. Biomass density at the root ball edge ($\overline{RAR}_{PS}(L_{rb})$) is an order of magnitude greater for cottonwood than oak, a results of the greater dispersion of from the trunk. This is also reflected in the single-root equivalent diameter (d_1).

RAR and d_1 when measured at the root ball seem to be lower than expected. Personal observations by the author of trees uprooted due to wind loading seem to have much greater than 10–20 cm^2 of root cross-sectional area along the perimeter of exposed root plate. Because L_{rb} is estimated as a circle, *RAR* and d_1 are different in the upslope and downslope direction, yet both are similar in magnitude. Although a definition of L_{rb} that is correlated to *RAR* from the biomass distribution relationship might provide a more realistic estimate of actual root conditions, given the lack of correlation to *DBH* the current approach is a reasonable approximation.

The log-linear correlation used for weight causes large diameter trees to quickly become large. In addition to kg and lb, tree weight is expressed as an equivalent number of light-duty trucks for comparison (assuming 2,300 kg or 5,000 lb per truck). A large variation of 1–14 trucks is found between the 0.5 m cottonwood and the 1.5 m oak, but only 1–9 for the cottonwood. It should be noted that cottonwood trees generally reach a much larger size than oaks. While an oak is at least 50% heavier than a cottonwood of the same diameter, its root ball radius is also larger, spreading weight and wind forces over a larger area. However, biomass decreases more rapidly with the oak, as evidenced by *RAR* at the root ball edge and shorter maximum root extent. Further insight of biomass can be gained through spatial distribution of *RAR*.

Table 5.7: Biomass model results for 0.5, 1.0 and 1.5 m *DBH* cottonwood trees.

Variable	Tree 1		Tree 2		Tree 3	
	SI	USC	SI	USC	SI	USC
DBH (m, ft)	0.5	1.6	1.0	3.3	1.5	4.9
L_u (m, ft)	3.51	11.50	4.84	15.90	5.57	18.30
L_d (m, ft)	5.06	16.60	8.87	29.10	12.20	40.10
L_{rb} (m, ft)	1.22	4.01	1.42	4.64	1.61	5.28
y_{PS} (m, ft)	15.0	49.2	15.0	49.2	15.0	49.2
$\overline{RAR}_{PS}(+L_{rb})$ (%)	0.104	0.104	0.181	0.181	0.204	0.204
$\overline{RAR}_{PS}(-L_{rb})$ (%)	0.213	0.213	0.389	0.389	0.468	0.468
m_t, W_t (kg, lb)	1490	3300	7820	17200	20600	45400
m_t, W_t (trucks)	1	1	3	3	9	9
$d_1(L_u)$ (cm^2, in^2)	5.3	0.8	6.2	1.0	6.7	1.0
$d_1(L_d)$ (cm^2, in^2)	6.4	1.0	8.4	1.3	9.9	1.5
$d_1(L_{rb,u})$ (cm^2, in^2)	10.1	1.6	14.3	2.2	16.2	2.5
$d_1(L_{rb,d})$ (cm^2, in^2)	14.4	2.2	21.0	3.3	24.5	3.8

Table 5.8: Biomass model results for 0.5, 1.0 and 1.5 m *DBH* oak trees.

Variable	Tree 1		Tree 2		Tree 3	
	SI	USC	SI	USC	SI	USC
DBH (m, ft)	0.5	1.6	1.0	3.3	1.5	4.9
L_u (m, ft)	2.87	9.42	3.91	12.80	4.47	14.70
L_d (m, ft)	4.08	13.40	6.96	22.80	9.43	30.90
L_{rb} (m, ft)	1.28	4.20	2.39	7.84	3.50	11.50
y_{PS} (m, ft)	15.0	49.2	15.0	49.2	15.0	49.2
$\overline{RAR}_{PS}(+L_{rb})$ (%)	0.033	0.033	0.018	0.018	0.009	0.009
$\overline{RAR}_{PS}(-L_{rb})$ (%)	0.057	0.057	0.061	0.061	0.057	0.057
m_t, W_t (kg, lb)	2190	4830	11800	26100	31800	70100
m_t, W_t (trucks)	1	1	5	5	14	14
$d_1(L_u)$ (cm^2, in^2)	4.8	0.7	5.6	0.9	6.0	0.9
$d_1(L_d)$ (cm^2, in^2)	5.7	0.9	7.5	1.2	8.7	1.4
$d_1(L_{rb,u})$ (cm^2, in^2)	5.8	0.9	5.9	0.9	4.9	0.8
$d_1(L_{rb,d})$ (cm^2, in^2)	7.6	1.2	10.8	1.7	12.6	2.0

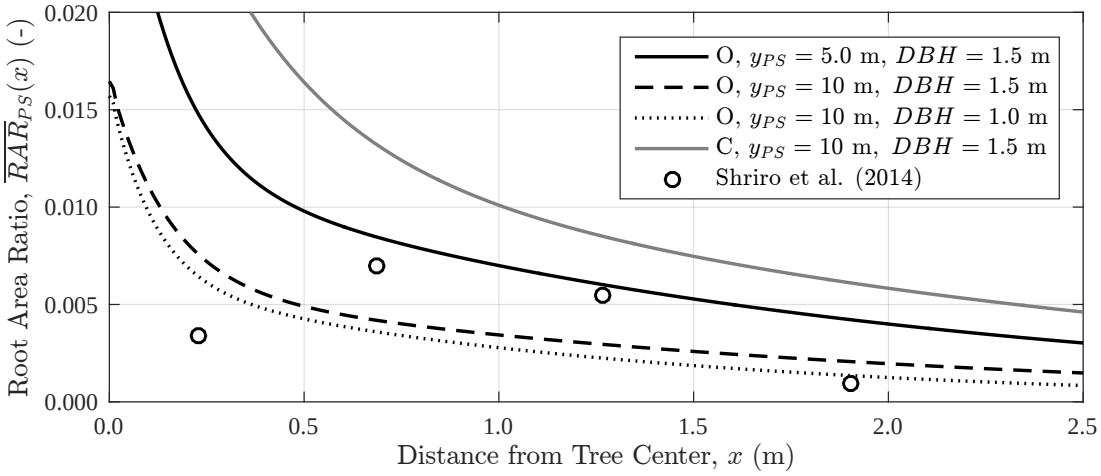

Figure 5.17: Depth-averaged plane-strain root area ratio, $\overline{RAR}_{PS}(x)$, compared to field data of Shriro et al. (2014) for a 1.0–1.5 m *DBH* eucalyptus. Reported data is from root cross sectional area logged in four 1.8 m deep trenches that has been converted to $\overline{RAR}_{PS}(x)$. Biomass model is computed for oak and cottonwood with two tree diameters and plane-strain widths, with solid black line being best estimate of field conditions.

Computed *RAR* is comparable to empirical data reported for California levee sites other than those of Berry and Chung (2013). Gray et al. (1991) and Shields and Gray (1992) measured *RAR* from 1e–5 to 1e–2 in 1 m deep trenches on levees for oak, willow, elderberry, black locust and non-tree vegetation. However, most of the data between 0.1–1.0 m had *RAR* from 1e-3 to 5e-3 (0.1%–0.5%), which is consistent with values outside the biomass model root ball. While the trenches were located along the tree dripline, exact distance from each trunk and *DBH* are not provided and cannot be directly compared to the biomass model. Shriro et al. (2014) recorded root position and diameter in four 1.8 m deep trenches downslope of an approximately 1.0–1.5 m *DBH* eucalyptus tree stump. The data was converted to *RAR* by finding the total root area measured in each trench and dividing by the estimated area, which is equivalent to depth-averaged plane-strain root area ratio from the biomass model, $\overline{RAR}_{PS}(x)$. Figure 5.17 compares computed $\overline{RAR}_{PS}(x)$ of an oak and cottonwood for several combination of *DBH* and y_{PS}. All four estimates for the trench compare well with predicted biomass, although the cottonwood parameters over estimate more than those for oak. The trench data closest to the trunk shows a decrease in biomass, which is likely caused by a lack of large roots near the surface being recorded on the trench profiles. Overall, the biomass model is capable of estimating biomass for real root systems.

Figure 5.18 illustrates plane-strain *RAR* for a 1.0 m cottonwood tree from the biomass model. Contours in the plot represent values that would be measured in a root zone trench through the trunk centerline from upslope to downslope direction ($\hat{x}$). *RAR* decreases from 10% near the origin (contour not visible) to $RAR_{min} = 10^{-4}$ at the maximum root extents (L_u and L_d). The model estimates that *RAR* decreases to the minimum value within 3–9 m of the trunk, depending on the slope direction, which is consistent with empirical data. Note the relatively small diameter of the root ball when compared to the overall size of the root zone; this illustrates the small area over which weight and wind effects are applied versus root reinforcement. Despite asymmetry in the up

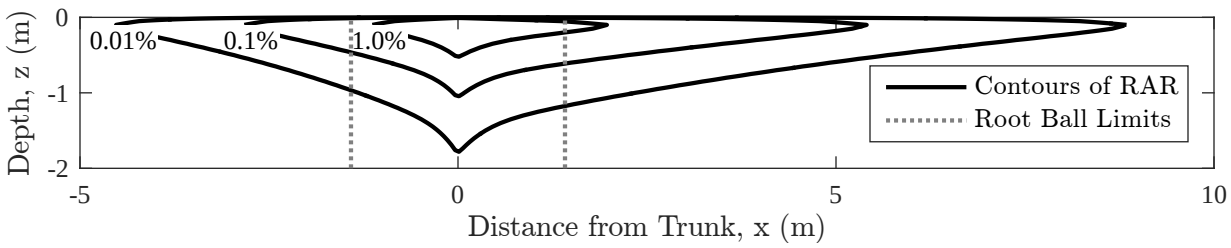

Figure 5.18: Contours of $RAR(x,z)$ for a 1 m diameter cottonwood tree on sloped ground for a plane-strain spacing of $y_{PS} = 15.0$ m and RAR_{min} =1e–4.

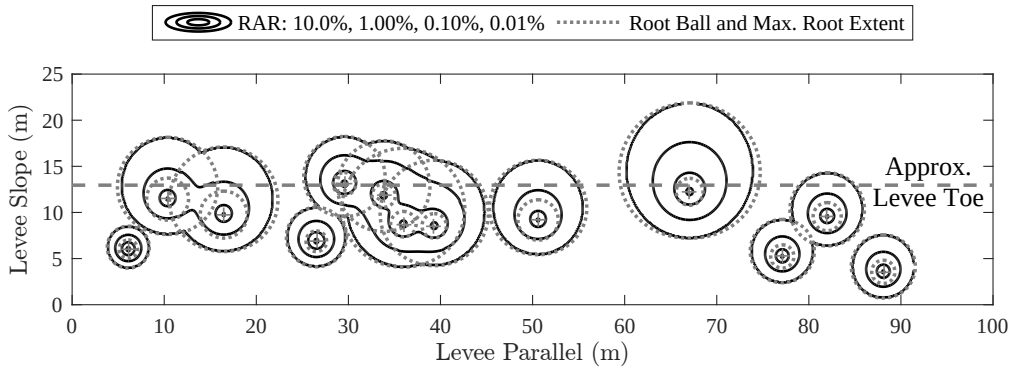

Figure 5.19: Plan view of waterside levee slope at Pocket site illustrating maximum root extent, root ball radius and contours of *RAR* for 13 trees.

and downslope directions, *RAR* is about 1% near the edges of the root ball. Finally, the influence of vertical biomass distribution causes *RAR* to diminish rapidly with depth, especially away from the trunk and out of the root ball. This area is characterized by the presence of a handful of single roots which would be noticeable in an excavation, but have a limited impact on levee performance.

To further illustrate the spatial distribution of root density for various trees, Figure 5.19 is a plot of *RAR* contours for the 13 trees measured along the Pocket Levee waterside slope (*DBH* ranged from 0.2 to 1.1 m). The plan view starts at the waterside hinge where the y-axis is zero, and measures horizontal distance along the slope to the waterside toe, at about 25 m. Maximum root extents are mapped, along with root ball limits; as with the profile view of *RAR*, note the significantly smaller region covered by the root ball compared to the entire root zone. It is also possible to observe the cumulative effect of *RAR* for trees that are spaced close enough to have overlapping roots systems. While the *RAR* increases at these locations (e.g., 32 m along the *x*-axis and 14 m along the *y*-axis), the effect is not large; *RAR* generally does not increase more than an order of magnitude.

Figure 5.19 is especially useful for identifying locations where a potential failure surface may be located. Although the root systems cover a significant portion of the slope, there are definite regions where *RAR* is small nor non-existent and would provide no reinforcing effect to the lateral edge of a failure surface. Alternatively, it is clear that if the top or bottom edge of a failure surface were located along a line of trees (e.g., between 5 to 15 m along the *y*-axis) there would definitely be a reinforcing effect on that surface.

Chapter 6

Influence of Vegetation on Levee Seepage and Stability

Tree objective of the analyses presented herein is to evaluate the influence of root reinforcement, tree weight and wind loading on levee stability. Root reinforcement is determined from root area ratio, whereas weight and wind utilize root volume (Figure 6.1). All computations are performed for each slice in a potential slope stability failure surface. If the slice is determined to be within the root zone of any tree, an evaluation of *RAR* and *RV* is made, subject to the particular settings for root system geometry and vegetation settings. When tree weight and wind forces are determined, the proportion of root volume in any slice relative to the total root ball volume is used to distribute loads (Figure 6.2). Weight and wind loads are only applied within the root ball and are scaled by root volume in the root ball.

6.1 Root Reinforcement

Roots are known to have a reinforcing effect on soil by increasing its compressive and tensile strength, as well as its erosion resistance. Increased soil strength due to roots can be estimated in two ways within a slope stability analysis: increasing the apparent cohesion of a soil layer or applying single root elements within the root zone (equivalent to reinforcing elements in slope sta-

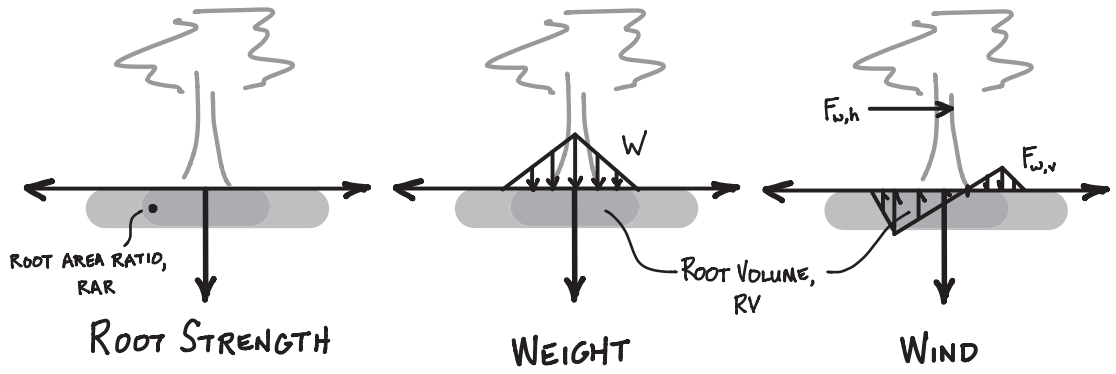

Figure 6.1: Schematic of tree effects on slope stability

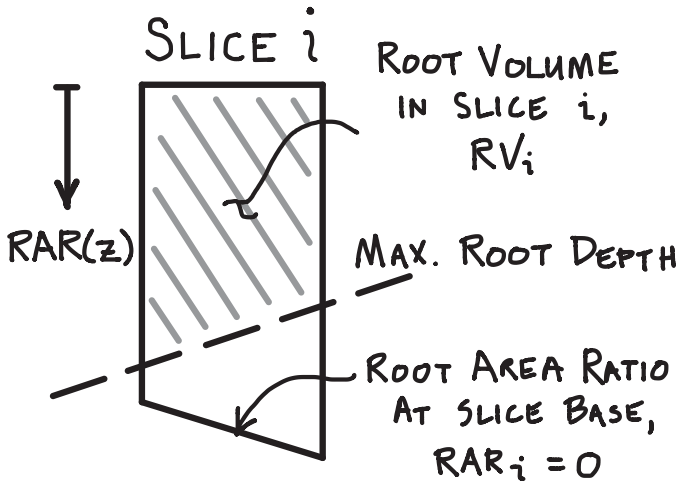

Figure 6.2: Proportion of root volume and root area ratio used for scaling the contribution of weight and wind loads to slice i in a slope stability analysis, represented by hatched area. Root reinforcement is only applied if the slice base midpoint is located within the root zone.

bility literature; e.g., Duncan and Wright (2005)). Cohesion is the simplest method to implement and there are published relationships available relating cohesion to *RAR*; however, it can cause numerical problems within the slope stability algorithm. Single root elements do not cause numerical problems, but it is difficult incorporate the location of the required elements into the soil for a given root zone, as well as determine an appropriate value for those loads. Computing a reinforcement load for an individual root is relatively straightforward given the diameter, species and soil strength; however, the biomass model is based on *RAR* and there are infinite combinations of root diameter with distance from a tree that depend on an assumed number of roots. Although Berry and Chung (2013) report root numbers for surveyed trees, it is difficult to apply this to an individual root-based model for root reinforcement; therefore, a cohesion-based model was selected.

Root density is proportional to the increase in soil cohesion, Δc_R, due to root reinforcement:

$$\Delta c_R = C_R RAR(x,y) \tag{6.1}$$

Where C_R has been reduced to a single value (units of stress) that depends on a variety of factors, including: vegetation species, soil type and moisture content, geometry of root and sliding surface and failure mode of root. Background for this model and appropriate parameter values can be found in Gray and Ohashi (1983), Gray and Sotir (1996), Shields and Gray (1992), Ziemer (1981) and Wu et al. (1979). Although the linear relationship between *RAR* and Δc_R is a simplification of the non-linear relationship between reinforcement concentration and strength increment (Shewbridge & Sitar, 1989), it is considered impractical to develop a more representative relationship in the biomass model. This would require estimates of root diameter and stiffness, for which data is not available to estimate with confidence. Instead, the non-linear relationship is represented by the root reinforcement parameters C_{rb} and C_{po}, described below, which are generally based on the fiber bundle models of Pollen and Simon (2005) and Pollen and Simon (2006). A typical value for C_R is approximately 2300 kPa, as used by Shields and Gray (1992) to analyze sandy levees in the

Central Valley of California with root densities of 640 kg m^{-}3 (40 pcf). Thus, a *RAR* value of 0.01 results in an increased cohesion of 23 kPa (480 psf), which is what would be found near the root ball boundary (refer to Figure 5.18). Although implementation of C_R as a single-valued constant may over simplify the physical problem, modeling C_R as a random variable provides an estimate of its influence on slope stability. Within slope stability computations Δc_R is computed by evaluating $RAR(x,z)$ at the midpoint and bottom of any slice located within a root zone. Consequently, root reinforcement is only included in the analysis when a potential sliding surface intersects the root zone.

A numerical problem is encountered when root reinforcement is included as cohesion in stability computations. Slope stability analyses use Spencer's Method of slices to solve for FS, which is formulated with Mohr-Coulomb model of soil strength, S, with soil parameters cohesion, c', and friction angle, ϕ':

$$S = c' + N\tan\phi' \tag{6.2}$$

Normal force on each slice, N, along with FS, is solved for iteratively as part of the stability algorithm. When cohesive soils (i.e., $c' > 0$) are included near the surface of a slope and N becomes small due to low overburden, stability computations can produce negative normal forces. This can prevent the stability algorithm from converging on a solution for N and FS, and also implies tension between slices at the top of the slope. Fortunately this issue is most common with very shallow surfaces, which are a small subset of failure geometries that generally unlikely to cause complete levee failure (e.g., the non-linear surface in Figure 4.3). Despite this, the numerical issue must be prevented to understand the incremental effect of vegetation on levee stability.

Soil is typically considered incapable of supporting tensile loads, and a common practice is to truncate the sliding surface such that tensile forces do not occur, referred to as a tension crack (Duncan & Wright, 2005). Rankine active earth pressure theory is used to estimate the maximum possible crack depth by solving for the depth where horizontal stresses are zero (i.e., the transition from tension to compression forces):

$$z_{crack} = \frac{2c}{\gamma\tan(45-\phi/2)} \tag{6.3}$$

An alternative solution is to eliminate strength when tensile forces are present (Duncan & Wright, 2005) by which tension can occur in soil. This is problematic because the inability of (rootless) soil to carry tension is used to justify the two solutions to the numerical problem, which no longer applies. Fortunately, the physical characteristics of root reinforcement can be used to justify limits on Δc_R, preventing a majority of numerical issues in addition to addressing the shortcomings of a linear reinforcement model.

Roots are limited in their capacity for soil reinforcement by failing in two modes: rupture, when the maximum strength of individual roots is exceeded; and pullout, when shear resistance of the bond between root and soil is exceeded. Rupture is governed by tensile strength of the root, whereas pullout is controlled primarily by properties of the soil (Waldron & Dakessian, 1981); specifically shear strength and moisture. Pollen and Simon (2005) provide good background on the various root models and their deficiencies. Large roots are certainly capable of resisting significant tensile forces; however, the relatively shallow depth of large roots makes mobilization of entire capacity unlikely. Further justification comes from maximum rooting depths on the order of 2m and the local variations in actual failure surface geometry that are capable of finding a path to avoid

the largest roots. Parameters C_{rb} and C_{po} are defined as limiting values for Δc_R and are introduced to account for the limiting effect of reinforcement due to rupture (i.e., root breakage, "*rb*," or rupture) and pullout ("*po*"), respectively. C_{rb} is the maximum stress that can be added to the soil before root rupture would occur, whereas C_{po} is a fraction of the estimated vertical effective stress, defined by the following equation:

$$C_{po} = f \cdot \sigma'_v = f \cdot (W_i - u_i) \tag{6.4}$$

Subscript i indicates the weight and pore pressure (W and u) are found for an individual slice.

Although a proportional coefficient for C_R over estimates root reinforcement due to the assumption that all roots are perpendicular to the shear surface and break simultaneously (Pollen-Bankhead et al., 2013) and by ignoring pullout (Sonnenberg et al., 2011), the root limits C_{rb} and C_{po} provide a mechanism for limiting the unrealistic values of Δc_R. However, lack of available data and numerous influencing factors make it difficult to set appropriate values. Various estimates are available for small roots, for example, Waldron and Dakessian (1981) measured reinforcement of around 2.5 kPa in saturated clay loam, limited by pullout failure of the 2 mm diameter (average) roots. Pollen and Simon (2005) considered both failure modes and found a maximum reinforcement of 5 kPa for roots under 1 cm in diameter. Pollen and Shields (2007) applied maximum root reinforcement of 0.84–20 kPa to low cohesion silty sand channel slopes with vegetation conditions varying from grass to mature trees. These are lower values than would be realized in the high *RAR* zone near the trunk and ground surface, so care must be taken to prevent Δc_R from being too low. Therefore, C_{rb} and C_{po} parameters are only used to limit tension forces when numerical issues prevent FS from being computed. When C_{rb} and C_{po} are applied the complete root reinforcement model is defined by Equation 6.5:

$$\Delta c_R = \begin{cases} C_{po} \cdot \sigma'_p, & \text{if } C_R \cdot RAR(x,y) > C_{po} \cdot \sigma'_p \\ C_{rb}, & \text{if } C_R \cdot RAR(x,y) > C_{rb} \\ \min\{C_{po}, C_{rb}\}, & \text{if } C_{po} \text{ and } C_{rb} \text{ apply} \\ C_R \cdot RAR(x,y), & \text{otherwise} \end{cases} \tag{6.5}$$

These limits can dramatically influence computed FS and should be used with caution. Numerical issues generally occur for very shallow slices and that are located close to the trunk center where *RAR* is relatively high. As will be seen, it is relatively easy for a slope failure surface to avoid zones of high cohesion which results in a lower computed FS; it is not realistic to force a potential sliding surface through a high root density zone. Thus, root reinforcement limits can be applied within reason despite a lack of data as long as a new minimum FS surface is found relative to the non-vegetation case. Furthermore, since root reinforcement has a positive effect on stability and C_{rb} and C_{po} scales the magnitude of ΔFS, root limits provide a conservative estimate of FS for slope stability.

In summary, *RAR* can adequately capture soil reinforcement due to roots with a linear model, although numerical problems may occur when Δc_R causes tension at the top of the sliding surface. There is clear physical justification for limiting root reinforcement to mitigate the problem in high *RAR* zones near the trunk and near the ground surface, especially when vertical effective stress is low due to rupture and pullout failure of roots. Unfortunately there is insufficient data to set the limiting values for every case; however, the parameters are easily applied when needed to allow computation of FS.

6.2 Tree Weight

Due to the small proportion of root volume at large distances from the trunk, it is inappropriate to apply tree weight across the entire root zone of a tree. The root ball is used as a structurally significant zone where most of the tree loads are concentrated; since it marks the limit where trees pulled out of the ground, it should be close to the zone over which they transfer loads into the ground. Root ball radius is used to represent the area where tree weight (and wind) forces are applied to the soil. Total tree weight is computed from mass, $W_t = g \cdot m_t$, and is applied to a particular slope stability slice as a proportion of root volume within slice i to total root volume in the root ball, RV_{rb}:

$$W_i = W_t \frac{RV_i}{RV_{tot}} \tag{6.6}$$

Given the exponential decay of root density with distance, most of the total weight is applied near the trunk center. Weight is divided by plane-strain spacing, y_{PS}, when applied in the slope stability analysis. Since root volume is a relatively smooth function it better represents reality than a single line load. Furthermore, a smooth function avoids numerical issues that may occur due to discontinuities from a single line load during minimum FS searches or reliability analyses.

6.3 Effect of Root Reinforcement and Weight on Stability

Incremental effects of a tree on safety factor are evaluated using two strategies: the tree location is fixed and the biomass parameters are varied; and, the biomass parameters are fixed and tree location is allowed to vary. A 1 m diameter cottonwood is used as a base case scenario, using a plane-strain tree spacing of 15 m. Since the lateral maximum root extent for a tree of this size is 13.7 m, the spacing is analogous to a case where a majority of the levee has roots present, but there is no overlap between the root zones of adjacent trees.

Figure 6.3 shows how FS is changed for the landside hinge circle (minimum FS) given 4 different diameter cottonwood trees located 1 m downslope of the landside levee hinge (the landside hinge has a X-coordinate of 80 m). The smallest tree (0.5 m) has a small positive effect and the largest tree (2.0 m) has a larger negative effect; the 1.0 m tree has a nearly neutral effect. As hydraulic loading increases the magnitude of change to FS decreases. Incremental change in FS is 0.1–0.2.

A similar analysis is presented in Figure 6.4 for four additional slip surface types. The tree size increases stability for the shallow and wedge surfaces (plots c and d), with the opposite (and much smaller magnitude) true for the entire crest failure (b). Although only the circular failure surface is shown in Figure 6.4b, the same behavior was observed in the non-circular case. For the lower water levels and landside hinge non-circular surface (plot a), FS increases with tree size; however the trend changes for higher water, and FS cannot be computed, which is problematic. This is an example of tensile stresses near the crest preventing convergence of the stability algorithm, caused by root reinforcement of the tree. This is a scenario when root reinforcement limits can allow Spencer's method to converge. The magnitude of ΔFS is greatest for the surface with the smallest cross-sectional area, which is a two-part effect. Shallow surfaces have higher root density and any reinforcement has a larger relative impact on strength. An additional consideration is that tree weight with respect to overall sliding mass. For the complete crest circle a negligible root

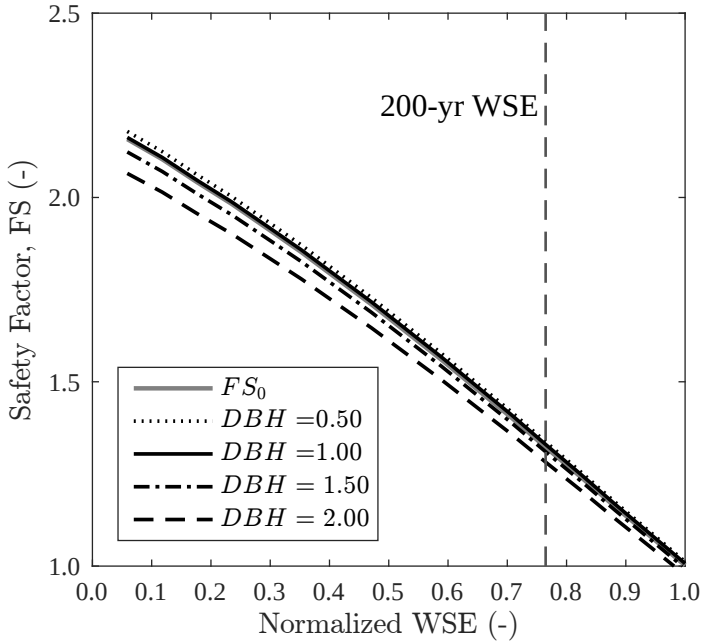

Figure 6.3: Slope stability FS for landside hinge sliding surface and a 0.5–2 m *DBH* tree located 1 m downslope from hinge (X_{tree} = 81 m). Computed with $y_{PS} = 15$ m. Root reinforcement produces net positive effect due to tree when *DBH* is 0.5 and 1.0 m, with weight increasing and causing net negative effect when *DBH* is 1.5 and 2.0 m.

density influences stability, and ΔFS is entirely due to weight, which is small. Further insight can be gained by separating these effects.

Influence of tree location is shown in Figure 6.5, found by changing the position of various diameter trees from waterside slope to beyond the landside toe. Plots in the left column include root reinforcement and weight while plots on the right have root reinforcement removed for different failure surfaces: complete crest wedge (e), landside hinge (a) and complete crest circle (c), in order of largest to smallest vegetation effects. Deeper sliding masses are affected less by the tree due to root reinforcement and weight having a smaller impact. No decrease in FS occurs for the wedge surface; this is a result of the planar geometry, which precludes a change in moment when tree weight is incorporated into the analysis. This is also observed to a lesser extent in other non-circular surfaces where the upper sliding surface is located within the cohesionless soil layer in the embankment.

In general, a tree has a effect on computed FS as the root zone approaches the entry or exit point for each circle. The exponential increase in ΔFS is related to increasing *RAR* at the sliding surface edge, and maximum increase in FS occurs when the tree is located directly on the circle entry/exit. This is due to the influence of cohesion in the root zone, and the computed values of FS asymptotically approach $+\infty$, which is not realistic. All sliding surfaces considered show this effect. As the tree increasingly overlaps upslope sliding surface (i.e., left edge) a negative influence on FS is seen, caused by the reduction in root reinforcement and increasing influence of weight.

The right side of Figure 6.5 has ΔFS with only weight considered, which has an effect on the two circular surfaces, decreasing FS by about 0.10 and 0.02 when near the crest and increasing FS by 0.2 and 0.1 when near the toe for shallow and deep circles, respectively. Figures 6.5f illustrates the negligible influence weight has on planar failure surfaces. When the tree is located within the sliding mass near the levee crest there is a negative effect on stability due to an increase in driving force, whereas the opposite is true on the downslope end. For each case the positive effect of

weight, i.e. a combined effect of resisting force and increased soil strength, is greater in magnitude than the negative effect. Although the sliding surface might be of similar depth at the top and bottom of the slope, high pore pressures in the blanket layer reduce effective stress and thus affect the strength more near the levee toe. Thus, the applied tree weight increases FS more in this area. All weight is applied through the root ball, which causes a linear increase in FS as the root ball moves downslope and is entirely within the sliding mass. The neutral point occurs when the tree is located below the radius origin for the circular surface, as no moment is applied to the sliding mass at this point. Weight does not have an influence on the wedge surface because moments have no effect on the stability of a planar wedge and the increase in weight results in a counteracting increase in strength.

Root reinforcement limits, C_{rb} and C_{po}, are applied to the tree position analyses and are presented in Figure 6.6. C_{rb} is set to 23 kPa and is an independent maximum value placed on Δc_R. For reference, this value represents the root reinforcement expected where RAR is about 1%, which is near the root ball area of a tree (Figures 6.6a, c and e). C_{po} limits Δc_R to a fraction of vertical effective stress, in this case 1.0 (Figures 6.6b, d and f). Both parameters are effective at limiting the dominating (and unrealistic) asymptotic effect of root reinforcement. The peaks near sliding surface entry and exit are still present, and they are much less pronounced; although still a noticeable effect, weight has taken a larger share of the vegetation effect.

Slope stability analyses with root reinforcement limits removed illustrates the significant effect on FS by the cohesion term C_R. Although results show the numerical effect of these parameters in preventing unrealistic results, in reality a lower FS sliding surface exists within close proximity to the surface. As such, the true estimate of ΔFS can be found by fixing tree location and performing a search for minimum FS using the biomass model.

Minimum Safety Factor Surface with Vegetation

A critical component of geotechnical slope stability analyses is finding the potential sliding surface with the minimum safety factor given a set of conditions. Once found, sensitivity studies can be performed to evaluate the effect of changing parameters. This approach is sufficient when parameters are applied to soil layers that contain large portions of the minimum FS surface because a changed value has a consistent effect on all surfaces with similar geometry. This is not the case when vegetation is considered on a slope, as tree effects are concentrated in a relatively small area relative to sliding surface extent. Previous discussion has considered the numerical effect on FS when trees are added in various locations on the slope and sliding surfaces are defined relative to the non-vegetation case. The true assessment of ΔFS, however, is found by comparing ΔFS between the minimum FS surface without vegetation, F_{min}, and the new minimum FS surface when vegetation has been added to the slope, $FS_{min,V}$. Although circular surfaces can capture some of these effects, the flexible geometry of non-circular surfaces is capable of finding lower $FS_{min,V}$; however, the planar geometry and shallow depth found in non-circular surfaces requires limits for root reinforcement.

Figures 6.7–6.9 present three suites of results that are representative of the interaction between FS_{min} and $FS_{min,V}$, circular and non-circular surfaces and four tree scenarios. For each suite of analyses subfigures (b)–(d) compare FS_{min} and $FS_{min,V}$ surfaces for the tree scenario shown, which are shown in combination on subfigure (a) compares all surfaces. Root reinforcement and weight effects are applied to the slope for a 1 m DBH cottonwood in all cases with $z_{max} = 1$ m and

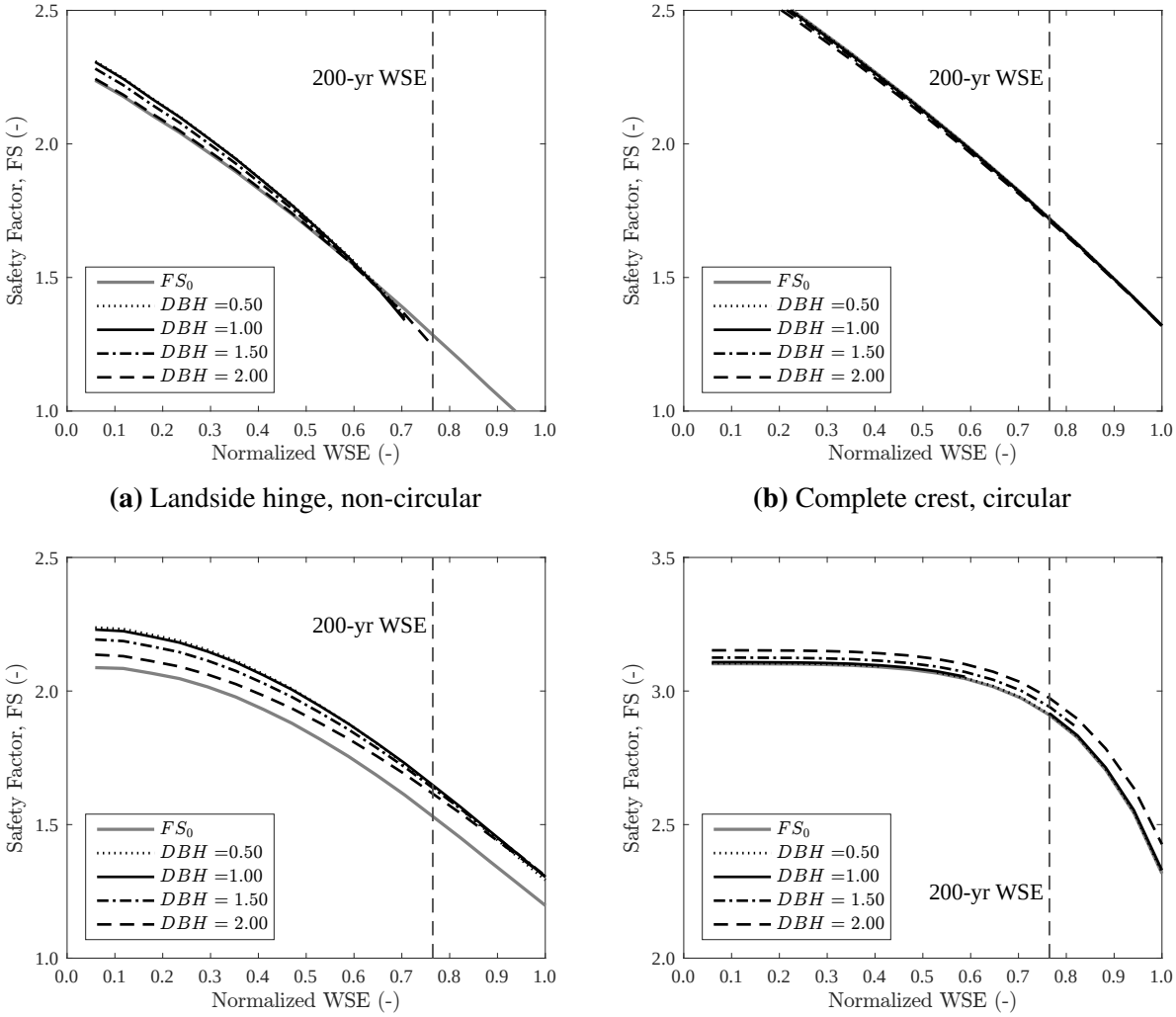

(a) Landside hinge, non-circular

(b) Complete crest, circular

(c) Shallow circular cosmetic surface

(d) Wedge, complete crest

Figure 6.4: Slope stability FS for 4 sliding surfaces and a 0.5–2 m DBH tree located 1 m downslope from hinge ($X_{tree} = 81$ m). Computed with $y_{PS} = 15$ m.

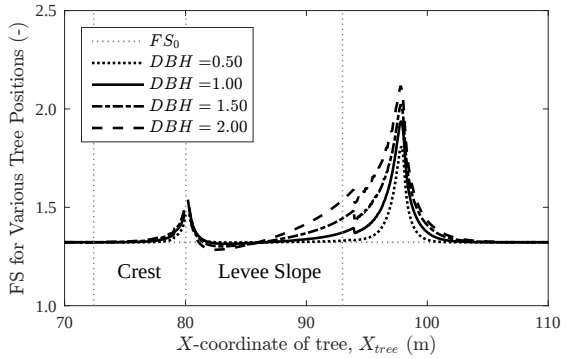

(a) Landside hinge, circular

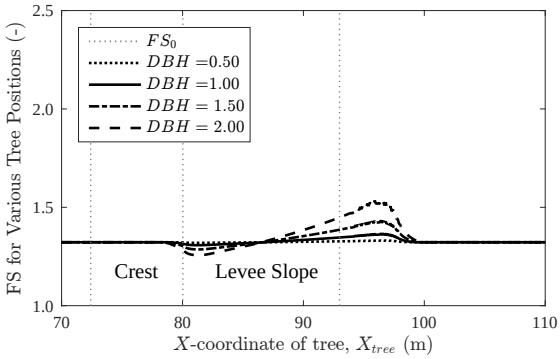

(b) Landside hinge, circular; weight only

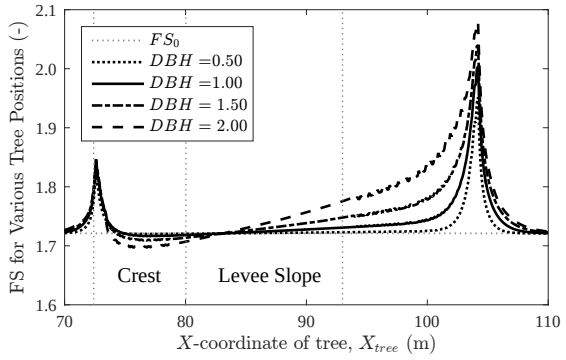

(c) Complete crest, circular

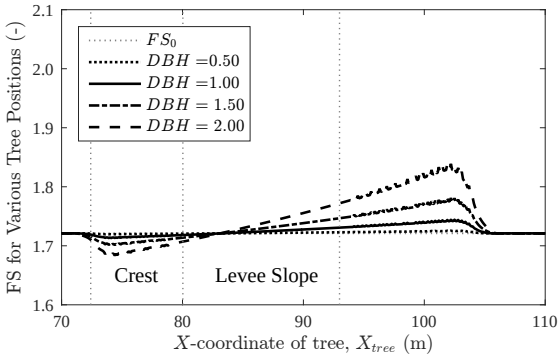

(d) Complete crest, circular; weight only

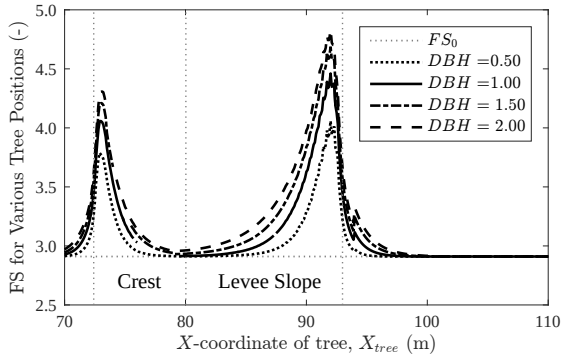

(e) Complete crest, wedge

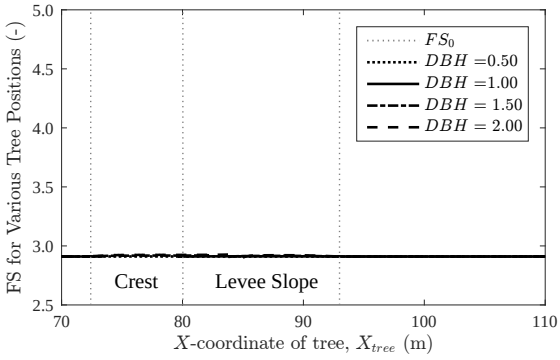

(f) Complete crest, wedge; weight only

Figure 6.5: Slope stability FS for four sliding surfaces and a 0.5–2 m DBH with tree position varied. Results in a, c and e include root reinforcement, Δc_R, and weight, W_t; b, d and f only include weight. Computed with $y_{PS} = 15$ m. Scale of FS is the same as for wind loading in Figures 6.10a–6.10d.

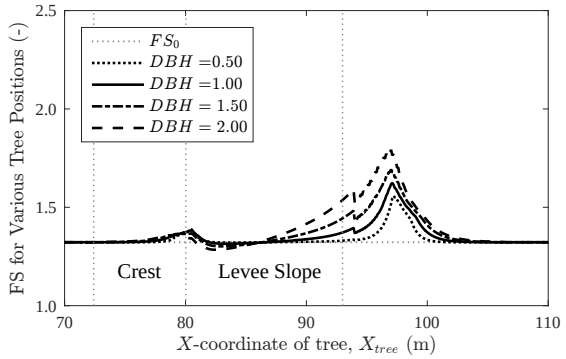

(a) Minimum FS, circular; $C_{rb} = 23$ kPa

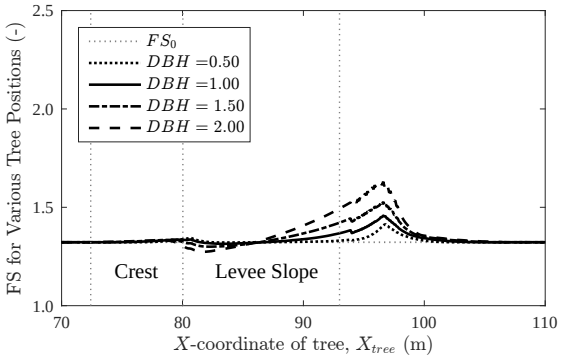

(b) Minimum FS, circular; $C_{po} = 1.0$

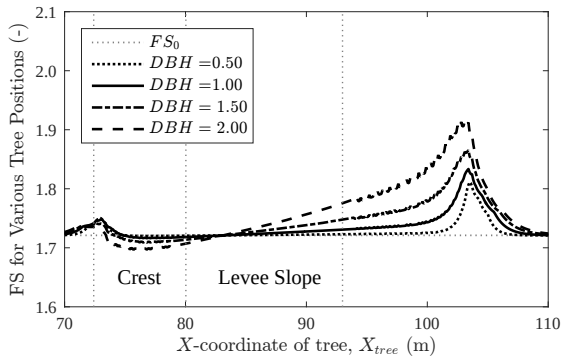

(c) Complete crest, circular; $C_{rb} = 23$ kPa

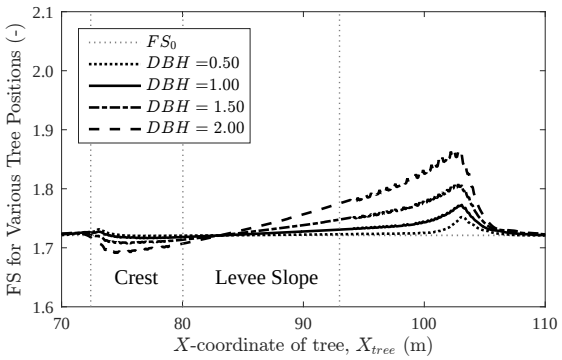

(d) Complete crest, circular; $C_{po} = 1.0$

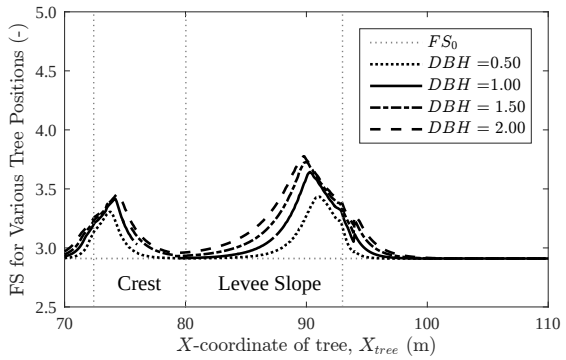

(e) Complete crest, wedge; $C_{rb} = 23$ kPa

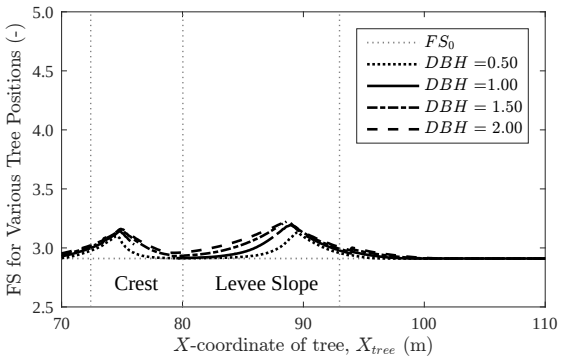

(f) Complete crest, wedge; $C_{po} = 1.0$

Figure 6.6: Slope stability FS with reinforcement limits for four sliding surfaces and a 0.5–2 m DBH with tree position varied. Results in a, c and e use root breakage limit $C_{rb} = 23$ kPa; b, d and f use pullout limit $C_{po} = 1.0$. Computed with $y_{PS} = 15$ m. Scale of FS is the same as for wind loading in Figures 6.10a–6.10d.

$y_{PS} = 15$ m located at $x_{tree} = 81$ m (1 m from landside hinge), 86.5 m (slope midpoint), 93 m (toe) or at all three locations. Maximum root extent is illustrated by the shaded area within the contour of RAR_{min} =1e–4, along with a darker zone illustrating root ball limits; the tree itself is not drawn to scale. Results of FS on each figure report the minimum FS surface found with no tree considered ("no tree, FS_{min}"), the same surface considering the tree scenario shown (i.e., no new search; FS_{min}) and the minimum FS surface found considering the tree scenario shown ($FS_{min,V}$). In all cases the most important observation is that new minimum FS surfaces do not change significantly for the tree scenarios considered, and differences between all three values computed for FS are small, generally $|\Delta FS| < 0.1$, with a few exceptions.

Tree effects increase FS for all locations when evaluating stability with circular surfaces, although the maximum increase is only $\Delta FS = +0.043$ for a tree located at the levee toe. The minimum FS search produces a ΔFS for $FS_{min,V}$ on the order of 0.01 below the original minimum FS surface. Tree location has a significant influence in the small values observed for ΔFS, since only small adjustments in the circular geometry are necessary to move away from the root ball. This effect is most clearly illustrated in Figures 6.7b and 6.7d, where the tree is located close to the surface. For the mid-slope case the change in sliding surface is negligible because root reinforcement is not a factor. As such, there is only a small increase in FS of 0.005 due to weight. The FS computed without vegetation for each $FS_{min,V}$ surface in subfigures (b)–(d) is 1.338, 1.324 and 1.328, greater than FS_{min} by a maximum of $\Delta FS = 0.016$.

When non-circular surfaces are considered stability is only improved when the tree is located at the toe, in this case by $\Delta FS = +0.043$. In this case the geometry changes more significantly than the circular surface, as it is topologically capable of completely avoiding the entire root zone of the tree, following the contour of RAR_{min} =1e–4 closely. Furthermore, $FS_{min,V}$ is 1.328 for the non-circular case, which is lower than $FS_{min,V}$ =1.365 for the circular case. Although the non-circular sliding surface does not enter the root zone, the tree still has an effect on the slope by forcing the minimum FS surface to a more stable condition.

Stability is negatively impacted when the tree is higher on the slope, decreasing by 0.078 when located at the hinge and 0.040 at the slope midpoint as a result of weight. The surface completely avoids the root zone of the tree at the slope midpoint, thus there is no root reinforcement effect. There is little difference in geometry between minimum FS surfaces, but it is sufficient to cause a completely different levee response, as the FS_{min} case has an increase in FS of 0.003. As shown in the previous section, weight has little impact on the landside hinge surface when the tree is located near the slope midpoint. However, when the sliding surface is allowed to vary, only a small adjustment is necessary to maximize the effect of weight as a driving force on the sliding mass and result in a lower value for $FS_{min,V}$.

A more significant change in geometry is found for the non-circular case when the tree is at the levee hinge. The surface cannot completely avoid the root zone, but it does move away from the root ball, avoiding the highest zone of root reinforcement. Root reinforcement plays a significant role in this scenario, as $FS_{min,V}$ cannot be computed without a tree. Computations fail when C_R in the first slice falls below about 20 kPa ($C_{po} \lesssim 6$), implying a high tensile strength in the smallest portion of the sliding mass that is likely not realistic. If C_{po} is reduced, the non-circular failure surface search produces a shape that becomes more non-linear as the upper end avoids the high RAR zone, causing additional problems in the method of slice computations. Furthermore, computation of FS using the FS_{min} surface is only possible with $C_{po} \gtrsim 0.75$, as the applied C_R is too high near the trunk center. It is impossible to determine an appropriate limit for root reinforcement

when the tree is located within shallow stability slices at the top of a slope without assuming the number and size of individual roots. However, it is clear that despite root reinforcement, tree weight causes a slight decrease in FS when located at the top of the slope.

Evaluating three trees on the levee at once produces the most dramatic changes in sliding surface geometry, with circular and non-circular cases moving deeper to avoid root reinforcement at the entry and exit points and shallow locations on the slope. Overall stability is increased in every case, which is a logical result considering the positive effects of trees located at the levee toe are generally greater than the negative effects at the hinge. Reported $FS_{min,V}$ are lower than FS_{min} by 0.050 for the circular surface and 0.190 for the non-circular case, the most significant difference in the suite of analyses described in this section. Given the plane-strain condition of $y_{PS} = 15$ m and inclusion of three large trees on the levee slope, this scenario represents a highly vegetated condition. Thus, it seems that an upper limit for ΔFS due to root reinforcement and weight is on the order of +0.1 for landside slope failures.

Results reported in Figure 6.9c illustrate the influence of root reinforcement with respect to overall levee stability. The $FS_{min,V}$ surface finds the least stable condition by avoiding root reinforcement at the top of the slope, which is limited by $C_{po} = 1$ to allow a solution to be reached for the FS_{min} surface. With respect to the no vegetation case of $FS_{min} = 1.285$, a maximum increase on the order of 0.2 is computed. If root reinforcement is eliminated entirely, $\Delta FS = +0.049$, due entirely to weight. Thus, selection of C_{po} effectively scales the magnitude of the predicted positive effect on stability for the three tree scenario. Unfortunately an assessment of root number and diameter must be made to determine an appropriate value for this increase.

When the sliding surface is forced to exit the levee toe it cannot avoid the root zone as effectively as the other surfaces considered. Given the relatively low soil mass represented by this geometry, problems with high tensile stresses due to root reinforcement become more problematic. As reported in Figure 6.9d, C_{po} must be set to 1 to obtain a solution, with ΔFS limited to +0.006 if root reinforcement is eliminated entirely. As described above, while C_{po} allows computation of a solution, it directly controls FS through C_R.

Evaluating the change in minimum FS surface due to root reinforcement and weight illustrates the change in FS due to trees, as well as behavior of the biomass model when included in slope stability analyses. Relatively small changes in surface geometry can significantly reduce the magnitude of computed vegetation effects relative to a fixed surface analysis. A smaller, but still significant reduction is found even when only the root ball can be avoided. This observation has implications for understanding the interaction of the root zone and 3D sliding surface geometry on the levee slope. Even though tree crowns may be closely spaced in a dense tree arrangement, the root ball extents are much smaller (see e.g., Figure 5.18) and a critical sliding surface could easily find a path of least resistance between them. Although it is expected the response would be similar for sliding surfaces with higher mass (i.e., the complete crest case), the magnitudes of ΔFS found in this section would be greatly reduced.

6.4 Wind Loading and Effect on Stability

Wind loading is dependent on tree size and wind velocity and is transferred to the slope through the root system. Because the acting location of the load is above ground (i.e., somewhere in the canopy) and the tree is not rigid, wind also applies a moment to the soil. Wind loads are transferred

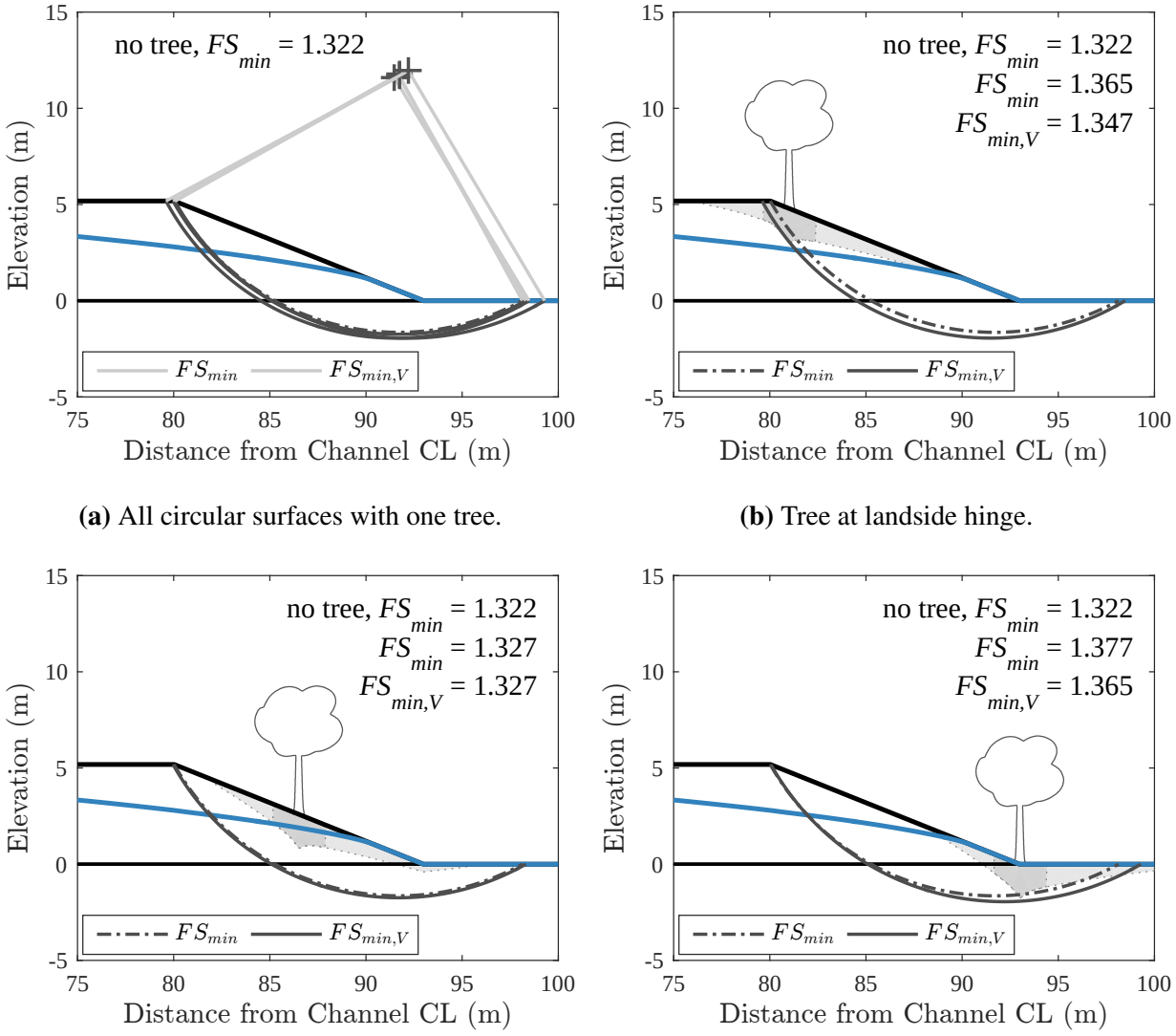

(a) All circular surfaces with one tree.

(b) Tree at landside hinge.

(c) Tree at slope midpoint.

(d) Tree at toe.

Figure 6.7: Minimum FS circular surfaces for 1 m *DBH* cottonwood on crest, slope or toe. Computed with $z_{max} = 1$ m, $y_{PS} = 15$ m for root reinforcement and weight effects. FS_{min} is the minimum FS circular surface found without vegetation effects, computed with and without the tree condition shown. $FS_{min,V}$ is the minimum FS surface found with the tree condition shown. Maximum root extent is represented by shaded contour of RAR_{min} =1e–4 and root ball by darker shaded region. Tree not drawn to scale.

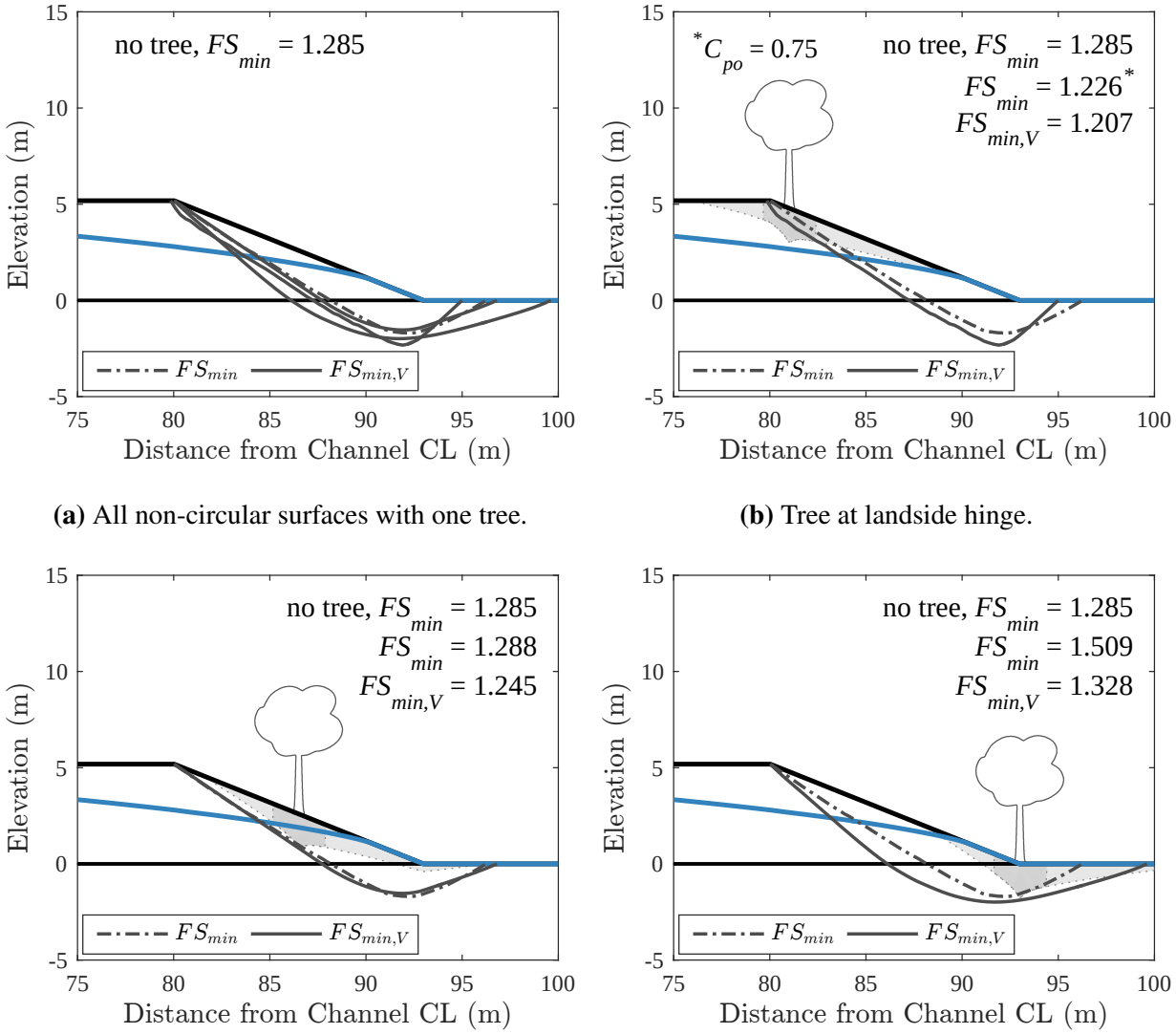

(a) All non-circular surfaces with one tree.

(b) Tree at landside hinge.

(c) Tree at slope midpoint.

(d) Tree at toe.

Figure 6.8: Minimum FS non-circular surfaces for 1 m DBH cottonwood on crest, slope or toe. Computed with $z_{max} = 1$ m, $y_{PS} = 15$ m for root reinforcement and weight effects. FS_{min} is the minimum FS non-circular surface found without vegetation effects, computed with and without the tree condition shown. $FS_{min,V}$ is the minimum FS surface found with the tree condition shown. Value of C_{po} reported when necessary to obtain solution for FS. Maximum root extent is represented by shaded contour of RAR_{min} =1e–4 and root ball by darker shaded region. Tree not drawn to scale.

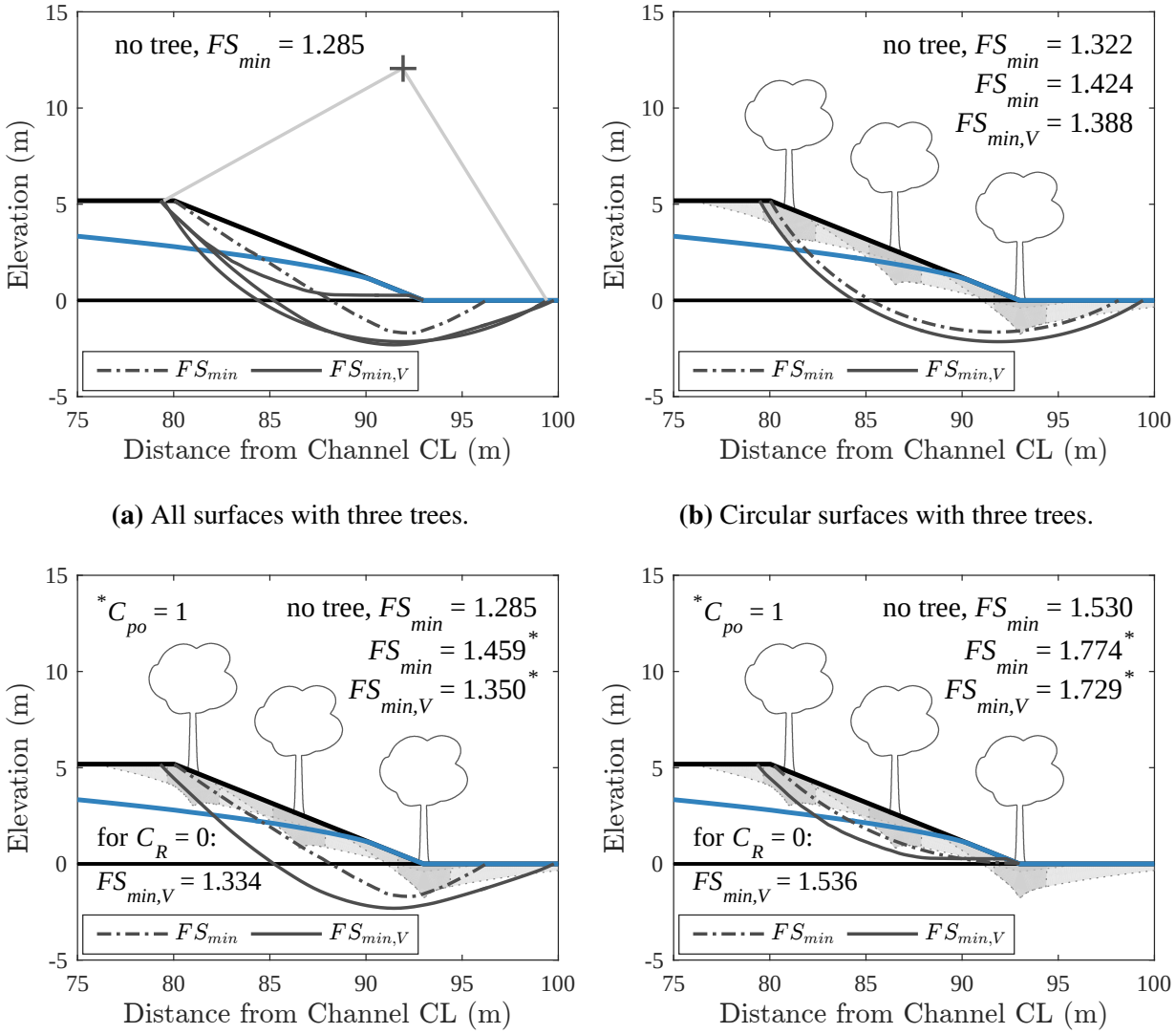

(a) All surfaces with three trees.

(b) Circular surfaces with three trees.

(c) Non-circular surfaces with three trees.

(d) Shallow surface exiting toe with three trees.

Figure 6.9: Minimum FS surfaces for 1 m DBH cottonwood on crest, slope and toe. Computed with $z_{max} = 1$ m, $y_{PS} = 15$ m for root reinforcement and weight effects. FS_{min} is the minimum FS surface found without vegetation effects, computed with and without the tree condition shown. $FS_{min,V}$ is the minimum FS surface found with the tree conditions shown. Value of C_{po} reported when necessary to obtain solution for FS. Maximum root extent is represented by shaded contour of RAR_{min} =1e–4 and root ball by darker shaded region. Tree not drawn to scale.

to the relatively stiff part of the root system, the root ball (as with weight; Figure 6.1), and can be separated into a horizontal force due to the wind itself and vertical forces due to the overturning moment transferred from tree to soil by the roots (Figure 6.1).

A typical approach for estimating wind load would require canopy area, drag coefficient and wind velocity for a tree (Coder, 2014; Stathers et al., 1994; USACE, 2011). Once these parameters are estimated a horizontal load can be estimated along with an equivalent moment if an acting height is assumed. Unfortunately, the parameters required to complete the analysis for this research are difficult to estimate using allometric relationships, even if they were well supported by existing data. As an alternative, critical moment data from Peterson and Claassen (2012) can be used as an upper limit to wind loads, which were calculated from winching tests discussed above. Critical moment, M_{crit}, represents the ultimate load a tree can transmit to the soil before failing in windthrow, after which it is no longer capable of transferring wind loads to an embankment. As illustrated on Figure 5.11, a crude upper bound to wind load is $M_{crit} = 1000 \cdot DBH$, measured in kN−m (per 1 m width). While some data are above this ratio, the majority are below, with every result greater than $M_{crit} = 100 \cdot DBH$. In general, M_{crit} is closer to 100 kN-m for DBH below 0.5 m. The parameter C_w is defined as the moment coefficient for wind, relating DBH to moment applied to a slope due to wind load, having units of [kN] (per 1 m width): $M_w = C_w \cdot DBH$. Using M_w to evaluate the effect of wind loads on levee stability is similar to the deterministic approach for setting WSE at a high level, since it assumes an event has occurred when performing computations. As such, FS with wind load effects can be considered the worst-case scenario for a levee when subjected to a wind velocity that causes uprooting for the specified tree.

Data related to stresses in a root system subjected to external loads is sparse. In general, it is difficult to obtain data experimentally, as strain must be actively measured in roots during winching tests (Watson, 2000); although Stokes (1999), for example, was able to obtain strain data illustrating the formation of tension and compression zones. Coder (2010) and Coder (2014) summarize available data and provide guidance for wind loading computations, although emphasis in the literature is on evaluation of tree failure rather than load transfer to a slope, as needed for this research.

To quantify wind loads in slope stability analyses using a method of slices, $F_{w,h}$ and $F_{w,v}$ must be computed for any slice i intersecting the root ball of a tree, denoted $F_{w,h,i}$ and $F_{w,v,i}$. The force on each slice is computed using an assumed distribution within the root ball. Horizontal loads are found from the following equations, which require an assumption for acting heigh, h_w:

$$F_{w,h} = \frac{M_w}{h_w} = \sum_i F_{w,h,i} \qquad\qquad F_{w,h,i} = F_{w,h} \frac{RV_i(\Delta x_i, y_{PS}, \Delta z_i)}{RV_{rb}} \tag{6.7}$$

where RV_{rb} is total root volume in the root ball and $RV_i(\Delta x_i, y_{PS}, \Delta z_i)$ is the fraction of root volume in slice i , resulting in the higher horizontal loads near the trunk that decrease towards the root ball edge. Root volume is integrated over slice width Δx_i and depth Δz_i, measured vertically from the midpoint and bottom of slice i. Vertical forces are computed from overall wind moment using several possible shapes of distributed load, $f_{w,v}(x)$. All distributions are applied such that the vertical forces sum to zero and are equivalent to the total wind moment:

$$F_{w,v} = \sum_i F_{w,v,i} = 0 \qquad\qquad M_w = \int_{-L_{rb}}^{+L_{rb}} x f_w(x)\, \mathrm{d}x = \sum x_{r,i} F_{w,v,i} \tag{6.8}$$

where $x_{r,i}$ is the moment arm of each force relative to the trunk for slice i. The vertical load applied to each slice is found by integrating the distributed load across slice width Δx_i and scaling by vertical biomass using the *RAR* density function:

$$F_{w,v,i} = \int_{\Delta z_i} f_{RAR}(z)\,\mathrm{d}z \cdot \int_{\Delta x_i} x f_{w,v}(x)\,\mathrm{d}x \tag{6.9}$$

Because the density function $f_{RAR}(z)$ integrates to 1 over z_{max}, integrating over Δz_i is the fraction of biomass in slice i relative to the entire root zone at x_i. While Equation 6.9 should be normalized to z_{pit} instead of z_{max}, given the rapid decay of *RAR* with depth the quantitative difference does not warrant incorporating an extra paramter and computations into the biomass model. Furthermore, consistent application of $f_{RAR}(x)$ across the root zone implies the computed proportionality is consistent for biomass fraction in the root ball. All wind forces are applied at the midpoint of each slice in the horizontal and vertical plane when the slice is within the root zone. If the slice base is below the root zone wind forces are applied at $\Delta z_i/2$. Note that vertical forces due to the overturning moment balance to zero; however, the vertical force magnitude on each slice in a slope stability analysis will influence the safety factor, especially if only part of the root ball overlaps the sliding surface analyzed.

Wind is a rapid loading phenomenon, as maximum wind gusts generally only occur for a few seconds at a time (Oliver & Mayhead, 1974), typically 1.5–2.0 times the sustained average wind speed (Coder, 2014). Furthermore, the natural frequency of oscillation for a tree makes it sensitive to short gusts with respect to windthrow failure (see e.g., Stathers et al., 1994). As such, wind acts like an undrained loading condition for soil, although that term is avoided to prevent confusion with other methods of standard geotechnical practice. The slope stability algorithm used for analyses herein was modified to conservatively ignore the increase in soil strength due to wind. In other words, $F_{w,h}$ and $F_{w,v}$ should be incorporated into the limit equilibrium equations as external forces which interact with normal and interslice forces, but should not allowed to modify soil strength. Unfortunately, within the method of slices normal forces are dependent on external loads and are also used in strength computations. To isolate these effects the algorithm for simultaneously satisfying force and moment equilibrium was completed twice: first, ignoring wind forces to solve for FS and obtain the strengths computed along the base of each slice; then, solving for FS again with wind forces included but strengths from the first analysis held constant. This method allows wind forces to act on the sliding mass but not influence soil strength.

Incorporation of the wind load into a plane-strain analysis is accomplished by dividing wind forces by the plane-strain spacing, y_{PS}, which represents the average loading on a levee for a given tree spacing, y_{TS} (for analyses presented herein $y_{PS} = y_{TS}$). Note that it is inappropriate to use a plane-strain spacing equivalent to the root ball diameter ($y_{PS} = 2L_{rb}$), as this implies continuously spaced trees adjacent root balls, dramatically over-estimating the load applied to a levee. With y_{PS} applied, the horizontal force applied to the sliding mass in a slope stability analysis can be computed as:

$$F_{w,h} = \frac{M_w}{h_w y_{PS}} = \frac{C_w DBH}{h_w y_{PS}} \tag{6.10}$$

per 1 m width. Using the upper limit for moment capacity of a tree, $M_w = 1000$ kN–m, $F_{w,h}$ is computed in Table 6.1 for various combinations of h_w and y_{PS}, which is useful for evaluating parameter selection. In general, h_w and y_{PS} are correlated, since both increase with increasing

Table 6.1: Horizontal wind load, $F_{w,h}$ for varied acting height (h_w), plane-strain spacing (y_{PS}) and moment coefficient $C_w = 1000$ kN, computed as $F_{w,h} = C_w\, DBH\, h_w^{-1} Y_{PS}^{-1}$ for $DBH = 1$ m. Values in table are the magnitude of load applied in 2D slope stability analyses as kN (per 1 m width), with kips in parenthesis. An appropriate upper limit for $F_{w,h}$ used in slope stability analyses is on the order of $1\,DBH$–$10\,DBH$ kN, given $C_w \sim \mathcal{O}(100-1000)$ kN, $h_w \sim \mathcal{O}(10)$ m and $y_{PS} \sim \mathcal{O}(10)$ m.

$F_{w,h}$ in kN (kip) ($M_w = 1000$ kN–m)		Plane-Strain Width, y_{PS} (m)			
		3	5	10	15
Wind Load Acting Height, h_w (m)	1	330 (75)	200 (45)	100 (22)	67 (15)
	5	67 (15)	40 (9.0)	20 (4.5)	13 (3.0)
	10	33 (7.5)	20 (4.5)	10 (2.2)	6.7 (1.5)
	15	22 (5.0)	13 (3.0)	6.7 (1.5)	4.4 (1.0)

DBH. As such, values in the lower right corner of the table are more appropriate for stability analyses. It should not be forgotten that the lower-bound for tree moment capacity is one-tenth the values in the table (i.e., $C_w = 100$). Considering trees with $DBH = 1$ m have a height above ground on the order of 30 m and h_w is typically in the middle third, even the worst case of $C_w = 1000$ kN produces a horizontal load on the order of 1–10 kN (1 kip), which corresponds to the lowest values in Table 6.1. Most importantly, since ΔFS must be computed with a specific *DBH* tree, Equation 6.10 and Table 6.1 provide a means of equating different assumptions to the same horizontal load applied to a slope.

Results of slope stability analyses with wind forces are presented in Figure 6.10 using a range of loading conditions: $F_{w,v}$ =0.67, 6.7 and 67 kN (per 1 m width). Root reinforcement and weight are *not* included. Subfigures on the left are for wind in the downslope (i.e., destabilizing) direction and those on the right are for wind in the upslope direction. For each of the three potential sliding surfaces used a similar shape response is produced, with the maximum ΔFS for $C_w = 1000$ kN approximately –0.3, –0.2 and –1.5 for landside hinge, complete crest circle and wedge surfaces with wind in the downslope direction, and +0.6, +0.3 and +2.0 for the upslope direction. Although the $C_w = 1000$ case represents an inappropriately high load condition, it illustrates the numerical effect on FS when wind is included in slope stability analyses. Broken lines in the figures reflect the inability of Spencer's method to reach convergence for a solution due to high loads in limit equilibrium equations, especially for the wedge case, which is a planar surface. High frequency variations in ΔFS are caused by edge effects as the root zone begins to overlap the sliding surface edge and individual slices receive a wind load, defined at the slice midpoint. For lower (and more reasonable) values of C_w the response becomes more regular, with $|\Delta FS|$ gradually increasing as the root zone overlaps the sliding surface edge. For circular surfaces, maximum values of $|\Delta FS|$

are less than 0.025, and less than 0.2 for the wedge surface.

Three different models of vertical force distributions were tested, all of which assume a hinge point, the location $x_{w,v0}$ within the root ball such that $f_{w,v0}(x_{w,v0}) = 0$ at a distance one-third of the root ball width from the leeward end, per Coder (2010). Vertical forces imply a tension zone upslope from the hinge point and a compression zone downslope. Models 1, 2 and 3 incorporate constant, linear and triangular distributions, respectively, in each zone. Thus, models 1 and 2 imply non-zero vertical loads at the edge of the root ball; however, scaling by relative biomass proportion in the root ball prevents large forces from being incorporated at the limits. Note that due to the asymmetry of tension and compression zones, the maximum absolute magnitude of force distribution must be larger for compression to satisfy $\sum F_{w,v,i} = 0$.

Wind effects are generally constant for reasonable values of horizontal load when the tree root zone is located entirely within the horizontal limits of the sliding mass. Figure 6.11 examines the response of FS as the root zone becomes overlapped with the upslope edges of the complete crest circle and wedge surface for a 1 m *DBH* cottonwood with $L_{rb} = 1.4$ m (total root ball with of 2.8 m; downslope edge effects were similar). Computed ΔFS is plotted for total wind load, horizontal only and vertical only, for models 1–3 of ditributed load. Clearly the model choice for vertical load distribution has a minimal effect on FS, and once the root ball overlaps the sliding surface all models produce a small ΔFS, approximately +0.01 for the circle and –0.001 for the wedge. A positive change for the circle is due to a stabilizing moment from the downslope wind direction; a similar negative change is obtained when wind is in the upslope direction. There is essentially not change for the wedge surface because moments do not influence limit equilibrium equations for the planar geometry. Horizontal loads steadily increase as the root ball overlaps the sliding surface edge, reaching maximum values in each case of approximately –0.15 and –1.15. Finally, it is apparent that the overall effect on FS is a superposition of the individual effects from vertical and horizontal loads.

Although not presented herein, vertical force distributions were varied to evaluate the effect on stability, such as the location of $x_{w,v0}$ and alternate distribution shapes. All alternatives considered had a negligible effect on the response of FS, except predictable changes in edge effects where the root zone begins to overlap the sliding surface, as discussed above. Due to the scaling of vertical loads by biomass proportion, only very small loads are applied at the root ball limits, $\pm L_{rb}$. This is inconsistent with the physical breakage or pullout of roots that control the root pit dimensions, implying a critically high tension within the roots at $x = \pm L_{rb}$. As such, lateral limits for vertical force application were extended beyond $x = \pm L_{rb}$ by Δx and maximum values of $f_{w,v}$ matched with $x = \pm L_{rb}$. This modifies the integration limits of Equation 6.8 to $x = (-L_{rb} - \Delta x, L_{rb} + \Delta x)$. As with other variations of vertical load distribution that were examined, this had a negligible effect on FS, except slightly altering the tree position where edge effects began.

Wind effects were evaluated for a range of loading using three sliding surfaces in Figure 6.12: landside hinge, complete crest circle and wedge. For each evaluation, a single tree is located entirely within the sliding mass, thus the scenario represents maximum $|\Delta FS|$ for any tree location, and Equation 6.10 can be used to extend results to any load condition. Actual computations were completed for a 1 m *DBH* cottonwood with $h_w = 1$ m, $y_{PS} = 10$ m and tree location at the levee toe ($x = 93$ m), or $x = 89$ m for the wedge surface. Given that reasonable wind loads should be on the order of 1–10 kN, results in Figure 6.12 show that $|\Delta FS|$ due to wind loading should be no more than ± 0.1. Finally, in summary:

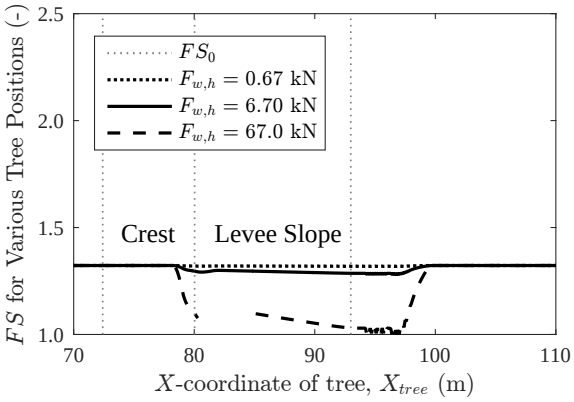

(a) Minimum FS, circular; downslope wind

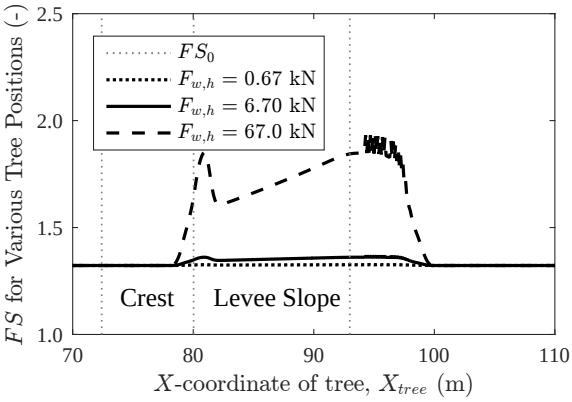

(b) Minimum FS, circular; upslope wind

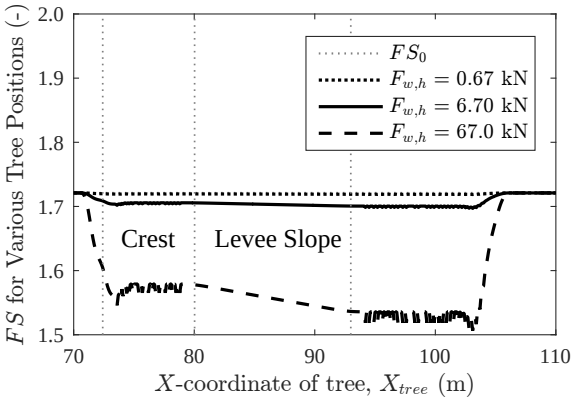

(c) Complete crest, circular; downslope wind

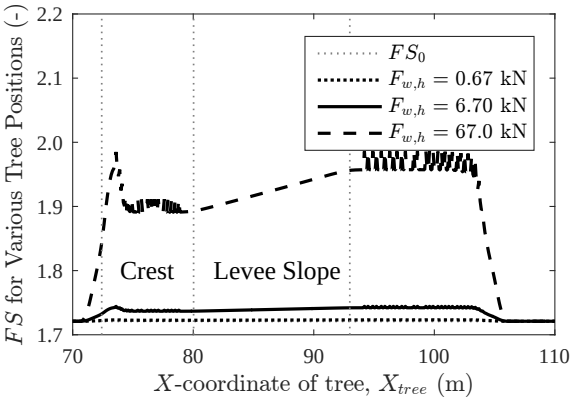

(d) Complete crest, circular; upslope wind

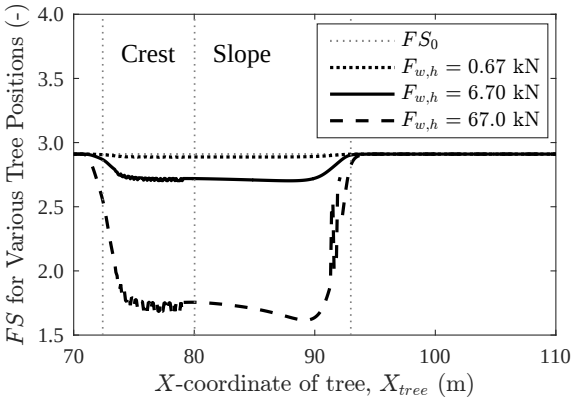

(e) Complete crest, wedge; downslope wind

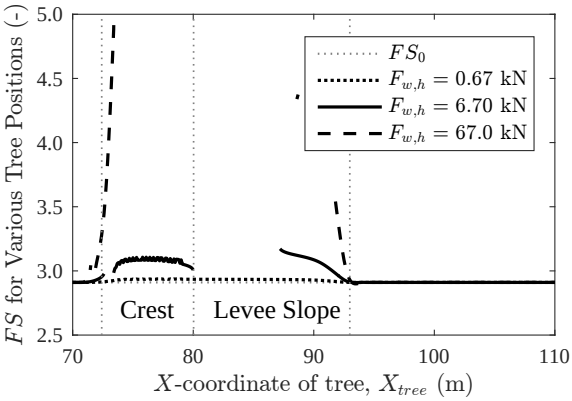

(f) Complete crest, wedge; upslope wind

Figure 6.10: Slope stability FS for three upslope and downslope horizontal wind loads, $F_{w,h} = 0.67$, 6.70 and 67.0 kN, with tree position varied across three potential sliding surfaces. Computed for a 1 m *DBH* cottonwood with $y_{PS} = 15$ m, $h_w = 1$ m and $C_w = 1$, 10 and 1000 kN (per 1 m width). A triangular distribution was used for vertical loads. Scale of FS in a–d is the same as for root reinforcement and weight in Figures 6.5 and 6.6. Root reinforcement and weight *not* included in these analyses.

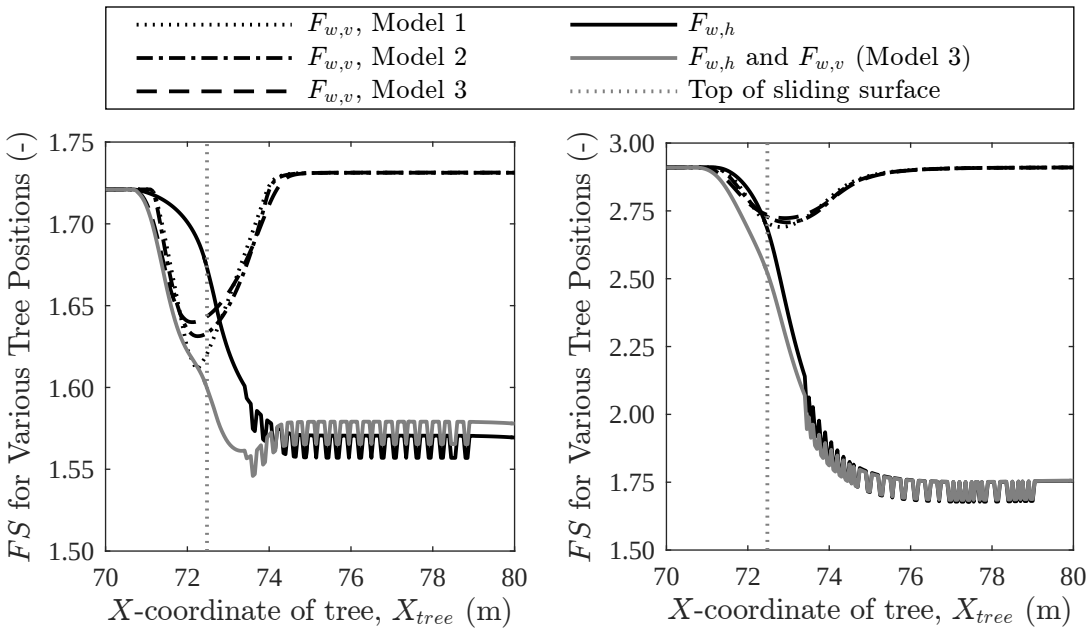

Figure 6.11: Wind loading effect at edge of for three models of vertical force distributed load: uniform, linearly and triangular. Hinge point is located 1/3 of the root ball width from the leeward edge. Computed for a 1 m *DBH* cottonwood with $F_{w,h} = 67$ kN ($y_{PS} =$ 15 m, $h_w = 1$ m and $C_w = 1000$ kN) applied to the complete crest circle and wedge surfaces on left and right, respectively (per 1 m width). Downslope edge effects were similar; root reinforcement and weight are *not* included here.

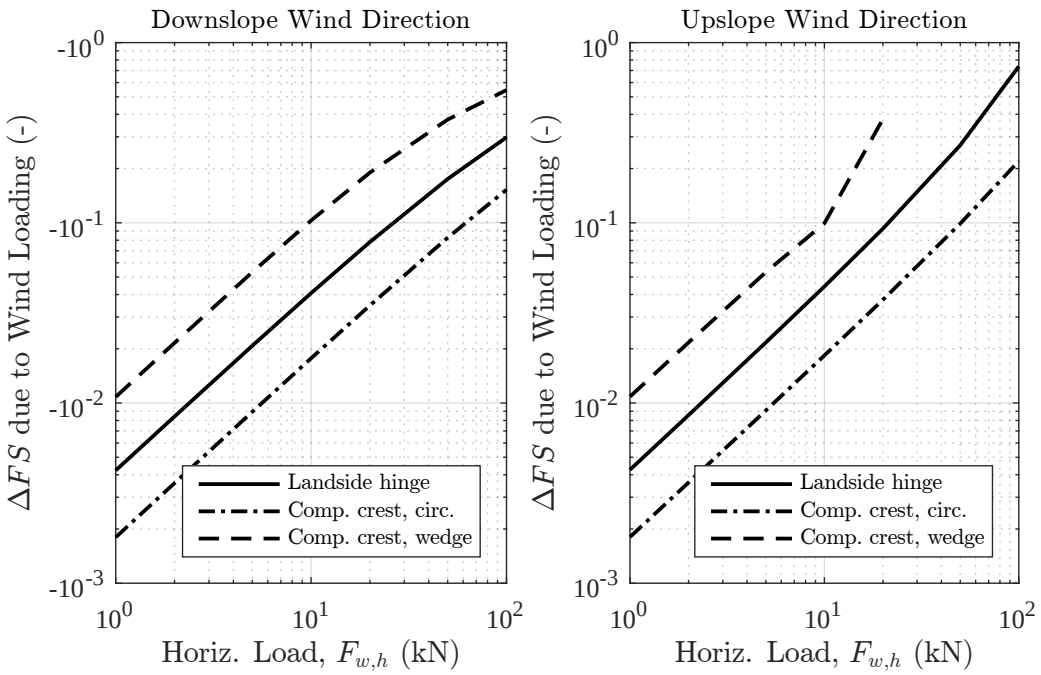

Figure 6.12: Change in FS for various loading conditions, represented by total horizontal load, $F_{w,h}$. Wind forces are applied to the landside hinge, complete crest circle and wedge sliding surfaces (per 1 m width). Using $F_{w,h}$ allows non-parameterized presentation of ΔFS using Equation 6.10. Actual values of ΔFS computed for a 1 m *DBH* cottonwood (i.e., $C_w = M_w$) with $h_w = 1$ m and $y_{PS} = 10$ m, with tree located at levee toe ($x = 93$ m; $x = 89$ m for the wedge), although ΔFS is constant when root ball is entirely within sliding mass. Root reinforcement and weight are *not* included here.

- *DBH*, horizontal load acting height, h_w, and plane-strain spacing, y_{PS} play a significant role in determination of horizontal load, $F_{w,h}$, which control ΔFS
- vertical loads, $F_{w,v}$, have a small overall effect on ΔFS
- although there is a wide range in the ultimate moment that could be transferred to soil, for typical conditions $F_{w,h}$ should be on the order of 1–10 kN
- ΔFS is independent of tree position when the root zone is not crossed by the sliding surface
- for typical conditions (i.e., 1–10 kN) wind effects should result in $|\Delta FS| < 0.1$

6.5 Vegetation Random Variables for Stability Analyses

There are many possibilities for implementation of vegetation parameters as random variables in FORM analyses, although many of them would likely have a small effect on reliability. To simplify results, vegetation random variables are grouped into two classes: biomass and load factors. Biomass analyses consider the variability of biomass parameters and choices, while the load factor

analyses consider the variability in loading. These random variables are generally selected to evaluate the effect of parameter choice and probability distribution parameters are selected to represent a reasonable range of possible values for each factor since appropriate data is not readily available.

The analyses were performed using tree position and *DBH* as random variables; however, they did not produce additional insights beyond those already described in sensitivity studies and deterministic slope stability results. Using deterministic analyses to evaluate the influence of position and *DBH* avoids the necessity of selecting a probability model for each variable, which is not readily available. Given the allometric basis of the biomass model, variability in *DBH* is implicit in the inclusion of biomass factors as random variables. Finally, because the response of slope stability evaluations is so dependent on tree position, including it as a random variable complicates interpretation of the effect of biomass and load factors.

Biomass Factors

To evaluate the variability of biomass model parameters a generic multiplication factor, B_x, can be defined to modify the deterministic values discussed in the previous chapter. Three different factors are presented herein, B_ν, B_{rb} and B_z, which are applied as a product to the following:

- rate of biomass decrease: $B_\nu \cdot \nu$
- root ball radius factor: modifies $B_{rb} \cdot L_{rb}$
- maximum rooting depth: $B_z \cdot z_{max}$

These three parameters were selected to emphasize the distinct behavior of overall root density (B_ν), width over which weight and wind loads are applied (B_{rb}) and vertical distribution (B_z). Each factor is assigned lognormal distribution to preclude negative values and is assigned $\lambda = 1.0$ to preserve the deterministic value as the distribution median. Parameter ζ controls the variance of each factor, with the one standard deviation (68.3%) confidence interval computed as $\pm \exp \zeta$ (Appendix A). Thus, B_x is essentially a scaling parameter that changes the related variable by factor 0.7–1.3 for $\zeta = 0.3$ or 0.4–2.7 for $\zeta = 1.0$ at the first confidence interval. The range of possible values for ν, L_{rb} and z_{max} considered in the previous chapter generally fall within the range provided by B_x when $\zeta = 1.0$. For example, $\nu_d \sim 2$ for a 0.2 *DBH* tree, which would result in a confidence interval of 0.8–5.4, whereas the maximum range of data for all ν is approximately 1–8 for $DBH < 0.2$ m but only 1–4 for $DBH > 0.2$ m.

Due to the sensitivity of FS computations for shallow sliding surfaces, reliability analyses have difficulty converging when the variability of B_z is high. Furthermore, the data supports a low value of $\zeta = 0.25$ for the probability distribution, which results in a confidence interval of 0.8–1.3 m. If the 99.7% confidence interval (3σ) is considered, z_{max} ranges from 0.5–2.1 m, which aligns well with the upper limit recommended by Coder (2010).

Mechanical Load Variables

Biomass model parameters influence the spatial distribution and magnitude of root density in a levee, but are not directly related to specification of mechanical loads on the slope. Parameters directly related to the magnitude of root reinforcement, weight and wind can be represented by random variables to evaluate their effect. A normal or lognormal distribution is used herein to evaluate the following parameters:

- C_R, root cohesion factor; N($\mu = 2300$kPa, δ) (4.7e+4 psf)
- ε_W, root mean squared error of tree mass regression; N($\mu = 0, \sigma$)
- C_w, moment coefficient describing load transfer from wind to soil; LN($\lambda = 5, \zeta$)

Note that ε_W is an error term in log units and when the normal distribution is applied it causes the prediction of weight from the log-linear regression to have a lognormal response. For wind loading, parameters $\lambda = 5$ and $\zeta = 0.5$ give C_w a median value of 150 kN and mean of 170 kN, which is within the range of values described above (i.e., 10–100 kN), and produces and appropriate horizontal load, $F_{w,h}$, for tree conditions considered herein.

6.6 Reliability of Levee Stability with Tree Effects

Reliability analyses for the levee model with vegetation random variables were performed using the FORM algorithm. In addition to the seven seepage and stability random variables described previously up to 6 vegetation random variables were included in three suites of analyses:

1. Mechanical load factors for root reinforcement, C_R, and tree weight, ε_W
2. Biomass factors (B_v, B_{rb} and B_z) and mechanical factors C_R and ε_W (i.e., all but C_w)
3. Wind loading, with root reinforcement and weight (i.e., all six)

The reliability analyses presented in this section incorporated $y_{PS} = 15$ m for a 1 m *DBH* cottonwood tree located at the landside hinge or 3 m away from the toe. When at the hinge the root zone overlaps the landside hinge surface but not the complete crest circle. The toe location was selected to have a similar overlap by the root zone of both surfaces.

Landside Hinge, Case 1 (C_R and ε_W)

It should be no surprise that importance measures for the two vegetation variables are small in comparison to WSE, z_B and γ_B. However, comparison to the reference analysis indicates the inclusion of vegetation has several effects on the FORM analysis when the tree is located at the landside hinge (ie., Tables 4.3 and 6.2), beginning with an increase of β from 2.99 to 3.05 and decrease of p from 1.4e–3 to 1.2e–3. Although changes in the design point are small, they reflect the additional stability due to the tree, for example, x_i^* for z_B decreases from 2.7 m to 2.6 m, indicating a slightly thinner blanket will be necessary for sliding to occur.

When the tree is located at the toe several results are found indicating a higher effect on stability, for example $\beta = 3.28$ and p =5.2e–4 (Table 6.3). Importance of tree weight is still relatively low, but has increased by an order of magnitude since it is now providing resistance at the bottom of the slope, counteracting low effective stresses. More important is the root reinforcement variable, C_R, which has become the fourth most important variable, after WSE, z_B and γ_B. Sensitivity measures indicate the mean of C_R has a significant effect on reliability, consistent with deterministic results.

Fragility curves and μ_{FS} provide further insight into reliability results across the upper range of WSE (Figure 6.13). Each plot compares fragility and μ_{FS} with and without vegetation, where confidence intervals for the vegetation case only include uncertainty due to vegetation probability distributions. The contribution of all random variables included in the analysis are ranked on each

figure. For both tree scenarios a small but positive improvement in is found, reflected by a lowering of the dark line for fragility and raising for FS (also evidenced by the increase in deterministic FS line). The shaded bands for the confidence intervals confirm a small overall effect of vegetation random variables on stability. Since root reinforcement has a much larger impact on computed FS when the tree is at the levee toe, uncertainty in the C_R leads to a wider confidence interval. Despite the increasing dependence on this parameter, it should be noted that even an extremely low value of C_R is unlikely to reduce FS or β significantly, as the uncertainty band with for both vegetation random variables does not even reach the best-estimate for the reference analysis that excludes vegetation.

Landside Hinge, Case 2 and Case 3

Cases 2 and 3 add more vegetation variables to the reliability analysis, resulting a more nuanced understanding of the problem at the cost of increasing complexity (Tables 6.4 and 6.5). For Case 2 results, water level was not included in the analysis since it was completed as part of a fragility curve. Furthermore, z_B and K_r were left out of the Case 3 analyses to facilitate FORM computations when WSE is included, since the large number of random variables makes convergence difficult to achieve. Because the random variables are different, the design point and β are not comparable, but importance vectors will maintain the same relative magnitudes. Together, these analyses show that WSE, γ_B and z_B still dominate stability with $|\alpha_i|$ for each generally on the order of 0.1. All vegetation variables have $|\alpha_i|$ an order of magnitude less with a consistent exception being the biomass factor B_ν, with $\alpha \sim +0.2$, it is a demand variable. Ranked uncertainty contributions on the fragility curves in Figure 6.14confirm these observations. Since ν controls the decrease in biomass, higher values concentrate root density closer to the trunk, thus limiting the lateral extent of root reinforcement. While this would seemingly imply weight would also be affected and should have a more significant role in stabilizing the slope, the importance of B_{rb} and ε_W indicate the opposite. In fact, the mechanical load C_R is not as important as B_ν for Case 3, as α is on the order of 1e–2. Although the difference is less significant in the Case 2 analysis, it is still less than α_i for B_ν. Thus, while deterministic analyses illustrate the effect of root reinforcement on stability, the reliability analysis illustrates that the rate of biomass decrease with distance from the trunk has a larger impact on FS than the reinforcing load itself. In other words, given the range of possible values at a specific location for RAR is more important than C_R.

Tables 6.5 and 6.6 present Case 3 results for wind in the downslope and upslope direction, respectively. For each case, the predicted probability of slope failure is 2.5e–2 and 2.7e–4, a difference that produces large differences between the two fragility curves in Figure 6.14, although both cases are safer than the case without vegetation. In comparison to Case 1, Cases 2 and 3 introduce greater uncertainty in the analysis, evidenced by the wider confidence interval bands in comparison to Figure 6.13. Relative changes in μ_{FS} are analagous, with a decrease in FS that still remains above the non-vegetation case. Since the tree is located at the levee toe it stabilizes the slope with weight and root reinforcement, thus increasing overall reliability.

Although not presented herein, additional fragility curves were produced with root reinforcement limited by $C_{po} = 1$. These analyses produced nearly identical results for β and p with predictable changes to sensitivity and fragility. As found in deterministic analyses, C_{po} directly controls the magnitude of ΔFS due to root reinforcement; in reliability analyses the same effect is evidenced as a reduction of importance measures for B_ν and C_R. The positive change with respect

Table 6.2: Reliability results for vegetation Case 1 (C_R and ε_W) for circular landside hinge sliding surface with 1 m *DBH* cottonwood located at levee hinge.

RV	Unit	$\mathbf{x}^*$	$\mathbf{u}^*$	α	δ	η
γ_B	kN/m^3	1.74e+1	–5.29e–1	–1.73e–1	1.73e–1	–9.16e–2
c_B	kPa	1.13e+0	–1.94e–1	–6.35e–2	6.35e–2	–1.23e–2
ϕ_B	°	3.58e+1	–1.22e–1	–3.94e–2	3.94e–2	–4.80e–3
γ_E	kN/m^3	1.86e+1	–2.01e–1	–6.57e–2	6.57e–2	–1.32e–2
ϕ_E	°	3.77e+1	–1.36e–1	–4.46e–2	4.46e–2	–6.05e–3
z_B	m	2.62e+0	–1.73e+0	–5.67e–1	–1.15e+0	7.33e+0
K_r	m/s	2.34e+3	2.12e–1	7.00e–2	–3.53e–1	3.30e–2
WSE	m	3.76e+0	2.42e+0	7.94e–1	–3.69e–1	–1.23e+0
C_R	kPa	2.15e+3	–9.55e–2	–3.11e–2	3.11e–2	–2.97e–3
ε_W	ln kN	6.13e–3	1.23e–2	4.01e–3	–4.01e–3	–4.92e–5

[a] $\beta = 3.045$ and $p = 1.163e-03$

[b] Order of Importance, α: WSE, z_B, γ_B, K_r, γ_E, c_B, ϕ_E, ϕ_B, C_R, W_t

[c] All vectors are unitless except design point, $\mathbf{x}^*$; alternate units: γ_B =111 pcf, c_B =23.5 psf, γ_E =118 pcf, z_B =8.59 ft, WSE =12.32 ft ($WSE/H = 0.72$)

Table 6.3: Reliability results for vegetation Case 1 (C_R and ε_W) for circular landside hinge sliding surface with 1 m *DBH* cottonwood located at levee toe.

RV	Unit	$\mathbf{x}^*$	$\mathbf{u}^*$	α	δ	η
γ_B	kN/m^3	1.74e+1	–5.12e–1	–1.55e–1	1.55e–1	–7.95e–2
c_B	kPa	1.13e+0	–1.88e–1	–5.71e–2	5.71e–2	–1.07e–2
ϕ_B	°	3.58e+1	–1.29e–1	–3.89e–2	3.89e–2	–5.02e–3
γ_E	kN/m^3	1.86e+1	–1.95e–1	–5.90e–2	5.90e–2	–1.15e–2
ϕ_E	°	3.78e+1	–1.30e–1	–3.94e–2	3.94e–2	–5.11e–3
z_B	m	2.42e+0	–1.88e+0	–5.71e–1	–4.24e–1	6.05e+0
K_r	m/s	2.45e+3	2.38e–1	7.29e–2	–3.65e–1	3.38e–2
WSE	m	3.97e+0	2.58e+0	7.88e–1	–3.48e–1	–1.28e+0
C_R	kPa	1.85e+3	–3.65e–1	–1.11e–1	1.11e–1	–4.04e–2
ε_W	ln kN	–6.81e–2	–1.36e–1	–4.13e–2	4.13e–2	–5.63e–3

[a] $\beta = 3.283$ and $p = 5.138e-04$

[b] Order of Importance, α: WSE, z_B, γ_B, C_R, K_r, γ_E, c_B, W_t, ϕ_E, ϕ_B

[c] All vectors are unitless except design point, $\mathbf{x}^*$; alternate units: γ_B =111 pcf, c_B =23.6 psf, γ_E =118 pcf, z_B =7.95 ft, WSE =13.02 ft ($WSE/H = 0.77$)

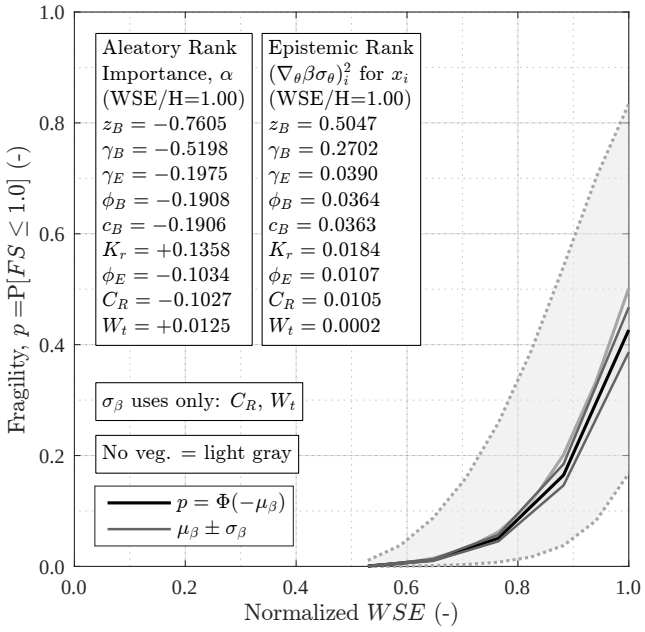

(a) Fragility with tree at levee hinge.

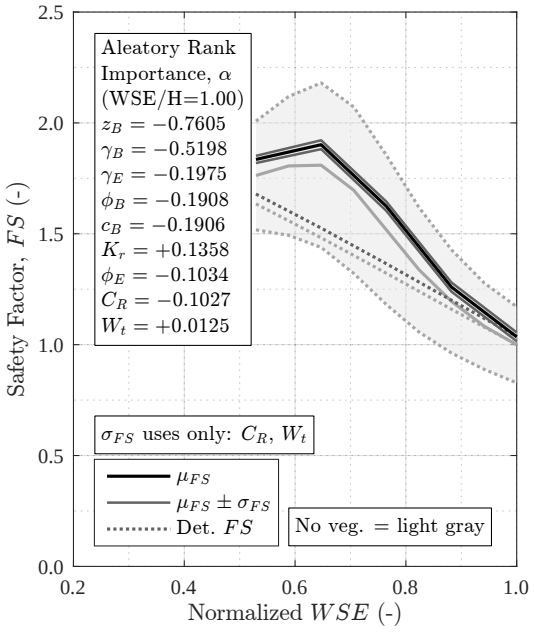

(b) μ_{FS} with tree at levee hinge.

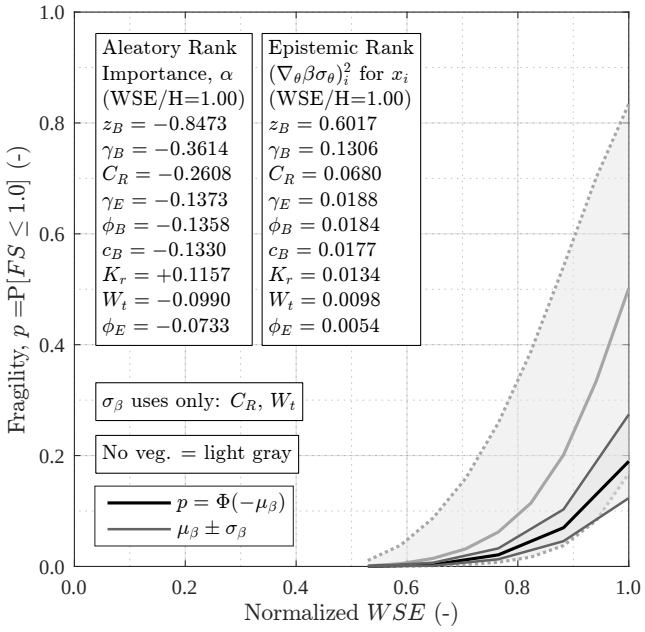

(c) Fragility with tree at levee toe.

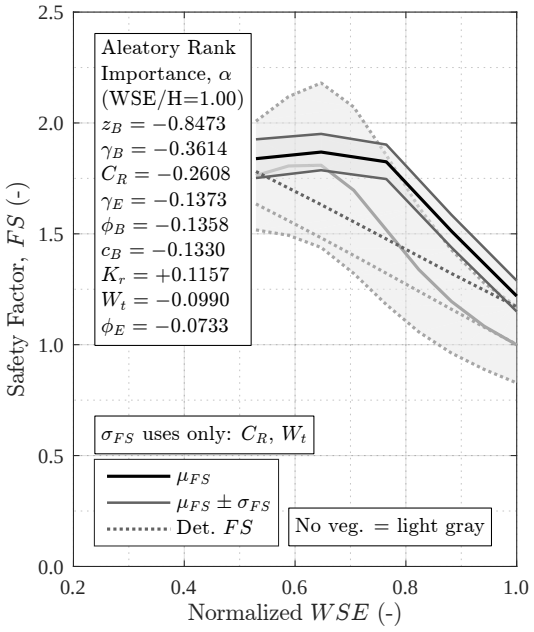

(d) μ_{FS} with tree at levee toe.

Figure 6.13: Reliability results for vegetation Case 1 (C_R and ε_W) for circular landside hinge sliding surface with 1 m *DBH* cottonwood located at levee hinge and toe. Fragility curves compare FORM analysis with vegetation effects included to a reference analysis of the same sliding surface without vegetation (light gray). Confidence intervals for vegetation case only include uncertainty from vegetation variables.

to the non-vegetation case is reduced for fragility curves, in addition to the confidence interval band decreasing in width. However, even with root reinforcement limited, there is still a positive overall influence of vegetation on levee response.

Reliability results for the landside hinge sliding surface indicate that the influence of vegetation on stability is within the confidence interval bounds on aleatory uncertainty for fragility and within a standard deviation of the mean estimate of FS. Vegetation parameters are generally less important for overall stability than the strength and seepage parameters that were also included in the analysis, although the distribution of root density and root reinforcement parameter can come close. Finally, while these observations can be generalized for various tree locations, they must take into account the size of the potential sliding mass and proximity of the root zone to the sliding surface.

Complete Crest Circle

Reliability results for the complete crest circular sliding surface are illustrated with fragility curves for vegetation Cases 2 and 3 in Figure 6.15. Importance and sensitivity results can be obtained from the rankings on the fragility curves. In comparison to the landside hinge surface, fragility of the complete crest geometry is much more stable. As found with deterministic analyses, the effect of vegetation is relatively small, illustrated by the deviation of vegetation curves from the results of cases without vegetation. Sensitivity due to vegetation parameters is essentially negligible, implying no combination of unfavorable parameters could significantly affect the stability assessment of this surface. Since wind is included in this analysis, it implies that even the most extreme wind loading event would be unlikely to be problematic.

Of all the vegetation variables, weight (ε_W) has the largest impact, as it is located on a portion of the slope where weight has a positive effect on stability. However, it is still less important than all other non-vegetation variables. Since the tree is located away from the sliding surface root reinforcement has negligible influence on stability.

Overall, reliability results for the complete crest sliding surface illustrate that vegetation has a small effect on stability for such a large mass, and even the large range of possible values for biomass and mechanical loading parameters are insignificant when compared to the range and likely values of strength and seepage properties.

Table 6.4: Reliability results for vegetation Case 2 (B_v, B_{rb}, B_z, C_R and ε_W) for circular landside hinge sliding surface with 1 m *DBH* cottonwood located at levee toe. Results are from a fragility curve analysis, therefore *WSE* is not included as a random variable.

RV	Unit	$\mathbf{x}^*$	$\mathbf{u}^*$	α	δ	η
γ_B	kN/m^3	1.74e+1	–4.99e–1	–2.54e–1	2.54e–1	–1.27e–1
c_B	kPa	1.13e+0	–1.84e–1	–9.35e–2	9.35e–2	–1.72e–2
ϕ_B	°	3.58e+1	–1.34e–1	–6.83e–2	6.83e–2	–9.17e–3
γ_E	kN/m^3	1.86e+1	–1.88e–1	–9.60e–2	9.60e–2	–1.81e–2
ϕ_E	°	3.78e+1	–1.28e–1	–6.50e–2	6.50e–2	–8.31e–3
z_B	m	2.55e+0	–1.78e+0	–9.05e–1	–1.51e+0	1.11e+1
K_r	m/s	2.38e+3	2.20e–1	1.12e–1	–5.64e–1	5.26e–2
B_v	–	1.61e+0	4.79e–1	2.43e–1	–4.24e–1	8.00e–2
B_{rb}	–	1.01e+0	5.04e–3	2.55e–3	–5.45e–3	1.61e–3
B_z	–	1.03e+0	1.28e–1	4.62e–2	–4.84e–2	5.49e–3
C_R	kPa	2.03e+3	–2.05e–1	–1.03e–1	1.03e–1	–2.11e–2
ε_W	ln kN	–6.69e–2	–1.34e–1	–6.81e–2	6.81e–2	–9.10e–3

[a] $\beta = 1.967$ and $p = 2.462e-02$

[b] Order of Importance, α: z_B, γ_B, B_v, K_r, C_R, γ_E, c_B, ϕ_B, W_t, ϕ_E, B_z, B_{rb}

[c] All vectors are unitless except design point, $\mathbf{x}^*$; alternate units: γ_B =111 pcf, c_B =23.6 psf, γ_E =119 pcf, z_B =8.37 ft

Table 6.5: Reliability results for vegetation Case 3 (B_v, B_{rb}, B_z, C_R, ε_W and C_w) for circular landside hinge sliding surface with 1 m *DBH* cottonwood located at levee toe. Wind is in the downslope direction. Random variables $z-B$ and K_r were left out to facilitate convergence of a FORM solution.

RV	Unit	$\mathbf{x}^*$	$\mathbf{u}^*$	α	δ	η
γ_B	kN/m^3	1.71e+1	–7.74e–1	–2.23e–1	2.23e–1	–1.73e–1
c_B	kPa	1.09e+0	–2.89e–1	–8.31e–2	8.31e–2	–2.40e–2
ϕ_B	°	3.54e+1	–3.37e–1	–9.68e–2	9.68e–2	–3.26e–2
γ_E	kN/m^3	1.85e+1	–2.96e–1	–8.51e–2	8.51e–2	–2.52e–2
ϕ_E	°	3.77e+1	–1.73e–1	–4.99e–2	4.99e–2	–8.64e–3
WSE	m	4.95e+0	3.24e+0	9.34e–1	–3.42e–1	–1.82e+0
B_v	–	1.93e+0	6.59e–1	1.87e–1	–2.99e–1	4.04e–2
B_{rb}	–	1.05e+0	5.21e–2	1.51e–2	–3.17e–2	9.06e–3
B_z	–	1.03e+0	1.10e–1	6.80e–2	–7.14e–2	9.20e–3
C_R	kPa	1.97e+3	–2.52e–1	–7.15e–2	7.15e–2	–1.80e–2
ε_W	ln kN	–1.01e–1	–2.01e–1	–5.79e–2	5.79e–2	–1.16e–2
C_w	*kN*	1.64e+2	2.04e–1	5.86e–2	–7.07e–2	1.54e–2

[a] $\beta = 3.462$ and $p = 2.685e-04$

[b] Order of Importance, α: WSE, γ_B, B_v, ϕ_B, γ_E, c_B, C_R, B_z, C_w, W_t, ϕ_E, B_{rb}

[c] All vectors are unitless except design point, $\mathbf{x}^*$; alternate units: γ_B =109 pcf, c_B =22.8 psf, γ_E =118 pcf, WSE =16.24 ft ($WSE/H = 0.96$)

Table 6.6: Reliability results for vegetation Case 3 (B_v, B_{rb}, B_z, C_R, ε_W and C_w) for circular landside hinge sliding surface with 1 m *DBH* cottonwood located at levee toe. Wind is in the upslope direction. Random variables $z - B$ and K_r were left out to facilitate convergence of a FORM solution.

RV	Unit	$\mathbf{x}^*$	$\mathbf{u}^*$	α	δ	η
γ_B	kN/m^3	1.70e+1	–8.66e–1	–2.37e–1	2.37e–1	–2.05e–1
c_B	kPa	1.08e+0	–3.25e–1	–8.87e–2	8.87e–2	–2.88e–2
ϕ_B	°	3.54e+1	–3.42e–1	–9.30e–2	9.30e–2	–3.18e–2
γ_E	kN/m^3	1.84e+1	–3.13e–1	–8.59e–2	8.59e–2	–2.69e–2
ϕ_E	°	3.77e+1	–1.66e–1	–4.52e–2	4.52e–2	–7.52e–3
WSE	m	5.25e+0	3.42e+0	9.33e–1	–3.26e–1	–1.90e+0
B_v	–	1.98e+0	6.85e–1	1.85e–1	–2.90e–1	3.68e–2
B_{rb}	–	1.05e+0	4.80e–2	1.28e–2	–2.68e–2	7.67e–3
B_z	–	1.03e+0	1.18e–1	3.23e–2	–3.38e–2	4.12e–3
C_R	kPa	1.94e+3	–2.83e–1	–7.54e–2	7.54e–2	–2.13e–2
ε_W	ln kN	–1.13e–1	–2.25e–1	–6.14e–2	6.14e–2	–1.38e–2
C_w	*kN*	1.36e+2	–1.78e–1	–4.85e–2	6.73e–2	–2.91e–2

[a] $\beta = 3.665$ and $p = 1.237e-04$

[b] Order of Importance, α: WSE, γ_B, B_v, ϕ_B, c_B, γ_E, C_R, W_t, C_w, ϕ_E, B_z, B_{rb}

[c] All vectors are unitless except design point, $\mathbf{x}^*$; alternate units: γ_B =108 pcf, c_B =22.6 psf, γ_E =117 pcf, WSE =17.22 ft ($WSE/H = 1.01$)

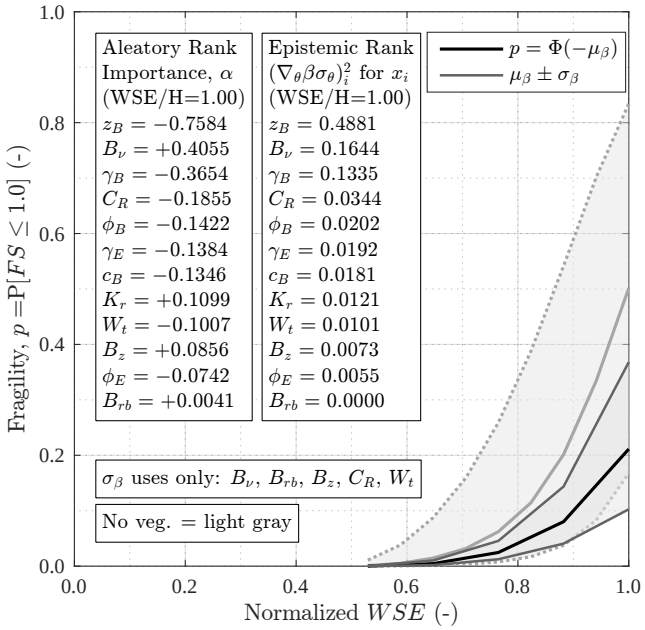

(a) Fragility with tree at levee toe, Case 2.

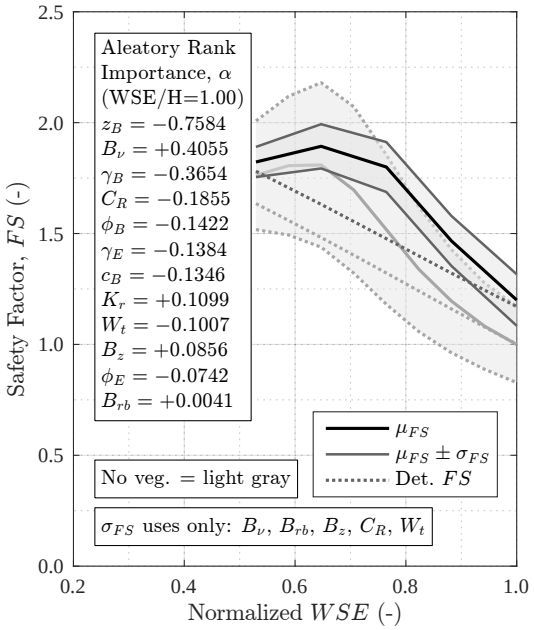

(b) μ_{FS} with tree at levee toe, Case 2.

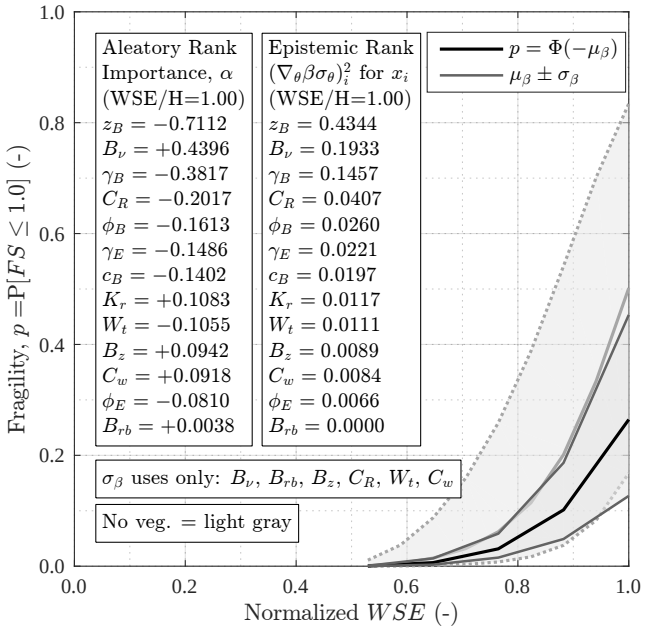

(c) Fragility with tree at levee toe, Case 3.

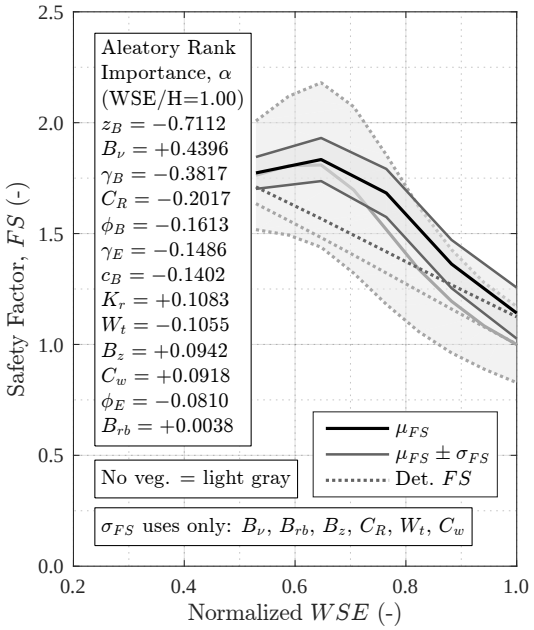

(d) μ_{FS} with tree at levee toe, Case 3.

Figure 6.14: Reliability results for vegetation Case 2 (B_ν, B_{rb}, B_z, C_R and ε_W) and Case 3 (Case 2 with C_w for wind) for circular landside hinge sliding surface with 1 m *DBH* cottonwood located at levee toe. Wind is in the downslope direction. Fragility curves compare FORM analysis with vegetation effects included to a reference analysis of the same sliding surface without vegetation (light gray). Confidence intervals for vegetation case only include uncertainty from vegetation variables.

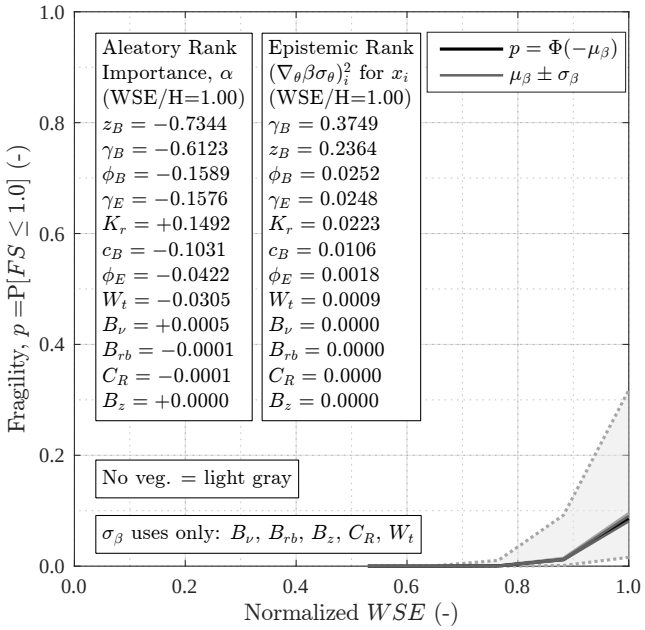

(a) Fragility with tree at levee toe, Case 2.

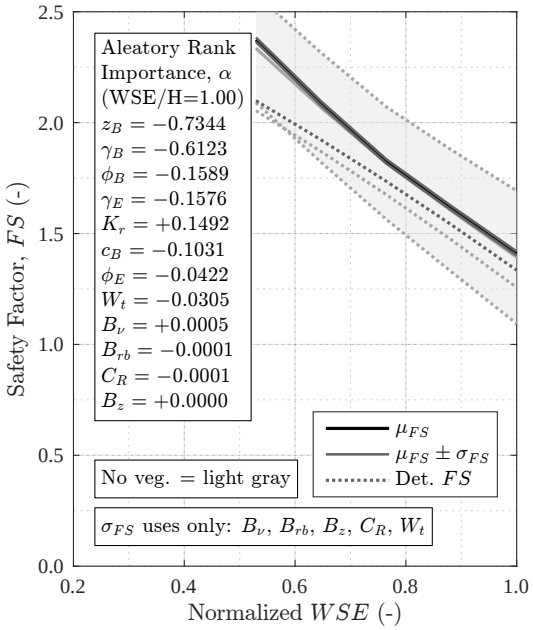

(b) μ_{FS} with tree at levee toe, Case 2.

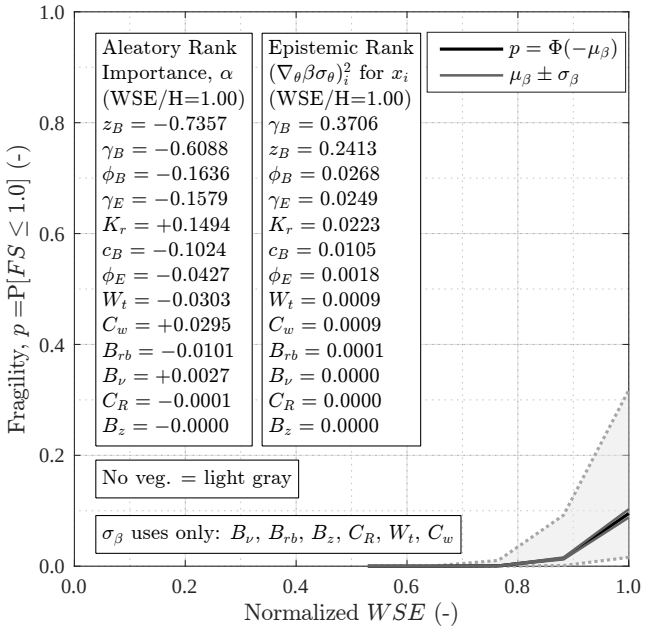

(c) Fragility with tree at levee toe, Case 3.

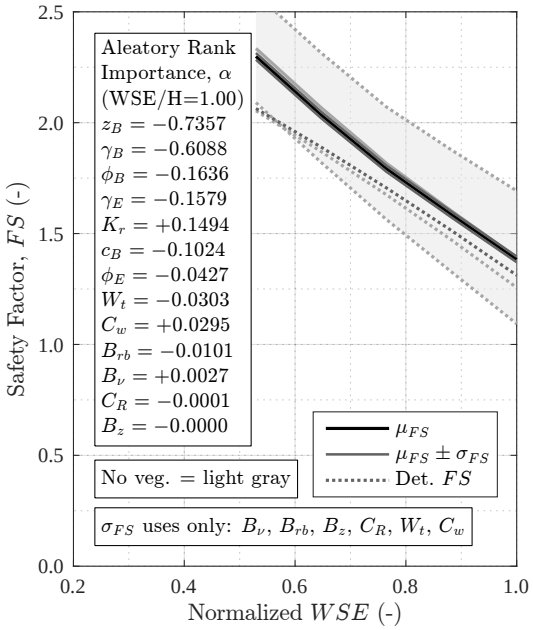

(d) μ_{FS} with tree at levee toe, Case 3.

Figure 6.15: Reliability results for vegetation Case 2 (B_ν, B_{rb}, B_z, C_R and ε_W) and Case 3 (Case 2 with C_w for wind) for complete crest circular sliding surface with 1 m *DBH* cottonwood located at levee toe. Wind is in the downslope direction. Fragility curves compare FORM analysis with vegetation effects included to a reference analysis of the same sliding surface without vegetation (light gray). Confidence intervals for vegetation case only include uncertainty from vegetation variables.

Chapter 7

Conclusions and Recommendations

A reliability model of levee stability incorporating a robust model of tree roots, weight and wind loads in the presence of seepage forces has been developed. This model has been used to quantify the effect of vegetation for different scenarios and evaluate the sensitivity of the solutions to the input parameters. Stability is assessed with factor of safety against sliding (FS) for deterministic analyses and probability of the factor of safety less than one (p) for stochastic analyses, using the first-order reliability method (FORM) to compute a reliability index. Results show that under steady-state seepage conditions blanket layer properties control slope stability with vegetation generally an order of magnitude or less in importance. However, there are scenarios where the quantitative effects of vegetation are more significant, which can be understood through the paradigm of small and large potential sliding surfaces (corresponding primarily to results from the landside hinge and complete crest surfaces).

When the geometry of a potential sliding surface is fixed, effects due to root reinforcement, weight and wind are generally determined by tree location and are scaled by the size of the sliding mass. For small slope failures, root reinforcement can have a large effect on FS, reaching a maximum when the tree is located directly at the sliding surface entry or exit point. For large slope failures the effect on FS is reduced due to sliding mass and the small proportion of the sliding surface that can be influenced by root reinforcement. Root reinforcement, weight and wind effects were generally found to have an additive effect on ΔFS and p.

Root reinforcement is computed proportionally to RAR and has a greater effect on stability than weight when the tree center is close to the sliding surface, although for $RAR \gtrsim$1–10% root reinforcement produces unreasonably high ΔFS. Root limits are applied that are related to breakage and pullout of roots and are effective at keeping root reinforcement values reasonable and preventing numerical issues with FS computations, but specific values for the limits were not possible to incorporate in the biomass model due to lack of data describing the lateral distribution of root number and diameter. Root reinforcement limits C_{rb} and C_{po} were generally used to prevent unrealistic tension forces between slices in the upslope portion of the sliding mass and their numerical effect resulted in scaling of ΔFS between zero and the value without reinforcement limits. When needed, C_{rb} and C_{po} were consistent with ultimate capacities reported by published root studies and result in a conservative estimate of FS as long as a search is performed for the minimum FS surface.

Tree weight decreases stability when a tree is located near the crest and linearly increases stability as it moves towards the toe, with a neutral point located near the center of a circular sliding surface centroid (and a similar location for non-circular surfaces). The increment of ΔFS is

greater at the toe due to a greater relative increase in effective stress for the blanket layer soil with relatively low pore pressure. Overall, tree weight resulted in a change to FS on the order of $\pm 1\%$.

Wind loads are included by specifying the ultimate moment that can be carried by a tree, which is then applied to the slope as equivalent vertical and horizontal forces. When appropriate plane-strain averaging and horizontal force acting height are used to distribute wind load the effect on FS is small and independent of tree position when the root ball is completely within the sliding mass. Upslope and downslope wind directions have roughly equal and opposite effects on FS, and an upper limit for most sliding surfaces should be on the order $\Delta FS = \pm 0.01$–0.1 (i.e., $\lesssim 1\%$). Although high wind loads for marginally stable slopes can be applied to a slope stability analysis and produce a condition where $FS < 1.0$, reliability analyses show that the uncertainty in estimated FS due to aleatory and epistemic uncertainty in strength and seepage properties is far greater than the relative change in FS due to wind.

Using a fixed sliding surface and evaluating the effect of vegetation on stability overestimates the magnitude of ΔFS and because the minimum FS surface is highly sensitive to the local variations of biomass. To properly quantify ΔFS due to vegetation a potential sliding surface search must be performed with vegetation effects included in the model. For a small non-circular sliding surface with $FS = 1.285$ for no vegetation, the inclusion of root reinforcement and weight resulted in $\Delta FS =$–0.059, +0.003 and +0.224 for a tree located at hinge, slope midpoint and toe. When a search was performed with vegetation included, minimum FS surfaces were found with similar geometry but with $\Delta FS =$–0.078, –0.040 and +0.043 for identical tree conditions. Furthermore, non-circular sliding surfaces must be used to evaluate vegetation effects, as circular surfaces cannot accomodate the contours of root density in the subsurface. For a small circular sliding surface with $FS = 1.322$ the same suite of tree conditions produced ΔFS of +0.043, +0.005 and +0.055 for the minimum FS surface without vegetation, and +0.025, +0.005 and +0.043 for the minimum FS surface with vegetation. Although similar effects were observed for a large sliding mass, the quantitative differences were at least an order of magnitude less.

Aleatory uncertainty is represented by the unknown values of input parameters used in levee seepage and stability models, and is quantified with fragility curves, $p(WSE)$, and reliability index. Epistemic uncertainty is represented herein by the choice of probability distribution and parameters for each random variable, and is quantified using parameter sensitivities from FORM. Epistemic uncertainty is graphically reported as confidence bounds on fragility curves and mean estimate of safety factor, μ_{FS}. These curves were reported several vegetation conditions and compared to the non-vegetation case for the same potential sliding surface. In all cases the effect on p and μ_{FS} due to vegetation reflected those reported for deterministic results, but more importantly, the change in p and μFS due to vegetation is within than the single standard deviation confidence interval estimate for each. In other words, the range of possible values for the best estimate of FS and p is greater than the ΔFS or Δp due to vegetation effects. This condition becomes more dramatic as the sliding mass increases and root reinforcement effects are minimized.

Results for μ_{FS} illustrate the inherent conservatism of deterministic analyses, as FS consistently plots below μ_{FS}. The difference is due to evaluation of the probability density of FS at the design point for FORM analyses as opposed to evaluation of FS at the best-estimate or mean value of each random variable for deterministic analyses.

A biomass model was developed that incorporated an exponential decrease in root area ratio in the lateral direction and a lognormal distribution with depth. Scaling of root area ratio in three dimensions using allometric relationships with *DBH* that were verified using existing empirical

data. Outputs of the biomass model were used to determine the mechanical effect of trees on slope stability using the method of slices. Overall, results show that the biomass model can provide useful insight into the incremental effect of vegetation on levee stability, especially with respect to the spatial extent of roots and the root ball. While uniform root reinforcement effects and point loads may be sufficient to analyze infinite or large circular failure surfaces, incorporating the lateral extent of roots in 2D analyses is critical for the deeper circular and non-circular failure geometries that control levee stability.

The term "failure" has been consciously avoided throughout this document because the occurrence of a slope failure does not necessarily result in failure of an entire levee system. As such, conclusions described herein are generally applicable to vegetation effects for an individual slope stability assessment, but not for the overall performance of a levee. To evaluate the true overall effect of vegetation, results presented herein should be incorporated in an event tree analysis. However, given the relatively small magnitude of effects quantified herein, the influence of vegetation is expected to be small.

Vegetation effects can be quantified effectively using the methods described herein, and while there are endless scenarios that can be constructed to illustrate the potential for vegetation to cause levee failure, the overall effect on the levee is small when compared to other influencing factors such as strength or seepage. Although reliability analyses require extra computational effort and introduce cumbersome numerical issues, the FORM approach provides useful insight to the levee seepage and stability problem and incremental effects due to vegetation.

7.1 Future Research

While certain aspects of the biomass model could be improved through consideration of additional data, given the relatively small impact of vegetation on levee performance, additional effort may not be warranted. Regardless, an allometric spatial relationship of root diameter is necessary to appropriately define the reinforcing effect of roots, which is fundamentally related to root size and tensile strength for a given species. It is likely that the 3D LiDAR data such as obtained by Berry and Chung (2013) could provide such information.

Given the problems associated with high cohesion values from roots in the active zone of a slope stability surface, better modeling of root reinforcement effects may be had if tensile forces are used instead. This would require assumptions be made regarding the number and size of roots spatially in the root zone. Although it would be more difficult to implement in the slope stability source it may produce results with higher numerical stability.

Managing FORM analyses when convergence was difficult to achieve is time consuming. Future work with levee seepage and reliability, or any problem with the potential for discontinuous function response (e.g., finite element solutions or method of slices) should consider implementation of a response surface approach. A response surface uses discrete function evaluations to produce a smooth parametric surface for reliability analysis, thus eliminating discontinuities. While the function may lead to unrealistic design points, a solution can be checked for validity by evaluating the limit-state function at the response surface design point.

The source code developed for this research is capable of searching for minimum β surfaces; however, reaching a solution is computationally intensive. Incorporation of a response surface as described above would greatly improve computation time and allow for this functionality.

Parameter List

General:

FS = Factor of safety; ratio of resisting forces to driving forces, [–]

WSE = Water surface elevation, measured from base of levee, [m]

H = Levee height, [m]

γ = Unit weight of soil, [kN/m^3] or [pcf]

c = Soil cohesion, [kPa] or [psf]

ϕ = Soil friction angle, [$^\circ$]

K = Hydraulic conductivity, [m/s]

z_B = Thickness of blanket layer, [m]

Reliability and Probability:

R = Reliability of an event or condition, related to probability by $R = 1 - p$

P, p = Probaility of an event or condition, related to reliability by $p = 1 - R$

β = Reliability index, related to probability by: $p = \Phi(-\beta)$

x_i = Random variable i, of n total

$\mathbf{x}$ = Vector of n random variables

$\mathbf{u}$ = Vector of n random variables transformed to the standard normal space

$g(\mathbf{x})$ = Limit-state function

$\mathbf{x}^*$ = Design point in the original space

$\mathbf{u}^*$ = Design point in the standard normal space

α = Importance vector; sensitivity of β with respect to $\mathbf{x}$

$\delta =$ Sensitivity vector of β with respect to mean, $\delta_i = \mu_i \dfrac{\partial \beta}{\partial \mu_i}$

$\eta =$ Sensitivity vector of β with respect to standard deviation, $\eta_i = \sigma_i \dfrac{\partial \beta}{\partial \sigma_i}$

$\theta =$ Vector of parameters, θ_i, in reliability analysis, e.g., distribution, $g(\mathbf{x})$, etc.,

$\mathbf{p} =$ Vector of probability distribution parameters, p_i

Biomass, General:

$\hat{x} =$ Levee perpendicular direction, positive to land side of levee

$\hat{y} =$ Levee parallel direction

$\hat{z} =$ Depth below surface, downward positive

$\hat{l} =$ Radial distance from tree trunk center

$\theta =$ Angle in the horizontal plane relative to the downslope direction aligned with $\hat{x}$; counterclockwise positive from above

$O, C =$ Subscripts for oak (*Quercas lobata*) and cottonwood (*Populus fremontii*)

$DBH =$ Diameter at breast height, [m]

$RAR =$ Root Area Ratio, $[-]$

$RAR(x,y,z) =$ Point estimate of $RAR(z)$; $RAR(x,y,z) = f_{RAR}(z) \cdot \overline{RAR}(\mathrm{z})$, $[-]$

$RAR_{min} =$ Minimum Root Area Ratio considered in biomass model, $[-]$

$\overline{RAR} =$ Depth-averaged root area ratio, $[-]$

$\overline{RAR}_{xy} = \overline{RAR}$ at (x,y), integrated from surface to z_{max}, $[-]$

$\overline{RAR}_z = \overline{RAR}$ integrated from z_1 to z_2, $[-]$

$RCSA =$ Root cross-sectional area, [m^2]

$\alpha_0 =$ Biomass regression intercept ((Berry & Chung, 2013)), [ln m^2];

$A_{cyl} =$ Area of cylindrical virtual trench profile, per Berry and Chung (2013)

$A_0 =$ Biomass regression intercept, $[m^2]$; $A_0 = \exp(\alpha_0)$

$\nu =$ Rate of biomass decrease, $[-]$; ν_u, ν_d for upslope and downslope direction ($-\hat{x}$ and $+\hat{x}$, respectively)

$\Delta\nu_{ud} =$ Difference in biomass reduction rate, $[-]$; typically 0.5

$\beta_0, \beta_1 =$ Regression parameters, where subscripts refer to regressed variable;
linear regressions in arithmetic and logarithmic space

$B_x =$ Random variable for evaluating effects of biomass model parameters;
subscript refers to specific parameter x, e.g., B_{rb} for root ball, $[-]$

Biomass Lateral Extent:

$MRE =$ Maximum root extent measured across tree width (i.e., not radial), [m]

$L_{MRE} = MRE$ computed by biomass model using RAR_{min}, from trunk center, [m]

$L_u, L_d = L_{MRE}$ in upslope and downslope directions, measured from trunk center, [m]

$L_{rb} =$ Root ball radius measured from trunk center, [m]

$y_{MRE} =$ Maximum root extent in $\hat{y}$ direction, [m]

$y_{PS} =$ Plane-strain integration interval, measured along $\hat{y}$, [m]; typically set to y_{TS}

$y_{TS} =$ Tree spacing, measured along $\hat{y}$ between trunks, [m]

$\overline{RAR}_{PS} =$ Depth-averaged plane-strain Root Area Ratio, $[-]$; defined along $\hat{x}$

$RV =$ Root volume, $[m^3]$

$l_1 =$ Radial distance where $RAR = 1.0$, [m]

$d_1 =$ Single-root equivalent diameter; represents RAR at distance l, [m]

Biomass Vertical Extent:

$z_{pit} =$ Pit depth from uprooting by Peterson and Claassen (2012), [m]

$z_a =$ Average rooting depth, [m]

$z_{\%} =$ Depth above which specified percentage lies, [m]

$z_{50} =$ Median rooting depth, [m]

$z_{mo} =$ Mode rooting depth, [m]

$z_{max} =$ Maximum rooting depth, [m]

$z_{90a} =$ Ratio of z_{90}/z_a, used for setting vertical distribution spread, $[-]$

$f_{RAR}(z) =$ Density function of RAR with z,
integrated over $0 < z < z_{max}$) becomes $\overline{RAR}$, $[-]$

Biomass Engineering Parameters:

Δc_R = Effective soil cohesion increment due to roots, [kPa]

C_R = Root reinforcement factor, relating cohesion, Δc_R, to RAR, [kPa]

C_{po} = Root reinforcement limit, related to pullout, [kPa]

C_{rb} = Root reinforcement limit, related to root breakage, or rupture, [kPa]

m_t = Tree mass, [kg]

W_t = Tree weight, [kN]

ε_W = Root mean squared error of mass regression, [ln kg]

F_W = Force due to tree weight, [kN]

M_{crit} = Critical moment for uproting by Peterson and Claassen (2012), [kN· m]

M_w = Moment due to wind on tree, [kN· m]

C_w = Moment coefficient, relating M_w to DBH, [kN]

h_w = Acting heigh of wind load on tree, [m]

$F_{w,h}$ = Horizontal force due to wind on tree, [kN]

$F_{w,v}$ = Vertical force due to wind moment on tree, [kN]

$f_{w,v}$ = Vertical force distribution function within the root ball, [kN/m]

$x_{w,v0}$ = Hinge point location, where $f_{w,v}(x_{w,v0}) = 0,$ [m]

V_w = Wind velocity, [m/s]

A_t = Cross-sectional tree canopy, for computing wind load, [m^2]

X_t = Tree position for reliability analysis, measured in $\hat{x}$ direction relative to levee coordinate system, [m]

D_t = Diameter of tree for reliability analysis, [m]

References

Aitchison, J. & Brown, J. A. (1957). *The lognormal distribution with special reference to its uses in economics*. Cambridge University Press.

American Society of Civil Engineers. (2010). *So, you live behind a levee!: what you should know to protect your home and loved ones from floods*. Princeton Architectural Press.

Ang, A. H. & Cornell, C. A. (1974). Reliability bases of structural safety and design. *Journal of the Structural Division*, *100* (Proc. Paper 10777).

Ang, A. H. & Tang, W. H. (1975). *Probability concepts in engineering planning and design, Volume I, basic principles*. Wiley, New York.

Apel, H., Thieken, A. H., Merz, B., & Blöschl, G. (2004). Flood risk assessment and associated uncertainty. *Natural Hazards and Earth System Science*, *4*(2), 295–308.

Baecher, G. B. & Christian, J. T. (2003). *Reliability and statistics in geotechnical engineering*. Wiley & Sons, Inc.

Batool, A., VandenBerge, D., & Brandon, T. (2015). Practical application of blanket theory and the finite-element method to levee underseepage analysis. *Journal of Geotechnical and Geoenvironmental Engineering*, *141*(4).

Bellugi, D., Milledge, D. G., Dietrich, W. E., McKean, J. A., Perron, J. T., Sudderth, E. B., & Kazian, B. (2015). A spectral clustering search algorithm for predicting shallow landslide size and location. *Journal of Geophysical Research: Earth Surface*, *120*(2), 300–324.

Benjamin, J. R. & Cornell, C. A. (1970). *Probability, statistics, and decision for civil engineers*. McGraw-Hill, New York.

Benjasupattananan, S. (2013). *Deterministic and probabilistic approaches for modeling levee underseepage* (D.Eng. University of Delaware).

Benson, C. H. (1993). Probability distributions for hydraulic conductivity of compacted soil liners. *Journal of Geotechnical Engineering*, *119*(3), 471–486.

Berry, A. M. & Chung, S.-M. (2013). *Tree root architecture: how and where do tree roots grow on and in levees?* California Levee Vegetation Research Program.

Bischetti, G. B., Chiaradia, E. A., Simonato, T., Speziali, B., Vitali, B., Vullo, P., & Zocco, A. (2005). Root strength and root area ratio of forest species in Lombardy (Northern Italy). *Plant and Soil*, *278*(1), 11–22.

Bolte, A., Rahmann, T., Kuhr, M., Pogoda, P., Murach, D., & Gadow, K. v. (2004). Relationships between tree dimension and coarse root biomass in mixed stands of European beech (Fagus sylvatica L.) and Norway spruce (picea abies L. Karst.) *Plant and Soil*, *264*(1), 1–11.

Bourinet, J. (2010, July). *FERUM 4.1 User's Guide*.

Buijs, F., Simm, J., Wallis, M., & Sayers, P. (2005). *Performance and reliability of flood and coastal defences,* Joint Defra/EA Flood, Coastal Erosion Risk Management R&D Programme, Technical Report FS2318/TR 2, Department for Environment, Flood, and Rural Affairs.

California Levee Vegetation Research Program. (2011). *California future research needs/priorities*. Workshop on the Direction of Future Research to Study Woody Vegetation on Levees, December 13–14, 2011, Sacramento, CA.

Casciati, F. & Faravelli, L. (1985). Methods of non-linear stochastic dynamics for the assessment of structural fragility. *Nuclear Engineering and Design*, *90*(3), 341–356.

Casciati, F. & Faravelli, L. (1991). *Fragility analysis of complex structural systems*. Taunton, Somerset, England: Research Studies Press.

Cedergren, H. R. (1997). *Seepage, drainage, and flow nets*. John Wiley & Sons.

Chowdhury, K., Millet, R., Punyamurthula, S., Hong, G.-T., & Tollefson, N. (2012). It is seepage indeed—a sensitivity study on seepage and seepage-induced slope stability of levees. In *USSD annual meeting and conference* (pp. 659–689). New Orleans, Louisiana.

Chung, S.-M. (2013). *Tree root system architecture on levee slopes: 3D quantitative model building, biomass estimation, and spatial pattern characterization* (Doctoral dissertation, University of California, Davis).

Coder, K. D. (2010). *Root strength & tree anchorage*. Warnell School of Forestry & Natural Resources, University of Georgia.

Coder, K. D. (2014). *Trees & storm wind loads*. Warnell School of Forestry & Natural Resources, University of Georgia.

Cornell, C. A. (1969). A probability-based structural code. *ACI Journal Proceedings*, *66*(12).

Crow, E. L. & Shimizu, K. (1988). *Lognormal distributions: theory and applications*. Marcel Dekker.

Dalrymple, T. (1960). *Flood-frequency analyses, manual of hydrology: Part 3, flood-flow techniques water-supply paper 1543–A*. USGS.

Department of Water Resources, (2012a, June). *2012 Central Valley flood protection plan*. Central Valley Flood Protection Program.

Department of Water Resources, (2012b, June). *2012 Central Valley flood protection plan, Attachment 8E: levee performance curves*. Central Valley Flood Protection Program.

Department of Water Resources, (2012c). *Urban levee design criteria, FloodSAFE, California*.

Der Kiureghian, A. (1989). Measures of structural safety under imperfect states of knowledge. *Journal of Structural Engineering*, *115*(5), 1119–1140.

Der Kiureghian, A. (2005). First-and second-order reliability methods. *Engineering design reliability handbook*, 14–1.

Der Kiureghian, A. & Ditlevsen, O. (2009). Aleatory or epistemic? Does it matter? *Structural Safety*, *31*(2), 105–112.

Der Kiureghian, A. & Fujimura, K. (2009). Nonlinear stochastic dynamic analysis for performance-based earthquake engineering. *Earthquake Engineering & Structural Dynamics*, *38*(5), 719–738.

Der Kiureghian, A., Haukaas, T., & Fujimura, K. (2006). Structural reliability software at the University of California, Berkeley. *Structural Safety*, *28*(1), 44–67.

Ditlevsen, O. & Madsen, H. O. (2005). *Structural reliability methods*.

Drexhage, M. & Colin, F. (2001). Estimating root system biomass from breast-height diameters. *Forestry: An International Journal of Forest Research*, *74*(5), 491–497.

Duncan, J. M., O'Neil, B., Brandon, T. L., & VandenBerge, D. R. (2011). *Evaluation of potential for erosion in levees and levee foundations*. CGPR.

Duncan, J. M. & Wright, S. G. (2005). *Soil strength and slope stability*. New Jersey: John Wiley & Sons, Inc.

Fenton, G. A. & Griffiths, D. V. (2008). *Risk assessment in geotechnical engineering*. Wiley Online Library.

Fredlund, D. G. & Krahn, J. (1977). Comparison of slope stability methods of analysis. *Canadian Geotechnical Journal*, *14*(3), 429–439.

Freeze, R. A. (1975). A stochastic-conceptual analysis of one-dimensional groundwater flow in nonuniform homogeneous media. *Water Resources Research*, *11*(5), 725–741.

Gardoni, P., Der Kiureghian, A., & Mosalam, K. M. (2002a). Probabilistic capacity models and fragility estimates for reinforced concrete columns based on experimental observations. *Journal of Engineering Mechanics*, *128*(10), 1024–1038.

Gardoni, P., Der Kiureghian, A., & Mosalam, K. M. (2002b). *Probabilistic models and fragility estimates for bridge components and systems*. Pacific Earthquake Engineering Research Center, UC Berkeley, PEER 2002/13.

GEI Consultants, Inc. & HDR. (2015, October). *Embankment and foundation stability memorandum, Sacramento River East Levee Improvement Project, Sacramento, California*. for Sacramento Area Flood Control Agency.

Goff, N. L. & Ottorini, J.-M. (2001). Root biomass and biomass increment in a beech (fagus sylvatica L.) stand in North-East France. *Ann. For. Sci. 58*(1), 1–13.

Gray, D. H. & MacDonald, A. (1989). The role of vegetation in river bank erosion. In M. A. Ports (Ed.), *1989 national conference on hydraulic engineering*. New Orleans, LA: ASCE.

Gray, D. H., MacDonald, A., Thomann, T., Blatz, I., & Shields, F. D., Jr. (1991). *The effects of vegetation on the structural integrity of sandy levees*. USACE Environmental Laboratory, Technical Report REMR–EI–5.

Gray, D. H. & Ohashi, H. (1983). Mechanics of fiber reinforcement in sand. *Journal of Geotechnical Engineering*, *109*(3), 335–353.

Gray, D. H. & Sotir, R. B. (1996). *Biotechnical and soil bioengineering slope stabilization: a practical guide for erosion control*. John Wiley & Sons.

Greenwood, J. R. (2006). SLIP4EX—a program for routine slope stability analysis to include the effects of vegetation, reinforcement and hydrological changes. *Geotechnical & Geological Engineering*, *24*(3), 449.

Gumbel, E. J. (1958). *Statistics of extremes*. New York: Columbia University Press.

Haldar, A. & Mahadevan, S. (2000). *Probability, reliability, and statistical methods in engineering design*. John Wiley.

Hall, J., Deakin, R., Rosu, C., Chatterton, J. B., Sayers, P., & Dawson, R. (2003). *A methodology for national-scale flood risk assessment*.

Harr, M. E. (1996). *Reliability-based design in civil engineering*. Mineola, NY: Dover.

Harr, M. E. (2012). *Groundwater and seepage*. Courier Corporation.

Hasofer, A. M. & Lind, N. C. (1974). Exact and invariant second-moment code format. *Journal of the Engineering Mechanics Division,, ASCE*, *100*(1), 111–121.

Haukaas, T. (2003). *Finite element reliability and sensitivity methods for performance-based engineering*. University of California, Berkeley.

Haukaas, T. & Der Kiureghian, A. (2006). Strategies for finding the design point in non-linear finite element reliability analysis. *Probabilistic Engineering Mechanics*, *21*(2), 133–147.

Helsel, D. R. & Hirsch, R. M. (2002). *Statistical methods in water resources techniques of water resources investigations, Book 4, Chapter A3*. U.S. Geological Survey.

Hohenbichler, M. & Rackwitz, R. (1981). Non-normal dependent vectors in structural safety. *Journal of the Engineering Mechanics Division*, *107*(6), 1227–1238.

Holtz, R. D. & Kovacs, W. D. (1981). *An introduction to geotechnical engineering*. Prentice Hall.

HR Wallingford & University of Bristol. (2004). *Risk assessment for flood and coastal defence for strategic planning (RASP), R&D technical report W5B–030/TR*.

Hui, R., Jachens, E., & Lund, J. (2016). Risk-based planning analysis for a single levee. *Water Resources Research*, *52*(4), 2513–2528.

Intel Corporation, (2016). *Intel Parallel Studio XE Composer Edition for Fortran Windows, compiler 16.0, update 1*.

Interagency Advisory Committee on Water Data. (1982). *Guidelines for determining flood flow frequency, Bulletin 17B*. Hydrology Commission.

Jackson, R. B., Canadell, J., Ehleringer, J. R., Mooney, H. A., Sala, O. E., & Schulze, E. D. (1996). A global analysis of root distributions for terrestrial biomes. *Oecologia*, *108*(3), 389–411.

Jenkins, J. C., Chojnacky, D. C., Heath, L. S., & Birdsey, R. A. (2003). National-scale biomass estimators for United States tree species. *Forest Science*, *49*(1), 12–35.

Jenkins, J. C., Chojnacky, D. C., Heath, L. S., & Birdsey, R. A. (2004). Comprehensive database of diameter-based biomass regressions for North American tree species.

Jones, A. L., Kramer, S. L., & Arduino, P. (2002). *Estimation of uncertainty in geotechnical properties for performance-based earthquake engineering*. Pacific Earthquake Engineering Research Center.

Kelley, R. (1998). *Battling the inland sea: floods, public policy, and the Sacramento Valley*. Univ of California Press.

Ketchum, E., Perlea, M., Kynett, M., & Deus, A. (2011). Geotechnical risk and reliability evaluation of the levees protecting the City of Sacramento, California. In *Geo-frontiers 2011* (pp. 3018–3028). American Society of Civil Engineers.

Koduru, S. D. & Haukaas, T. (2010). Feasibility of form in finite element reliability analysis. *Structural Safety*, *32*(2), 145–153.

Kokutse, N. K., Temgoua, A. G. T., & Kavazoví, Z. (2016). Slope stability and vegetation: conceptual and numerical investigation of mechanical effects. *Ecological Engineering*, *86*, 146–153.

Kottegoda, N. T. & Rosso, R. (2008). *Applied statistics for civil and environmental engineers*. Blackwell Malden, MA.

Kulhawy, F. & Mayne, P. (1990). *Manual on estimating soil properties for foundation design* (tech. rep. No. EPRI–EL–6800). Electric Power Research Institute.

Langbein, W. (1960). Plotting positions in frequency analysis. *Flood frequency analysis: US Geol. Survey Water-Supply Paper*, 48–51.

Lanzafame, R., Teng, H., & Sitar, N. (2017). Stochastic analysis of levee stability subject to variable seepage conditions.

Law, J. (1944). A statistical approach to the interstitial heterogeneity of sand reservoirs. *American Institute of Mining, Metallurgical, and Petroleum Engineers*, *Technical Publication 7*(3), 202–221.

Lee, I. K., White, W., & Ingles, O. G. (1983). *Geotechnical engineering*. Pitmans Books Limited.

Limpert, E., Stahel, W. A., & Abbt, M. (2001). Log-normal distributions across the sciences: keys and clues: on the charms of statistics, and how mechanical models resembling gambling machines offer a link to a handy way to characterize log-normal distributions, which can provide deeper insight into variability and probability—normal or log-normal: that is the question. *BioScience*, *51*(5), 341–352.

Liu, P.-L. & Der Kiureghian, A. (1991). Optimization algorithms for structural reliability. *Structural Safety*, *9*(3), 161–177.

Lumb, P. (1966). The variability of natural soils. *Canadian Geotechnical Journal*, *3*(2), 74–97.

Lumb, P. (1971). Precision and accuracy of soil tests. In P. Lumb (Ed.), *Proceedings, first international conference on applications of statistics & probability to soil & structural engineering* (pp. 329–345). Hong Kong.

Makkonen, L. (2006). Plotting positions in extreme value analysis. *Journal of Applied Meteorology and Climatology*, *45*(2), 334–340.

MathWorks, I. (2015). Matlab release 2015b.

Montgomery, D. R., Schmidt, K. M., Dietrich, W. E., & McKean, J. (2009). Instrumental record of debris flow initiation during natural rainfall: implications for modeling slope stability. *Journal of Geophysical Research: Earth Surface*, *114*(F1).

Namm, B. H. & Berrill, J.-P. (2012). *Accounting for variation in root wood density and percent carbon in belowground carbon estimates*. U.S. Forest Service General Technical Report PSW–GTR–238.

Neuman, S. P. (1972). *Finite element computer programs for flow in saturated-unsaturated porous media*. Hydraulic Engineering Laboratory,Technion.

Nielsen, D., Biggar, J., & Erh, K. (1973). Spatial variability of field-measured soil-water properties. *California Agriculture*, *42*(7), 215–259.

Oliver, H. & Mayhead, G. (1974). Wind measurements in a pine forest during a destructive gale. *Forestry: An International Journal of Forest Research*, *47*(2), 185–194.

Pellinen, P. (1986). *Biomasseuntersuchungen im kalkbuchenwald*. Dissertation Forstl. Fachbereich Georg-August-Universität Göttingen. 145 pp.

Perlea, M. & Ketchum, E. (2011). Impact of non-analytical factors in geotechnical risk assessment of levees. In *Geo-risk 2011* (pp. 1073–1081). American Society of Civil Engineers.

Peterson, C. J. & Claassen, V. (2012). *Windthrow potential on levees: stability of two species of Central Valley trees on river levees, evaluated by static winching tests*. California Levee Vegetation Research Program.

Phoon, K.-K., Becker, D., Kulhawy, F. H., Honjo, Y., Ovesen, N., & Lo, S. (2003). Why consider reliability analysis for geotechnical limit state design? In *Proceedings of the international workshop on limit state design in geotechnical engineering practice: massachusetts institute of technology, usa, 26 june 2003* (p. 19). World Scientific.

Phoon, K.-K. & Kulhawy, F. H. (1999). Evaluation of geotechnical property variability. *Canadian Geotechnical Journal*, *36*(4), 625–639.

Polanco, L. & Rice, J. (2014). Reliability-based evaluation of the effects of geometry on levee underseepage potential. In *Geo-congress 2014 technical papers* (pp. 860–871).

Pollen, N. & Shields, F. D., Jr. (2007). Effects of removal of riparian vegetation on levee stability on the Sacramento River. In *AGU Fall Meeting abstracts*.

Pollen, N. & Simon, A. (2005). Estimating the mechanical effects of riparian vegetation on stream bank stability using a fiber bundle model. *Water Resources Research*, *41*(7).

Pollen, N. & Simon, A. (2006). Temporal and spatial variability in the root-reinforcement of streambanks: incorporating variations in soil shear strength and soil moisture into the rip-root model. In *World environmental and water resource congress 2006* (pp. 1–10).

Pollen-Bankhead, N., Simon, A., & Thomas, R. E. (2013). The reinforcement of soil by roots: recent advances and directions for future research. In *Treatise on geomorphology* (pp. 107–124). San Diego: Academic Press.

Punyamurthula, S., Shulters, J., Heinzen, R., Strnad, G., Kabir, N., & Bean, F. (2011). *The influence of vegetation on levee past performance—a review of historic data based on the levee evaluation program database*. URS Corporation. Prepared for California Department of Water Resources, Division of Flood Management.

Rackwitz, R. & Flessler, B. (1978). Structural reliability under combined random load sequences. *Computers & Structures*, *9*(5), 489–494.

Ricciardi, K. L., Pinder, G. F., & Belitz, K. (2005). Comparison of the lognormal and beta distribution functions to describe the uncertainty in permeability. *Journal of Hydrology*, *313*(3–4), 248–256.

Rice, J. & Polanco, L. (2012). Reliability-based underseepage analysis in levees using a response surface–Monte Carlo simulation method. *Journal of Geotechnical and Geoenvironmental Engineering*, *138*(7), 821–830.

Rickard, O. C. & Sitar, N. (2012). *bSLOPE: a limit equilibrium slope stability analysis code for iOS*. UC Berkeley Report UCB/GT/12–01.

Roering, J. J. (2008). How well can hillslope evolution models "explain" topography? simulating soil transport and production with high-resolution topographic data. *Geological Society of America Bulletin*, *120*(9-10), 1248–1262.

Roering, J. J., Schmidt, K. M., Stock, J. D., Dietrich, W. E., & Montgomery, D. R. (2003). Shallow landsliding, root reinforcement, and the spatial distribution of trees in the Oregon coast range. *Canadian Geotechnical Journal*, *40*(2), 237–253.

Schwarz, M., Lehmann, P., & Or, D. (2010). Quantifying lateral root reinforcement in steep slopes—from a bundle of roots to tree stands. *Earth Surface Processes and Landforms*, *35*(3), 354–367.

Seed, R. B., Cobos-Roa, D., Pestana, J. M., Athanasopoulos-Zekkos, A., & Inamine, M. (2012). U.S. levee and flood protection engineering in the wake of Hurricane Katrina. In *Geotechnical engineering state of the art and practice* (pp. 294–334).

Shewbridge, S. E. & Sitar, N. (1989). Deformation characteristics of reinforced sand in direct shear. *Journal of Geotechnical Engineering*, *115*(8), 1134–1147.

Shields, F. D. (2014). *Synthesis of levee vegetation research results (2007–2014)*. California Levee Vegetation Research Program, California Department of Water Resources.

Shields, F. D., Jr. & Gray, D. H. (1992). Effects of woody vegetation on sandy levee integrity. *JAWRA Journal of the American Water Resources Association*, *28*(5), 917–931.

Shinozuka, M., Feng, M. Q., Lee, J., & Naganuma, T. (2000). Statistical analysis of fragility curves. *Journal of engineering mechanics*, *126*(12), 1224–1231.

Shriro, M., Bray, J. D., Sitar, N., & Cobos-Roa, D. (2014). Influence of tree roots and mammal burrowing activity on levee performance: Volume 2—parallel trench wetting front test, North

levee of the American River at Cal Expo Sacramento, California. *University of California, Berkeley*, *UCB GT 13–03 vol. 2*.

Sibley, H. M., Vroman, N. D., & Shewbridge, S. E. (2017). Quantitative risk-informed design of levees. In *Geo-risk 2017*.

Singh, V. P. (1998). Log-Pearson Type III distribution. In *Entropy-based parameter estimation in hydrology* (pp. 252–274). Dordrecht: Springer Netherlands.

Sitar, N. & Cawlfield, J. D. (1984). Program `UNSAT1` modified from Neuman (1972) to run on IBM PC, December, 1984.

Sonnenberg, R., Bransby, M. F., Bengough, A. G., Hallett, P. D., & Davies, M. C. R. (2011). Centrifuge modelling of soil slopes containing model plant roots. *Canadian Geotechnical Journal*, *49*(1), 1–17.

Spencer, E. (1967). A method of analysis of the stability of embankments assuming parallel inter-slice forces. *Géotechnique*, *17*(1), 11–26.

Stathers, R., Rollerson, T., & Mitchell, S. (1994). *Windthrow handbook for British Columbia forests.* Ministry of Forests Research Program, Victoria, British Columbia, BC Working Paper 9401.

Stedinger, J. R. & Griffis, V. W. (2008). Flood frequency analysis in the United States: time to update. *Journal of Hydrologic Engineering*, *13*(4), 199–204.

Stokes, A. (1999). Strain distribution during anchorage failure of Pinus pinaster Ait. at different ages and tree growth response to wind-induced root movement. *Plant and Soil*, *217*(1), 17–27.

Sudret, B. & Der Kiureghian, A. (2000). *Stochastic finite element methods and reliability, a state-of-the-art report*. University of California, Berkeley.

Sudret, B. & Der Kiureghian, A. (2002). Comparison of finite element reliability methods. *Probabilistic Engineering Mechanics*, *17*(4), 337–348.

Tabarroki, M. (2011). *Computer aided slope stability analysis using optimization and parallel computing techniques* (Doctoral dissertation, University of Science Malaysia).

Thorne, C. R. (1990). Effects of vegetation on riverbank erosion and stability. *Vegetation and erosion*, 125–144.

URS Corporation. (2014). *Guidance document for geotechnical analyses, v14*. prepared for: California Department of Water Resources.

URS Corporation & Jack R. Benjamin & Associates, Inc. (2008a, May). *Delta Risk Management Strategy, Phase 1, levee vulnerability technical memorandum*. Prepared for California Department of Water Resources.

URS Corporation & Jack R. Benjamin & Associates, Inc. (2008b, December). *Delta Risk Management Strategy, Phase 1, Section 7, flood risk analysis*. Prepared for California Department of Water Resources.

U.S. Army Corps of Engineers. (1956). *Investigation of underseepage and its control, lower Mississippi River levees*. Waterways Experiment Station, Technical Memoradum (TM) 3–424.

U.S. Army Corps of Engineers. (1999). *Risk-based analysis in geotechnical engineering for support of planning studies*. Engineering Technical Letter (ETL) 1110-2-556.

U.S. Army Corps of Engineers. (2000). *Design and construction of levees*. Department of the Army, U.S. Army Corps of Engineers.

U.S. Army Corps of Engineers. (2005). *Design guidance for levee underseepage*.

U.S. Army Corps of Engineers. (2010). *Beyond the factor of safety: developing fragility curves to characterize system reliability*. Geotechnical and Structures Laboratory, SR–10–1.

U.S. Army Corps of Engineers. (2011). *Initial research into the effects of woody vegetation on levees, Volume III of IV: numerical model simulation*. ERDC.

U.S. Army Corps of Engineers. (2014a). *Development of envelope curves for predicting void dimensions from overturned trees*. ERDC, TR–14–27.

U.S. Army Corps of Engineers. (2014b). *West Sacramento Project, general reevaluation report, draft report documentation, hydraulic index*. Sacramento District.

U.S. Bureau of Reclamation & U.S. Army Corps of Engineers. (2015). *Reservoir and river stage exceedance probabilities, Chapter II–1, best practices in dam and levee safety risk analysis*.

Uzielli, M., Lacasse, S., Nadim, F., & Phoon, K.-K. (2006). Soil variability analysis for geotechnical practice. *Characterization and engineering properties of natural soils*, *3*, 1653–1752.

Veneziano, D., Casciati, F., & Faravelli, L. (1983). *Method of seismic fragility for complicated systems*.

Vick, S. G. (2002). *Degrees of belief: subjective probability and engineering judgment*. ASCE.

Vogel, R. M., Thomas, W. O., & McMahon, T. A. (1993). Flood-flow frequency model selection in Southwestern United States. *Journal of Water Resources Planning and Management*, *119*(3), 353–366.

Vorogushyn, S., Merz, B., & Apel, H. (2009). Development of dike fragility curves for piping and micro-instability breach mechanisms. *Nat. Hazards Earth Syst. Sci. 9*(4), 1383–1401.

Waldron, L. & Dakessian, S. (1981). Soil reinforcement by roots: calculation of increased soil shear resistance from root properties. *Soil science*, *132*(6), 427–435.

Wang, Y., Cai, Z., & Q, Z. (2011). Differential evolution with composite trial vector generation strategies and control parameters. *IEEE Transactions on Evolutionary Computation*, *15*(1), 55–66.

Water Resources Council, Hydrology Committee. (1967). *A uniform technique for determining flood flow frequencies*.

Watson, A. (2000). Wind-induced forces in the near-surface lateral roots of radiata pine. *Forest Ecology and Management*, *135*(1–3), 133–142.

Weibull, W. (1939). A statistical theory of the strength of materials. *Ingeniors Vetenskaps Akademien*.

Willardson, L. S. & Hurst, R. L. (1965). Sample size estimates in permeability studies. *Journal of the Irrigation and Drainage Division*, *91*(1), 1–10.

Wood, E. F. & Rodríguez-Iturbe, I. (1975). A Bayesian approach to analyzing uncertainty among flood frequency models. *Water Resources Research*, *11*(6), 839–843.

Wu, T. H., McKinnell Iii, W. P., & Swanston, D. N. (1979). Strength of tree roots and landslides on Prince of Wales Island, Alaska. *Canadian Geotechnical Journal*, *16*(1), 19–33.

Zhang, Y. & Der Kiureghian, A. (1995). Two improved algorithms for reliability analysis. In R. Rackwitz, G. Augusti, & A. Borri (Eds.), *Reliability and optimization of structural systems: proceedings of the sixth IFIP WG7.5 working conference on reliability and optimization of structural systems 1994* (pp. 297–304). Boston, MA: Springer US.

Ziemer, R. (1981). Roots and the stability of forested slopes, IAHS No. 132. *International Association of Hydrological Sciences, Christchurch, New Zealand*, *15*.

Appendix A

Probability Distributions

A.1 Normal

The normal, or Gaussian, distribution is commonly used to evaluate probabilistic science and engineering problems and also as a paradigm for understanding statistics and variability in general. It is also widely understood that 68.3, 95.4 and 99.7% of data from a sample will fall within 1, 2 and 3 standard deviations from the mean, denoted: $\mu \pm \sigma$, $\mu \pm 2\sigma$ and $\mu \pm 3\sigma$. Alternatively stated, if the concept is applied to the possible value of a variable described by the normal distribution: there is a 68.3% the value will be within 1 standard deviations from the mean, $\mu \pm \sigma$. Coefficient of variation, δ, is best understood as a measure of dispersion in the context of these bounds.

A normal distribution is symmetric about the mean, median and mode (all of which are equal) and has two parameters, μ and σ, equivalent to the population mean and standard deviation, $\bar{x}$ and $\bar{s}$. Although easy to understand and apply, the distribution can cause problems due to the asymptotic (i.e., non-zero) probability density for extreme values, which is why the lognormal distribution is often used as a substitute.

Distribution parameters μ and σ are scale and shape parameters, respectively. Increasing μ shifts the position of the distribution, whereas increasing σ flattens the bell-shaped curve that is such an iconic symbol of the normal. The title scale parameter refers to scaling of the$x$-axis, which has no effect on the overall shape of the distribution. Although they behave differently for each distribution, scale and shape parameters are a useful paradigm for understanding how probability density changes with changing parameter values.

Standard Normal

A random variable, U, with the standard normal distribution has a mean of zero and standard deviation of 1: $U \sim \mathrm{N}(0,1)$. All distributions can be tranformed to the standard normal distribution $X \rightarrow U$, which is a critical component of the FORM procedure. This is a useful construct for describing the value of a particular parameter with respect to the distribution average and standard deviation: the sign of u indicates a value above or below the median; magnitude of u is the distance from a central tendency measure scaled by fraction of standard deviation. For example, $u = -1.0$ is one standard deviation below the mean whereas $u = +2.3$ is 2.3σ above. Transformations between the standard normal space ("U-space") and original space ("X-space") provide a consistent frame-

work for discussing variability and interpreting results of reliability analyses. For a non-standard normal variable, transformation to the standard normal space is:

$$u = \frac{x-\mu}{\sigma} \tag{A.1}$$

The PDF and CDF of the standard normal are often denoted $\phi(\cdot)$ and $\Phi(\cdot)$, respectively.

A.2 Truncated Normal

Truncation of the normal distribution by specifying minimum or maximum values prevents the distribution carrying probability density to $\pm\infty$. Referred to as the truncated normal distribution (Kottegoda & Rosso, 2008), it is used when extreme values are not physically possible or may cause problems with numerical computations; see, for example, Baecher and Christian (2003) or Rice and Polanco (2012). Although typically used to cap the distribution tails, which have negligible probabiltiy density, truncation limits can have significant influence on the resulting PDF and CDF if care is not taken to consider the imposed changes. Notation of the truncated normal is: $X \sim \mathrm{N}_t(\mu,\sigma,x_l,x_u)$. Due to its relation to the normal distribution, the truncated normal uses parameters μ and σ; where needed, distribution paramters of the truncated normal will be labeled with a subscript t, thus $X \sim \mathrm{N}_t(\mu_t,\sigma_t,x_l,x_u)$ and δ_t. The PDF is found by scaling the normal PDF by cumulative probability density within the truncated limit(s) using the same parameters μ and σ. Thus, after Bourinet (2010):

$$f(x) = \begin{cases} \frac{1}{\sigma}\frac{\phi(x)}{\Phi(x_u)-\Phi(x_l)}, & \text{if } x_l \le x \le x_u \\ 0, & \text{otherwise.} \end{cases} \tag{A.2}$$

$$F(x) = \begin{cases} 0, & \text{if } x < x_l \\ \frac{\Phi(x)-\Phi(x_l)}{\Phi(x_u)-\Phi(x_l)}, & \text{if } x_l \le x \le x_u \\ 1, & \text{if } x > x_u \end{cases} \tag{A.3}$$

Central tendency measures are:

$$x_a = \mu - \sigma\frac{\phi(x_u)-\phi(x_l)}{\Phi(x_u)-\Phi(x_l)} \tag{A.4}$$

$$x_{50} = \mu + \sigma\Phi^{-1}\left(\frac{\Phi(x_u)+\Phi(x_l)}{2}\right) \tag{A.5}$$

$$x_{mo} = \begin{cases} x_l, & \text{if } \mu < x_l \\ \mu, & \text{if } x_l \le \mu \le x_u \\ x_u, & \text{if } \mu > x_u \end{cases} \tag{A.6}$$

Variance of the distribution, σ_t^2, in terms of the distribution mean, x_a, is:

$$\sigma_t^2 = \mu^2 + \sigma^2 - \sigma\left\{\frac{\sigma\left[\left(\frac{x_u-\mu}{\sigma}\right)\phi(x_u) - \left(\frac{x_l-\mu}{\sigma}\right)\phi(x_l)\right] + 2\mu\left[\phi(x_u)-\phi(x_l)\right]}{\Phi(x_u)-\Phi(x_l)}\right\} - x_a^2 \tag{A.7}$$

A.3 Lognormal

Many civil engineering applications have incorporated the lognormal distribution (Benjamin & Cornell, 1970), and it is widely used in other scientific fields (Aitchison & Brown, 1957; Crow & Shimizu, 1988). A random variable, X, is lognormally distributed if the logarithm of X is normally distributed, and is described by parameters λ and ζ such that $X \sim \text{LN}(\lambda, \zeta)$. This distribution is skewed right, defined only for non-negative values and has non-equal mean, median and mode; see Ang and Tang (1975) for a derivation of the distribution and notable properties. As illustrated in Figure A.1, the distribution becomes more narrow and skewed for increasing ζ, and although the median ($x_{50} = \lambda$) is held fixed, the mean (x_a) and mode (x_{mo}) diverge. Since the logarithm of X is normal, λ and ζ can also be thought of as the distribution parameters of $\ln X$ such that $\ln X \sim \text{N}(\mu_{\ln X} = \lambda, \sigma_{\ln X} = \zeta)$. The right side of Figure A.1 illustrates the Gaussian shape of the distribution when plotted as $\ln X$ on the horizontal axis. This property causes statistical paradigms of the normal distribution to be used for understanding variability of the lognormal variable; however, care must be taken to heed the mathematical implications (Limpert et al., 2001). For example, rather than $\mu \pm \sigma$ containing 68.3% of the distribution it is actually $X = \exp(\lambda \pm \zeta)$. While the lognormal distribution is widely used in geotechnical literature (Baecher & Christian, 2003; Benjamin & Cornell, 1970; Crow & Shimizu, 1988; Harr, 1996; USACE, 1999; Uzielli et al., 2006), varied nomenclature used by different scientific fields make interpretation of the distribution, parameters and population statistics difficult. Thus, care is taken in this document to define and adhere to the following concepts and nomenclature:

- λ and ζ are distribution parameters of the *lognormally* distributed random variable X; they also represent the mean and standard deviation of the *normally* distributed random variable $\ln X$
- μ is the arithmetic mean of the lognormally distributed variable X
- σ is the standard deviation the lognormally distributed variable X
- δ is the coefficient of variation of the lognormally distributed random variable X ($\delta = \sigma/\mu$)

Distribution parameters can be found from sample mean and standard deviation:

$$\begin{aligned} \lambda &= \ln\mu - 0.5\zeta^2 \\ \zeta &= \sqrt{\ln(1+\delta^2)} \end{aligned} \tag{A.8}$$

Furthermore, when δ is relatively small (below about 0.30) $\zeta \simeq \delta$ (Ang & Tang, 1975). Central tendency measures of X can be related to the distribution parameters:

$$\begin{aligned} \textit{mean}: \quad \mu = x_a &= e^{\lambda+0.5\zeta^2} \quad \rightarrow \quad \lambda = \ln\mu - 0.5\zeta^2 \\ \textit{median}: \quad x_{50} &= e^{\lambda} \quad \rightarrow \quad \lambda = \ln x_{50} \\ \textit{mode}: \quad x_{mo} &= e^{\lambda-\zeta^2} \quad \rightarrow \quad \lambda = \ln x_{mo} + \zeta^2 \end{aligned} \tag{A.9}$$

Finally, σ can be found in terms of distribution parameters:

$$\sigma = e^{\lambda+0.5\zeta^2}\sqrt{e^{\zeta^2}-1} \tag{A.10}$$

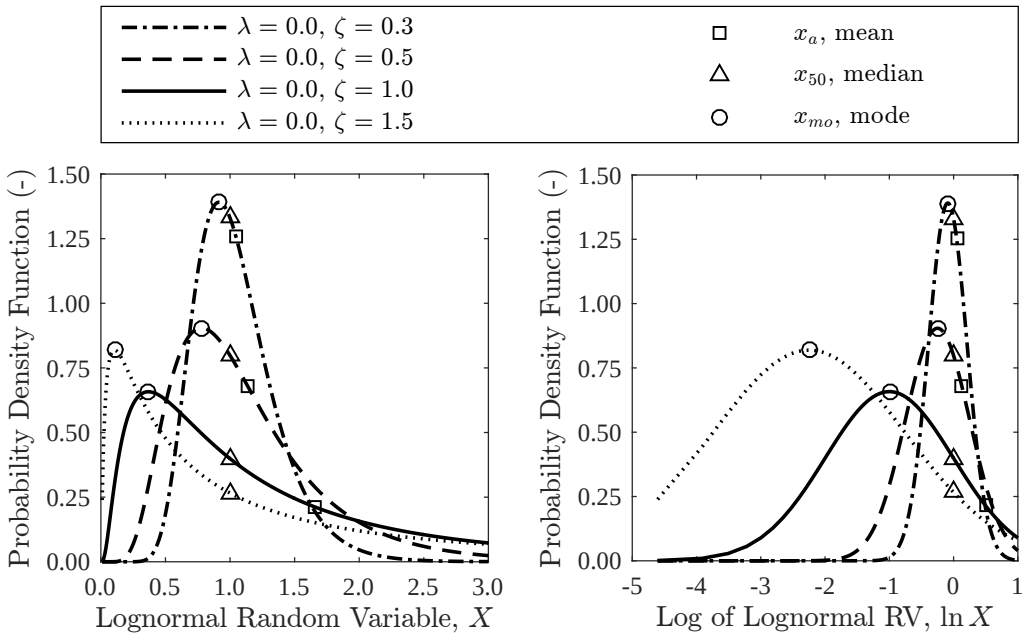

Figure A.1: Lognormal Distribution PDF for $\lambda = 0$ and Various ζ

Transformation of a lognormal variable to the standard normal space is:

$$U = \frac{\ln X - \lambda}{\zeta} \tag{A.11}$$

When compared with Equation A.1 it is easy to see the relationship of λ and ζ to a normally distributed $\ln X$ as an analogue for the relationship of μ and σ to a normally distributed X. Note that the translation of $\ln X$ by λ implies the standard variate U represents distance from the median of the variable, since distribution parameter λ represents the sample median.

Understanding dispersion of the distribution is essential for evaluating the influence of lognormal variables in reliability analyses. Unfortunately empirical data is almost always described in terms of the sample mean, which is a misleading measure of central tendency for a skewed distribution since x_a is dominated by extreme values. Inequalities $z_a > z_{50}$ and $z_{50} > z_{mo}$ are always true (Ang & Tang, 1975), and the differences become larger as ζ and δ increase. Because the median is a much more stable statistical value for skewed distributions, and is actually the parameter λ, it should be used to evaluate dispersion. Equation A.9 can be used to show the ratio of mean and mode to the median are only dependent on ζ:

$$\begin{aligned} X_a/X_{50} &= \exp(0.5\zeta^2) \\ X_{mo}/X_{50} &= \exp(-\zeta^2) \end{aligned} \tag{A.12}$$

Thus, as dispersion increases the mean and mode become increasingly far apart, with the mean quickly diverging for $\zeta \gtrsim 1$ (Figure A.2). Rewriting the standard normal transformation (Equation A.11) shows the dependence of confidence intervals on ζ:

$$X_{\lambda+\zeta} = \exp(\lambda \pm \zeta) = X_{50}\exp(\pm\zeta) \tag{A.13}$$

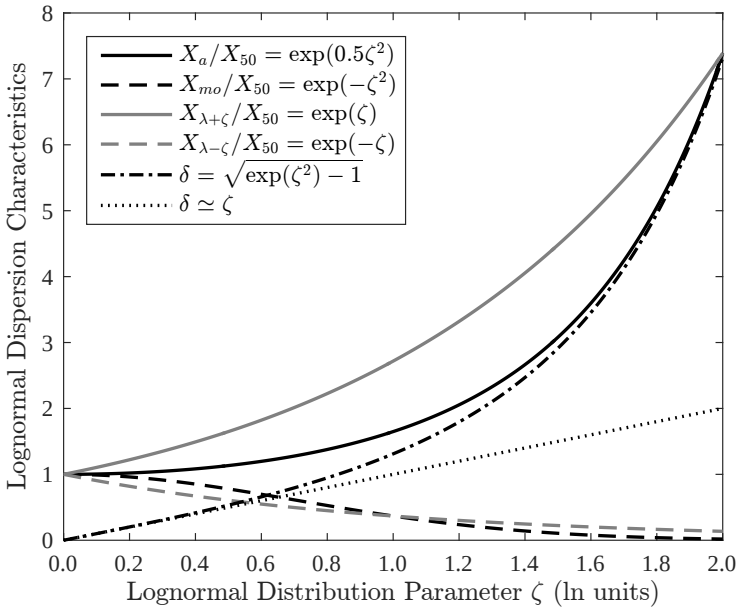

Figure A.2: Dispersion Effects of the Lognormal Distribution

As analogue to the normal distribution, 68.3% of the lognormal distribution is within the bounds defined by the multiplication and division of the median by $\exp(\zeta)$, which is illustrated in Figure A.2. The mode is very close to the $\exp(-\zeta)$ for all values of ζ; however, the mean remains well below the upper confidence bound until steeply rising beyond $\zeta \gtrsim 1.5$. In summary, evaluation of the dispersion characteristics show the lognormal distribution to be similar to the normal distribution in shape for low values of ζ. Alternatively, as ζ increases the measures of central tendency and distribution spread becomes increasingly extreme. Thus, care should be taken when selecting lognormal distribution parameters that they are representative of the random variable population.

A.4 Extreme Value Distributions

Many problems are governed by the smallest or largest possible values that might be encountered from a population, which represent tail regions of a random variable probability distribution. Flood frequency is an excellent example of this case: while the flow at any given point in time may follow a normal distribution, it is the infrequent peak flows that drive design of a flood control system. Extreme value distributions are used to model the frequency with which maximum or minimum values are expected to occur. While Gumbel (1958) is often cited as a classical reference, Kottegoda and Rosso (2008) present the generalized form succinctly, and numerous modern texts describe other important applications and characteristics (Baecher & Christian, 2003; Benjamin & Cornell, 1970; Haldar & Mahadevan, 2000). Only the Type I Largest, or Gumbel distribution was used for analyses in this document, which has two parameters, u and α controlling location and scale of the PDF. Sampling of extreme values from a distribution with an exponential tail, such as the normal, converge to the Gumbel$\sim$ Gmb(u, α). Expressions for the PDF and CDF are:

$$f(x) = \alpha\, e^{-\alpha(x-u)} \exp\left[-e^{-\alpha(x-u)}\right] \tag{A.14}$$

$$F(x) = \exp\left[-e^{-\alpha(x-u)}\right] \tag{A.15}$$

Central tendency measures and standard deviation can be computed from the distribution parameters:

$$x_a = u + \frac{\gamma}{\alpha} \tag{A.16}$$

$$x_{50} = u - \frac{\ln(\ln(2))}{\alpha} \tag{A.17}$$

$$x_{mo} = u \tag{A.18}$$

$$\sigma = \frac{\pi}{\sqrt{6}\,\alpha} \tag{A.19}$$

where γ is Euler's constant, 0.57721566.

A.5 Gamma

The gamma distribution has several forms and special cases that include other distributions, including the exponential and chi-squared. Time to the kth arrival in a Poisson process can be modeled with a gamma distribution, although it is not necessary to limit k to the integer case (Kottegoda & Rosso, 2008). Represented $Gam(k,\lambda)$, the distribution PDF and CDF are:

$$f(x) = \frac{\lambda(\lambda x)^{k-1}\exp(-\lambda x)}{\Gamma(k)} \tag{A.20}$$

$$F(x) = \frac{\Gamma(k,\lambda x)}{\Gamma(k)} \tag{A.21}$$

where $\Gamma(k)$ is the gamma function and $\Gamma(k,\lambda x)$ is the incomplete gamma function. Parameters k and λ represent shape and rate of the distribution; other forms of the gamma often use a scale parameter, which is the inverse of rate. Changing only the shape parameter, k, modifies the appearance of the PDF, with higher values moving the mode further to the right, reducing skew; for $k \leq 1$ the distribution has an exponential shape (i.e., a Poisson process). Changing only the rate parameter, λ, scales the x-axis without changing the PDF shape. Central tendency measures and standard deviation are found from the distribution parameters:

$$x_a = \frac{k}{\lambda} \tag{A.22}$$

$$x_{mo} = \frac{k-1}{\lambda} \text{ when } k \geq 1 \tag{A.23}$$

$$\sigma = \frac{\sqrt{k}}{\lambda} \tag{A.24}$$

There is no general form for the median x_{50}.

In United States practice, WSE is often modeled with a Log-Pearson III distribution (Section A.7), which is a shifted form of the gamma distribution. Log-Pearson is similar to relationship between lognormal and normal distribution, where a variable X has Log-Pearson III if $\ln X$ has Pearson III.

A.6 Functions of Random Variables

A stochastic parameter of interest is sometimes most easily understood as a mathematical combination of other random variables, for example, the ratio of hydraulic conductivity, K_r. Probability distributions can be derived for the function of random variables in terms of the stochastic parameters of the participating variables. While there are many exact and approximate strategies (Ang & Tang, 1975; Baecher & Christian, 2003; Fenton & Griffiths, 2008; Harr, 1996; USACE, 1999), only two simple cases will be discussed here. As proven by the central limit theorem, a random variable, X, represented by the sum of normally distributed random variables, x_i, is itself normally distributed. It follows that the mean and standard deviation of X are given by:

$$\mu_X = \sum_i \mu_i \qquad \sigma_X = \sqrt{\sum_i \sigma_i^2} \tag{A.25}$$

Now consider a function of random variables, X, represented by the product of logrnomally distributed random variables x_i and take the logarithm of the function:

$$X = \prod_i x_i \qquad \rightarrow \qquad \ln X = \sum_i \ln x_i \tag{A.26}$$

This is why the lognormal distribution is often referred to as a multiplicative distribution (Baecher & Christian, 2003; Benjamin & Cornell, 1970). Since $\ln X$ is normal when X is normal, it follows that the lognormal distribution parameters of X can be found similarly to the normal case:

$$\lambda_X = \sum_i \lambda_i \qquad \zeta_X = \sqrt{\sum_i \zeta_i^2} \tag{A.27}$$

Thus, for the example of hydraulic conductivity ratio, $K_r = K_{a,h}/K_{b,v}$:

$$\lambda_{K_r} = \lambda_{K_{a,h}} - \lambda_{K_{b,v}} \qquad \zeta_{K_r} = \sqrt{\zeta_{K_{a,h}}^2 + \zeta_{K_{b,v}}^2} \tag{A.28}$$

A.7 Flood Frequency

Hydrologic Records

Flood control systems must be designed to withstand the highest water level experienced in a given year, which are aleatory events that can vary substantially between watersheds and over time as watershed development occurs. Flood frequency relations are used to describe the annual probability of exceeding a given water level and are created using a number of analytic methods that typically consider a record of annual peak flow (Helsel & Hirsch, 2002). Although there are different approaches to processing flow data depending on dataset condition and application

(U.S. Bureau of Reclamation & U.S. Army Corps of Engineers, 2015), the Weibull (1939) formula is widely used in practice, which computes the mean fraction of trials exceeding x in n trials:

$$f_{X>x} = \frac{x}{n+1} \tag{A.29}$$

Hydrologic records are processed such that maximum flow from each year is identified and ranked against all years in the record from 1 to N for smallest to largest data. Thus, when applied to flood frequency, the Weibull formula represents the mean value of probability, P, that the peak annual flow of rank m is exceeded in N trials (Langbein, 1960):

$$P = \frac{m}{N+1} \tag{A.30}$$

Note that the mean value, P, is not probability of exceedance for a water level associated with rank m in N years, which must be found using the binomial distribution. Equations for exceedance probability, P_e, and associated return period, R, described succinctly by Makkonen (2006), are:

$$P_e = 1 - P = \frac{N-m+1}{N+1} \qquad R = \frac{1}{1-P} = \frac{1}{P_e} = \frac{N+1}{N-m+1} \tag{A.31}$$

Common practice has long plotted the result on Gumbel paper (a type of scaled probability paper) for estimating return period, where the Weibull equation (and other similar ranked estimators) for P is referred to as plotting position (Dalrymple, 1960; Helsel & Hirsch, 2002; U.S. Bureau of Reclamation & U.S. Army Corps of Engineers, 2015). Equations A.30 and A.31 are mean probability estimates of extreme values observed in any given year, and the empirical data can be modeled with a number of distributions to evaluate the probability associated a flood level of interest.

Probability Distributions for High Water Events

Numerous probability distributions have been used for flood frequency evaluations, including (Benjamin & Cornell, 1970; Dalrymple, 1960; Gumbel, 1958; Helsel & Hirsch, 2002); see Appendix 14 of IACWD (1982) for a select overview, and Vogel et al. (1993) for a quantitative comparison of several distributions. The Hydrology Commission of the Water Resources Council, charged by United States law with assessing water supplies and regional river basin plans, has recommended use of the Log-Pearson III distribution for estimating flood frequency since 1967 (IACWD, 1982; WRC, 1967). US policy is to use plotting position functions and a specified procedure to fit the three parameters of to hydrologic records. Although there may be room for improvement in fitting procedures, the distribution has proven generally successful (Stedinger & Griffis, 2008); Singh (1998) provides a succinct history and formulation of the distribution. URS/JBA (2008b) used the Log-Pearson III in for flows in the Delta. Bayesian statistics have been used to create composite weighted distribution models (Wood & Rodríguez-Iturbe, 1975); a relatively recent study considered Lognormal, Gumbel, Weibull and Log-Pearson III, corresponding to increasing weight assigned from the analysis (Apel et al., 2004).

Appendix B

Numeric Considerations

This Appendix summarizes numerical issues encountered with integration of the seepage, stability and reliability source code used for this research. All analyses were completed using Matlab (MathWorks, 2015), which incorporated the following existing applications: `UNSAT` for seepage analysis (Sitar & Cawlfield, 1984; Neuman, 1972), written in Fortran; `USlopeM` for stability analysis (Tabarroki, 2011), written in Matlab; and `FERUM` for reliability analysis (Bourinet, 2010; Der Kiureghian et al., 2006). In general, numerous Matlab scripts and functions were written to facilitate communication of software input/output between `UNSAT`, `USlopeM` and `FERUM`, process results of analyses and troubleshoot source code "bugs" that arose during implementation. Most numerical issues were related to precision of various parameters and computation of the limit-state function gradient.

Analyses were run on three different computers with the following specifications:

- 4-core Intel Core i5-3330 processor at 3.00GHz with 8 GB memory running Windows 7
- 4-core Intel Core i7-2600 processor at 3.40GHz with 16 GB memory running Windows 7
- 12-core Intel Xeon E5-2630 processor at 2.60GHz with 32 GB memory running Windows 8

A steady-state seepage solution generally requires 10 seconds to solve, whereas a single evaluation of FS for stability requires 0.1 seconds. A minimum FS search requires anywhere from tens of minutes to tens of hours depending on the whether a circular or non-circular surface is analyzed, the number of kinematically admissible surfaces found by the search algorithm and the number of processor cores available. In general, the maximum number of FS evaluations is on the order of 1e4 for circular surfaces, whereas non-circular surfaces are on the order of 1e+5. If a coarse set of vertices is used for non-circular surfaces (i.e., if a jagged or block-like surface is acceptable) non-circular surface searches could be reduced closer to 1e+4 FS evaluations.

Reliability analyses are dependent on the number of random variables and whether seepage must be evaluated; no parallel capability was implemented. Each random variable adds a function evaluation due to the finite difference approximation required to estimate $\nabla g(\mathbf{x})$. For FOSM methods, the number of evaluations is thus on the order of $1+n_{rv}$. A FORM analysis is iterative and the number of iterations, n_i is dependent on convergence criteria described in this Appendix, thus, the number of function evaluations is on the order of $n_i(1+n_{rv})$. Given that a n_i is typically greater than three, a reliability analysis with seepage generally takes 5–10 minutes for FORM and 1 minute with FOSM methods. Without seepage parameters as random variables, computation

times drop to tens of seconds. For minimum reliability index sliding surface searches, computations times increase dramatically, since 1e4 to 1e5 reliability evaluations are required; these can take over a day for non-circular surfaces even when the parallel processing is employed.

B.1 Precision in Seepage and Stability Analyses

Quantitative analyses for levee failure modes (e.g., FS against blanket heave or stability) need not be reported with more precision that three or four significant digits due to the uncertainty of underlying geotechnical parameters. However, some computational algorithms require increased precision to reach a solution; for example, slope stability methods of slices should be solved with a precision of at least 0.0001 to search for an solve the minimum FS failure surface (Duncan & Wright, 2005). Because the method of slices used for stability computations solves system of equations for force and moment balances using an implicit iteration scheme, a single tolerance determines precision of the resulting FS. Precision of seepage solutions is more subtle, as a stable result is dependent on a transient analysis reaching a steady state. Furthermore, coupling of pore pressures from a seepage solution into the stability computation results in a dependence of stability precision on that of the seepage algorithm. As such, stability results can be used to understand the effect of various parameters on precision of levee failure modes. To illustrate, Figure B.1a plots 501 values of FS for a 0.5 m range of WSE, corresponding to an increment of $\Delta WSE = 0.001$ m (using the landside hinge circle from Figure 4.3. There are obvious steps in what should theoretically be a smooth relationship between increasing pore pressures from higher WSE and decreasing FS. The steps are discontinuities caused by the discrete finite element seepage solution. WSE is specified as head at every finite element node on the waterside levee slope and there exists a set of consecutive nodes where pressure head switches from a positive value to zero, defining the beginning of the phreatic surface as it enters the embankment prism. When the pair of bounding nodes changes and discrete nature of the finite element mesh cause the resulting steps in the pore pressure solution. When an arbitrary range of WSE from Figure B.1a (i.e., WSE from 4.60 to 4.68 m) is used to create a least-squares linear regression of $FS(WSE)$ and subtracted from computed values, an estimate of the numeric error can be found, as presented in Figure B.1b. Each step is approximately $\Delta FS = 0.002$ and occurs for an increase in WSE on the order of 10 cm.

Other variables used in seepage and stability analyses cause the discontinuous step effect in computed values, although the scale is much smaller than that for WSE described above due to finite element discretization. Critical increments for each parameter of interest are described below:

- Strength and unit weight properties (i.e., c, ϕ and γ, referred to here as X,) cause a step of $\Delta FS =$1e$-$7 at increments of $\Delta X =$1e$-$5 (1e$-$6 for c_B) in SI units; controlled directly by a method of slice precision of 1e$-$6 in this case
- Hydraulic conductivity ratio, K_r causes a step of $\Delta FS =$1e$-$8 at increments of $\Delta K_r =$1e$-$8
- Blanket layer thickness, z_B causes a step of $\Delta FS =$1e$-$5 at increments of $\Delta z_B =$1e$-$3 m; due to limit in precision of finite element mesh geometry, but issues may also arise if the bottom of the blanket layer intersects the sliding surface being analyzed (Section B.2)
- Water surface elevation, WSE causes a step of $\Delta FS =$1e$-$7 at increments of $\Delta WSE =$1e$-$5 m; this is a smaller scale effect than that of finite element discretization described above

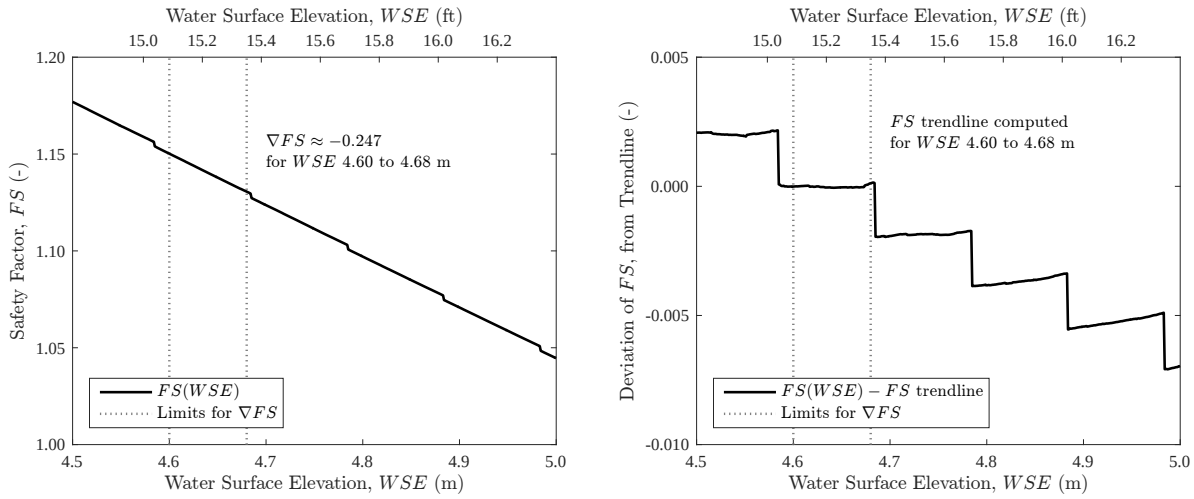

(a) $FS(WSE)$ with trendline limits

(b) Error in FS as deviation from trendline

Figure B.1: Precision of FS with changing WSE using an increment of $\Delta WSE = 0.001$. Portion between dotted lines in (a) is used to compute a trendline for calculating deviation of FS in (b). Results in this Figure are used for gradient (∇FS) computations in Figure B.2.

Strength, unit weight and hydraulic conductivity ratio cause discontinuities in FS, but their occurrence is generally small and can be directly controlled by tolerance and precision settings within the software. Blanket layer thickness produces a ΔFS that is orders of magnitude greater and cannot be controlled without significant source code modification; however, since the step in ΔFS occurs over a small Δz_B, a relatively large increment can be selected to minimize the resulting error. In contrast, discontinuities in FS caused by changes in ΔWSE on the order of 0.1 m are significant and must be considered when performing reliability analyses.

B.2 Seepage Model

Seepage analyses are completed using a modified version of program `UNSAT1`, written in Fortran by Neuman (1972) and modified by Sitar and Cawlfield (1984). Several changes were made to `UNSAT1` (elsewhere in this document referred to as `UNSAT`) to allow compatibility with reliability analyses completed with `FERUM`, including:

- implemented dynamic memory allocation for finite element solver
- increased precision of hydraulic conductivity (K) material property from `E10.3` to `E22.15` to allow sufficient precision of output
- increased precision of pressure head (ψ) input and solution output from `E10.3` to `E24.15`
- increased maximum number of materials defined by input file

The source code was compiled with Parallel Studio XE by Intel (2016) on a PC running Windows 7, 64-bit. All other modifications consisted of relatively minor reformatting of input and output

files and command line printing. Initial precision of K and ψ UNSAT were not accurate enough to allow for small changes in WSE, K_r or z_B required for converging to a the FORM solution (Lanzafame et al., 2017).

Blanket Layer and Finite Element Mesh

There are two numerical issues associated with the blanket layer: precision of z_B in the finite element mesh and numerical noise in computed pore pressures. Nodal positions in UNSAT were originally specified with a precision of E10.3, which unfortunately cannot be modified without significant restructuring of the Fortran source code due to the maximum input file line width. As such, increments of z_B less than $1e{-}3$ may not produce a change in seepage or stability response, which is consistent with the behavior recognized in Section B.1. Numerical noise arises in results when the finite element mesh is changed due to an adjusted blanket layer thickness. Pore pressures applied at the base of each slice in the slope stability algorithm are interpolated between finite element nodes using shape functions is therefore dependent on the finite element mesh. Input files for UNSAT specify coordinates of FEM nodes, the position of which are determined from the bottom of the model up. As such, a change in blanket layer thickness changes the vertical coordinates of all nodes within the blanket layer. Early attempts at solving the seepage-stability algorithm with FORM could not find a solution due to small-scale variations in the computed FS, caused by a mesh that was changing at each iteration. For example, $\Delta z_B = 1.0$ m generally resulted in $\Delta FS \sim 0.05$ but local variations of $\Delta FS \sim 0.005$ occurred on a much smaller scale of z_B. Since FORM requires a continuously differentiable limit-state function local variations in the derivative prevented convergence to a design point. The solution was to allow nodal points nearest the blanket layer base to be adjusted vertically to match the value of z_B required by each FORM iteration; only a single row of nodes at the bottom of the blanket layer were adjusted, keeping all other nodes constant. Furthermore, the minimum value of the truncated normal distribution for z_B was set to a value greater than the deepest potential slip surface to be considered, preventing the FORM algorithm from modifying the finite element mesh within the sliding mass during an iteration and/or minimum β slip surface search.

B.3 Stability Model

A copy of the Matlab source code for USlopeM (Tabarroki, 2011) was used to develop the slope stability application used for analyses in this document, along with documentation of the algorithm by Rickard and Sitar (2012). The software uses the generalized limit equilibrium (GLE) formulation (Fredlund & Krahn, 1977) to solve Spencer's method of slices (Spencer, 1967) and incorporates a search algorithm unique to slope stability applications to find the minimum safety factor sliding surface (Rickard & Sitar, 2012; Wang et al., 2011). To produce software capable of integrating seepage, stability and reliability together significant modifications to USlopeM were needed, as listed below:

- integration of cross-section geometry and material properties with UNSAT
- evaluation of pore pressure at position (x, y) of slice base midpoints using Delaunay triangulation of finite element solution of UNSAT

- inclusion of line loads and moments into GLE formulas for solving Spencer's method of slices
- limiting strength in the passive zone (bottom of slope) to maximum shear strength on the failure plane defined by a Mohr-Coulomb failure envelope (Duncan & Wright, 2005)
- modification of GLE equations and Newton-Raphson solution for FS to apply rapid loading (e.g., wind) to a sliding mass but prevent it from influencing drained soil strength
- correcting a sign error for pore pressure in the GLE normal force equation
- integration of random variable values and software input/output with reliability software `FERUM` (Bourinet, 2010) allowing `USlopeM` to perform evaluation of limit-state function
- integration of `FERUM` within search algorithm of `USlopeM` to search for minimum reliability index (maximum probability) sliding surface

Justification of and analytic results from these modifications are presented elsewhere in this document.

Gradient of Stability Response

Levee response can be measured in terms of safety factor against heave, piping or stability, pore pressures for a specific location, breakout height or any number of computed parameters. Gradient of the response with respect to a specific input parameter, x_i, can be represented by $\nabla_X f(X)$, computed with a forward finite difference scheme:

$$\nabla_{x_i} f(x_i) = \frac{\partial f(x_i)}{\partial x_i} = \frac{f(x_i + \Delta x_i) - f(x_i)}{\Delta x_i} + \varepsilon \tag{B.1}$$

Thus if the error term is left off, the gradient can be approximated:

$$\nabla_{x_i} f(x_i) \simeq \frac{\Delta f(x_i)}{\Delta x_i} = \frac{f(x_i + \Delta x_i) - f(x_i)}{\Delta x_i} \tag{B.2}$$

The response gradient is closely related to gradient of the limit-state function; therefore, it is important to understand the sources of numerical discontinuities that prevent computation of a smooth function.

Gradient must be approximated using a discrete selection of Δx_i. As illustrated in Figure B.2a (using the same values as in Figure B.1), $\nabla_{WSE} FS(WSE)$ (hereafter referred to as ∇FS) is computed for various ΔWSE using $WSE = 4.60$ m as a reference point; all values are plotted such that the x–axis represents $WSE = 4.60 + \Delta WSE$. Clearly the numerical noise in ∇FS is significant and localized, where values range between -0.38 and -0.23, and the sawtooth relationship is such that each discontinuity corresponds to the steps described in the previous section. Thus, the response of FS to WSE may appear smooth locally, however, there is enough noise that the gradient becomes erratic. Using the approximation of ∇FS over WSE 4.60 to 4.68 as a reference, the error term ε from Equation B.1 can be approximated, which is plotted in Figure B.2b. Depending on step size ΔWSE there is a maximum numerical noise on the order of 0.02 when the step size is above 0.1 m, although error decreases to the order of 0.001 for step sizes below 0.1 m. These results show that care must be taken to select finite difference step sizes in context of the discrete steps of ΔX and

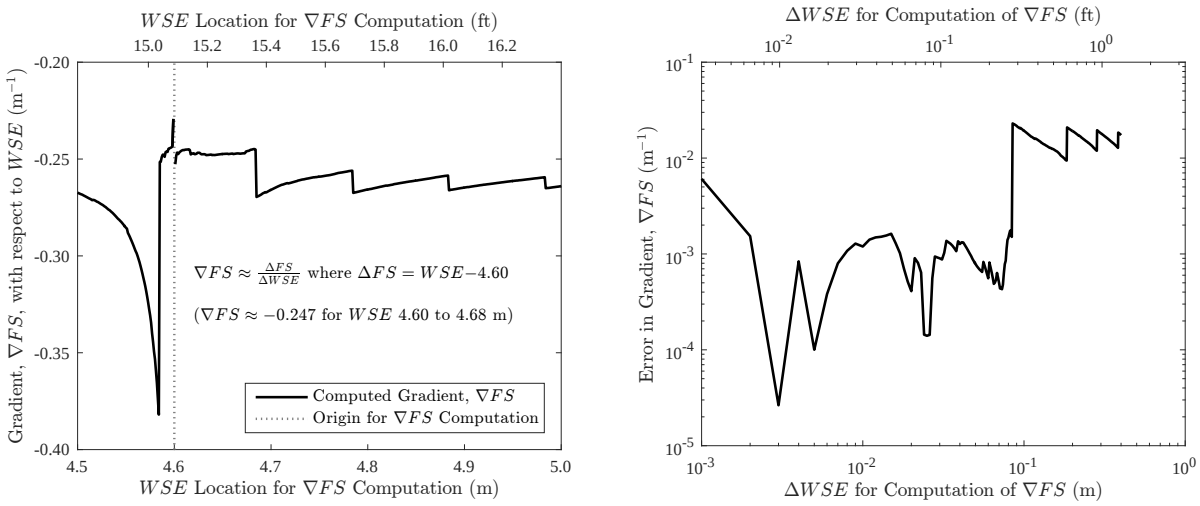

(a) ∇FS plotted against location of ΔWSE **(b)** Error in ∇FS as deviation from trendline

Figure B.2: Precision of gradient, ∇FS, for various finite difference increments, ΔWSE. The 200-yr WSE is used as the origin point for finding ΔWSE and ∇FS is plotted against $WSE = WSE_{200} + \Delta WSE$ in (a). Error in ∇FS is computed with respect to the trendline in Figure B.1

$\Delta f(X)$ implicit to the seepage and stability algorithms. While errors in gradient approximations may be small in the region between steps, computed values can be infinite if Δx_i happens to cross one.

B.4 Reliability Model

`FERUM` (Bourinet, 2010; Der Kiureghian et al., 2006) is used to conduct FORM analyses and must repeatedly evaluate the limit-state function for various combinations of random variables in x. The limit-state function is dependent on seepage and stability analysis, therefore, `FERUM` was integrated with the software `UNSAT` and `USlopeM` in Matlab. Careful attention must be given to numerical details to ensure the FORM algorithm converges to a solution, which are described in this section. Convergence of FORM becomes problematic when no closed-form solution of the limit-state function or its derivative is available, especially when finite element method (FEM) solutions are involved (Haukaas, 2003; Koduru & Haukaas, 2010; Sudret & Der Kiureghian, 2002); fortunately the iHL-RF algorithm (Zhang & Der Kiureghian, 1995) is most stable and least computationally expensive (Sudret & Der Kiureghian, 2000). In this research two problems prevented convergence during the iterative solution process: a) values of $\mathbf{x}$ were reached that had no solution for $g(\mathbf{x})$; and b) discontinuities in the limit-state function gradient, $\nabla g(\mathbf{x})$, prevented satisfaction of convergence criteria.

The limit-state function cannot be computed for all possible values of all random variables. For example, negative hydraulic conductivity ratio has no physical meaning, and therefore no solution in seepage or stability problems. Values of $\mathbf{x}$ required by FORM during the iHL-RF algorithm are directed by probability density and $\nabla g(\mathbf{x})$, and though an inadmissible solution does not necessarily stop the algorithm, it increases computation time at best and prevents convergence at worst.

To limit this occurrence, random variables can be truncated due to physical and numerical limits on parameters; however, as described for the truncated normal distribution, this has a quantitative effect on the PDF for the random variable. If a phyiscal limit for a random variable exists, for example with K_r or ϕ, it is logical that the PDF reflect this condition. Alternatively, if numerical limits may exist, for example, high effective cohesion due to root reinforcement may prevent Spencer's method from converging for a potential sliding surface. In this case, values should be limited to facilitate computation of a solution, but should not affect the PDF. Thus, physical limits should result in scaling of the PDF, whereas numerical limits should not. Fortunately FORM doesn't necessarily evaluate $g(\mathbf{x})$ across a wide range of the PDF for a specific random variable. For relatively reliable system components, extreme values of the most important parameters will be reached to result in $g(X) \leq 0$; it is in this region that numerical issues might occur. For example, for low WSE the blanket would need to be exceptionally thin to allow pore pressures to cause $FS \leq 1.0$, and convergence to steady-state pore pressures might not occur, or the mesh geometry must change within the sliding surface region, causing instability in the approximated limit-state function gradient. In this situation, an accurate assessment of β may not be possible, and relative comparisons should be employed for random variable importance and sensitivity measures. Alternatively, FORM iterations may reach the limit of a truncated distribution, for example, if the design point reaches the lower limit selected for z_B. For this case, physical distribution limits may be altered (while still preserving the desired PDF characteristics) to allow a solution, after which convergence to β may be achieved. In summary, consideration of the iteration values of $\mathbf{x}$ and the non-convergence design point can be used to adjust distribution parameters to reach FORM convergence.

For case b, above, the two criteria for assessing convergence of the FORM solution in the iHL-RF algorithm must be considered:

$$\left| \frac{G(\mathbf{u})}{G(\mu_{\mathbf{x}})} \right| \leq \varepsilon_1 \tag{B.3}$$

$$\left\| \mathbf{u}_i - \alpha_i \mathbf{u}_i \alpha_i^{\mathbf{T}} \right\| \leq \varepsilon_2 \tag{B.4}$$

where the subscript refers to iteration i. The condition for ε_1 ensures the design point, $\mathbf{u}^*$, lies on the limit state surface (i.e., $g(\mathbf{u}^*)$ is sufficiently close to zero), whereas ε_2 forces the design point to be normal to the origin, ensuring the design point is located in a maximum probability density region. Der Kiureghian et al. (2006), Haukaas (2003) recommend 0.001 for ε_1 and ε_2. Numerical noise in FEM analysis causes difficulty in reaching FORM convergence due to discontinuities in the limit-state function gradient (Haukaas & Der Kiureghian, 2006), which directly affects equation B.4 since α is a function of $\nabla g(\mathbf{x})$. This research uses a forward finite difference scheme (FFD) to evaluate $\nabla g(\mathbf{x})$ (Equation B.2), and as described in Section B.1, z_B and WSE are the two random variables that cause relatively large discontinuities in $FS(\mathbf{x})$ that cannot be controlled with software parameters or simple source code modification. As such, forward finite difference step size, Δx_{ffd}, must be selected to minimize gradient discontinuities. Ideally a Δx_{ffd} should be chosen much larger than the increment causing a discontinuity, which would minimize the error in gradient computations. Fortunately this is possible for z_B, since discontinuities occur for relatively small Δz_B of about 0.001 m. For WSE, the discontinuities are much larger (0.1 m), and are close to the second (and larger scale) ΔWSE that causes gradient errors. If the design point is located close to a discontinuity in $g(WSE)$ modifications to the FERUM algorithm for FFD computations

is necessary. FERUM uses a single parameter, f, to select Δx_{fd} as a function of the standard deviation for a random variable: $\Delta x_{fd} = \sigma_i / f$. If f or Δx_{fd} can be selected as an absolute value for each parameter, better control over FORM convergence can be achieved. For the case of z_B, $\Delta x_{fd} \gg 0.001\,\text{m}$, and for WSE, $1\text{e}-5\,\text{m} \ll \Delta WSE_{fd} \ll 0.1\,\text{m}$. Because the distance between problematic step scales is small for WSE, if the direction of the finite difference step can switch (i.e., $\Delta WSE_{fd} < 0$) depending on the estimated error of $\nabla g(WSE)$, convergence could be improved, thus "avoiding" the step in $g(WSE)$. Definition of x_{fd} as a specific value is referred to in this document as a Type I finite difference approximation; definition as a specific value with dynamic direction selection is referred to as Type II.

Selection of x_{fd} for Type I FD should simply be selected to span discontinuous step(s) and provide an acceptable approximation for $\nabla g(\mathbf{x})$. For Type II, $g(\cdot)$ must evaluated twice at $x \pm x_{fd}$, effectively setting up a forward or backward finite difference approximation. The differences $\text{d}g_f = |g(x_0 + x_{fd}) - g(x_0)|$ and $\text{d}g_b = |g(x_0 - x_{fd}) - g(x_0)|$ are compared to a user-defined value, $\text{d}g_{min}$, which corresponds to the minimum expected discontinuous step. For the example of WSE, this would be ~ 0.002 m (Figure B.1b). If a single step exists in the region $x \in (x_0 - x_{fd}, x_0 + x_{fd})$ then it will be implicitly added to $\text{d}g_f$ or $\text{d}g_b$, thus if $(\text{d}g_f - \text{d}g_b) > \text{d}g_{min}$ a step is assumed to be present. As implemented in the modified source code of FERUM, if $\text{d}g_f$ and $\text{d}g_b$ are less than $\text{d}g_{min}$ the averaged value is used for $\nabla g(\mathbf{x})$. If $\text{d}g_f$ *or* $\text{d}g_b$ is greater than $\text{d}g_{min}$ a discontinuity is assumed and the other value is used for $\nabla g(\mathbf{x})$. If $\text{d}g_f$ and $\text{d}g_b$ are greater than $\text{d}g_{min}$ the average is used (and Type II FD is ineffective). This approach successfully allowed for convergence of the FORM algorithm in the order of 10 iterations for $\varepsilon_1 = \varepsilon_2 = 0.001$ where convergence could not be reached in at least 250 iterations otherwise. It is especially useful when used with the random variable WSE. Note, however, that if $\nabla g(x_i) \sim 0$ for $x \in (x_0, x_0 + x_{fd})$ or $x \in (x_0 - x_{fd}, x_0)$ Type II FD will fail, although the unmodified version of FORM will also not likely reach convergence. Using Type I or II FD has a numerical effect on the solution; however, the effect is typically small and should result in a better estimate of reliability since Δx_{fd} is chosen with respect to the specific numerical characteristics of each random variable. For example, when $\Delta_{ffd} = 0.01$ (in SI units) for γ, c and ϕ, 0.1 m for z_B, 100 for K_r and 0.01 m for WSE convergence is achieved in 9 iterations instead of 10 with β changing from 2.949 to 2.984 (p goes from 0.16% to 0.14%). Although differences in importance vectors with and without the Type I correction are generally 10%, the relative magnitudes of each are random variable are preserved.

Although the iHL-RF algorithm is generally capable of finding the FORM design point consistently numerical issues can prevent convergence. Preliminary analyses with FORM using relaxed tolerances to find an approximate solution can provide guidance for adjusting parameters to improve convergence and reach a more precise solution. Careful selection of random variable distribution parameters and FFD step size and direction are the best methods available. Although this approach adds additional analyses and complexity to the algorithm, it is likely to reduce overall computation time by eliminating unnecessary iterations due to oscillating steps in the FORM algorithm caused by numeric noise.